Title
HEAVY ION EXPERIMENTS

Author
Scott, David K.

Publication Date
1977-07-01

Lectures presented in part at the
Scottish Universities' Summer School
in Physics (St. Andrews, 1977) and the
Latin American Summer School in Physics
(Mexico City, 1977)

LBL-7111 c. 2
Preprint

HEAVY ION EXPERIMENTS

David K. Scott

July 1977

Prepared for the U. S. Department of Energy
under Contract W-7405-ENG-48

HEAVY ION EXPERIMENTS

David K. Scott

Lawrence Berkeley Laboratory, University of California
Berkeley, California 94720

1.

1.1 Introduction

Heavy-ion reactions have created great enthusiasm among nuclear researchers and funding agencies all over the world. The progress over the last five years in understanding the potentially highly complicated processes of two composite systems in collision can only be described as astonishing. It is a tribute to the ingenuity of experimentalists and theoreticians alike, although it presents a sobering prospect to lecturers, hoping to cover the field in six lectures. Heavy-ion beams as massive as uranium up to 10 MeV/A and lighter beams up to 2 GeV/A are now available, so that it has become feasible to study the characteristics of nucleus-nucleus interactions over a wide range of incident energies and for a large variety of colliding nuclei. (Useful sources on developments in the field are contained in Refs. 1 - 16.)

The motivation for such developments becomes obvious when we take a panoramic view of the stability diagram(17) for nuclear species in Fig. 1.1. There are only 300 stable nuclear species. During the last half-century only some 1300 additional radioisotopes have been identified and studied. It is estimated, however, that in the interaction of 2 GeV U + U ions, 6000 different isotopes could be formed. In our present state of ignorance, an attempt at extrapolation of our current state of knowledge to the description of all nuclear species is analogous to describing the geography of the United States by extrapolation from a detailed study of the floor of the Grand Canyon — in the words of D. A. Bromley.(17)

Heavy-ion reactions permit a large scale attack on the uncharted territory of this diagram. They will enable us to probe the limits of nuclear stability, to see whether extremely neutron-rich isotopes such as ^{28}O and ^{70}Ca are stable. They will enable us to discover new modes of motion of the nucleus, in the form of high-spin states, and new regions of deformation. They lead to totally new reaction mechanisms, possibly to new forms of nuclear matter under extraordinary conditions of temperature and pressure.

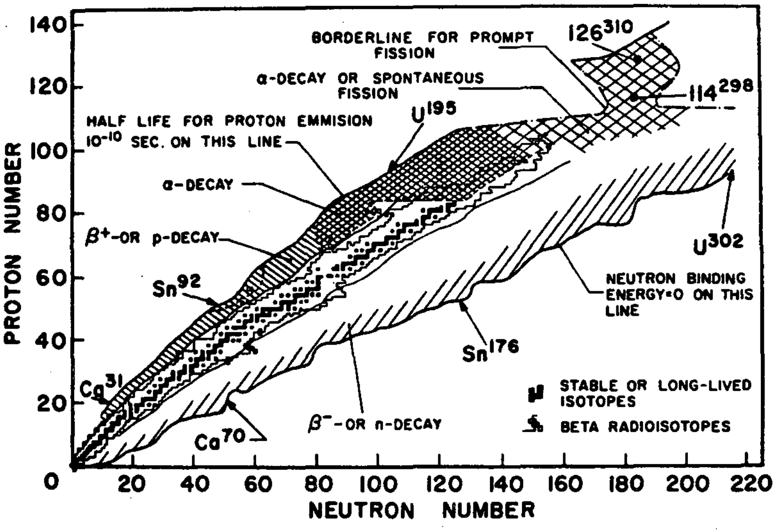

XBL 777-9479

Fig. 1.1

Figure 1.2 is a useful navigation chart to the types of phenomena heavy-ion reactions are likely to reveal,(18,19) some of which will be covered in these lectures. The abscissa is the projectile energy in

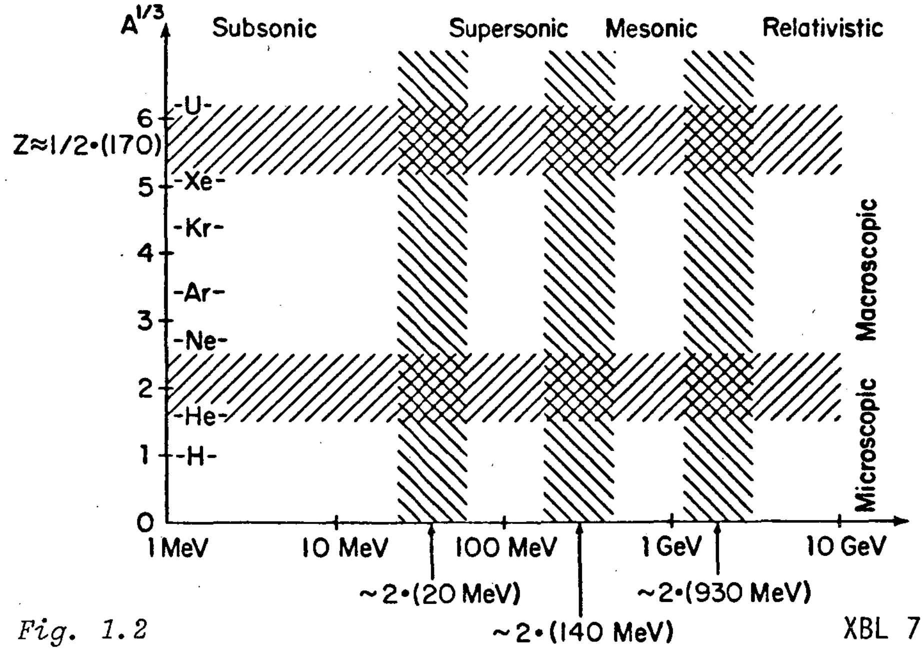

Fig. 1.2

XBL 754-2816

MeV/nucleon and the ordinate is the projectile mass plotted as $A^{1/3}$. The shaded bands define certain regions of fundamental parameters, such that when one crosses a band, one is confident that the underlying physics will change. The three characteristic center-of-mass energies of 20 MeV, 140 MeV, and 930 MeV/A are estimates of where the subsonic, supersonic, mesonic, and relativistic domains merge. Macroscopic phenomena come into prominence when $A^{1/3} >> 1$. The band at $Z \approx \frac{1}{2}$ (170) is a reminder of the changes that may occur when (2Z × fine structure constant) begins to be large compared to unity. Most of this space is unexplored, apart from the two axes, the left-hand side with low energy heavy-ion machines and the horizontal axis with high energy proton accelerators. Only recently has it become possible to make an excursion along the first horizontal band.

1.2 *Scheme of the Lecture*

These lectures will attempt to survey the experiments (and the interpretations) on heavy-ion reactions, both in the old and new regions of the space in Fig. 1.2. The organization is as follows:

Lecture 1: Some characteristic features of heavy-ion reactions, applied mainly to elastic scattering phenomena.

Lecture 2: Transfer reactions. The characteristic mechanisms and excitation of new types of discrete states and new nuclei with heavy-ion reactions.

Lecture 3: More drastic perturbations of the nucleus, leading to our knowledge of new states, high in the continuum, and new modes of motion. Mainly compound nuclear reactions.

Lecture 4: Fusion and fission with heavy ions — i.e., more drastic still than Lecture 3; macroscopic phenomena.

Lecture 5: The new characteristic heavy-ion reaction mechanisms, particularly deeply-inelastic scattering; microscopic and macroscopic approaches.

Lecture 6: Up in energy; the evolution of reaction mechanisms with heavy ions from MeV/A to GeV/A. Some exotic new phenomena.

In the lectures I shall attempt to give physical insight into the processes of heavy-ion collisions by resorting to analytical formulations which do not do justice to the remarkably precise calculations in existence. Also I hope that the lectures will convey some idea of the unity of the different branches into which heavy-ion physics is increasingly divided — microscopic and macroscopic, low and high energy, etc.

1.3 Characteristics of Heavy-Ion Collisions and Elastic Scattering

In the collision of nuclei with charge and mass numbers Z_1, A_1 and Z_2, A_2, some useful quantities are defined in Fig. 1.3.

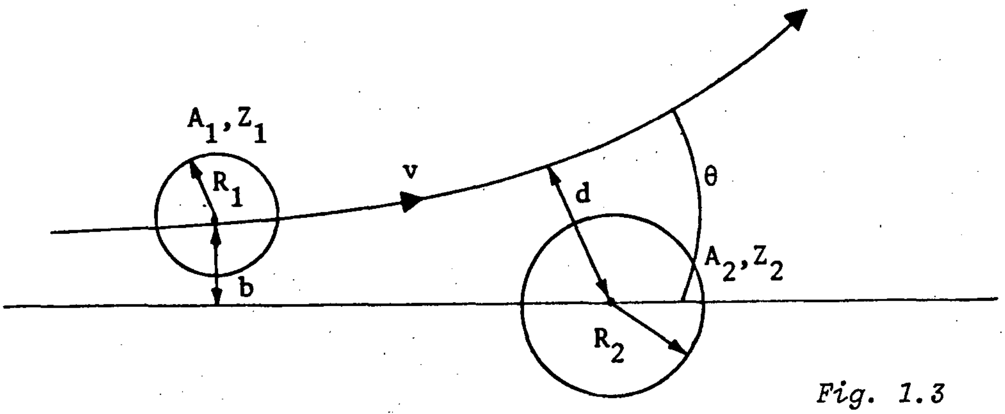

Fig. 1.3

Reduced mass $\mu = \frac{mA_1A_2}{A_1+A_2}$, m = nucleon mass . (1.1)

Relative velocity = v

$$\frac{v}{c} = \sqrt{\frac{E_{lab}}{469A_1}} , \quad \text{E in MeV} . \tag{1.2}$$

Wave number $k = \frac{1}{\lambda\!\!\!^{-}} = \frac{\mu v}{\hbar} = \frac{4{\cdot}8A_1A_2}{A_1+A_2}\left(\frac{v}{c}\right)$. (1.3)

Kinetic energy of relative motion $E = \frac{1}{2}\mu v^2$. (1.4)

Half distance of closest approach in head-on collision

$$a = \frac{Z_1Z_2e^2}{\mu v^2} = \frac{Z_1Z_2}{2E_{cm}}\left(\frac{e^2}{\hbar c}\right)\hbar c . \tag{1.5}$$

Sommerfeld parameter $\eta = ka = \dfrac{Z_1 Z_2 e^2}{\hbar v}$ (1.6)

Classical impact parameter = b.

Associated angular momentum = kb = ℓ (partial wave).

Scattering angle = θ

Strong interaction radius $R = R_1 + R_2 = r_o(A_1^{1/3} + A_2^{1/3})$.

For a Rutherford orbit,

$$\begin{aligned} d &= a(1 + \operatorname{cosec} \theta/2) \\ &= a + \sqrt{a^2 + b^2} \\ &= \eta/k \;(1 + \sqrt{1 + (\ell/\eta)}^2 \end{aligned} \quad (1.7)$$

Critical scattering angle θ_g or θ_c when $d = R$.

$$\sin \frac{\theta_c}{2} = \frac{a}{R - a} \quad (1.8)$$

$$b_c = R\sqrt{1 - 2a/R} \quad (1.9)$$

$$\ell_c = kb_c = kR(1 - 2\eta/kR) \quad (1.10)$$

Heavy-ion reactions are characterized by large values $kR = R/\lambdabar \gg 1$, as illustrated in Fig. 1.4, which is a plot$^{(20)}$ of the ratio $R/\lambdabar$ for energies above the barrier, and of the ratio of the distance of closest approach in head-on collision to $\lambdabar$, below the barrier, for ^{40}Ar + Hg. Such considerations lead us to the concept of a semi-classical trajectory associated with different impact parameters (to be elaborated in Chapter 2).

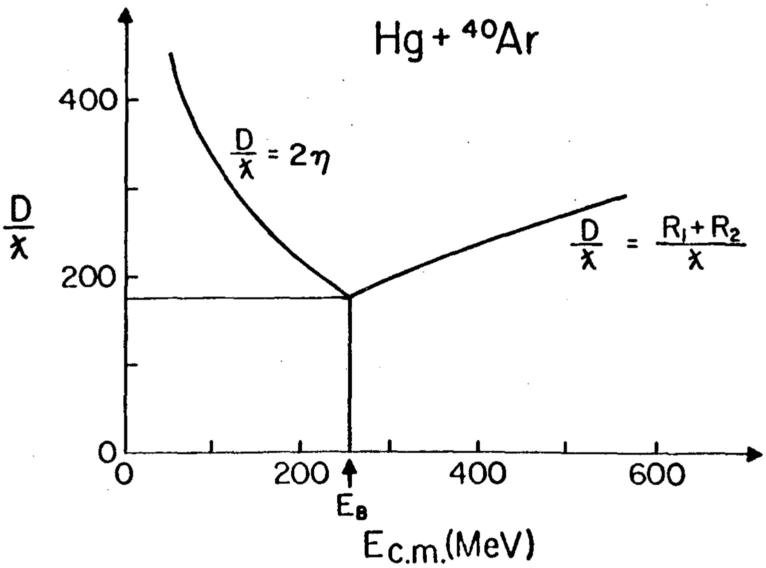

Fig. 1.4

XBL 777-9483

Figure 1.5 illustrates some computed trajectories for the scattering of ^{18}O on ^{120}Sn at 100 MeV.(21) Number 1 follows a Rutherford orbit (the circle marks the size of the two nuclei, and the axes are in Fermis) as does orbit g for the grazing collision. Orbit 2 begins to feel the attractive nuclear potential and is pulled forward to scatter at the same angle as 1 (the dotted line shows its path in the presence of the Coulomb potential only). Similarly, orbit 3 is pulled from the opposite side of the nucleus. The information on this diagram can be more concisely displayed in a *deflection function diagram*(21) (Fig. 1.6) which plots the relation between ℓ and θ.

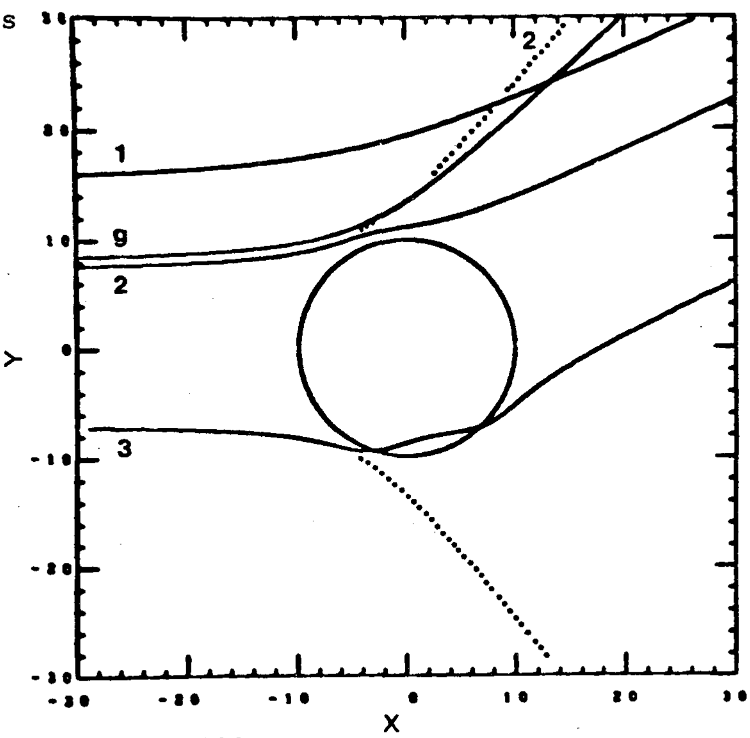

XBL 745-920

Fig. 1.5

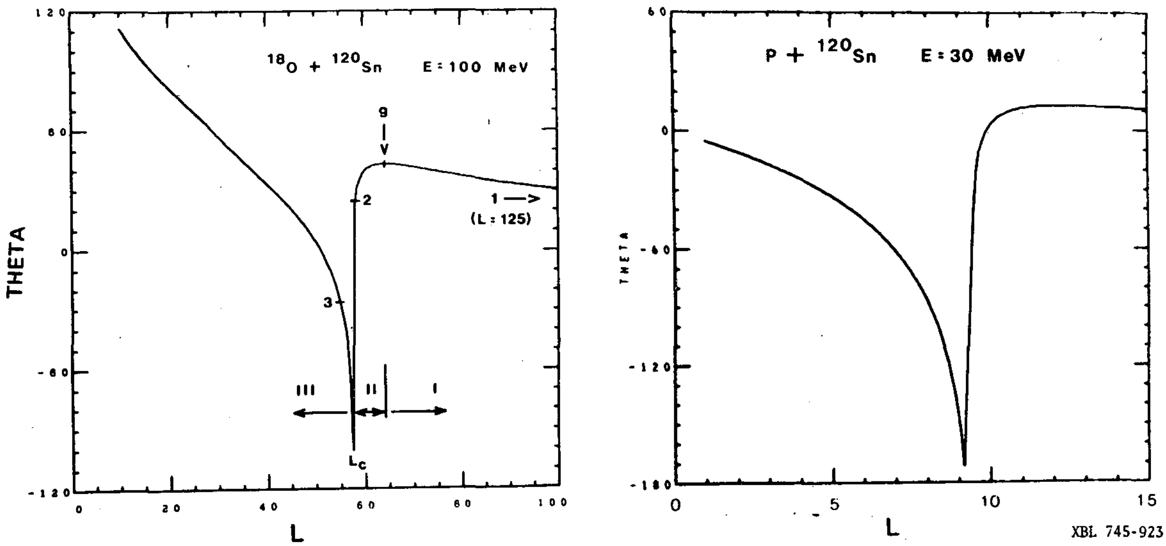

XBL 745-923A

(a)

(b)

Fig. 1.6

Classically ℓ can have any value, but in quantum mechanics only integer values are allowed. The deflection function for O + Sn is sampled at very small intervals, in contrast to a typical proton-induced reaction which is sampled very sparsely in ℓ. Only when the density of angular momentum states per unit impact parameter ($\ell/b = k$) is large does the classical description become useful. The diagram illustrates that several orbits scatter to the same angle (which is important for transfer reactions in the next section). For elastic scattering the orbits up to grazing are most important and lead us to predict an elastic scattering distribution (Fig. 1.7)

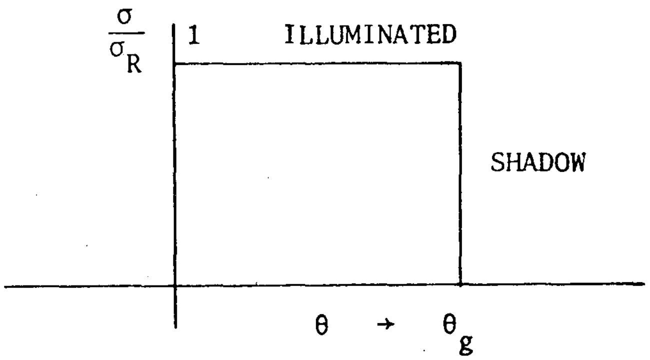

Fig. 1.7

We compare this zeroth order prediction with the two standard forms occurring experimentally in Fig. 1.8, which shows(22) the scattering of ^{16}O of 10 MeV/nucleon on ^{208}Pb and ^{12}C.

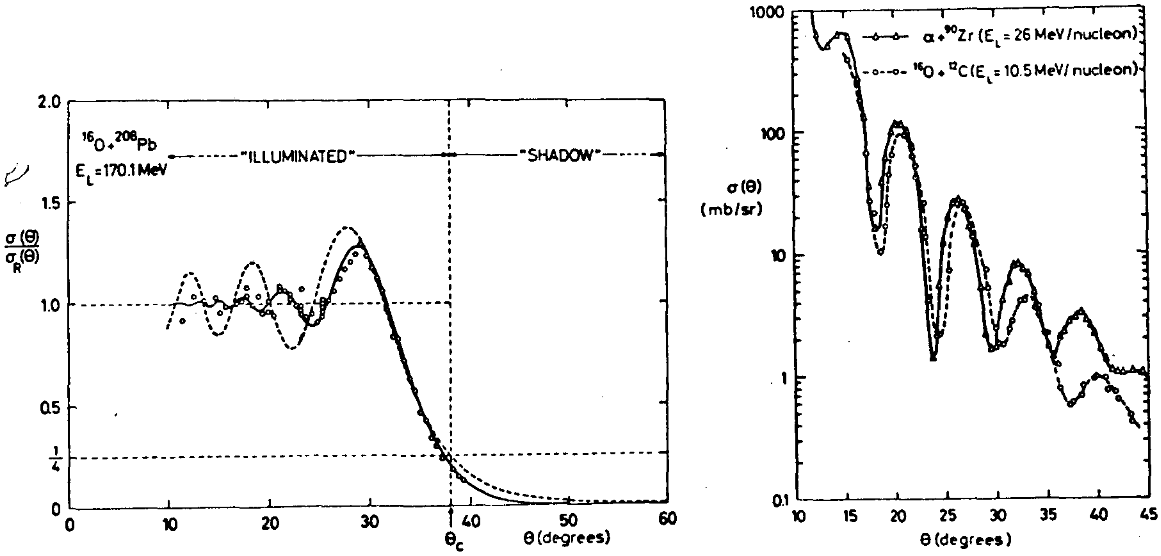

(a) *(b)*

Fig. 1.8

XBL 776-9497

These are examples of Fresnel and Fraunhoffer diffraction. In the case of ^{16}O + Pb, the scattering is Coulomb-dominated and the *average trend* is that of Fig. 1.7. At first sight it is paradoxical that Fresnel patterns should be observed in nuclear physics because the particle source (collimating aperture of the accelerator beam) and the point of observation (detector) are essentially at infinite distances compared to the dimensions of the scatterer. If the energy is high, so that $\lambdabar \ll R$ (as we have seen) we have the conditions for Fraunhoffer diffraction. The paradox is resolved by remembering that in Coulomb-dominated situations, the deflection of the trajectory brings the virtual source close to the scattering center$^{(22)}$ (see Fig. 1.9).

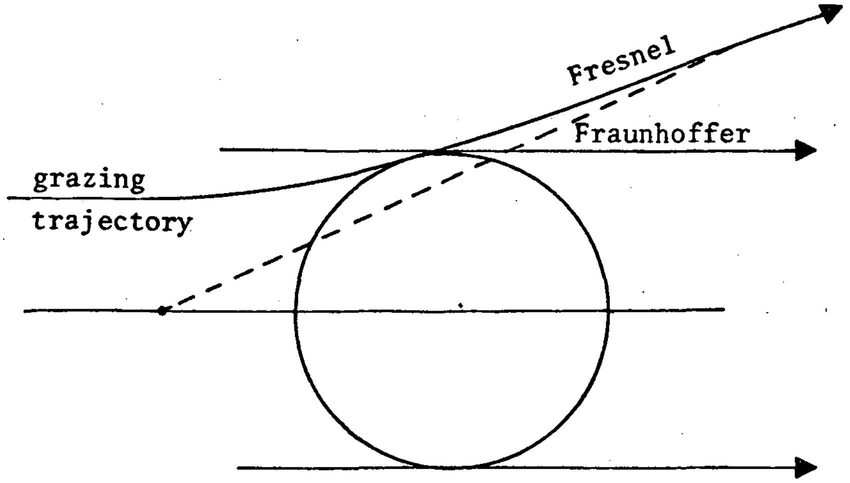

Fig. 1.9

Although an interpretation of *both diffractive patterns* is possible in the framework of Fig. 1.5, by introducing *complex* trajectories,$^{(23,24)}$ we shall not develop this approach further.

1.4 More Formal Treatment of Elastic Scattering

The scattering amplitude can be written

$$f(\theta) = \frac{1}{ik} \sum_{\ell} (2\ell+1) P_{\ell}(\cos\theta) \left(e^{2i\delta_{\ell}} - 1\right) \tag{1.11}$$

Using semi-classical ideas:$^{(25)}$

a) Replace ℓ by continuous variable L, $\ell + \frac{1}{2} \rightarrow L$.

b) Assume continuous variation of phase shift $\delta(L)$ with L.

c) Replace $P_{\ell}(\cos\theta)$ by an asymptotic form for large L.

d) Replace Σ by $\int$.

Then

$$f(\theta) \approx \frac{1}{ik} \int L \, dL \, J_o(L \sin\theta) \left(e^{2i\delta(L)} - 1 \right)$$

is valid if $\theta \lesssim \pi/6$.

1.4.1 Fraunhoffer scattering

If we set

$$e^{2i\delta(L)} = 1, \quad L > L_c$$
$$= 0, \quad L < L_c \; ,$$

(i.e., no scattering if $L > L_c$, complete absorption if $L < L_c$), the integral can be evaluated to give the diffractive cross section

$$\sigma_D(\theta) \approx (kR^2)^2 \left[\frac{J_1(kR\theta)}{kR\theta} \right]^2$$

where $L = kR$. This diffraction cross section has a characteristic oscillatory behavior with spacing

$$\Delta\theta_D \approx \pi/kR \; .$$

In order to discover the predicted trend of differential cross sections we tabulate some values of parameters in Table 1.1. We see that the $^{16}O + {}^{12}C$ reaction at 168 MeV has a small Sommerfeld parameter η and has similar values of η, kR, $\lambda\!\!\!^-$, a, R, θ_c to the reaction $\alpha + {}^{94}Zr$ at 104 MeV. There is therefore nothing mysterious about the almost exactly similar differential cross sections shown in Fig. 1.8(b), of the predicted Fraunhoffer diffraction spacing = 4.6°.

TABLE 1.1. Interaction radius computed as $r_o(A_1^{1/3} + A_2^{1/3})$ with r_o = 1.6 fm.

Ions	a	R (fm)	$\lambda\!\!\!^-$	E (MeV)	ν/c	η	θ_c	kR	$\Delta\theta_0$
$\alpha + {}^{94}Zn$	0.577	9.81	0.231	104	0.235	2.49	7.17	42	4.24
$^{16}O + {}^{12}C$	0.479	7.69	0.203	168	0.150	2.34	7.62	38	4.74
$^{16}O + {}^{208}Pb$	1.628	13.51	0.069	312	0.204	23.5	17.75	197	0.92
$^{238}U + {}^{238}U$	5.114	19.83	0.033	2380	0.053	1166	40.67	600	0.30

1.4.2 Fresnel diffraction

A reaction such as $^{16}O + {}^{208}Pb$ is characterized by a large η parameter and is Coulomb-dominated, leading to Fresnel scattering (the Fraunhoffer scattering would be difficult to observe experimentally since $\Delta\theta_D \approx 0.3°$).

In this case we make the large angle approximation in $f(\theta)$:

$$f(\theta) \approx \frac{1}{ik}\int_0^\infty L\,dL\left(\frac{2}{\pi L\sin\theta}\right)^{\frac{1}{2}}\cos\left(L\theta-\frac{\pi}{4}\right)\left(e^{2i\delta(L)}-1\right) \tag{1.16}$$

At a scattering angle θ, the main contribution to the integral comes from values of L near L_θ given by

$$2\left(\frac{d\delta(L)}{dL}\right)_\theta = \pm\theta \tag{1.17}$$

[Note: This is an equation for L_θ: for Coulomb phase shifts gives $L_\theta = \eta\cot(\theta/2)$.]

Expand $\delta(L)$ about L_θ:

$$\delta(L) = \delta(L_\theta) + \left(\frac{d\delta}{dL}\right)(L-L_\theta) + \frac{1}{2}\left(\frac{d^2\delta}{dL^2}\right)(L-L_\theta)^2 + \ldots. \tag{1.18}$$

$$\therefore\ 2\delta(L) = 2\delta(L_\theta) + \theta(L-L_\theta) + \frac{1}{2}\left(\frac{d\theta}{dL}\right)(L-L_\theta)^2 + \ldots. \tag{1.19}$$

Taking out slowly varying functions, and replacing the lower limit of integration by L_c (i.e., sharp cut-off model):

$$f(\theta) \approx \frac{1}{k}\sqrt{\frac{L_\theta}{2\pi\sin\theta}}\,e^{i\alpha(\theta)}\int_{L_c}^\infty dL\,\exp\left[\frac{i}{2}\left(\frac{d\theta}{dL}\right)_\theta(L-L_\theta)^2\right] \tag{1.20}$$

This is just the Fresnel integral (compare Fig. 1.8(a)).

Introducing a new variable x by

$$\pi x^2 = \left(\frac{d\theta}{dL}\right)_\theta (L-L_\theta)^2 \tag{1.21}$$

$$f(\theta) = \frac{1}{k}\sqrt{\frac{L_\theta(dL/d\theta)_\theta}{2\sin\theta}}\,e^{i\alpha(\theta)}\int_{x_c}^\infty dx\,\exp\left(\frac{i\pi}{2}x^2\right) \tag{1.22}$$

The integral can be evaluated, replacing $x_c \to -\infty$, i.e. $L_c \ll L_\theta$, as $\sqrt{2}\,e^{i\pi/4}$. Then

$$f(\theta) = \frac{1}{k}\sqrt{\frac{L_\theta(dL/d\theta)}{\sin\theta}}\; e^{i\bar{\alpha}(\theta)} \qquad \text{where} \qquad \bar{\alpha} = \alpha + \frac{\pi}{4}\left(\frac{d\theta}{dL}\right)_\theta \tag{1.23}$$

and

$$\sigma(\theta) = |f(\theta)|^2 = \frac{1}{\sin\theta}\left(\frac{bdb}{d\theta}\right) \tag{1.24}$$

where $L_\theta = kb_\theta$, which is just the classical scattering formula.

Now we note that if x_c is set equal to zero, i.e., $L = L_c$, we have the simple result that at the *critical angle* θ_c,

$$\frac{\sigma(\theta)}{\sigma_R(\theta)} = \frac{1}{4} \tag{1.25}$$

which is the origin of the famous "quarter-point" recipe.(26) We shall see that this point (and others closely related) dominate most heavy-ion elastic scattering experiments. To make further progress we either have to introduce more elaborate parameterizations of the phase shifts(27) (which *can* be done, e.g. smooth cut-off instead of sharp cut-off) or resort to the common practice of dressing everything up by an *optical potential.*

1.5 Optical Model Analysis of Elastic Scattering

1.5.1 Saxon-Woods potentials

Most analyses have used a Saxon-Woods nuclear optical potential. (The Coulomb and centrifugal potentials must also be included.)

$$U(r) = -V(e^x + 1)^{-1} - iW(e^{x'} + 1)^{-1} \tag{1.26}$$

where

$$x = (r - R)/a \qquad R = r_o(A_1^{1/3} + A_2^{1/3})$$

$$x' = (r - R')/a \qquad R' = r_o'(A_1^{1/3} + A_2^{1/3})$$

Most often the four-parameter form, $R = R'$ and $a = a'$, is used.

The most coherent picture would be that of quoting a global set of parameters, but we are not quite there yet. There are tremendous ambiguities associated with the potentials for the scattering of strongly absorbed particles, which are sensitive only to the extreme tail of the potential. Thus for large radial distances we obtain:

$$\mathrm{Re}\,U(r) \approx -\big(V \exp(R/a)\big) \exp(-r/a) \quad ,$$

and for a fixed value of a, *any* pair V,R which keep V exp(R/a) constant will give the same tail.

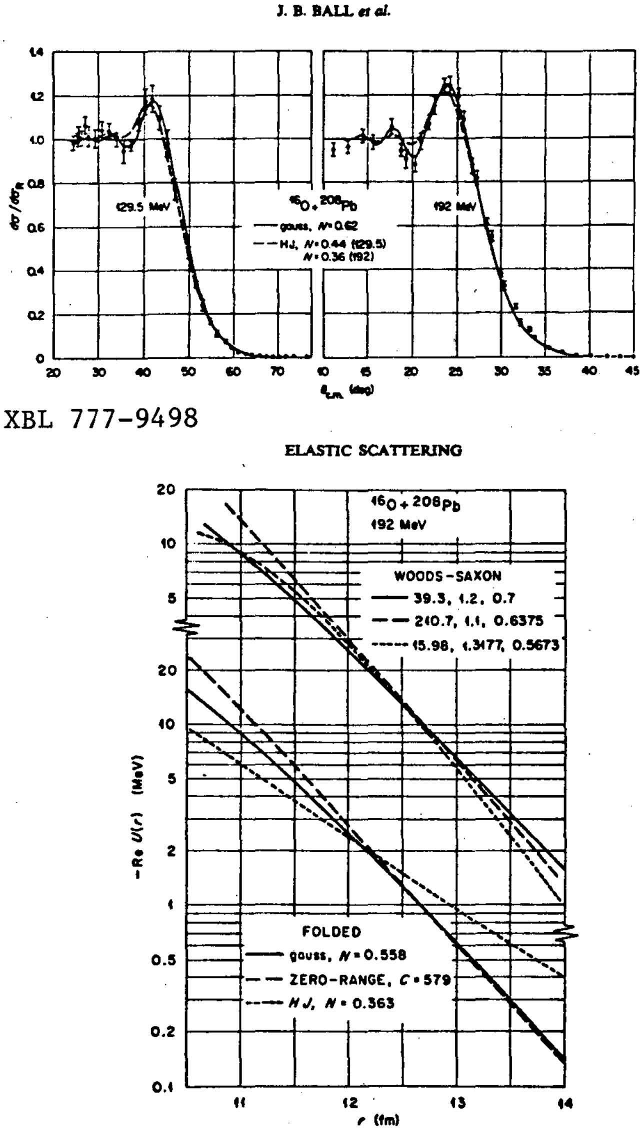

XBL 777-9498

Fig. 1.10

As an example, consider data for the reaction $^{16}O + ^{208}Pb$ at 192 MeV shown in Fig. 1.10(a) (similar to that shown in Fig. 1.8(a)). The analysis with Saxon-Woods potentials in Fig. 1.10(b) illustrates three potentials which fit the 192 MeV data equally well.(28) *Only the value of the potential at 12.5 fm is well determined.* Note that the actual value of the nuclear potential at this point (≈1 MeV) is very small compared to the Coulomb (≈75 MeV). The cross-over point is called the *sensitive radius* (R_s) and has the same significance as the Fresnel ¼-point discussed previously.(29) In fact, from Fig. 1.10(a), $\theta_{\frac{1}{4}} = 31.4°$. Then,

$$L_{\frac{1}{4}} = \eta \cot(\theta_{\frac{1}{4}}/2) = 105 \quad , \qquad \eta = 29.9 \tag{1.27}$$

and

$$R_{\frac{1}{4}} = \eta/k \left(1 + \sqrt{1 + (L/\eta)^2}\right) = 12.2 \text{ fm} \tag{1.28}$$

which is close to the 12.5 fm of the cross-over. The point also coincides with the radius associated with the ℓ-value at which the optical model transmission coefficient drops to ½, ($R_{\frac{1}{2}}$), and $L_{\frac{1}{2}} = 106$ in the above example. This distance is typically 2 or 3 fm *larger* than the sum of the radii of the two ions, at which their densities fall to one-half of the central value.(29) Even when absorption is almost complete, only the 10% regions overlap.

Increasing the bombarding energy might enable the potential to be sampled at smaller distances. The $^{16}O + {}^{208}Pb$ system has now been studied at a number of laboratories(30) from the barrier at 5 MeV/A to 20 MeV/A. The extracted values of R_s, $R_{1/4}$, $R_{1/2}$ are shown in Fig. 1.11. The penetration depth does not increase very much, and elastic scattering probes are severely limited to a region of the surface.

Higher bombarding energies have been used in an attempt to resolve the ambiguities in the $^{16}O + {}^{28}Si$ system.(31) The possibilities at 200 MeV are illustrated in Fig. 1.12, where the deep potential of 100 MeV gives rise to a "rainbow scattering" (associated with a turning point in the deflection function, see Fig. 1.6). The experimental data(32) appear in Fig. 1.13, and favor the potential:

$$V = 10 \;, \qquad W = 23.4 \;,$$
$$r_0 = 1.35 \;, \qquad r_0' = 1.23 \;,$$
$$a = 0.618 \;, \qquad a' = 0.552 \;.$$

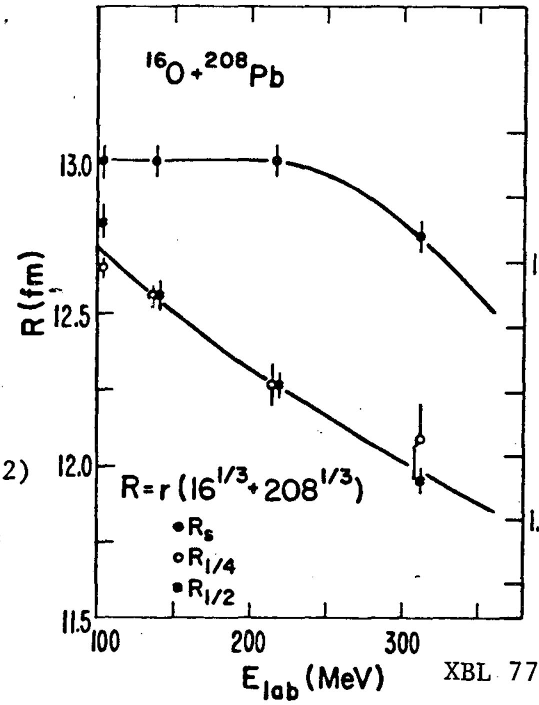

XBL 777-1419

Fig. 1.11

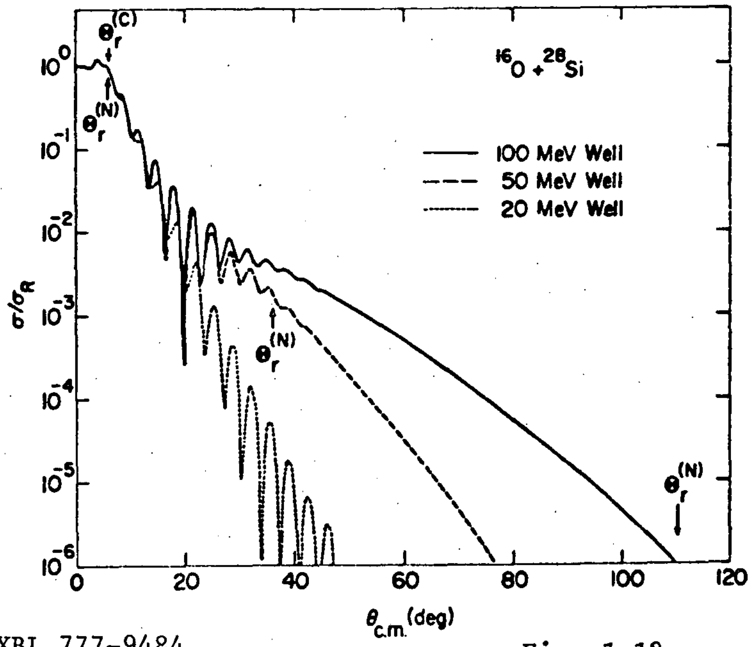

XBL 777-9484

Fig. 1.12

This potential is derived assuming energy independence, which is expected to be small for heavy-ion potentials.(33) Does the preference really mean that overlapping ^{16}O and ^{28}Si nuclei really have such a weak interaction? To gain more insight we now discuss derivation of potentials from more "fundamental" viewpoints, e.g., *folding potentials* and *proximity* *potentials.*

1.5.2 Folding potentials

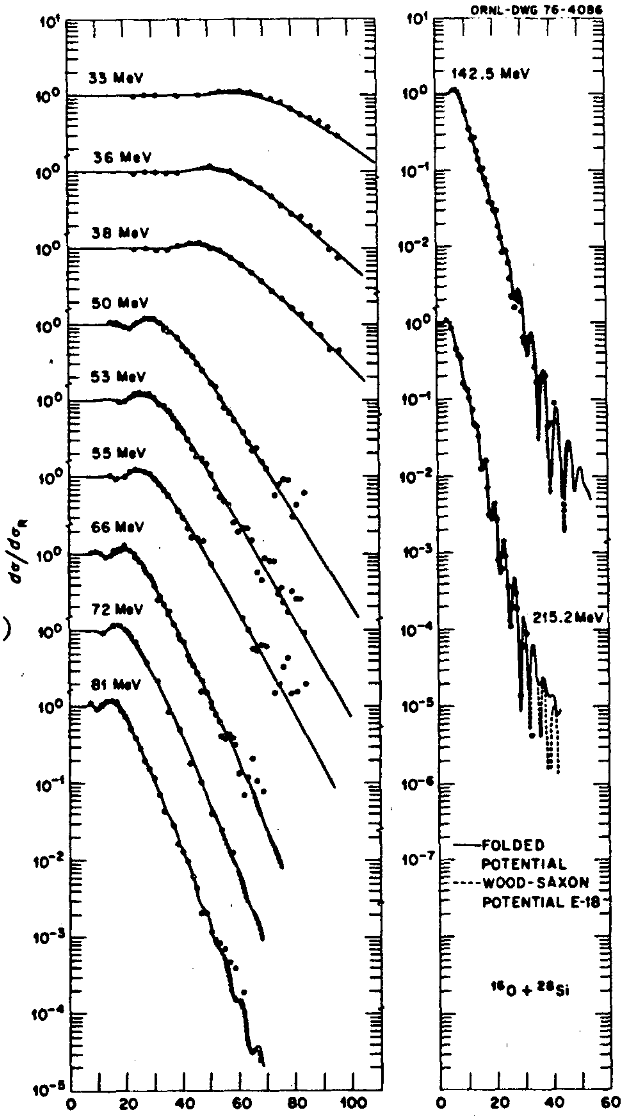

XBL 777-9494

Fig. 1.13

The philosophy behind the double-folding model is based on the fact that the scattering is dominated by the real potential at large distances.(28,34) In this low-density overlap region one can assume that nucleons interact as if they were free. Then,

$$U(r) = \int d\underline{r_1} \int d\underline{r_2}\, \rho_1(r_1)\, \rho_2(r_2)\, \nu(r_{12}) \tag{1.29}$$

where ρ is the matter distribution, and $\nu(r_{12})$ is the nucleon-nucleon interaction. The coordinates are shown in Fig. 1.14(a). The potentials generated by this model(29) are very deep in the center (see Fig. 1.14(b)), typically 600 MeV (compared to 10-50 MeV for Saxon-Woods potentials). Predicted distributions for $^{16}O + ^{208}Pb$ are shown in Fig. 1.10(a) for Gaussian and Hamada-Johnson nucleon-nucleon interactions, but these potentials still result in similar sensitive radii (Fig. 1.10(b)) to the S-W potential. What happens inside this radius seems to be irrelevant

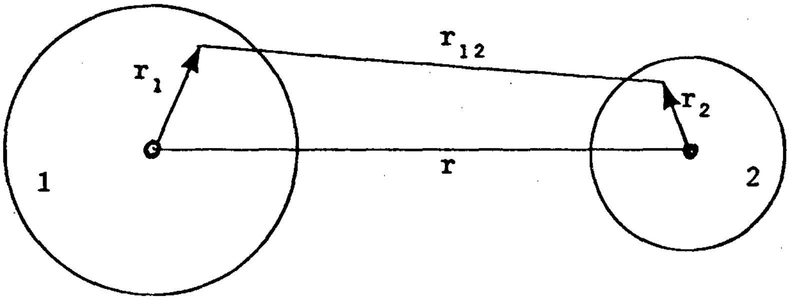

Fig. 1.14(a)

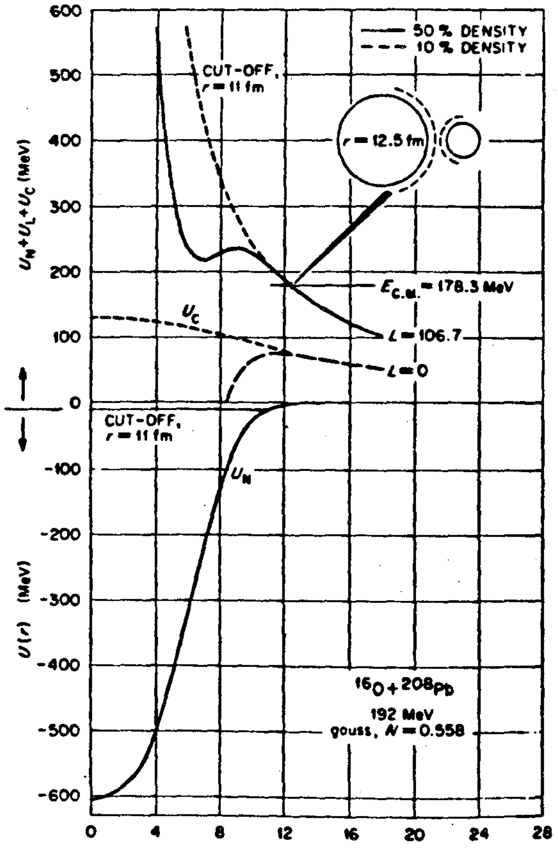

XBL 777-9496

Fig. 1.14(b)

as far as elastic scattering is concerned. The folding potential also fits the $^{16}O + ^{28}Si$ data (see Fig. 1.13). Recent results(35) on the scattering of ^{6}Li ions on ^{28}Si show effects of a nuclear rainbow similar to that observed in α scattering. The transition in scattering characteristics therefore appears to take place suddenly between Li and ^{12}C ions.

1.5.3 Potentials from the liquid drop model

For a *dynamical* description of heavy-ion reactions (which we shall need later) it is necessary to know the potential at much closer distances. Another distance where the nucleus-nucleus interaction is established can be estimated from the liquid-drop model. This is the distance corresponding to the sum of the half-density radii R_1 and R_2 where the attractive force can be estimated:(36)

$$F = 4\pi\gamma \frac{R_1 R_2}{R_1 + R_2} \qquad R_1 + R_2 = R_0 \qquad (1.30)$$

where $\gamma \approx 0.95$ MeV•fm^{-2} is the surface tension coefficient. The previously determined sensitive radius and the value of the potential at this point, together with the value of the force:

$$\left(\frac{dV}{dr}\right)_{r=R_0} = \frac{V}{4a} = 4\pi\gamma \frac{R_1 R_2}{R_0} \qquad (1.31)$$

determine the two parameters V and a. The sum of the half density radii $R_1 + R_2$ can be evaluated using expressions of the form:(37)

$$R_1 = 1.12\ A^{1/3} - 0.86\ A^{-1/3}$$

(The deviation from strict proportionality to $A^{1/3}$ comes from purely geometrical considerations of a spherical density distribution with a diffuse surface.) Using these equations, the nuclear potential can be calculated for any target projectile combination, and lead typically to potentials 60 MeV deep, of diffuseness 0.85 fm.

These simple considerations have been generalized by the *Proximity Force Theorem* which states:(38)

> *"The force between rigid gently curved surfaces is proportional to the potential per unit area between flat surfaces."*

For frozen, spherical density distributions, the force between two nuclei as a function of distance s between their surfaces is

$$F(s) = 2\pi \frac{R_1 R_2}{R_1 + R_2} e(s)$$

where e(s) is the potential energy per unit area, as a function of the distance between flat surfaces. The touching of two flat surfaces results in a potential energy gain per unit area equal to twice the surface energy coefficient,

$$\therefore \quad e(0) = -2\gamma$$

leading to the same maximum force as above. (The force becomes repulsive as the two density distributions overlap.)

For the potential we obtain,

$$U(s) = 2\pi \frac{R_1 R_2}{R_1 + R_2} \int_s^\infty e(s')\, ds'$$

where

$$s = r - (R_1 + R_2) \quad .$$

The interaction is given in terms of a universal function e(s); once known or calculated for one pair of nuclei, we immediately have information about other pairs. Although based on a liquid drop model, the formula is actually very general. Suppose that the interaction energy is represented by a folding formula with a δ-function interaction:

$$U = A \ \rho_1(r_1)\, \rho_2\,(r - r_1)\underline{dr_1} \tag{1.32}$$

If the densities ρ_1, ρ_2 have Saxon-Woods shapes,

$$\rho = \frac{\rho_0}{\left[1 + \exp\left(\frac{r - R}{a}\right)\right]} \tag{1.33}$$

then the integral can be evaluated:(39)

$$U(s) = 2\pi A\, \rho_0^2 \frac{R_1 R_2}{R_1 + R_2} \int_s^\infty \frac{s'ds'}{\exp \frac{s'}{a-1}} \qquad (1.34)$$

where $s = r - (R_1 + R_2)$, and has the proximity form with a particular expression for e(s). This result begins to link for us the *microscopic* and *macroscopic* approaches to potentials. Other generalized discussions of heavy-ion potentials using the energy density formalism are discussed in Refs. (39-41).

To compare with experiment, we write U(s) in the form

$$U = 4\pi\gamma \frac{R_1 R_2}{R_1 + R_2}\, b\phi(\zeta) \qquad (1.35)$$

where $\zeta = s/b$, $b = 1$ fm, and $\gamma \approx 0.95$ MeV•fm^{-2}. The universal function ϕ has been evaluated using the nuclear Thomas-Fermi method. We find:

$$\begin{aligned} \phi(\zeta < 1.25) &= -\tfrac{1}{2}(\zeta - 2.54)^2 - 0.85(\zeta - 2.54)^3 \\ \phi(\zeta > 1.25) &= -3.437 \exp(-\zeta/0.75) \end{aligned} \qquad (1.36)$$

and is plotted in Fig. 1.15.(42)

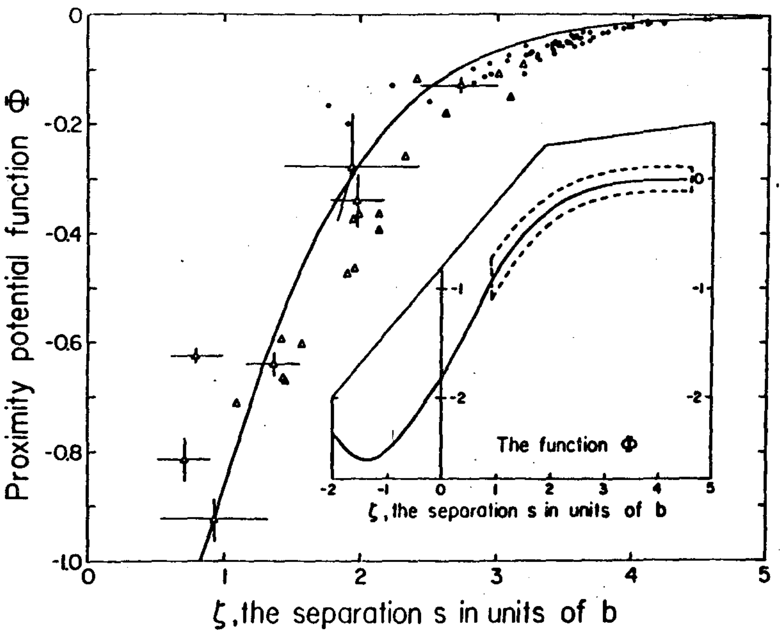

XBL 777-9482

Fig. 1.15

The theoretical proximity function $\phi(\xi)$ in the extreme tail region has been compared with nuclear potentials deduced from an analysis of elastic scattering data, leading to values of ϕ from 0 to -0.16, and are reproduced in the figure by circles.(42) We see (as expected) that elastic scattering tests the potential over only a small interval in ϕ at large values of ζ, i.e., radial distances near the strong absorption radius.

As we shall see in later sections, *inelastic* processes probe the potential to much smaller radii (see Chapter on Fusion and Fission). Values derived in this way are shown as triangles. The theoretical proximity potential is in excellent agreement with the data over the entire range of distances. Similar global comparisons are discussed in Ref. (43).

We therefore finally display(42) the total potential for interesting heavy-ion systems, $^{16}O + {}^{208}Pb$ and $^{84}Kr + {}^{209}Bi$ in Fig. 1.16. Here U = U(proximity) + U(Coulomb) + U(centrifugal). The attractive pocket in the potential for ^{16}O disappears for the heavy nucleus ^{84}Kr.

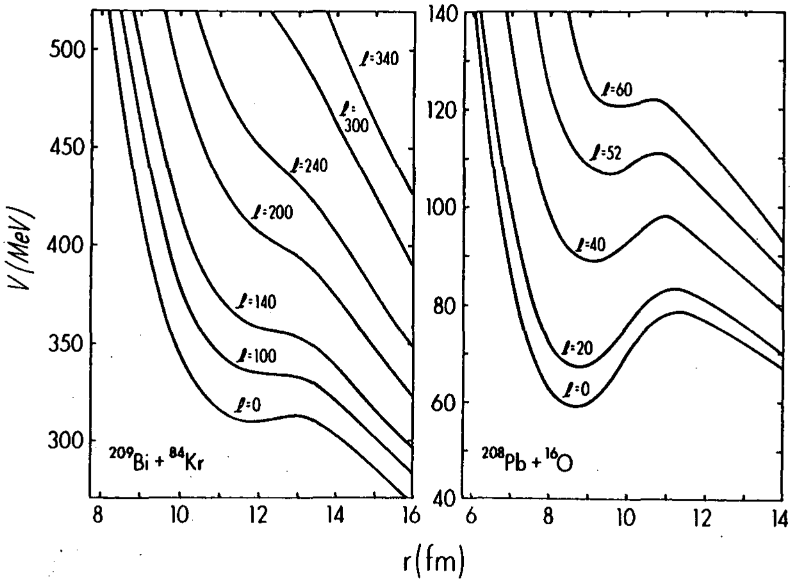

Fig. 1.16

XBL 777 9480

1.6 Recent Complications in Elastic Scattering

We now discuss situations where elastic scattering is more complicated than any of the foregoing discussions.

1.6.1 Light systems

Recall the system $^{16}O + {}^{28}Si$ which was studied earlier over a wide energy range. At incident energies in the region of 55 MeV, the data indicate oscillatory behavior which is not reproduced either by the Saxon-Woods or the folded potentials. These interferences appear to be a new phenomenon not described by Fresnel or Fraunhoffer diffraction.

The system has recently been studied over the whole angular range with high precision(44) (see Fig. 1.17). The forward region used the

1.6.2 Heavy systems

Now we discuss the elastic scattering of heavy systems at low energies such as $^{18}O + ^{184}W$ at 90 MeV (see Fig. 1.18). The scattering deviates dramatically$^{(46)}$ from the Rutherford and Fresnel behavior, compared to $^{18}O + ^{208}Pb$. The explanation lies in the inset, which shows that ^{184}W has a low-lying excited state at 111 keV. (The production of this spectrum is a remarkable achievement in itself, relying on the new Q3D, large, solid-angle magnetic spectrometers.) The effect is due to the long range of the Coulomb excitation interaction which has the effect of introducing *an imaginary potential into the Coulomb potential* of the form:$^{(47)}$

$$\mathcal{I}_m\, U_c(r) \approx \frac{W_c}{R^5} \qquad (1.38)$$

The effect of including this imaginary potential into the usual *nuclear* optical potential (which also has real and imaginary parts) is shown in Fig. 1.19, and for comparison the Fresnel pattern obtained by omitting the Coulomb imaginary potential.

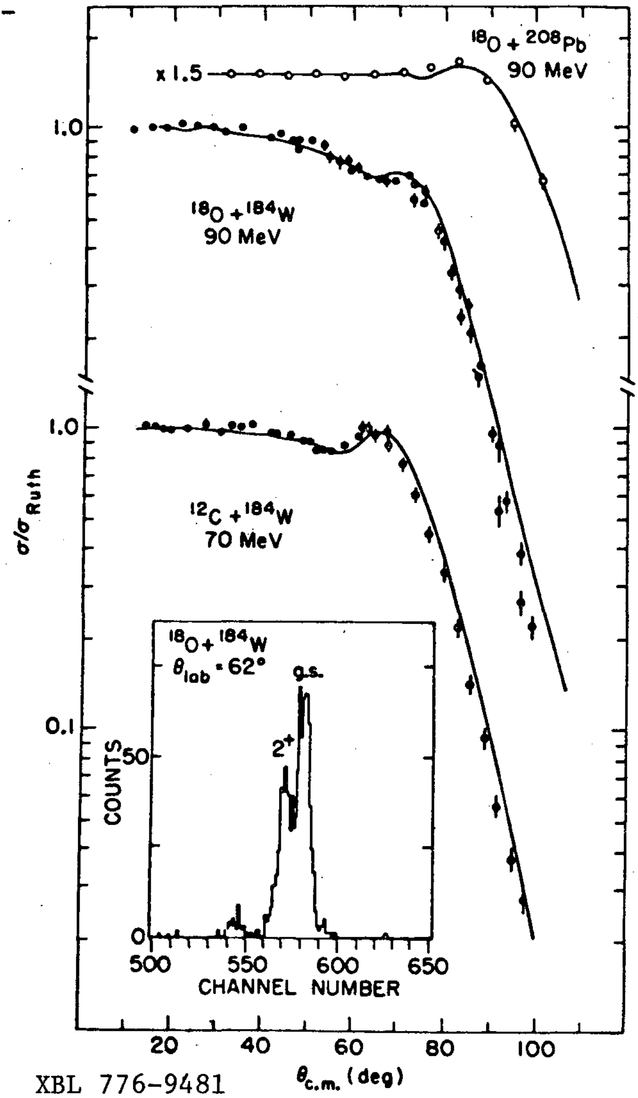

XBL 776-9481

Fig. 1.18

A more dramatic example is given in Fig. 1.20(a) for the heavy system $^{84}Kr + ^{209}Bi$ at 600 MeV. Here the Coulomb excitation is so strong that the nuclear potential has little opportunity to act at all.$^{(47)}$ Consequently it will be difficult to learn about the nuclear potentials of such systems with the energies currently available. Remarkably enough, experimental data for this system exist$^{(48)}$ (Fig. 1.20(b)) and reveal a plausible Fresnel pattern. The explanation is that the data contain inelastic scattering (the resolution of which is a formidable experimental problem yet to be overcome) which restores the flux drained by the imaginary potential. Recently an elegant analytical formulation of the Coulomb absorption has been presented for the case of sub-Coulomb elastic scattering.(49)

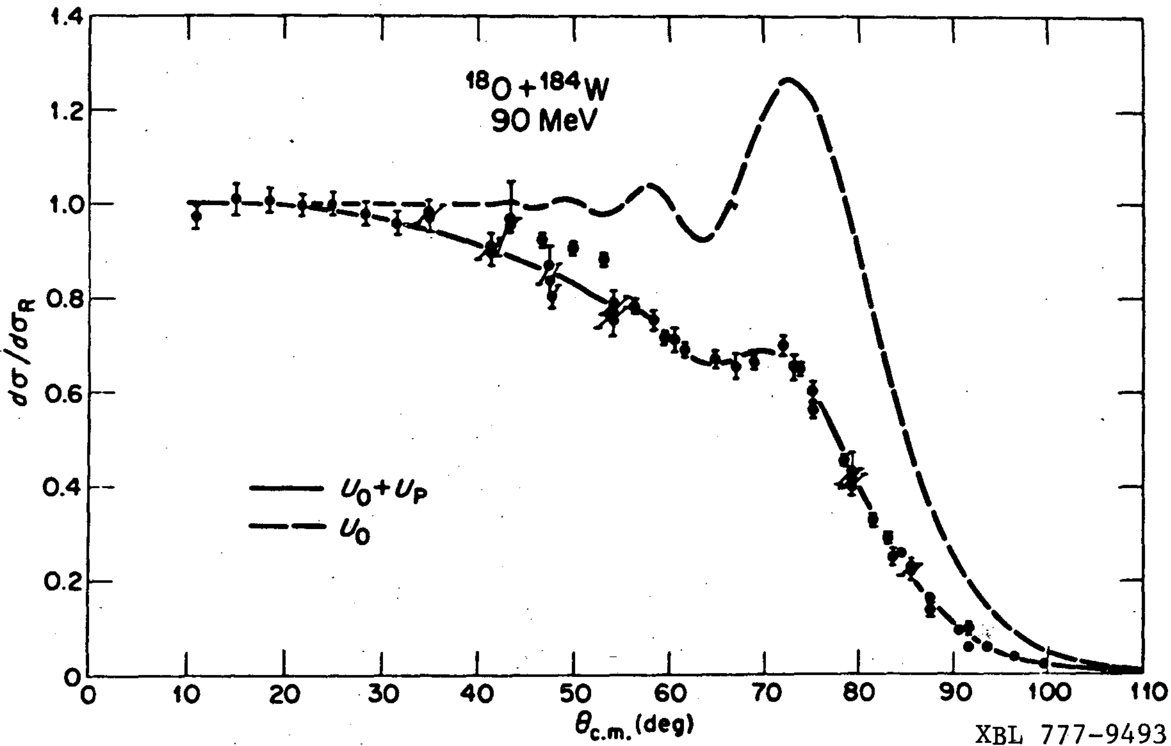

XBL 777-9493

Fig. 1.19

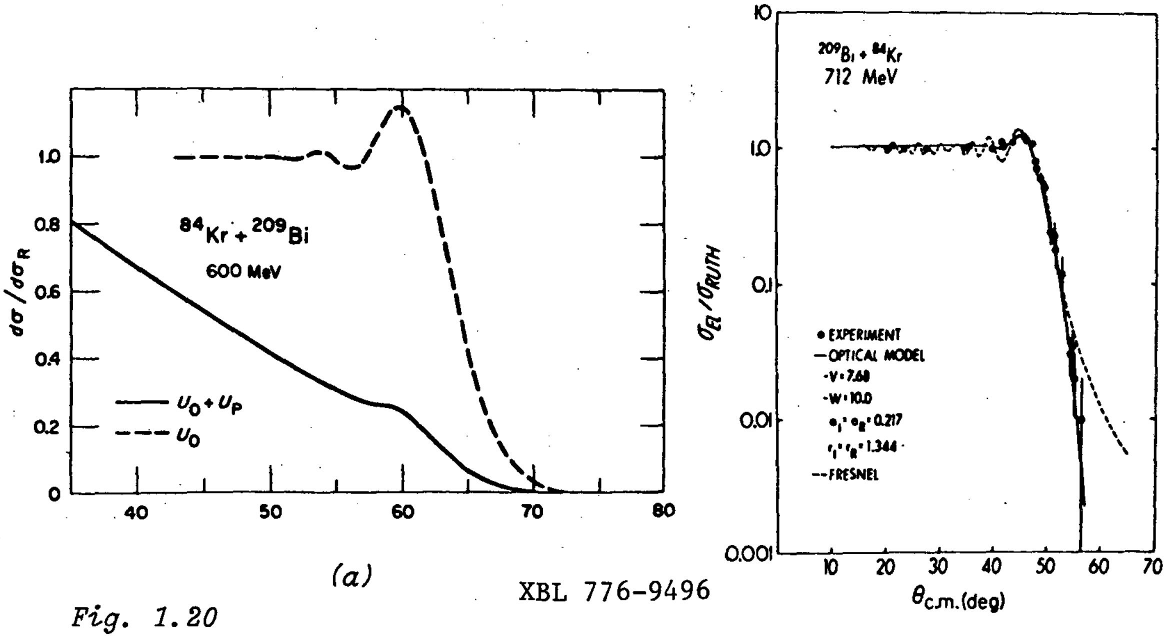

(a)

XBL 776-9496

(b)

Fig. 1.20

2.

TRANSFER REACTIONS TO DISCRETE STATES USING HEAVY-ION REACTIONS

Heavy-ion reactions open up new possibilities for us in the study of *new nuclei*, and *new types of states in nuclei*, and of *new reaction mechanisms*.

2.1 New Nuclei

An expanded view of the first portion of the chart of nuclides$^{(50)}$ is shown in Fig. 2.1. Stable nuclei are indicated by black squares; nuclei for which an accurate mass has been determined, by shaded squares; nuclei for which only nucleon stability has been established, by white squares. Nuclei with known masses but which are nucleon-unstable, such as ^{8}C and ^{10}Li, are indicated by shading but not included in a black box. Heavy-ion transfer reactions are the only general means of producing neutron excess nuclei more than three neutrons from stability. For example, most of the nuclei in white squares were produced in one spectacular effort$^{(51,52)}$ of bombarding ^{232}Th with ^{40}Ar at 290 MeV, and established the heaviest isotopes of N → F that we now know as ^{21}N, ^{24}O, and ^{25}F.

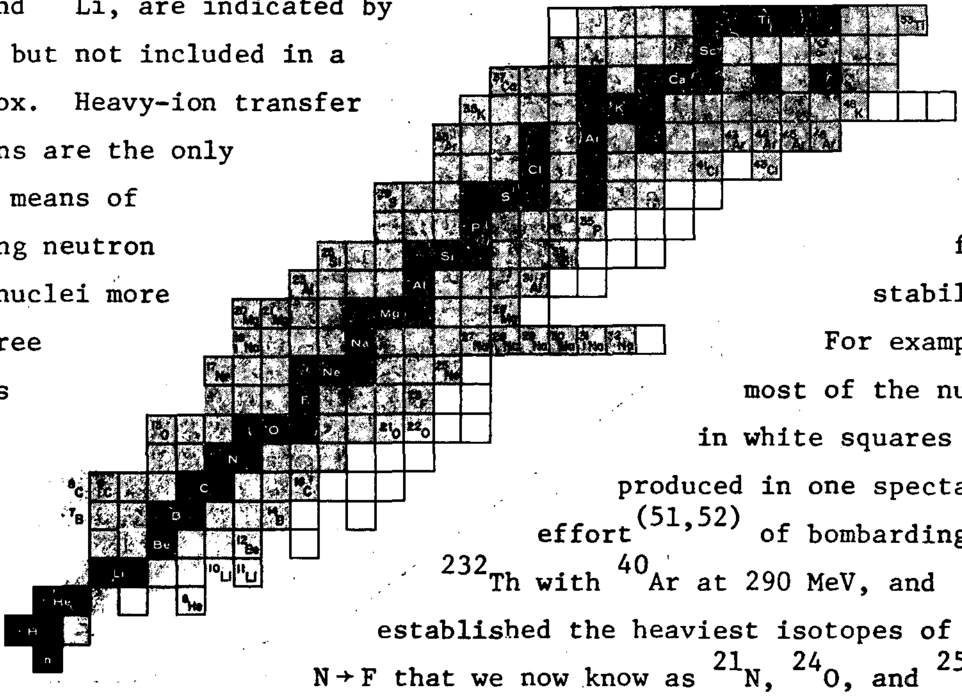

Fig. 2.1

The question of how many neutrons a specified number of protons can bind is a well-defined query of great interest to nuclear structure physics. Will the nuclear shell model so successful in the valley of stability, be equally successful for more exotic species? In trying to determine the limit of stability at present, theory and experiment go hand in hand towards the edge.$^{(53,54)}$

The experimental problems are formidable. Cross sections less than 1 nb/sr must be detected in the fact of competing reactions over 10^{6}

times stronger. To sift out these rare exotic species calls for a sophisticated detection system. An example used for the study of exotic nuclei,(55) and for heavy-ion transfer reactions in general, is shown in Fig. 2.2. (For a review of heavy-ion detection systems, see Ref. (56)).

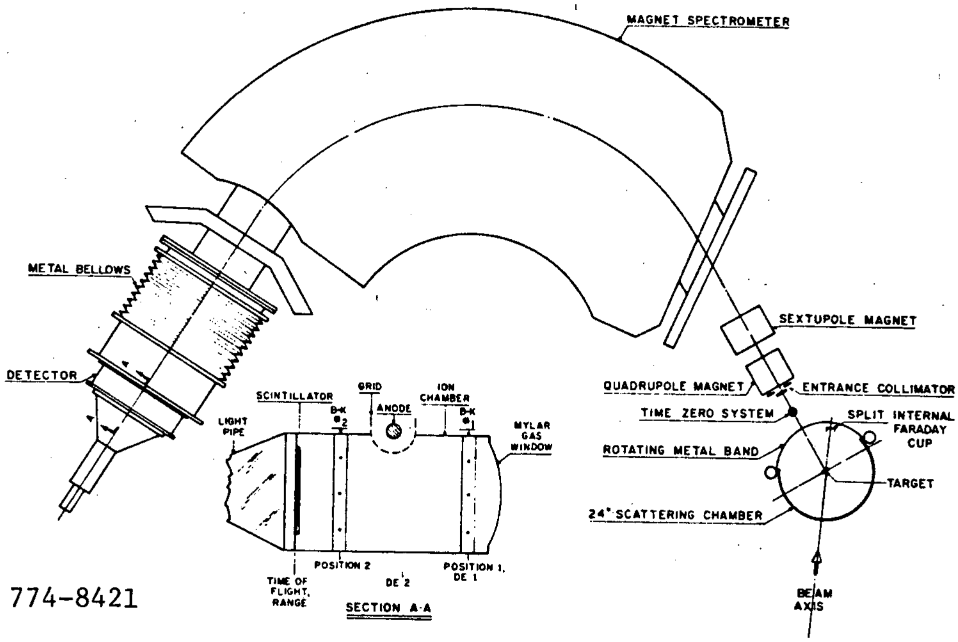

XBL 774-8421

Fig. 2.2

To identify a heavy ion, which may emerge from the target in different charge states, we must measure A, Z, and Q, in addition to the reaction quantities E and θ. To obtain high resolution, magnetic spectrometers with position-sensitive detectors in the focal plane are employed. This system determines:

a) Bρ from measurements of the position in two separated Borkowski-Kopp counters. From these the angle of the trajectory through the spectrometer is also measured (important for correcting effects of aberrations).

b) dE/dx (from energy loss in ion-chamber between the position detectors):

$$\left(\frac{dE}{dx}\right) \propto \frac{AZ^2}{E} \Rightarrow (B\rho)^2 \ \frac{A^2Z^2}{Q^2}$$

since $E \propto (B\rho)^2 \ Q^2/A$.

c) Time-of-flight ∝ 1/v ∝ (1/Bρ)A/Q, determined by "time-zero" system at entrance to the spectrometer and a large scintillator in the focal plane. Corrections to dE/dx and T.O.F. can be made as a function of position, i.e. of (Bρ).

d) The energy of the particle is also measured in the scintillator,

$$E \propto (B\rho)^2 \frac{Q^2}{A} \quad . \tag{2.2}$$

e) Vertical position is measured by comparing the response of the ion chamber drift with the scintillator.

Figure 2.3 is an example of identifying exotic nuclei, e.g., ^{21}O, by such techniques, in the $^{18}O + ^{208}Pb$ reaction.(57) Also shown is the energy spectrum from which the mass of ^{21}O can be extracted. <u>Question</u>: Are the properties of one level in an exotic nucleus such as ^{21}O or ^{22}O worth more than 50 levels in ^{16}O? Figure 2.4 indicates the measure of agreement(50) between experiment and theory for $T_Z = 5/2$ nuclei. The predictions are essentially based on iterative techniques;(58,59)

$$\begin{aligned} M(N,Z) - M(N+2, Z-2) &= \\ M(N, Z-1) - M(N+1, Z-2) &+ \\ M(N+1, Z) - M(N+2, Z-1) &, \end{aligned} \tag{2.3}$$

e.g., $^{25}Mg - ^{25}Ne = ^{24}Na - ^{24}Ne + ^{26}Mg - ^{26}Na$. As the experimentalists probe further out from stability, the results are fed back into the theory. A measurement out at the limit of stability would be a more stringent check to see if the theory was on the right track.

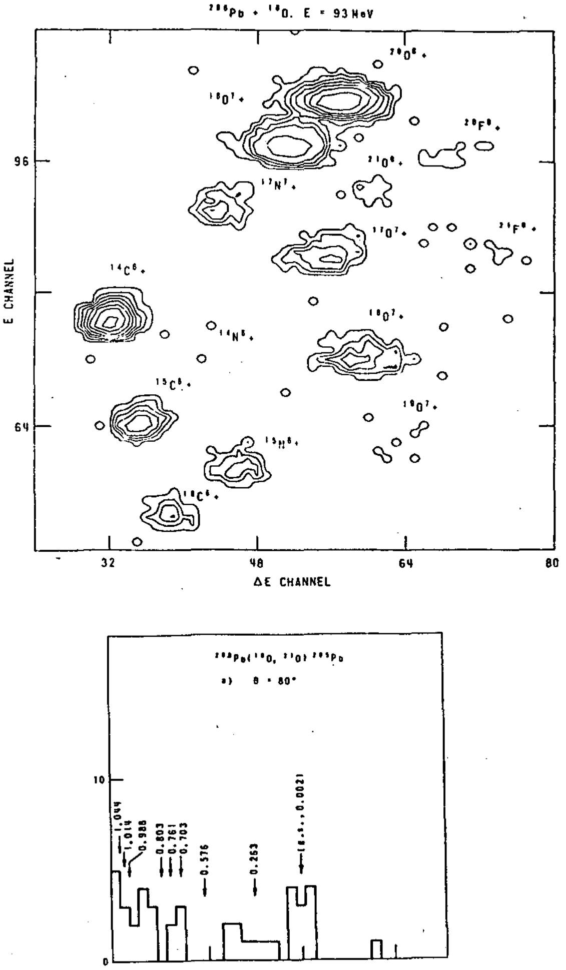

Fig. 2.3

XBL 776-9510

The most exotic nuclei — if they exist — would be the superheavy nuclei with A beyond the highest observed transuranics. At Z = 114 and N = 184 (a double-closed shell), they may have observably long lifetimes. Possible *transfer reactions* (which are able to encompass the complete range of lifetimes) to reach them are, e.g.:

$$^{244}\mathrm{Pu} + {}^{94}\mathrm{Zr} \rightarrow {}^{298}\mathrm{X} + {}^{40}\mathrm{Ca}\ .$$

With the advent of accelerators capable of producing large beams of ^{94}Zr, such experiments will be attempted. However, it is important to have a good understanding of such massive cluster transfers, and we now survey some experiments directed to that goal.

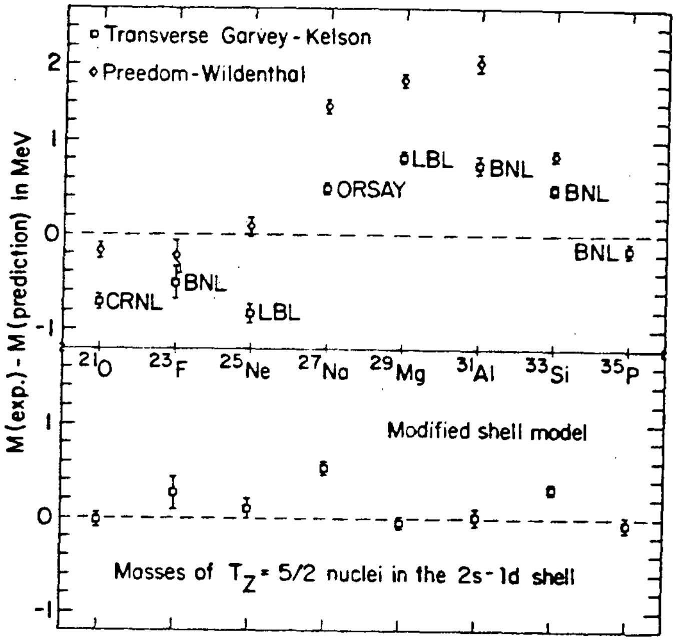

Fig. 2.4

XBL 766-2966A

2.2 *New States in Nuclei Using Heavy-Ion Transfer Reactions*

In order to discover *new* types of states in nuclei, we must study first the nature of the mechanisms of heavy-ion transfer reactions. Several recent reviews$^{(60-62)}$ have covered the developments in the subject.

2.2.1 *General characteristics*

Heavy-ion transfer has characteristic angular distributions,$^{(63)}$ of bell-shaped form, e.g., as in Fig. 2.5. They peak at an angle associated with the strong absorption radius discussed in Chapter 1. The reason can be traced to the maximum in the *deflection function* (see Fig. 1.6(a)), due to the attractive nuclear field counterbalancing the Coulomb repulsion, which for non-penetrating orbits leads to a maximum scattering, the *grazing angle*.

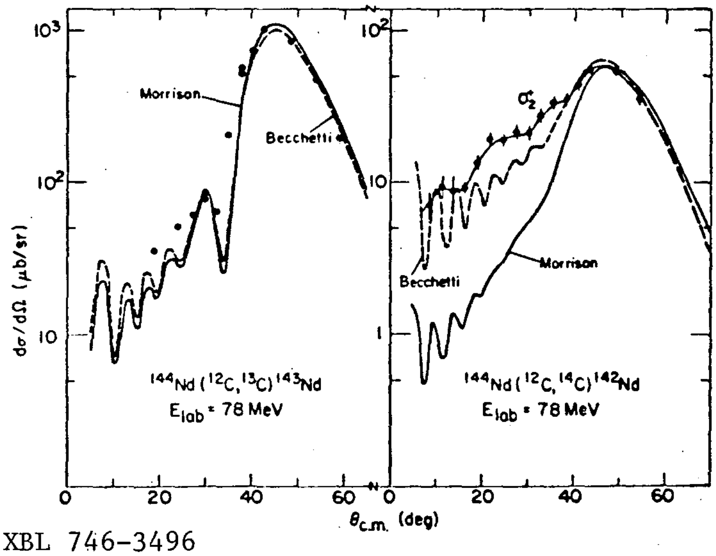

XBL 746-3496

Fig. 2.5

More penetrating orbits can scatter forward or backward of this angle but suffer attenuation by absorption, while more distant orbits, which only scatter forward, contribute little to transfer reactions because of the small probability of finding a particle out there. The quantitative calculation of S_ℓ, the amplitude in the outgoing channel for a typical two-neutron transfer reaction(21) (for the same reaction as illustrated in Figs. 1.5 and 1.6) is plotted in Fig. 2.6, which shows that the grazing partial wave is $\ell_g \approx 57\hbar$, whereas the spread of significant ℓ-values is much smaller ($\Delta\ell \approx 15\hbar$) — one of the requirements for an orbit picture.

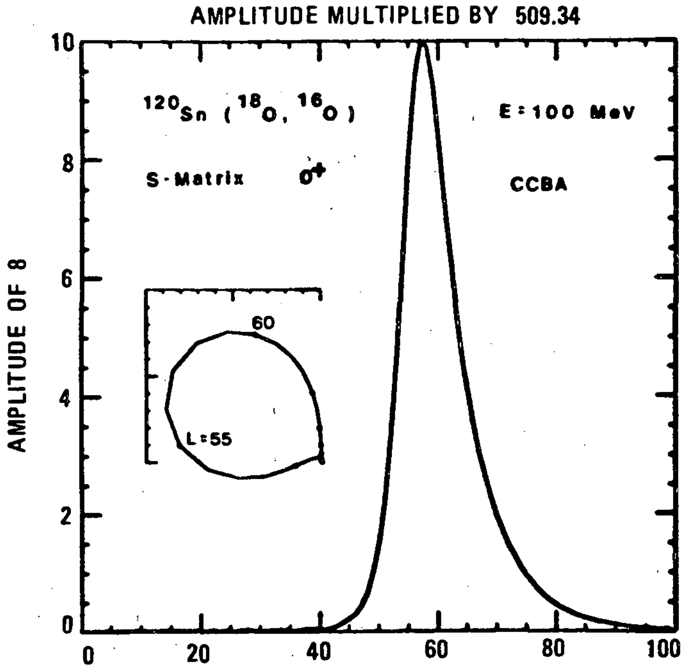

XBL 745-924

Fig. 2.6

To gain more insight we write the scattering amplitude,

$$f(\Theta) = \frac{1}{2ik} \sum (2\ell+1)\, \eta_\ell\, e^{2i\delta_\ell}\, P_\ell(\cos\Theta) \tag{2.4}$$

and the reaction amplitude, assuming the peripheral nature of the reaction, as a Gaussian distribution (justified by the output of "exact" DWBA calculations, e.g. see Fig. 2.6),

$$\eta_\ell = \eta_{\ell_0} \exp - \left[\frac{(\ell - \ell_0)^2}{(\Delta\ell)^2} \right] . \tag{2.5}$$

As in our discussion of elastic scattering, $P_\ell(\cos\Theta)$ is replaced by the asymptotic expression valid for large ℓ, and $\sin\Theta > 1/\ell$,

$$P_\ell(\cos\Theta) \approx [\tfrac{1}{2}(\ell+\tfrac{1}{2})\pi \sin\Theta]^{-\frac{1}{2}} \sin[(\ell+\tfrac{1}{2})\Theta + \pi/4] \ . \tag{2.6}$$

For δ_ℓ we make the Taylor expansion:

$$\delta_\ell = \delta_{\ell_0} \pm \left(\frac{d\delta}{d\ell}\right)_{\ell=\ell_0} (\ell - \ell_0) + \tfrac{1}{2}\left(\frac{d^2\delta}{d\ell^2}\right)_{\ell=\ell_0} (\ell - \ell_0)^2 + \ldots. \tag{2.7}$$

On account of the WKB classical relationship for the scattering angle corresponding to partial wave ℓ,

$$\Theta_\ell = 2\,\frac{d\delta_\ell}{d\ell} \tag{2.8}$$

we can write

$$\delta_\ell = \delta_{\ell_0} \pm \frac{\Theta_0}{2}(\ell - \ell_0) + \tfrac{1}{4}\left(\frac{d\Theta_\ell}{d\ell}\right)_{\ell=\ell_0} (\ell - \ell_0)^2 + \ldots. \tag{2.9}$$

where Θ_0 is the classical angle of deviation for the tangential trajectory (not necessarily purely Coulomb). Substituting in(2.4)and converting the summation to an integral gives

$$\frac{d\sigma}{d\Omega} = |f(\Theta)|^2 \propto \exp\left\{-\frac{(\Theta-\Theta_0)^2}{(\Delta\Theta)^2}\right\} + \exp\left\{-\frac{(\Theta+\Theta_0)^2}{(\Delta\Theta)^2}\right\} + \begin{pmatrix}\text{Interference}\\ \text{Term}\end{pmatrix} \tag{2.10}$$

We interpret the differential cross section as the interference of two classical distributions centered at the physical angle (Θ_0) and the unphysical $(-\Theta_0)$, corresponding to trajectories from opposite sides$^{(67)}$ of the nucleus (see Fig. 1.5). Consider first the term,

$$\frac{d\sigma}{d\Omega} \propto \exp -\left\{\frac{(\Theta - \Theta_0)^2}{(\Delta\Theta)^2}\right\} . \tag{2.11}$$

This equation describes a distribution of width$^{(64)}$

$$(\Delta\Theta)^2 = \frac{2}{(\Delta\ell)^2} + \tfrac{1}{2}\left(\frac{d\Theta_\ell}{d\ell}\right)^2 (\Delta\ell)^2 \ . \tag{2.12}$$

Using the classical Rutherford scattering expression

$$\ell = \eta\cot(\Theta/2) \tag{2.13}$$

we get $(d\Theta_\ell/d\ell) = 0.013$ for the reactions shown in Fig. 2.5, enabling us to construct the $\Delta\ell$ v $\Delta\Theta$ curve of Fig. 2.7. The curve has a minimum at

$$\Delta\ell = \sqrt{2\left(\frac{d\ell}{d\Theta}\right)_{\ell_o}} = \sqrt{\eta}\ \mathrm{cosec}\left(\frac{\Theta_o}{2}\right) \approx 12 \qquad (2.14)$$

For larger $\Delta\ell$ values the behavior is classical and $\Delta\Theta$ increases with $\Delta\ell$, with the opposite quantal behavior for smaller $\Delta\ell$ values.(68) Shown on the figure is the $\Delta\ell$ value derived from a full quantum mechanical DWBA calculation of the ^{144}Nd(^{12}C,^{13}C)^{143}Nd reaction and the resulting $\Delta\Theta = 9.2°$ is close to the observed half width at 1/e of the maximum. These one-nucleon transfer reactions are therefore well-described by the above treatment. Because the data correspond to the minimum of the $\Delta\ell$ v $\Delta\Theta$ curve, the width of the peripheral maximum is relatively stable against variations in $\Delta\ell$ brought about, for example, by variations of the optical model parameters in the DWBA calculation (so as in elastic scattering the data are not probing the potential very sensitively).

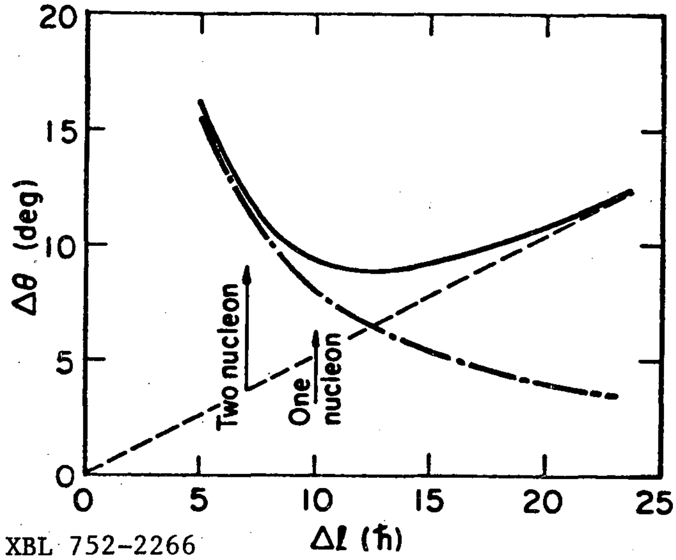

XBL 752-2266

Fig. 2.7

The two-neutron transfer data ^{144}Nd(^{12}C,^{14}C) in 2.5 are more helpful. Here a change in the radius parameter of the imaginary potential from 1.26 to 1.36 fm changes the forward cross section by a factor of 10. The two sets of potentials used were (for single nucleon transfer):

V	W	r_o	a	
-40	-15	1.31	0.45	solid line
-100	-40	1.22	0.49	dotted line

and for two-nucleon transfer, V = -40, W = -15, with r = 1.36 (dotted) and 1.26 fm (solid).

This discussion was meant to illustrate the physical mechanisms, and to help in understanding what happens. The very features which complicate full numerical calculations of heavy-ion reactions, high ℓ

and large η, are just those that may be turned to advantage in an analytical calculation.(27,69)

2.2.2 *Cluster transfer reactions — light nuclei*

Using a semi-classical model,(70) simple cluster states appear to have been located in heavy-ion transfers(71) (the discovery of such states should surely be one of the goals). The model assumes that the particles move on semi-classical trajectories and is illustrated schematically in Fig. 2.8. There are three kinematical conditions to be satisfied if the transfer probability of the cluster m (a nucleon or a group of nucleons) is to be large. The cluster starts in an initial state $(\ell_1\lambda_1)$ and ends in $(\ell_2\lambda_2)$.

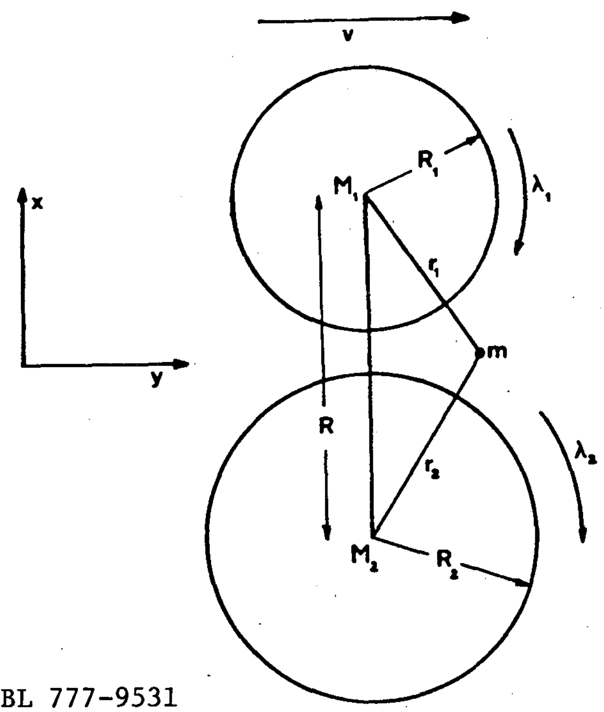

XBL 777-9531

Fig. 2.8

$$\Delta k = k_o - \frac{\lambda_1}{R_1} - \frac{\lambda_2}{R_2} \approx 0 \quad (2.15)$$

$$k_o = \frac{mv}{\hbar} .$$

where v is the speed of the particle at the transfer point.

$$\Delta L = \lambda_2 - \lambda_1 + \tfrac{1}{2} k_o (R_1 - R_2) + Q_{eff} \frac{R}{\hbar v} \approx 0 \quad (2.16)$$

$$Q_{eff} = Q - (Z_1^f Z_2^f - Z_1^i Z_2^i) \frac{e^2}{R} \quad (2.17)$$

$$\ell_1 + \lambda_2 , \quad \ell_2 + \lambda_2 \quad \text{even} \quad (2.18)$$

These conditions imply, respectively: conservation of the y-component of angular momentum of the transferred nucleon; conservation of angular momentum; and confinement of the transfer to the reaction plane, i.e., the angles Θ in the spherical harmonics of the single particle wave functions are $\approx \pi/2$. An approximate expression(71) for the transition probability is:

$$P(\lambda_2\lambda_1) \approx S_1 S_2 P_o(R) \left| Y_{\ell_1}^{\lambda_1}\left(\frac{\pi}{2},0\right) Y_{\ell_2}^{\lambda_2}\left(\frac{\pi}{2},0\right)\right|^2 \times \exp\left[-\left(\frac{R\Delta k}{\sigma_1}\right)^2 - \left(\frac{\Delta L}{\sigma_2}\right)^2\right] \quad (2.19)$$

where $P_o(R)$ is determined by the radial wave functions at the nuclear surface, and σ_1,σ_2 are the spreads in Δk, ΔL from zero allowed by the uncertainty principle. The total transition probability is then calculated by summing over the final magnetic substates and averaging over the initial substates, weighted by angular momentum coupling coefficients and the spectroscopic factors (S_1,S_2) for finding the cluster in the initial and final states. However, the localization and semi-classical aspects of the transfer usually mean that the reaction is "well matched" for a restricted range of λ_1,λ_2 and ℓ_1,ℓ_2.

Since most of the transfer cross sections in a heavy-ion reaction are found in the continuum (see, e.g. Fig. 2.9(b)) rather than populating discrete states, it is instructive first to consider the application of these equations to average quantities. Evaluating λ_2 from the first equation and substituting in the second gives

$$Q_{eff} \approx \frac{\lambda_1 hv}{R_1} - \frac{\hbar v}{R}\,\frac{k_o R}{2} \approx \frac{\lambda_1}{R_1}\,\hbar v - \tfrac{1}{2}mv^2 \qquad (2.20)$$

Since the incident ion is left in a "hole" state of the transferred particles, the sign of its polarization should be opposite to λ_1. Vanishing polarization is predicted at the "optimum" Q-value (best satisfying the semi-classical matching conditions),

$$Q_{opt} = -\tfrac{1}{2}\,mv^2 + (Z_1^f Z_2^{f'} - Z_1^i Z_2^i)\,\frac{e^2}{R} \qquad (2.21)$$

and if $Q > Q_{opt}$, the polarization is negative, and for $Q < Q_{opt}$, it is positive.

Just these features have been studied in the reaction ^{100}Mo(^{14}N,^{12}B)^{102}Ru at 90 MeV, by measuring$^{(72)}$ the β-decay asymmetry of products ^{12}B ($J^\pi = 1^+$, $E_{\beta_{max}} = 13.37$ MeV, $t_{1/2} = 20.3$ ms). The angular distribution of β-rays with respect to the polarization $\underline{P}$ is given by $W(\Theta) = (1 - P\cos\Theta)$. The apparatus is sketched in Fig. 2.9(a). The beam irradiation was cyclic and on alternate cycles the spin direction of the ^{12}B was reversed with an RF field to eliminate instrumental asymmetries. The results are shown in Fig. 2.9(b), which confirms qualitatively the predictions of the semiclassical model. We see that the energy spectrum of the ^{12}B (determined from N_β) peaks in the continuum at a Q value of ≈ -23 MeV, compared to the $Q_{opt} = -\tfrac{1}{2}mv^2 + \Delta V_c \approx -21$ MeV. We shall

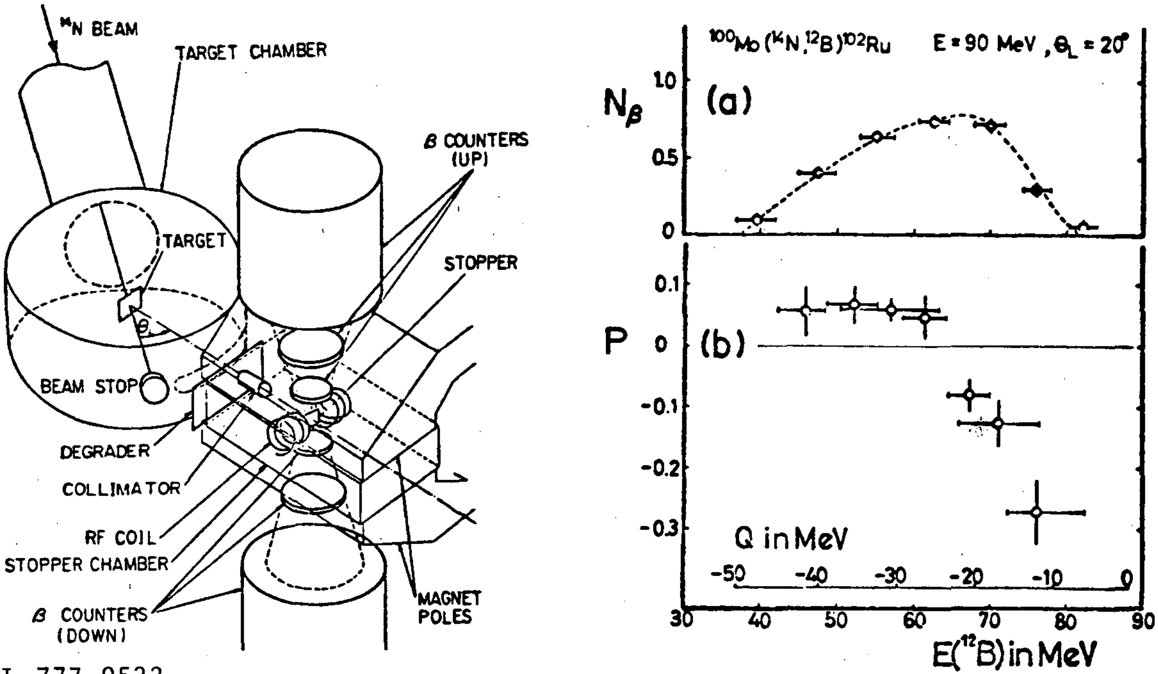

XBL 777-9533

(a)		*(b)*

Fig. 2.9

return to a discussion of the continuum and the significance of polarization measurements again in Chapter 5. A more formal discussion of polarization effects in heavy-ion direct transfer reactions is given in Ref. (74).

The semiclassical model, in addition to describing the above *average* features, gives a successful description of the excitation of discrete states. An example of the *selectivity* of the heavy-ion reactions for exciting four-nucleon "alpha cluster" states$^{(75)}$ is shown in Fig. 2.10 for the (^{13}C, ^{9}Be) reaction on ^{16}O. Only the two rotational bands

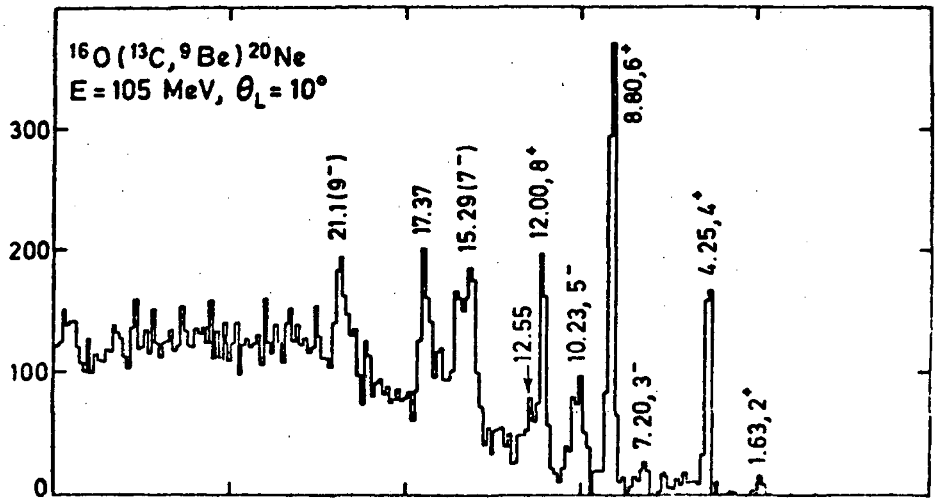

XBL 777-9513

Fig. 2.10

(positive and negative parity) are excited selectively. Remember that there are actually hundreds of levels per MeV in a nucleus such as ^{20}Ne at an excitation energy of 20 MeV. The alpha transfer amplitudes to the states in the ground state band of ^{20}Ne are disarmingly simple to calculate in the SU(3) model. The spectroscopic factors are just proportional to the intensities of the SU(3)[80] representation in each state, which are equal for all members of the band (terminates with 8^+) and the spectroscopic amplitudes should be equal. However, previous α-transfer experiments (done mainly with (^{6}Li,d) or (^{7}Li,t) reactions — not regarded by funding agencies as heavy ions!) have disagreed,(76) in particular for the 8^+ for which a spectroscopic amplitude < 0.1 of the other states was obtained. The data illustrated appear to resolve this problem. In Table 2.1 we show the experimental and theoretical cross sections, calculated with the semiclassical expression, for each state in the band, normalizing at the 4+ state. Equal spectroscopic factors were assumed.

TABLE 2.1 Spectroscopic factors for the reaction ^{16}O(^{13}C,^{9}Be)^{20}Ne.

J^π	Ex	dσ(expt) (mb/sr)	dσ (TH)	Sα SU3	Sα Shell model
0^+	0.00	--	0.03	0.23	0.18
2^+	1.63	1.18	1.59	0.23	0.19
4^+	4.25	11.45	11.45	0.23	0.18
6^+	8.78	23.10	22.20	0.23	0.19
8^+	11.99	13.20	15.70	0.23	0.17

2.2.3 Cluster transfer — heavy nuclei

The problem of four-nucleon correlations (quartets) in medium mass nuclei in the $f_{7/2}$ shell received much attention a few years ago via the (^{16}O, ^{12}C) reaction, and was partly responsible for the resurgence of interest in heavy-ion spectroscopy.(3,77) To gain a better understanding of four-nucleon transfer, a stringent test is afforded by a comparison of such reactions with the presumed inverse process, α-decay. Nuclei in the lead region are ideally suited to this test. For example, it is possible to derive a "reduced alpha width" ratio for ^{212}Po (0.727 MeV, 2^+) and ^{212}Po (gs) states from their decay to ^{208}Pb, from the formula

$$\delta^2 = h/\tau P \tag{2.22}$$

where τ is the mean life and P the penetrability. Then, $\delta^2(2^+)/\delta^2(0^+) = 0.61$, in excellent agreement with the spectroscopic factor ratio $S(2^+)/S(0^+) = 0.64$, deduced from a direct reaction analysis of ^{208}Pb(^{16}O,^{12}C)^{212}Po, leading to the conclusion that the basic quantities measured in alpha transfer and decay are homologous.(78,79) (There is, however, an intriguing problem that absolute values of the decay widths are underestimated by the shell model by a factor of 1000 — which may indicate substantial clustering of alphas in the surface region,(80,81) and therefore surface phenomena not presently described by the shell model.) However, one is encouraged to look for other alpha particle strengths.

The Pb region exhibits some of the clearest examples of pairing vibrational excitations so it should be reasonable also to look for alpha vibrations.(82) In ^{208}Pb a proton pair and a neutron pair should be organized in the same orbits and with the same correlations that they appear in ^{212}Po, and similarly four holes should be organized to simulate the ground state of ^{204}Hg:

$$|^{208}\mathrm{Pb}(\alpha\text{-vib})\rangle = |^{204}\mathrm{Hg(gs)}\rangle \otimes |^{212}\mathrm{Po(gs)}\rangle$$

and the energy of the state to lowest order is

$$\mathrm{Ex}(^{208}\mathrm{Pb}) = 2 \times \mathrm{B}(^{208}\mathrm{Pb}) - \mathrm{B}(^{212}\mathrm{Po}) - \mathrm{B}(^{204}\mathrm{Hg}) = 8.44\ \mathrm{MeV}$$

The cross section for $\sigma(\alpha\text{-transfer } ^{204}\mathrm{Hg} \rightarrow {}^{208}\mathrm{Pb}(\alpha\text{-vib}))$ should equal $\sigma(\alpha\text{-transfer } ^{208}\mathrm{Pb} \rightarrow {}^{212}\mathrm{Po(gs)})$, which we discussed above. Actually, the particle-hole monopole interaction is calculated to lower the excitation by ≈ 1.2 MeV, down to 7.2 MeV excitation.

Figure 2.11 shows that no single state could be identified(83) below 9 MeV, and at 7.2 MeV the *summed background* is less than 30% of the expected cross section (indicated). Therefore we are able to study new spectroscopy (and problems for theoreticians) via such heavy-ion reactions. In a less naive light, the problems of calculating the heavy-ion reaction dynamics in order to deduce the spectroscopy are complex, as we now discuss.

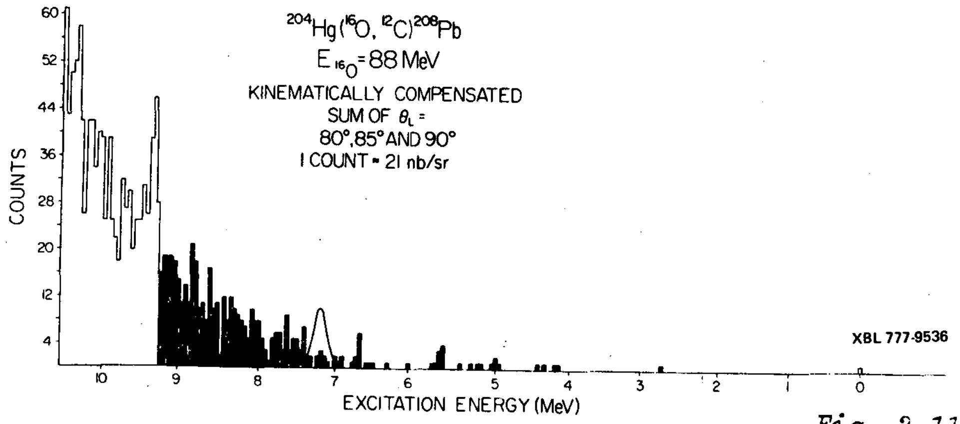

XBL 777-9536

Fig. 2.11

2.3 DWBA Formalism for Heavy-Ion Reactions

The formal quantal evaluation of heavy-ion direct reactions uses the DWBA. Symbolically the reaction can be written$^{(84)}$

$$(a+c)+b \rightarrow (b+c)+a$$

where a, b, are the heavy-ion cores and c is the transferred particle. Then

$$T_{fi}^{DWBA} = \langle \chi_f \, \phi_{b+c} \, \phi_a \, | V_{ac} | \, \chi_i \, \phi_{a+c} \, \phi_b \rangle$$

where χ_f, χ_i are distorted waves, the scattering eigenfunctions, and ϕ are the eigenfunctions of nuclear Hamiltonians (see Fig. 2.12). The interaction V_{ac} (or V_{bc}) causes the transition (as usual one assumes that the core-core interaction V_{ab} cancels the potential in the initial channel).

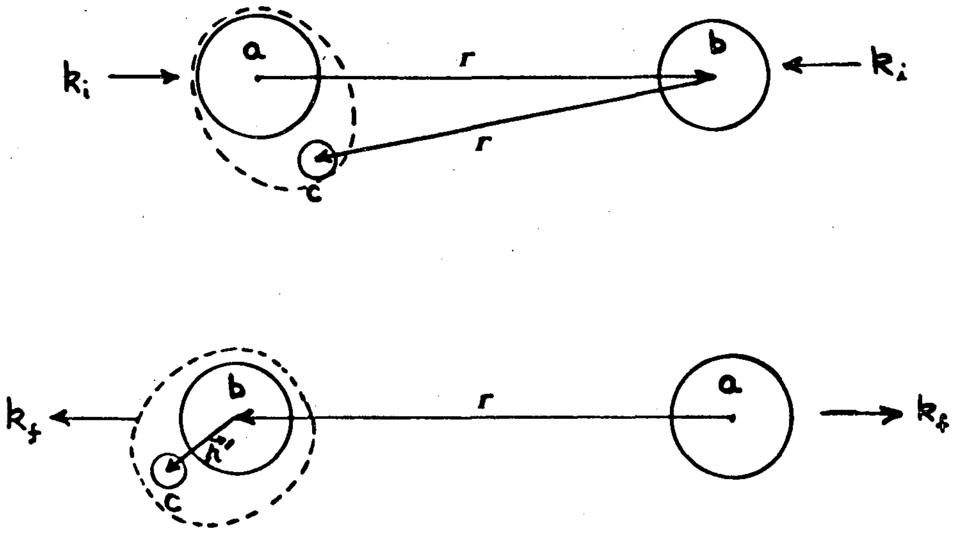

Fig. 2.12

Using the coordinates of Fig. 2.12,

$$T_{fi} = \int d^3r \int d^3r' \, \chi_f^{(-)*}\left(k_f;\, r - \frac{r'}{A_f}\right) u_f^*(r') \, V_{ac}(r+r') \, U_i(r+r') \, \chi_i^{(+)}\left(k_i;\, \frac{A_i - 1}{A_i} r - \frac{r'}{A_i}\right) \tag{2.24}$$

where u_i, u_f are bound-state wave functions for c in the initial and final states, and $A_i = m_a + m_c/m_c$, $A_f = m_b + m_c/m_c$. This integral can be evaluated exactly and the correct procedure for calculating transfer reactions is: determine the distorted waves from an analysis of elastic scattering where the potential is fixed by some prescription such as that of Section 1, and then use them in the transfer integral.(85) This prescription has had many successes, but we wish here to concentrate on *failures*. Therefore, it is instructive to disentangle the various contributions to the six-dimensional integral.

A great simplification occurs if "recoil effects" are dropped, i.e. r'/A_f and r'/A_i are removed from the distorted waves. Then:

$$T_{fi} = \int d^3r \, \chi_f^{(-)*} (\underline{k}_f;\underline{r}) \; \chi_i^{(+)}\left(\underline{k}_i;\, \frac{A_i - 1}{A_i}\, \underline{r}\right) G_{if}(r)$$

$$G_{if}(r) = \int d^3r' \, u_f^*(\underline{r}') \, V_{ac}(\underline{r}+\underline{r}') \, u_i(\underline{r}+\underline{r}') \tag{2.25}$$

and we have two 3-D integrals. If, in addition, we make the "zero range" approximation:

$$G_{if}(r) = u_f^*(-r) \, u_i(0)$$

and

$$T_{fi} \propto \int d^3r \, \chi_f^*(k_f,r) \, \chi_i(k_i,r) \, u_f^*(r) \quad . \tag{2.26}$$

As an example, take an initial state where (a+c) and b are in $\ell=0$ while in final state c is bound to b with orbital angular momentum L. The angular momentum transfer is L. Thus $u_f^* \propto \psi_L^*(r) \, Y_L^M(\hat{r})$. Simplifying still further to a ring locus model (strong absorption) with *plane waves* $e^{i\underline{k}\cdot\underline{r}}$, and if the z-axis is chosen perpendicular to the annulus, $\Theta = \pi/2$ in the spherical harmonics, then

$$\begin{aligned} T_{fi}^{LM} &\propto P_L^M(\pi/2)\int_0^{\pi} d\phi\ \exp[i(\underline{k}_i-\underline{k}_f)\cdot\underline{r}]\ \exp(im\phi) \\ &\propto P_L^M(\pi/2)\int_0^{2\pi} d\phi\ \exp(iqR\cos\phi+im\phi) \\ &= 2\pi\ P_L^M(\pi/2)\ J_M(qR) \end{aligned} \tag{2.27}$$

When the cross section is summed over all M-substates, the Legendre function requires L + M even, and therefore even L transfer will have oscillatory angular distributions characterized by:

$$\sum_M [J_M(2kR\sin\Theta/2)]^2 \tag{2.28}$$

with even M; likewise odd L-transfer will have only odd M and we arrive at the well-known phase rules.

It is found that the main contribution at low energies is associated with $|M| = L$. Classically this corresponds to the transferred particle making the transition between orbits which are nearly perpendicular to the reaction plane; furthermore, as Fig. 2.13 shows,(60) if the initial value of m is $+\ell_i$, the final value will be $-\ell_f$ and the transfer is likely to occur with a large change in the component of L along the z-axis.

The period of the angular oscillations (as usual) is $\approx \pi/kr$ at small angles. (Note that the interference oscillations also follow naturally from the earlier semiclassical treatment of transfer reactions.(69,86) Let us apply our insight to discuss some topical problems in heavy-ion transfer reactions.

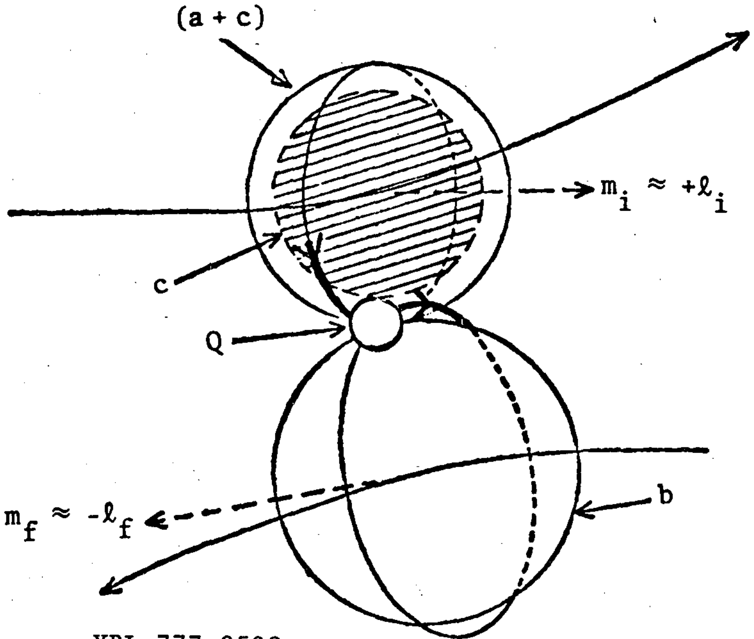

XBL 777-9532

Fig. 2.13

2.4 *Some Interesting Problems in Heavy-Ion Transfer*

2.4.1 *Oscillations*

Take the stripping and pick-up reactions ^{40}Ca(^{13}C,^{12}C)^{41}C and ^{40}Ca(^{13}C,^{14}N)^{39}K, which have been studied at 68 MeV. The data for both reactions$^{(87)}$ shown in Fig. 2.14 have oscillatory angular distributions of period $\pi/kR \approx 5°$ ($k \sim 4.97$ f^{-1} and $R \sim 8$ fm). For the stripping reaction, the DWBA (dashed line) works perfectly, but for pick-up (which should be mainly $L=1$ transfer) the oscillations are exactly out of phase — in fact, they fit with $M=0$, rather than $M=1$ in contradiction to our derived rules, and in contradiction to any reasonable attempts at rectification by the usual parameter juggling of optical model and bound-state parameters. A possible explanation lies in the inclusion of coupled channel effects.

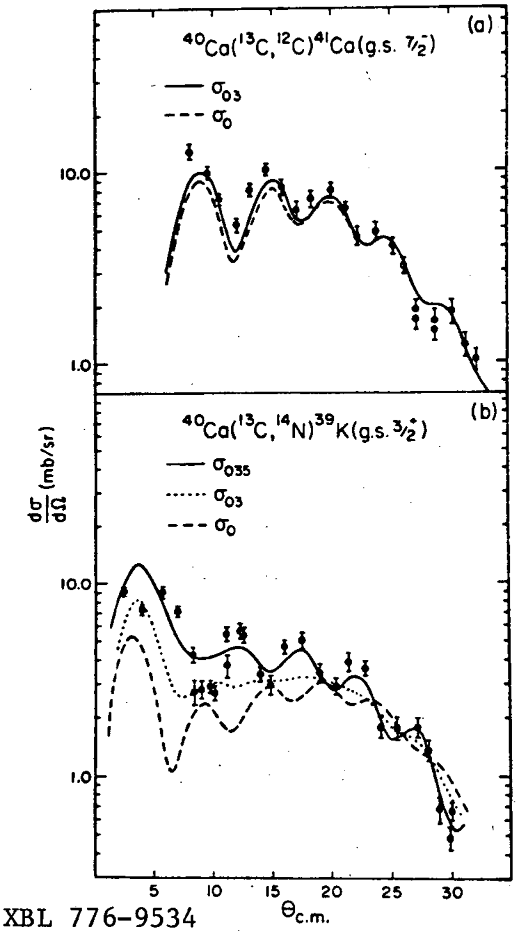

XBL 776-9534

Fig. 2.14

2.4.2 *Coupled channel effects*

It has been suggested that in addition to transferring the particle between the *ground states*, other routes may be important through, for example, pre-excitation of the ^{40}Ca prior to transfer.$^{(88)}$ (Such processes are two-step and go beyond the first-order perturbative treatment of the DWBA). Some possibilities are illustrated in Fig. 2.15. For the stripping reaction the ^{40}Ca gs can be reached by adding an $f_{7/2}$ particle to ^{40}Ca (a transition from ($\ell_i - \frac{1}{2}$) in ^{13}C to ($\ell_f + \frac{1}{2}$) in ^{41}Ca) *or* by adding a $d_{3/2}$ particle to the pre-excited ^{40}Ca, 3^- state (($\ell_i + \frac{1}{2}$) to ($\ell_f + \frac{1}{2}$)). Remember, by our earlier arguments the latter is disfavored; it is further inhibited by our discussion of optimum Q-values ($Q_{opt} \approx -\frac{1}{2}mv^2 + \Delta V_c$) which is not very negative for neutron transfer, where $\Delta V_c = 0$. Therefore inclusion of these routes

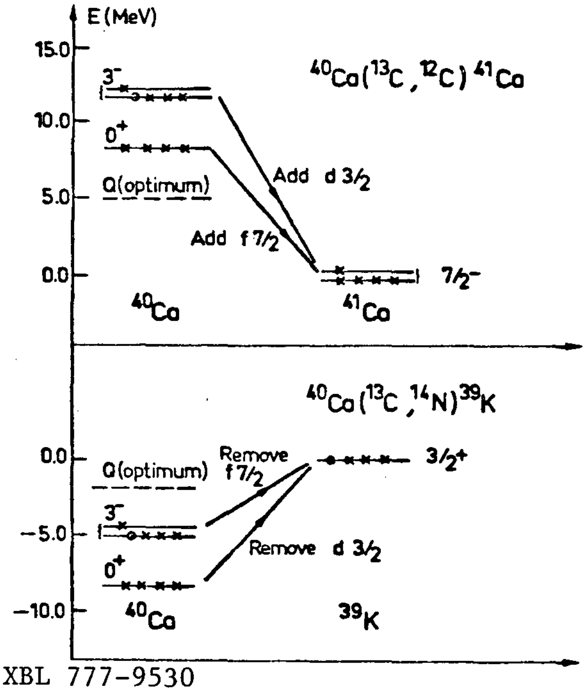

XBL 777-9530

Fig. 2.15

does not have much effect on the stripping reaction (see Fig. 2.14).

Both arguments are reversed for pick-up, and we see that inclusion of 3^- and 5^- excitations improve the agreement of the phase of the oscillations. This situation is not very satisfactory, because there are many other routes that could be included, and in fact inclusion of them all would far exceed present computational techniques. Furthermore, the strength required for the inelastic routes appears to exceed those observed experimentally.(89) However, they are still *too few* to produce the average couplings that we know how to handle via an absorptive potential. We can look on this situation as opening a Pandora's Box, or New Horizons, because here may be just where the unique, interesting heavy-ion physics lies for nuclear spectroscopy. Let us look at a striking example.

2.4.3 *Coupled channel interference effects*

Consider two-neutron transfer, stripping, and pick-up reactions, as illustrated in Fig. 2.16. In pick-up to the 2^+ state, route 2 is direct, and in stripping, 3 is direct. Routes 1 and 4 are branches of indirect routes which can also contribute to transfer via inelastic scattering in the initial and final states. For *vibrational* nuclei the sign of the amplitudes 2 and 3 is opposite and lead to opposite interference patterns with the indirect routes — destructive in stripping and constructive in pick-up.(21,90) A further refinement is introduced by the contribution of Coulomb and nuclear terms to the indirect routes, which contribute with opposite signs, and will interfere differently with the direct routes.

In the pick-up reaction ^{76}Ge(^{16}O,^{18}O)^{74}Ge, a very weak interference dip is observed(91) for the 2^+ of ^{74}Ge* but not of ^{18}O*. It turns out

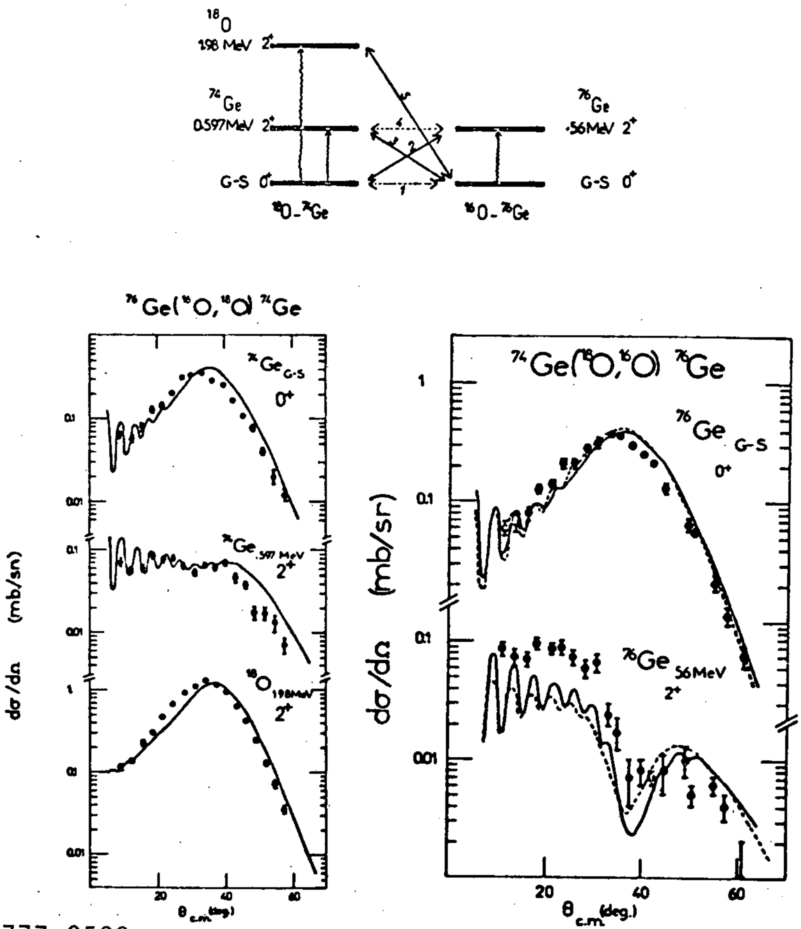

XBL 777-9509

Fig. 2.16

that the direct transition to the 2^+ of ^{74}Ge is negligible, corresponding to the removal of two neutrons from the gs BCS superfluid vacuum of ^{76}Ge, leaving ^{74}Ge in the 2^+ particle-hole vibration. The main population is from the two-step process, first by the removal of a neutron pair to the gs of ^{74}Ge, followed by the creation of a quasi-particle pair of the 2^+. The dip is then caused by Coulomb-nuclear interference in the inelastic scattering section. For the stripping reaction, on the other hand, the direct transition to the 2^+ of ^{76}Ge is strong, and interferes destructively with the nuclear amplitude of the indirect routes, giving rise to a pronounced modification of the characteristic bell-shaped differential cross sections. The ground state transitions are of course identical in the two reactions, since they correspond roughly to time-reversed processes. The theoretical calculations shown require as input optical model parameters for the initial and final channels, deformation parameters for the inelastic excitation, detailed spectroscopic amplitudes for all the states involved in the coupling. The success of the theory is an encouraging indicator that this field — almost unique to heavy-ion transfer — could become important for unravelling sensitive details of the structure of collective states.(92-95) There are severe technical problems in the exact computation of two-nucleon transfer, e.g. successive v. simultaneous transfer.(89,96-98)

2.4.4 *Energy dependence of heavy-ion transfer*

Recently it has become possible to study heavy-ion transfer reactions over a wide energy range from sub-Coulomb up to 20 MeV/A. An example of spectra for the $^{208}Pb(^{16}O,{}^{15}N)^{209}Bi$ reaction is shown in Fig. 2.17. Because of the variety of low-lying single particle states outside the doubly-magic ^{208}Pb, this reaction has almost become a standard for testing reaction theories.(30)

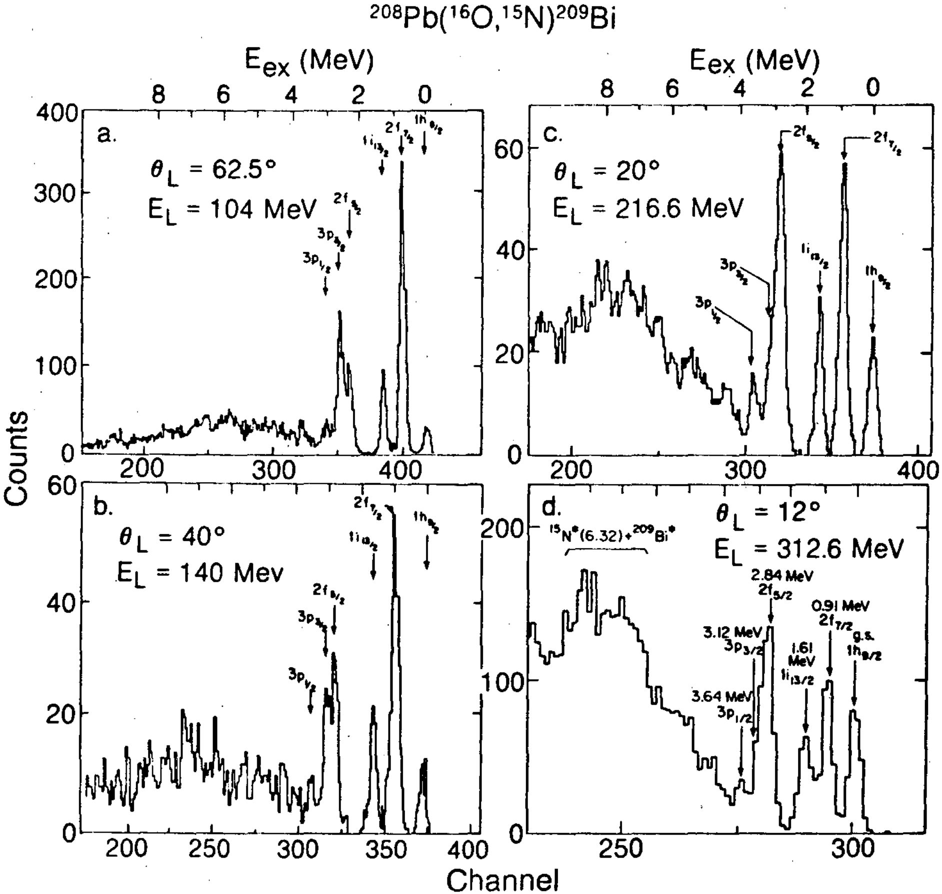

XBL 7612-4518

Fig. 2.17

With increasing energy there is a tendency to favor the population of $j = \ell - \frac{1}{2}$ states (e.g. $f_{5/2} > f_{7/2}$ at 312.6 MeV, but the reverse is true at 104 MeV). Remember that the low-energy semiclassical matching condition favored transitions from $j_<$ to $j_>$ at low velocities.(68,99) The reversal is due to the onset of recoil effects, the neglect of terms of order $1/A_i$ in the distorted waves. These normally introduce 1 to 10% corrections in the phase of the waves. However at energies of 20 MeV/A the momenta of the colliding ^{16}O and Pb nuclei are $\approx 15\ \mathrm{fm}^{-1}$ which, with the nuclear radius of 10 fm, implies $150\hbar$. Very little of this is transferred in the reaction; however the 10% recoil effect can contribute several units of $\hbar$ to the final nucleus.(84)

The effect on the distorted waves can be seen from the expansion(100,101)

$$\chi(\underline{k},\underline{r}+\underline{\delta r}) \approx e^{\underline{\delta r}\cdot\underline{\nabla}}\,\chi(\underline{k},\underline{r})$$

$$\cong e^{\underline{\delta r}\cdot\underline{p}(\underline{r})}\,\chi(k,r)$$

where $p(r)$ is the local momentum at r; then G_{fi} of Eq. (2.25) becomes

$$G_{fi}(r) = \int \underline{d^3r'}\ \exp(i\underline{p}\cdot\underline{r}')\ u_f^*(\underline{r}')\ V_{ac}(\underline{r}+\underline{r}')\ u_i(\underline{r}+\underline{r}') \tag{2.29}$$

and $p \approx k_i/A_i + k_f/A_f$. If the capturing nucleus b has a radius R_b, then we expect for forward scattering that $\ell_p \approx pR_b$ and we expect to find states of $L \approx \ell_p$ populated with high probability. (Note the close correspondence of pR_b to the term $R\Delta k$ in the semiclassical derivation, Eq. (2.15). In the (^{13}C, ^9Be) reaction on ^{16}O, which we discussed earlier, this term has the value of approximately $6\hbar$, which is indeed the strongest state in the spectrum of Fig. 2.10.)

The second major effect of the recoil term is to smooth out the oscillations for angular momentum transfers with $L > 0$. To see this, make the expansion:

$$\exp(i\underline{p}\cdot\underline{r}') = \sum_{\ell} (2\ell+1) i^{\ell}\ P_{\ell}(\cos\Theta')\ j_{\ell}(pr') \tag{2.30}$$

An approximately equal number of even and odd ℓ-values are contained in the plane wave $e^{i\underline{p}\cdot\underline{r}'}$ and the Legendre functions are even[odd] functions of $(\cos\Theta')$ if ℓ is even[odd]. Therefore the Θ' integral over $P_L^M(\cos\Theta')P_{\ell}(\cos\Theta')$ contributes equally for $(L+M)$ even and odd. For a given L, all M values now enter. The selection rules for a transition from an initial state j_i, ℓ_i to j_f, ℓ_f become $|j_i - j_f| \leq \Delta\ell \leq j_i + j_f$ and $|\ell_i - \ell_f| \leq \Delta\ell \leq \ell_i + \ell_f$. (A dramatic illustration(102) of the damping is given in Fig. 2.18.)

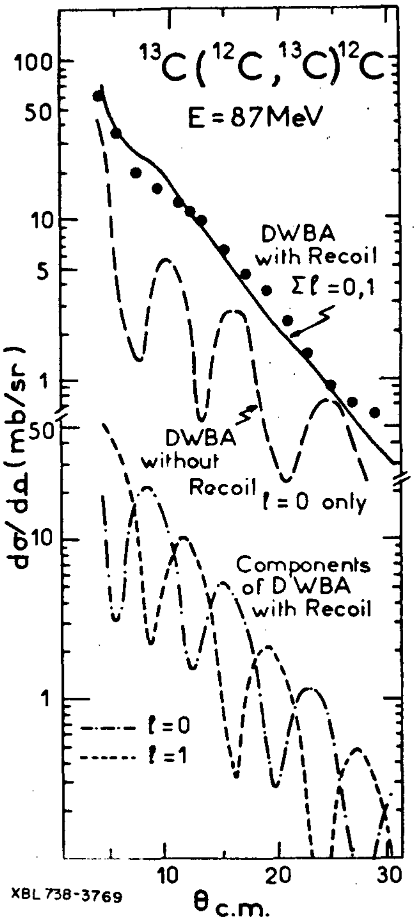

XBL 738-3769

Fig. 2.18

Techniques for evaluating the finite-range, recoil DWBA are available and have been applied to the $^{16}O + ^{208}Pb$ data as a function of energy.(30,85) Such a study is an ideal test of the reaction model, compared to data at a single or closely spaced energies, where deficiencies may be masked by the extreme sensitivity to extraneous details, e.g., the wave functions used to describe the initial and final bound states.

The calculations used optical parameters, $V = 51$, $r_v = 1.11$, $W = 51$, $r_w = 1.11$, $a_v = 0.79$, and $a_w = 0.74$. The bound states were generated in Saxon-Woods wells with the depth adjusted to reproduce the binding energy: for $^{208}Pb + p$, $r_v = 1.28$, $a_v = 0.76$, $V_{\text{spin-orbit}} = 6$ MeV, $r_{so} = 1.09$, and $a_{so} = 0.60$; for $^{15}N + p$, $r_v = 1.20$, $a_v = 0.65$, $V_{so} = 7$ MeV, $r_{so} = 1.20$ and $a_{so} = 0.65$. The resultant spectroscopic factors, normalized to unity for the ground state are shown in Table 2.2 and compared with other reactions and with theory. The satisfactory agreement is typical of the other beam energies *when each set of data is treated in isolation.*

TABLE 2.2 Spectroscopic factors for $^{208}Pb(^{16}O,^{15}N)^{209}Bi$ data at 312.6 MeV.

State	E_Λ	$S(^{16}O,^{15}N)$	$S(^{12}C,^{11}B)$	$S(^3He,d)$	S(Theory)
$1h_{9/2}$	0.00	1.00	1.00	1.00	1.00
$2f_{7/2}$	0.90	0.85	0.96	0.67	0.89
$1i_{13/2}$	1.61	0.77	0.89	0.48	0.74
$2f_{5/2}$	2.84	0.77	0.64	0.75	0.69
$3p_{3/2}$	3.12	0.74	0.82	0.57	0.78
$3p_{1/2}$	3.64	0.69	--	0.38	0.57

When we compare experiment and theory as a function of energy (using the theoretical spectroscopic factors with their absolute values, when $S(h_{9/2}) = 0.95$) a failure of the theory by almost a factor of 10 is encountered from the sub-Coulomb energy of 69 MeV up to 312.6 MeV (see Fig. 2.19). Of course such disagreements could be patched up, energy by energy, by ad-hoc variations of bound state parameters and optical potentials, sacrificing if necessary the qualitative relationship of the bound state potentials to the nucleon-nucleon optical potential, as well as the quality of the optical model fits to the elastic scattering. Such stratagems miss the spirit of the model and even worse have no predictive power. Rather we should say that the method has failed and look for possible causes.

2.4.5 *The two-center shell model and the DWBA*

There are other symptoms of failure of DWBA calculations for heavy ions. Some data exhibit a systematic discrepancy(103) when compared with DWBA, having three features: 1) for weakly bound states the angular distribution is shifted more forward than expected; 2) the shift grows with decreasing binding energy; 3) the magnitude decreases as the incident energy increases. Some of these features are illustrated in Fig. 2.20 (dashed lines are DWBA calculations).

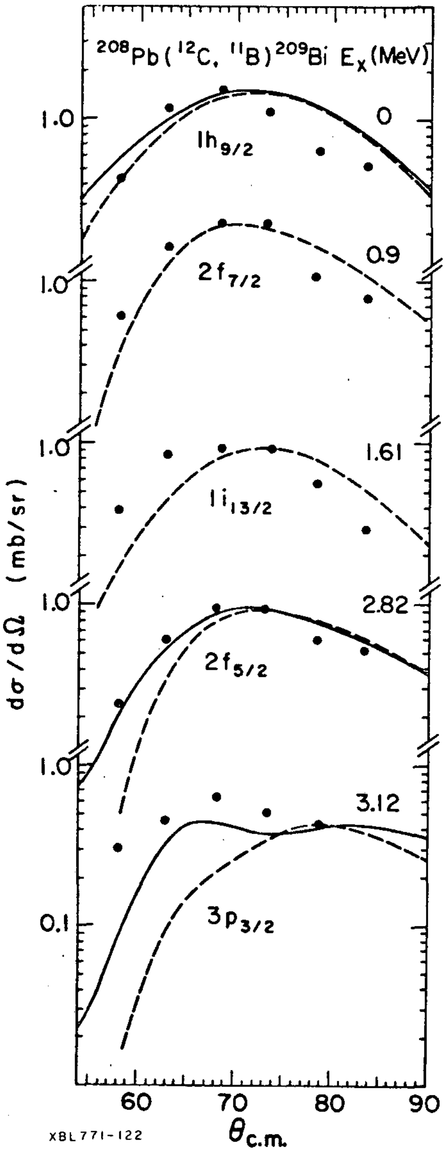

Fig. 2.20

It is possible that as the two heavy ions approach each other, the more weakly bound of the shell model states may be polarized by the field of the other.(104) The result is that a nucleon which is originally in one nucleus may have an appreciable probability of finding itself in the other when their surfaces are close. This polarization can be computed in the two-center shell model. Figure 2.21 is an example of an $^{16}O + ^{40}Ca$

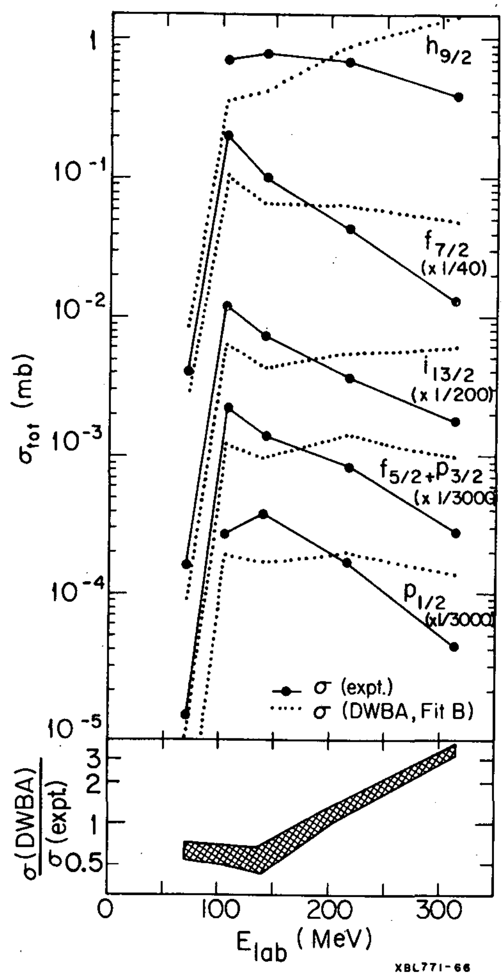

XBL771-66

Fig. 2.19

reaction and shows(105) the probability density for an $f_{7/2}$ state in ^{41}Ca, asymptotically and for the ^{15}N at the grazing distance of 10 fm. Whether during the time of a typical reaction, the shell model states undergo an adiabatic polarization depends on the ratio of the transit time to the nuclear period:

$$\frac{\text{transit time}}{\text{nuclear period}} \sim \left(\frac{E_{\text{Fermi}}}{E/A}\right)^{\frac{1}{2}} \approx 2.5$$

since typically $E_F \approx 30$ MeV and E/A ~ 5 MeV. This effect allows the transfer to take place at larger impact parameters and *shifts the distribution to smaller angles*. A pilot calculation (solid lines) contains the correct features.(106) It is unlikely that this effect could account for the energy-dependent problems of the previous section, because there the discrepancy *increased* with the energy. It illustrates however that heavy-ion transfer reactions, not surprisingly, brings us up against more dramatic perturbations than do light ions. These aspects will be the focus of the succeeding Chapters. Let us end this section with a brief discussion of another new facet of transfer reactions, unique to the heavy-ion situation, and which combines aspects of elastic scattering and of transfer.

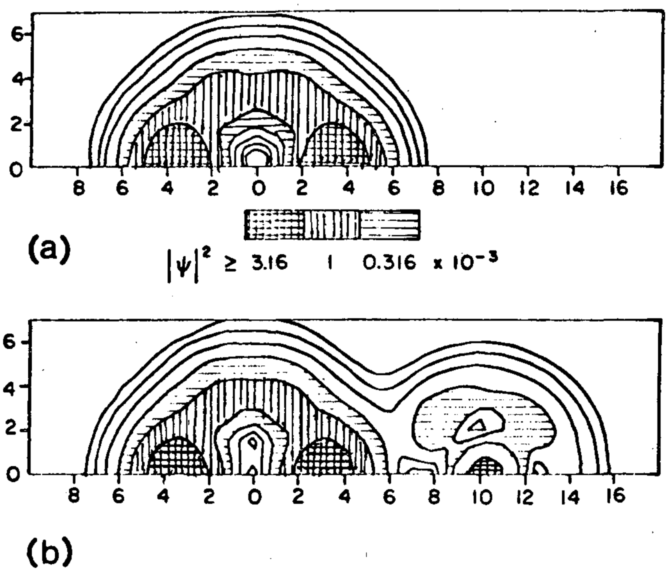

XBL 7610-4639

Fig. 2.21

2.4.6 *Elastic or inelastic transfer*

The scattering of two nuclei A and B in which elastic transfer occurs can be considered to consist of two processes:(107)

$$\begin{aligned} A+B \;=\; A_1+(A_2+b) \;&\rightarrow\; A_1 + (A_2+b) \qquad \text{Elastic} \\ &\rightarrow\; A_2 + (A_1+b) \qquad \text{Transfer} \end{aligned} \tag{2.32}$$

where A_1 and A_2 are identical. Both processes have zero Q-value and interfere coherently. The kinematic relationships are illustrated in Fig. 2.22. Since the transfer process depends (as always) on the amplitude for decomposition of B into $(A+b)$, the measurement of elastic transfer represents a unique way to extract this decomposition. The information is obtained not from the magnitude of the cross section (as in our discussion of $^{16}O+Pb$) but from the *interference pattern.*

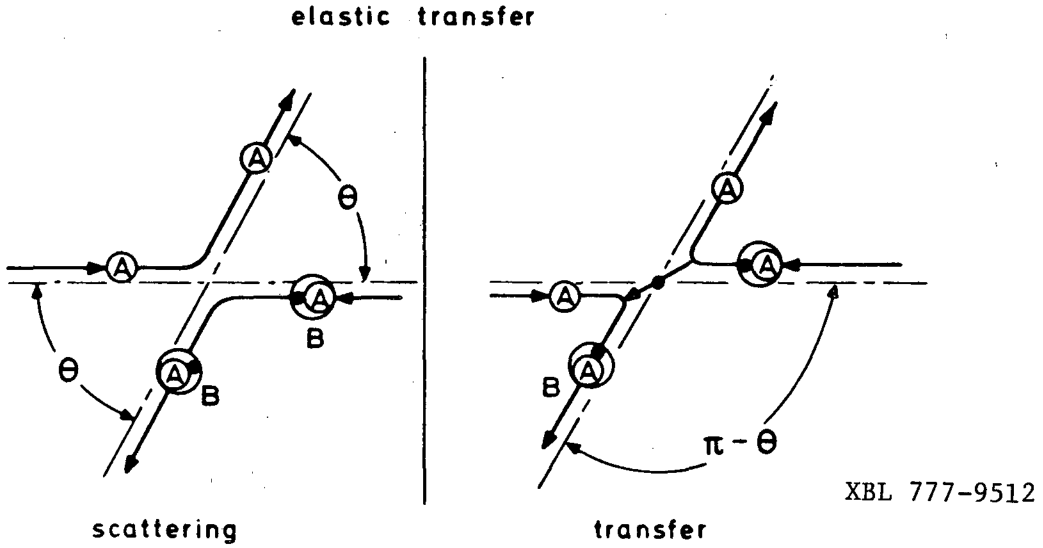

Fig. 2.22

The pattern is typical of Mott scattering. In that case (scattering of identical nuclei) the interference terms occur because of symmetrization of the total amplitude:

$$\frac{d\sigma}{d\Omega} = \left|f_{e\ell}(\Theta) + f_{e\ell}(\pi-\Theta)\right|^2 \tag{2.32}$$

It will be recalled that this formula leads for bosons to:

$$\left(\frac{Z^2e^2}{\frac{1}{2}\mu v^2}\right)^2\left[\frac{1}{16\sin^4\left(\frac{\Theta}{2}\right)} + \frac{1}{16\cos^4\left(\frac{\Theta}{2}\right)} + \frac{\phi}{\sin^2\left(\frac{\Theta}{2}\right)\cos^2\left(\frac{\Theta}{2}\right)}\right] \tag{2.33}$$

where $\phi = 1/8 \cos[\eta \ln(\tan^2 \Theta/2)]$, which determines the frequency of the oscillations. Figure 2.23 is an example$^{(108)}$ for $^{28}Si + ^{28}Si$. This figure shows that the oscillations, in the *cases including transfer, have the same period.* To understand this, we use a semiclassical model for the transfer probability as a perturbation on elastic scattering

$$f_{tr} = P_{tr}(\Theta)\, f_{e\ell}(\Theta) \tag{2.34}$$

Then

$$\left(\frac{d\sigma}{d\Omega}\right) = \left|f_{e\ell}(\Theta) + P_{tr}(\pi - \Theta)\, f_{e\ell}(\pi - \Theta)\right|^2 \tag{2.35}$$

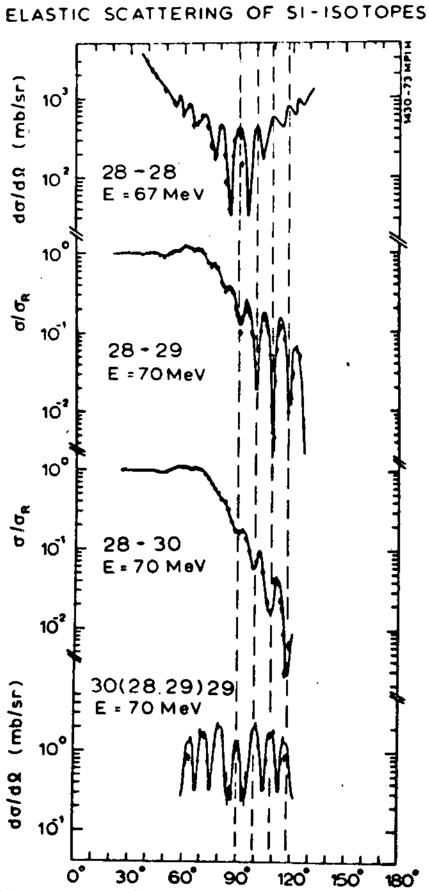

XBL 777-9514

Fig. 2.23

This cross section will obviously have the *same* width of interference structure as the Mott scattering. Because of the P_{tr} factor, the distributions are no longer symmetric (see the middle two diagrams in Fig. 2.23).

The relative phases of all four systems depends on their symmetry.$^{(108)}$ The symmetrized form of the $^{28}Si - ^{28}Si$ Mott scattering contains only even ℓ-values, and shows a maximum at 90°. The same is true for $^{30}Si(^{28}Si, ^{29}Si)^{29}Si$; assuming the incoming channel spin $S_i = 0$ is conserved, the two outgoing fermions also have $S_i = 0$, and therefore even ℓ. The phase of the system with particle exchange can be understood in the LCNO model (linear combination of nuclear orbitals) for which the basic equation is:

$$\{T_R + U_R + (-1)^L V_{exch}(R)\}\, \chi_L(R) = E\chi_L(R) \tag{2.36}$$

which describes the relative motion of the cores with an optical potential U and the exchange potential

$$V_{exch}(R) = \int \phi_\ell(r)\, V(r)\, \phi_\ell(r - R)\, d^3R \tag{2.37}$$

The zero spin of the cores and the exchange of S-nucleons determines that even scattering waves are submitted to an additional attractive potential. Odd waves are therefore *less absorbed* and dominate the scattering amplitude.

In elastic transfer we have the favorable situation that a small amplitude interferes with a large amplitude (elastic scattering). If we write the two amplitudes as f_1, f_2:

$$\frac{d\sigma}{d\Omega} = |f_1 + f_2|^2 = |f_1|^2 + |f_2|^2 + f_1^* f_2 + f_1 f_2^* \qquad (2.38)$$

Since $2\mathrm{Re}|f_1^* f_2| / |f_1|^2 \leq 2|f_2|/|f_1|$, a cross section $|f_2|^2$ only $1/10^3$ of $|f_1|^2$ gives rise to deviations of ±6%. Therefore in the vicinity of the Coulomb barrier, elastic transfer seems to be the best way of testing the existence of the nuclear Josephson effect.(109) As an illustration, Fig. 2.24 shows the case $^{86}\mathrm{Kr} + {}^{88}\mathrm{Sr}$, the lightest "superconductors." Remember, these oscillations are not the Fresnel or the Fraunhoffer types which have dominated our earlier discussions.

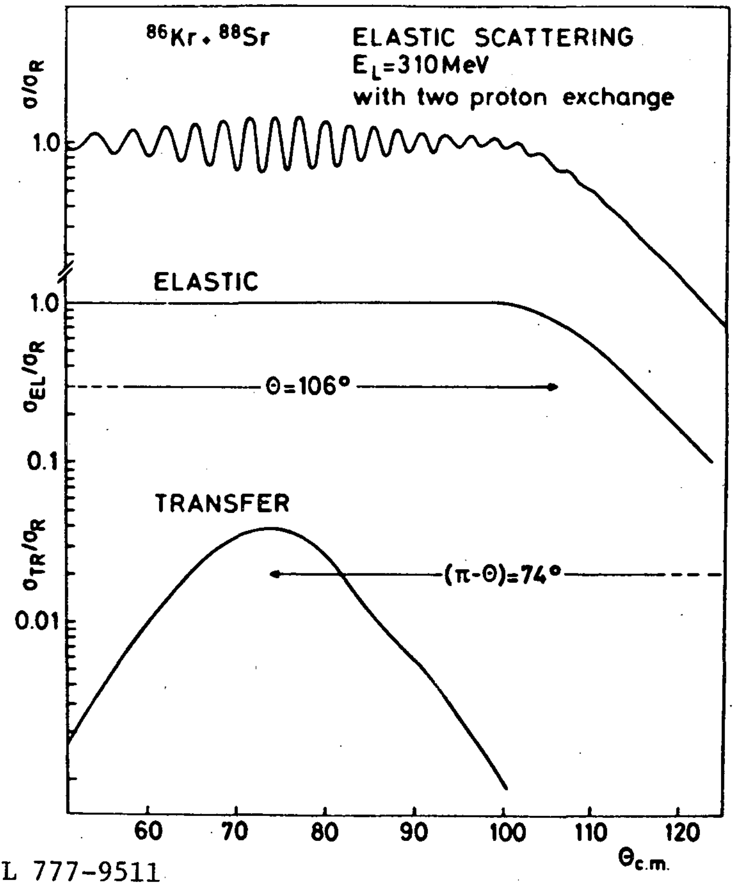

XBL 777-9511

Fig. 2.24

3.

HEAVY-ION COMPOUND NUCLEAR REACTIONS AND THE CONTINUUM

The first two Chapters dealt with processes that were essentially extensions of light-ion studies. Only small amounts of energy and matter were transferred between the ions. In this chapter much more drastic perturbations of the nucleus are introduced, enabling us to study nuclei in new modes of motion.

3.1 Compound Nuclear Reactions

It may have come as a surprise that the last section on transfer reactions had nothing to say about multinucleon transfers of more than four nucleons. Initially these were the great promising frontier for new spectroscopy with heavy ions. It was discovered that such reactions in fact proceed through the formation of a compound nucleus, with subsequent evaporation of a complex fragment. Take the $^{12}C(^{14}N,^{6}Li)^{20}Ne$ reaction, for which spectra at three energies(110,111) are shown in Fig. 3.1. At the lower energies the reaction possesses a certain selectivity — *reminiscent of direct reactions* — which disappears at 120 MeV. However, when *complete* angular distributions were measured (Fig. 3.2) they possessed symmetry about 90° with a form $(1/\sin\theta)$ characteristic of emission from a high spin compound nucleus(112) $(d\sigma/d\Omega \Rightarrow d\sigma/d\theta;\ d\theta/d\Omega \Rightarrow 1/\sin\theta$, since $d\sigma/d\theta$ is constant). We now show that the presence of selectivity (or its absence) is a characteristic feature of heavy-ion compound reactions,(113,114) which become an important spectroscopic tool in their own right.(111)

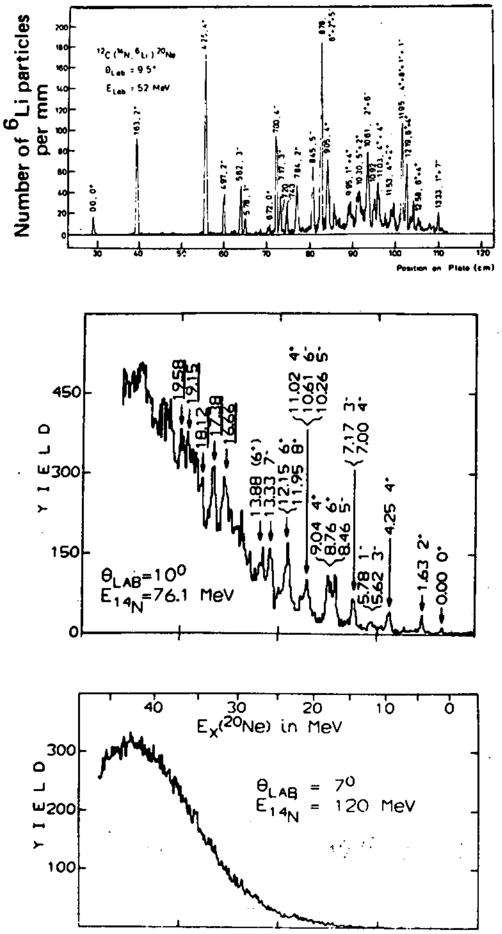

XBL 777-9565

Fig. 3.1

For the compound reaction:

$$a + A \rightarrow C^* \rightarrow b + B \quad ,$$

we have

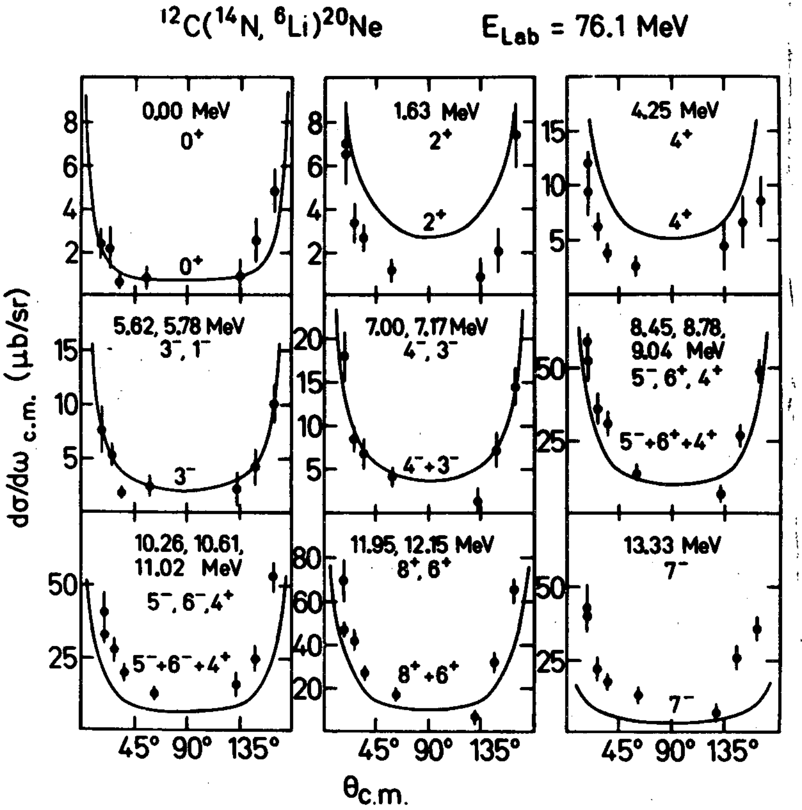

XBL 777-9573

Fig. 3.2

$$\sigma_{\mathrm{form}}(J) = \pi \bar{\lambda}^2 \frac{(2J+1)}{(2I_A+1)(2I_a+1)} \sum_{S_i=|I_A-I_a|}^{|I_A+I_a|} \ \sum_{\ell_i=|J-S_i|}^{|J+S_i|} T_{\ell_i}(E_{CM}) \qquad (3.1)$$

where T_{ℓ_i} is a transmission coefficient evaluated with the optical model. σ is shown in Fig. 3.3 at two bombarding energies, demonstrating that σ_{CN} is dominated by a few high L partial waves close to the grazing value. Further for the outgoing channel the transmission coefficients fall rapidly for $L_{out} > L_{out}^{grazing}$, and therefore it is plausible that only these levels located inside or near the curve defined by $L_{inc}^{grazing}$ and $L_{out}^{grazing}$ (which is a function of the Q-value and excitation energy of the reaction, i.e., $E_f = E_{CM} + Q - E_x$ and $L_{out}^{grazing} \approx R_f\sqrt{2M_fE_f}$) will be strongly excited. The shape of the spectrum is determined by the overlap between the curve and the yrast line of the final nucleus

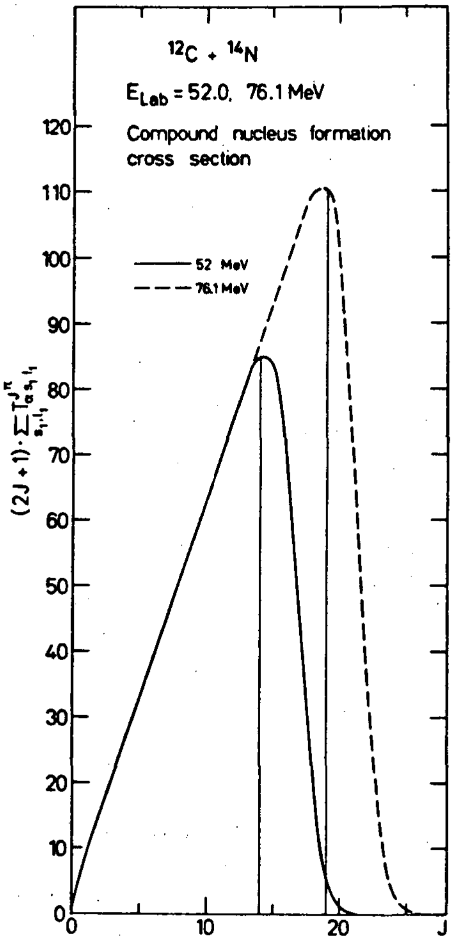

Fig. 3.3

XBL 777-9567

$$E_{\text{yrast}} \approx \frac{\hbar^2}{2\mathcal{J}} J(J+1) \tag{3.2}$$

which is the lowest excitation energy possible in the nucleus for a given angular momentum J. Above this locus the level density increases exponentially. So one expects, for example, from Fig. 3.4 that the $^{10}B(^{12}C,d)^{20}Ne$ reaction would be selective,(115) and the $^{10}B(^{14}N,\alpha)^{20}Ne$ not,(116) which is exactly the experimental observation. (A similar pair of reactions are illustrated in Fig. 3.5.)

In order to understand the $(^{14}N,^{6}Li)$ reaction, a more detailed analysis is required.(111) The total cross section for the excitation of an individual state of spin I_B at E^*_B is:

$$\sigma(E^*_B, I_B) = \sum_J \sigma_{\text{form}}(J) \frac{G(E^*_B, I_B, J)}{g(J)} \tag{3.3}$$

where G and g are the partial and total decay widths. The flux into all states of spin I_B existing in the energy interval dE^*_B at excitation

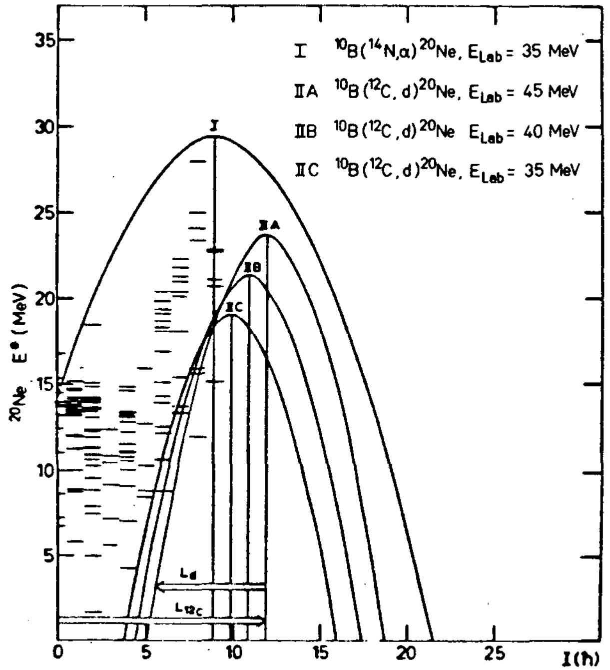

Fig. 3.4 XBL 777-9570

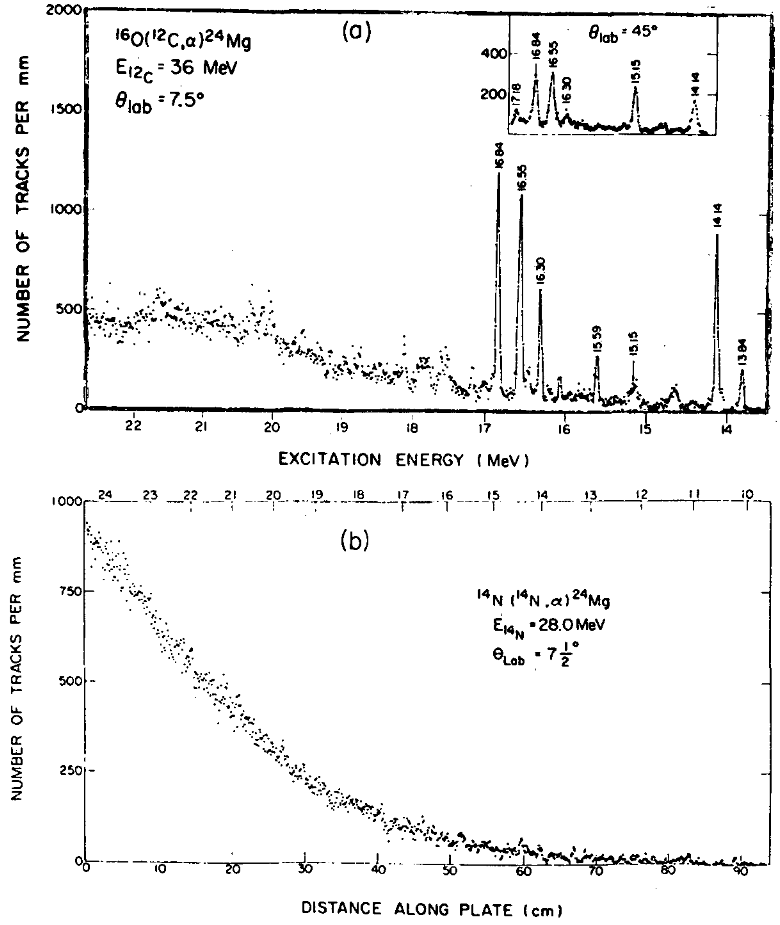

XBL 777-9569

Fig. 3.5

energy E_B^* is:

$$\frac{d\sigma(E_B^*,I_B)}{dE_B^*} = \rho_B(E_B^*,I_B)\ \sigma(E_B^*,I_B) \qquad (3.4)$$

where ρ_B is the level density in the final nucleus. And finally the total cross section per excitation energy interval dE_B^* independent of spin:

$$\frac{d\sigma(E_B^*)}{dE_B^*} = \sum_{I_B} \rho_B(E_B^*,I_B)\ \sigma(E_B^*,I_B) \ . \qquad (3.5)$$

These quantities can be evaluated in the Hauser-Feshbach formalism, although the technical and philosophical difficulties are enormous. We shall see, for example, that the summation over ℓ in the compound nuclear formation cross section may have to be truncated, because the compound nucleus may be unable to support large amounts — without fissioning. Spin cut-off and level density parameters have to be determined in the level density formulae:

$$\rho(E^*,I) = \frac{2I+1}{12\sqrt{2}\ a^{\frac{1}{4}}\ E^{\frac{5}{4}}\ 2\sigma^3}\ \exp(2\sqrt{aU})\ \exp\left[-\frac{(I+\frac{1}{2})^2}{2\sigma^2}\right] \qquad (3.6)$$

[Typical values are: $a \approx A/7.5$, $\sigma \approx (0.146\sqrt{aE}\ A^{2/3})^{1/2}$.] Nevertheless, the calculations have been accomplished and these quantities are shown in Fig. 3.6 for the reactions of Fig. 3.1.

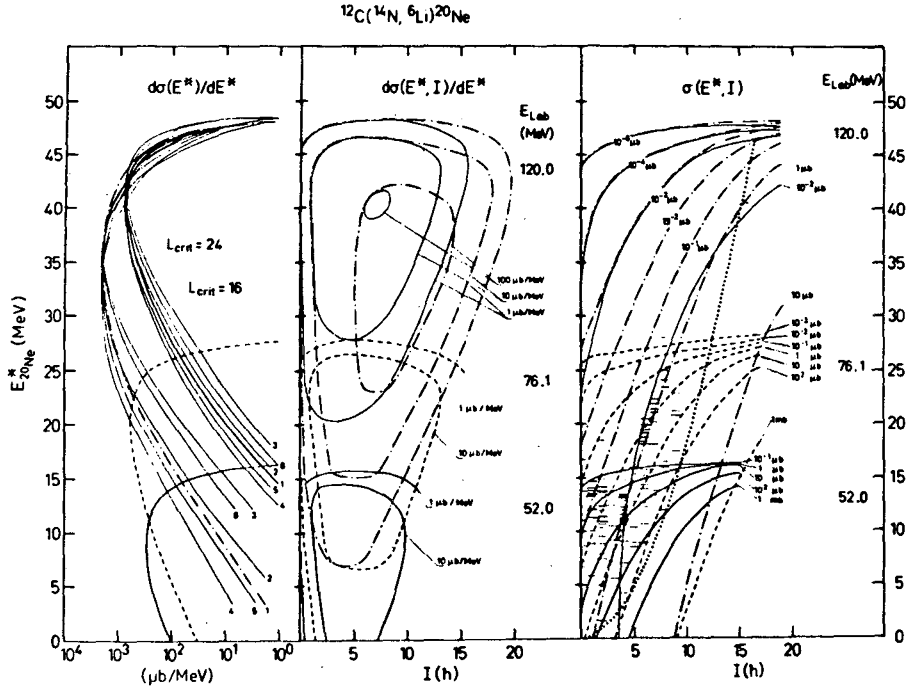

Fig. 3.6

The function $d\sigma(E^*)/dE^*$ gives the overall shape of the spectrum and its maximum fixes the "optimum Q-value" which agrees with the experimental spectra. The function $d\sigma(E^*,I)/dE^*$ shows which spins contribute mainly to the shape of the spectrum. Only if the gradient $d\sigma(E^*,I)/dI$, shown in the last part, is large and at the same time, the ratio of cross sections $\sigma(E^*,I)$ of individual levels near the yrast line (shown dotted) to the "background" given by $d\sigma(E^*)/dE^*$ in the first part of the figure is large, can one expect selectivity. Thus, for example, at 120 MeV in Fig. 3.1 there is no selectivity because the cross sections to individual states at the yrast line (shown dotted) are low compared to the average background. At 76 MeV the selectivity is excellent for 8^+ (11.95 MeV), 7^- (13.33 MeV) and 9^- (17.39 MeV). The Hauser-Feshbach predicted angular distributions agree well with the data, both in shape and absolute magnitude (see Fig. 3.2).

Now we consider the implications for spectroscopy. An important observation is the stability of the *ratio* of cross sections to different states against variations of level density parameters, although they do vary as a function of the cut-off in angular momentum for the formation of the compound nucleus, J_{crit} (Fig. 3.7). The fits of the ratio of statistical theory cross sections for the states at $E^* = 11.92$ and 12.14 in ^{20}Ne to the ratio of experimental cross sections$^{(118)}$ for different choices of the level density parameter "a" (curves 1 and 2 average "a" over shell effects ($a \sim A/6$); curve 3 takes into account shell effects in the different final nuclei) are shown in Fig. 3.8. Clearly J_{crit} can be deduced with high accuracy independent of "a" [$J_{crit} = 14 \pm 1$ for this reaction, $^{10}B(^{12}C,d)$ at $E = 45$ MeV].

We shall discuss the origins of J_{crit} in the next Chapter; however, it is clear that having determined it from states of *known spin*, the procedure may be reversed and *spin assignments made from relative cross sections*. For example, it has been proposed that there may exist in ^{20}Ne superbands, i.e. rotational states with moments of

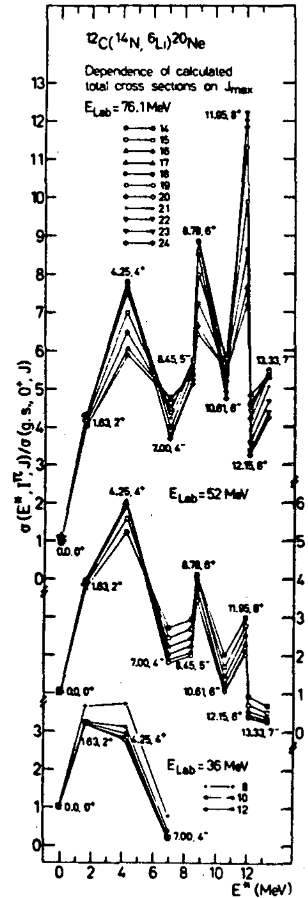

Fig. 3.7

XBL 777-9568

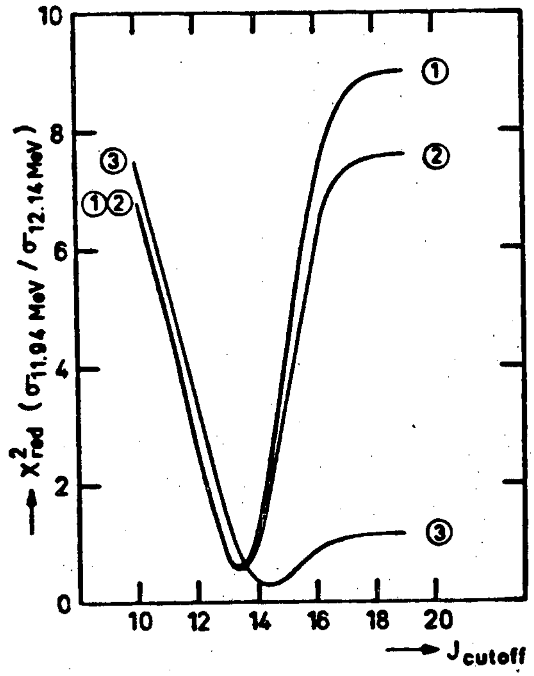

Fig. 3.8

XBL 777-9572

inertia much larger than for the ground state band.(119) Such states are shown in Fig. 3.9 by the double dashed lines; they rely on the 9^- assignment to state at 15.17 MeV which is then suggested to be a member of a 9p-5h or 7p-3h superband. Furthermore, the assumption that the 8^+ state at 11.95 MeV does not belong to the g.s. 4p-4h band but might be a member of an 8p-4h superband, would imply that the g-s band 8^+ and also higher members of the 8p-4h band should be located between 12 and 15 MeV. (Recall our earlier discussion of the state in Fig. 2.10.)

Looking at the spectrum of the reaction $^{10}B(^{12}C,d)^{20}Ne$ (Fig. 3.4 demonstrated its selectivity) in Fig. 3.10, it is already clear — even by inspection — that the 15.17 MeV level cannot be I = 9 (compare the intensity of the neighboring I = 7 at 15.38 MeV). In the statistical model analysis, the population of states in the final nucleus should be independent of the special configurations of the states. Therefore below E* = 16 MeV, there exists no state as a likely candidate for I = 9. The interesting hypothesis of superbands in ^{20}Ne seems very doubtful.

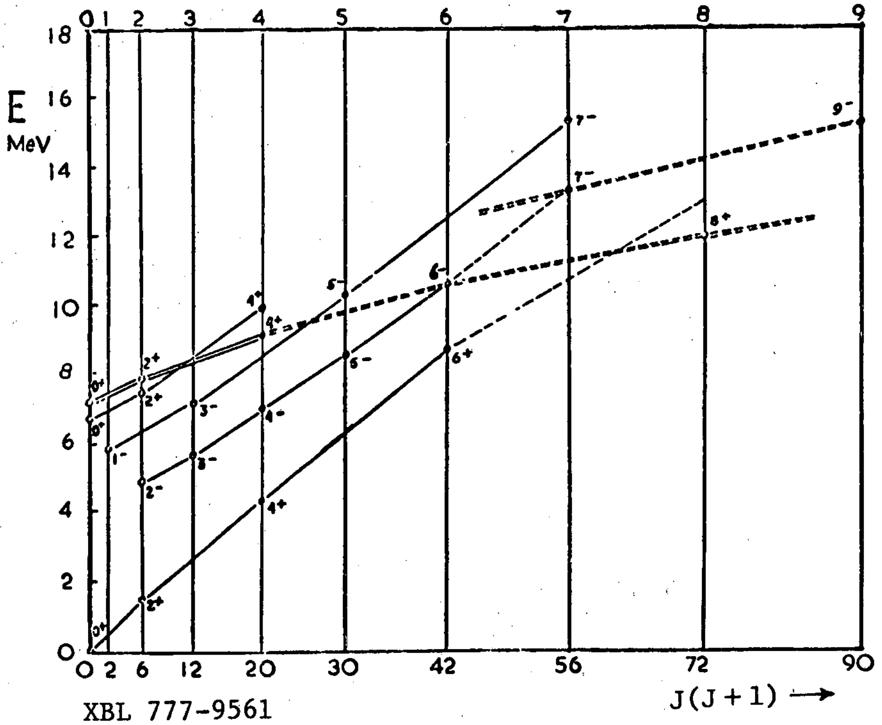

XBL 777-9561

Fig. 3.9

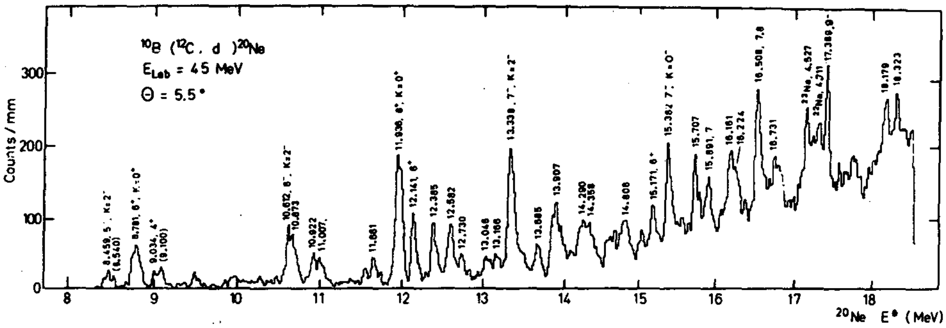

Fig. 3.10

XBL 777-9563

3.2 Compound Elastic Scattering

Here we discuss the evidence for nuclear molecular states, which are formed by the two colliding ions rotating in a dumbbell-like configuration.(120,121) These have manifested themselves as resonances in the excitation functions of heavy-ion elastic scattering and of reactions.

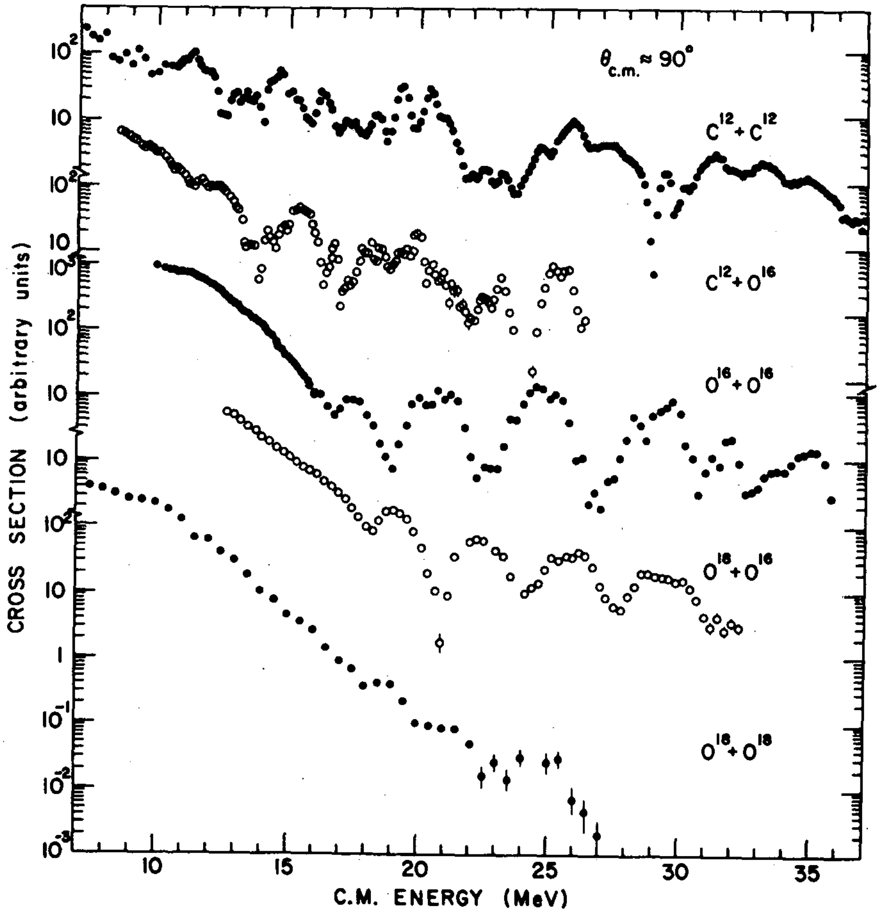

Fig. 3.11

XBL 747-1248

Figure 3.11 is a collection of the 90° excitation functions(122) for elastic scattering of systems ranging from $^{12}C + ^{12}C$ to $^{18}O + ^{18}O$.

There are wild oscillations for carbon on carbon. Some of the fluctuations are smoothed out with $^{12}C + ^{16}O$ systems and progressively disappear as we proceed to $^{18}O + ^{18}O$. Also the oscillations continue unabated to much higher energies(123) (Fig. 3.12). At the lower energies the gross oscillations (typically 3 MeV wide) have been fitted(124) with a potential of the forms shown in Table 3.1.

TABLE 3.1

System	V	R	a	W W	R_I	a_I
$C^{12} + C^{12}$	14	6.18	0.35	0.4 ± 0.1E	6.41	0.35
$O^{16} + O^{16}$	17	6.8	0.49	0.8 ± 0.2E	6.40	0.15

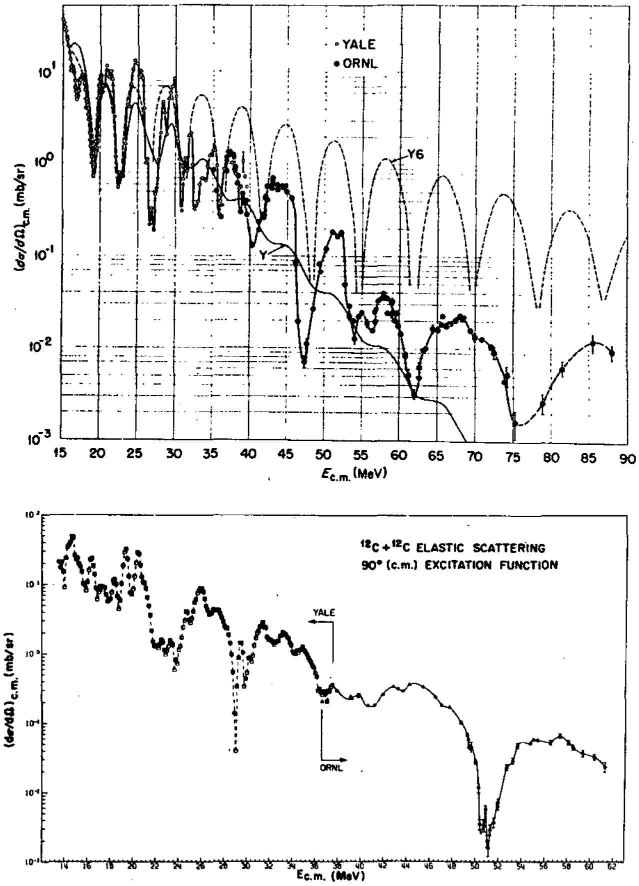

Fig. 3.12

XBL 777-9592

The fits obtained have the correct character (see Fig. 3.13), and at certain energies are almost pure $[P_L(\cos\theta)]^2$. The values of L are given on the right of the figure. At these energies the phase shifts are close to $\pi/2$. The small values of the imaginary potential are essential in order to obtain the observed oscillations in the cross section of the correct width. Recall that this width is equal to 2W. This transparency is crucial to molecular phenomena, since only if the surface regions remain transparent can the interacting nuclei retain their identity for a sufficiently long period to make a molecular description meaningful. The quality of fit for the $^{16}O + ^{16}O$ system up to high energies with the above potential is shown by the curve Y6 on Fig. 3.12.

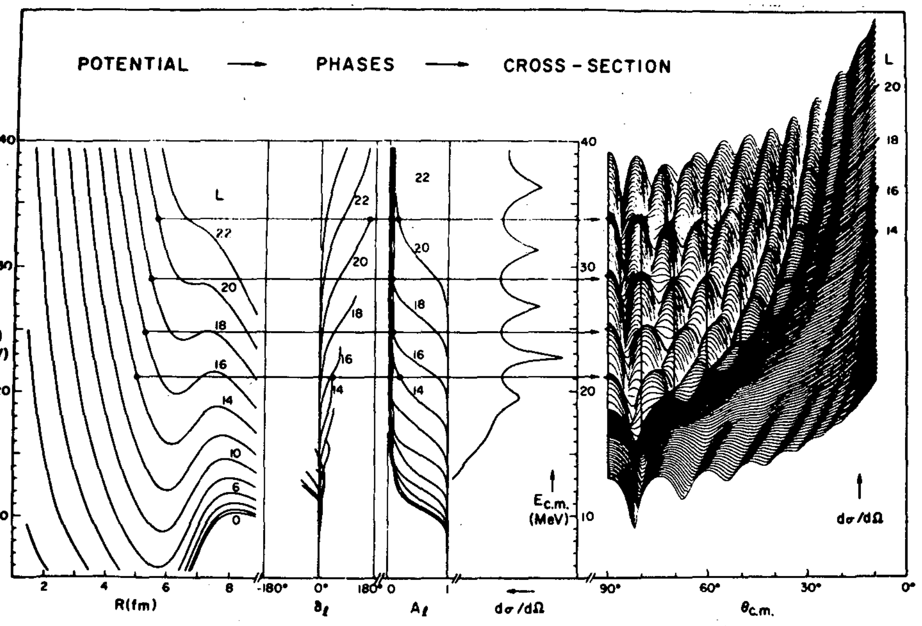

XBL 777-9566

Fig. 3.13

The weak absorption can be simulated by using an ℓ-dependent absorption, which cuts off in strength when ℓ exceeds a critical value. The cut-off becomes particularly important if the nuclei in the entrance channel bring in more angular momentum than any of the exit channels can carry away. A striking demonstration of the effect is evident in a comparison of the $^{16}O + ^{16}O$ and $^{20}Ne + ^{12}C$ systems, with the energy of the latter chosen to populate ^{32}S at roughly the same excitation energy and angular momentum as the $^{16}O + ^{16}O$ data.(125) The $^{20}Ne + ^{12}C$ exhibits only very weak resonance structure (see Fig. 3.14). The angular momentum

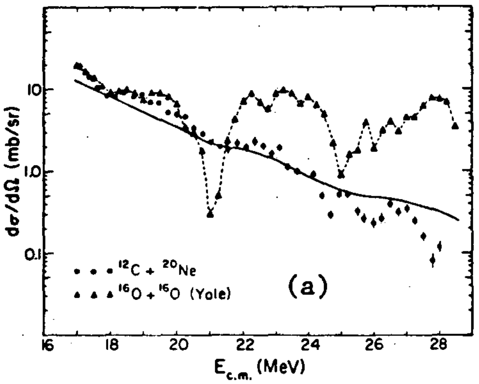

XBL 777-9575

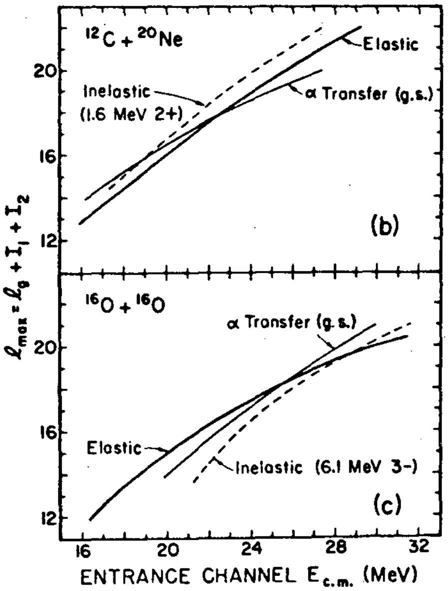

Fig. 3.14

carried out by some of the dominant contributing channels is shown in 3.14(b) and (c) for the two systems, which clearly demonstrates the inability of $^{16}O + ^{16}O$ to remove the necessary angular momentum. For efficient removal, the exit channel curves must lie at or above that of the entrance channel. This comparison seems to rule out the possibility that the ℓ-dependence of the potential is related to the angular momentum-dependent level density of the compound nucleus,(126) since the compound nucleus was prepared identically in the two reactions.

Closer examination of the excitation functions reveals that in addition to the *potential* shape resonances there is a superimposed fine structure of ≈ 100 keV width. Such structure has also been discovered in the excitation functions for many reaction channels. A good example is the $^{12}C(^{12}C,p)^{23}Na$ reaction illustrated in Fig. 3.15 for several different residual states of ^{23}Na, and compared with other outgoing α,d channels.(127) The equivalent excitation energies of the compound ^{24}Mg system is shown at the top. There exist pronounced narrow resonances at 11.4, 14.3, and 19.3 MeV, which are correlated strongly in different channels. By comparing the various branching ratios, spins of 8^+, 10^+, and 12^+ were assigned.

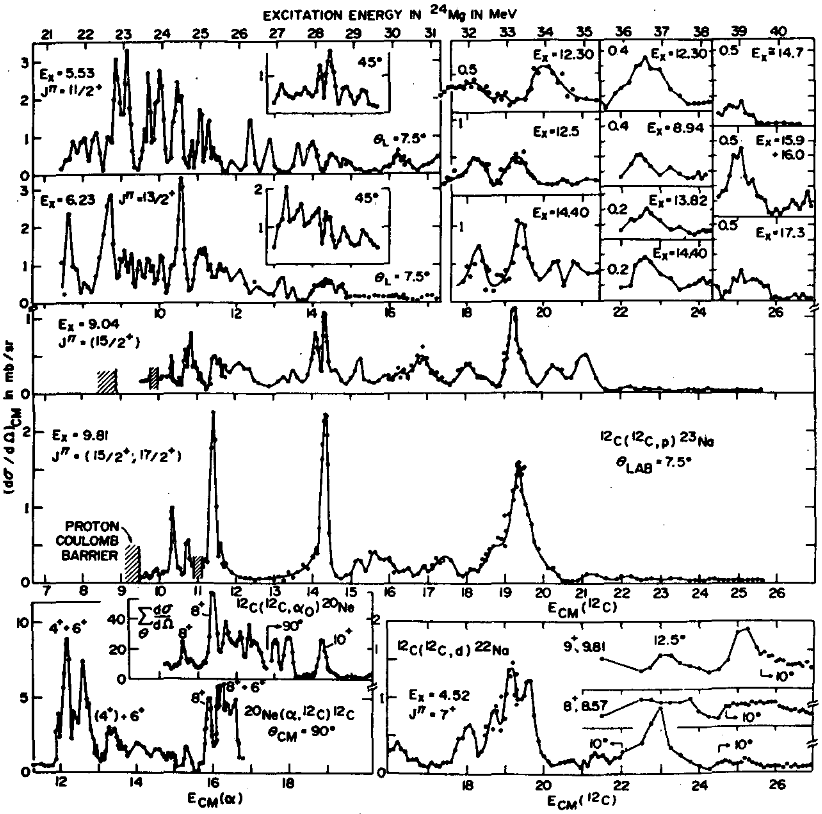

Fig. 3.15

XBL 777-9571

A summary of all reported resonances(121) appears in Fig. 3.16(a), and and we see that there are clusters of a given J^{π}. We now recall that the pockets in the potential for different partial waves (Fig. 3.13) are capable of causing quasi-molecular shape resonances. The values of E_{CM} at which the potential in our earlier

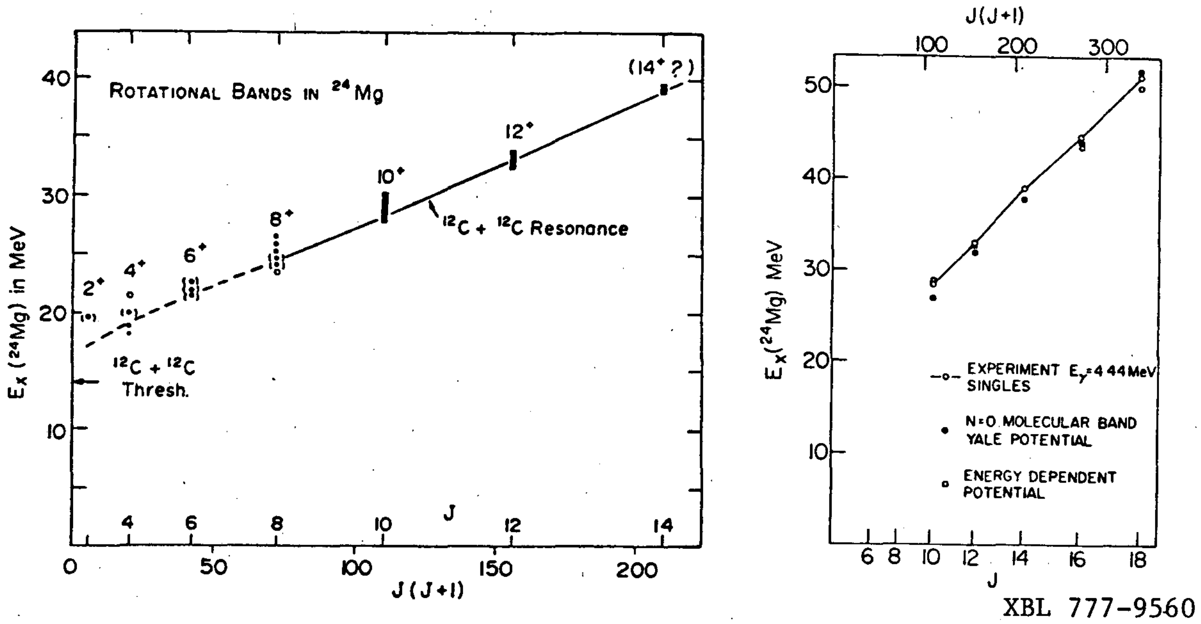

XBL 777-9560

Fig. 3.16

table for the ^{12}C + ^{12}C system gives a resonance can be determined by a Regge trajectory analysis$^{(128)}$ and corresponds to the horizontal lines in Fig. 3.13. The Regge trajectory generates a rotational molecular band,

$$E_J \propto \frac{h^2}{2\mathcal{I}} J(J+1) \tag{3.7}$$

and the slope of the line in Fig. 3.16(a) corresponds to $h^2/2\mathcal{I}$ = 100 keV, *just* the value we calculate for two carbon nuclei in dumbbell rotation at the grazing distance:

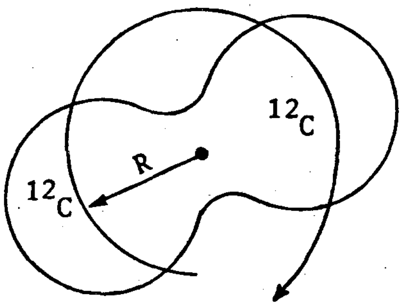

Fig. 3.17

$$\mathcal{I} = 2 \times 2/5\ MR^2 + 2\ MR^2$$

$$\hbar^2/2\mathcal{I} = 100\ \text{keV}$$

$$R \doteqdot 2.7\ \text{fm}$$

(For comparison, the $h^2/2\mathcal{I}$ of the ground-state band is ≈ 200 keV, i.e. a lower moment of inertia ≈ $2/5\ MR^2$.) Extrapolation of the band to the 0^+ member on the vertical axis shows that the band begins$^{(129)}$ almost at the threshold for ^{12}C + ^{12}C in ^{24}Mg.

Each shape resonance is fragmented into the superimposed fine structure. The incident wave in a given L state is weakly coupled to excited states of the system which fragments the shape resonance into components (the sum of the widths of all known 10^+ states is ≈ 2.65 MeV, just equal to a typical shape resonance observed in elastic scattering). These resonances are therefore examples of doorway states; the dynamics involved in the formation of these states might be the excitation of the ^{12}C nucleus to its 2^+ 4.43 MeV level, or the double excitation of both nuclei.(121,130-132) A resonance occurs at an energy such that after the excitation of the nuclei, they are in a quasi-bound state of the appropriate angular momentum. Thus the doorway state consists of excited ^{12}C nuclei trapped in a potential well pocket, as illustrated in Fig. 3.18 together with an example of the success of this model in reproducing the fine structure in an ^{16}O + ^{16}O shape resonance.(133)

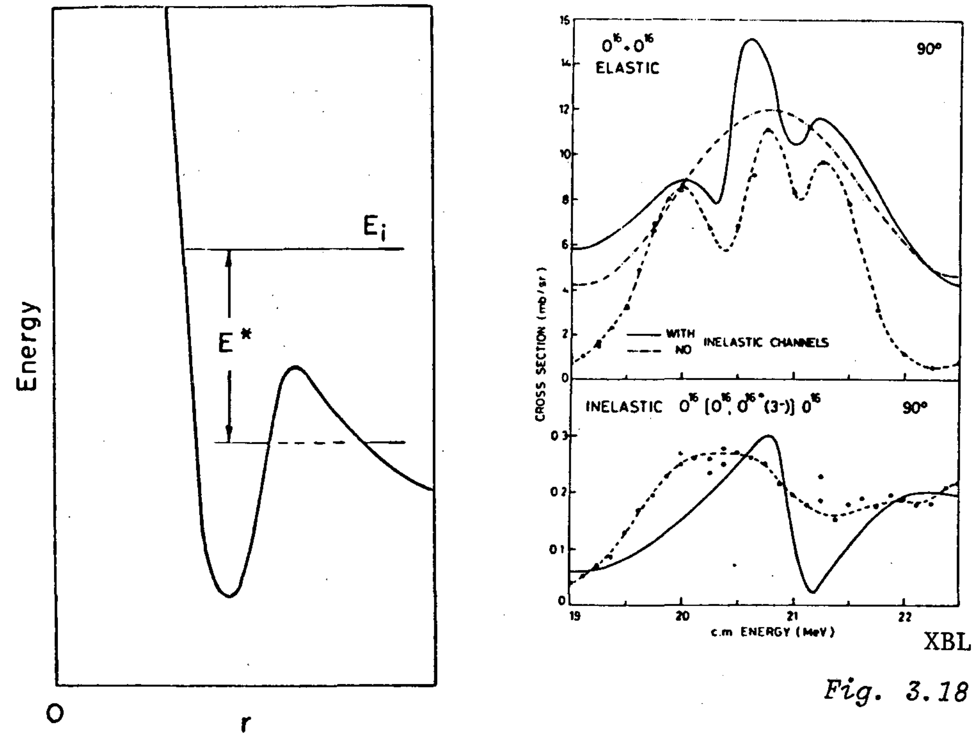

XBL 777-9559

Fig. 3.18

Support for this picture of the resonances comes from a study(134) of the angle-integrated cross section of the reaction ^{12}C(^{12}C, ^{12}C(2^+)) ^{12}C(2^+). Figure 3.19 shows that the excitation function (for the single excitation and double excitations) are dominated by broad resonances with fine structure; the upper three members fall on a continuation of the molecular band, with the same moment of inertia (see Fig. 3.16(b)). A comparison of the resonant energies and widths with those extracted from molecular band calculations is shown in Table 3.2.

A fine structure can also be observed in Fig. 3.19, which in many cases is correlated with the known resonances in light particle decay

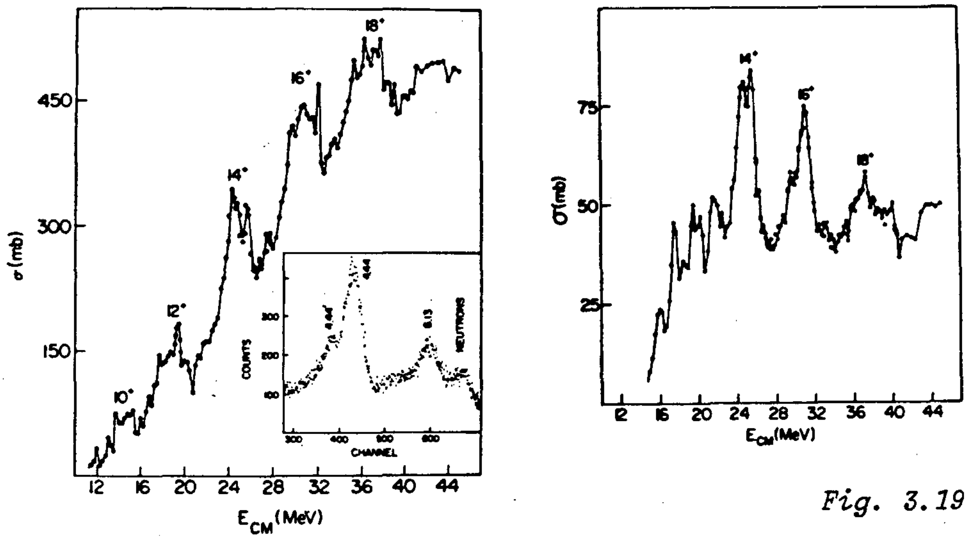

XBL 777-9562

Fig. 3.19

TABLE 3.2

		Experiment				Molecular Band	
J^π	$E_x(^{24}Mg)$	Γ_{tot}	Γ_{el}	$\Gamma_{2^+,2^+}$	$\Gamma_{2^+} + \Gamma_{CN}$	E_x	Γ_{tot}
10^+	28.5	1.8	--	--	--	28.6	1.1
12^+	33.0	2.9	--	--	--	32.8	2.0
14^+	39.0	2.3	≥ 0.10	≤ 2.2	1.4	37.8	3.4
16^+	44.7	3.0	≥ 0.13	≤ 2.9	1.76	43.5	4.5
18^+	51.0	4.3	≥ 0.12	≤ 4.2	2.87	50.0	5.0

channels (Fig. 3.15). If this structure corresponds to individual isolated doorway states, then the fact that all such states are observed in the mutual inelastic and single inelastic channels suggests that these channels are indeed important components of the doorway state wave functions.

The surface transparency arguments for closed shell nuclei such as $^{16}O + ^{16}O$ have led to the search for similar quasi-molecular structures in heavier systems, $^{28}Si + ^{28}Si$ and $^{40}Ca + ^{40}Ca$ — so far with negative results. Excitation functions for the $^{40}Ca + ^{40}Ca$ system are shown(135,136) in Fig. 3.20. Using the physical insight afforded by the semiclassical parameterizations of our earlier sections, it turns out that the gross structure has its origins(137) in the interference between amplitudes $f_+(\theta)$ and $f_-(\theta)$ which measure the importance of Fraunhoffer and Fresnel scattering. Of importance is the ratio:

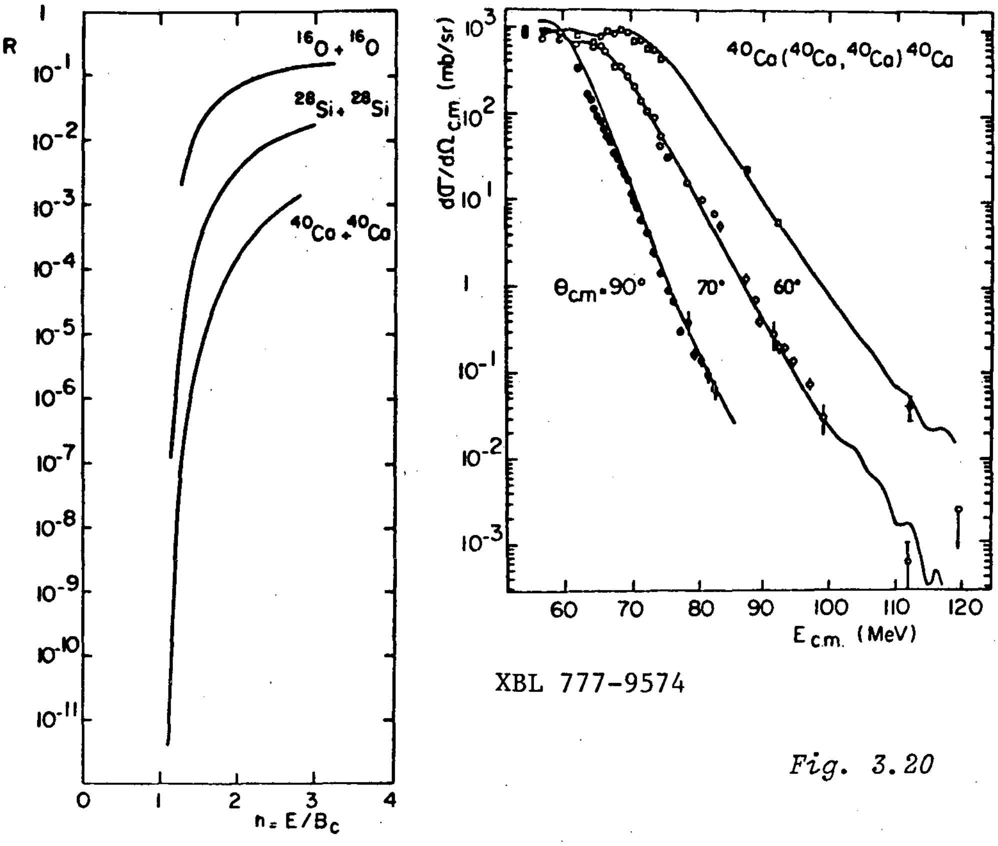

XBL 777-9574

Fig. 3.20

$$R = \frac{f_+}{f_-} \approx e^{-2\pi\Delta\theta_c} \tag{3.8}$$

where θ_c is the critical angle and where

$$\Delta = \frac{kd\left(1 - \frac{\eta}{kR}\right)}{\left(1 - \frac{2\eta}{kR}\right)^{\frac{1}{2}}} \tag{3.9}$$

which measures the width of the transition region over which the reflection coefficients vary from 0 to 1, when fitted by the expression:

$$T(\ell) = \left[1 + \exp\left(\frac{L^{opt} - \ell}{\Delta}\right)\right]^{-1} \tag{3.10}$$

A convenient expression for $\Delta = 6.6 \times 10^{-2}\, d(2h-1)/[r_o(h-1)]^{\frac{1}{2}} A^{4/3}$ where $h = E/B_c$ (B_c = Coulomb barrier), and at equal values of E/B_c, θ_c has equal values. The plot of R vs. h in Fig. 3.20, shows therefore, that the large interferences associated with light systems will disappear for Ca + Ca except possibly at much higher energies $\approx 5B_c$ or above 300 MeV, where there are no suitable accelerators available at present.

It appears therefore that the $^{12}C + {}^{12}C$ system is rather extraordinary, permitting us not only to observe shape resonances but also the next stage of complexity in finer doorway states. The carbon nuclei avoid both the Scylla of being too easily polarizable and the Charybdis of not being polarizable at all.(121) These experiments have provided evidence for the existence of molecular bands up to very high angular momentum (20ħ) and at very high excitation energy (up to 40 MeV) in light nuclei. In the last section we discuss the evidence in much heavier nuclei.

3.3 Very High Spin States in Nuclei

The discovery(138) in 1971 of a pronounced irregularity around spin 16ħ (called backbending) in the otherwise very regular behavior of the rotational sequence of even-even rare earth nuclei, has opened up a vigorous research field in the study of high angular momentum in nuclei.(139,140) An illustration of the backbending phenomenon appears in Fig. 3.21;

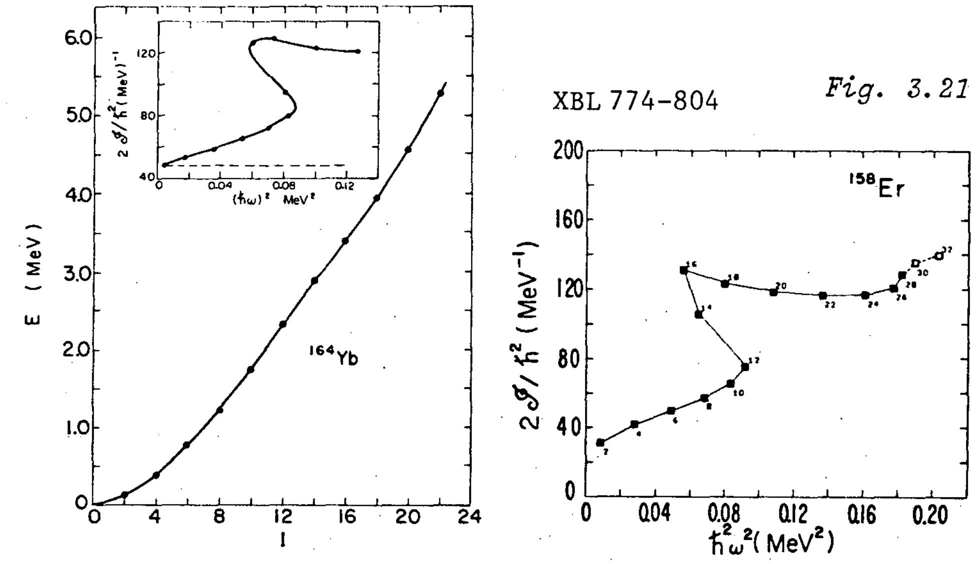

XBL 774-804

Fig. 3.21

a slight discontinuity is evident in the plot of:

$$E_J \propto \frac{\hbar^2}{2\mathcal{J}} J(J+1)$$

at J = 14. On the Variable Moment of Inertia model(141) we write:

$$E_J = \frac{\hbar^2}{2\mathcal{J}} J(J+1) + \tfrac{1}{2}C\left[\frac{\mathcal{J}}{\hbar^2} - \frac{\mathcal{J}_0}{\hbar^2}\right]^2 \qquad (3.11)$$

and

$$\frac{\mathcal{J}}{\hbar^2} = \frac{\mathcal{J}_0}{\hbar^2} + \frac{3}{4c}(\hbar\omega)^2 \qquad (3.12)$$

Therefore a plot of moment of inertia versus the rotational frequency squared should yield a straight line. The inset in Fig. 3.21 shows a marked departure from this trend, with a sudden incresae in the moment of inertia.

Three effects have been given serious consideration as the causes for backbending. These are:(140)

- a collapse of the pairing correlations;(142)
- a shape change, i.e. change of deformation;(143)
- an alignment of the angular momenta of two high j nucleons with that of the rotating core.(144)

The fact that the moments of inertia of most deformed nuclei are about one-half of the rigid body value is attributed to pairing correlations, which partly prevent the nucleons from following the rotation. It now appears more likely that backbending is due to the breaking of one pair rather than total pairing collapse (the gradual reduction of pairing appears rather to account for the variable moment of inertia up to the backbend). The physical process involved in breaking the pair is the Coriolis force which forces the angular momentum vector j of the particle to decouple from the deformation (symmetry) axis and align with the rotation axis. In the $i_{13/2}$ orbit, for example, this effect gives a total of 12ħ which can replace an equal amount of core rotational angular momentum.

On this model, at still higher angular momenta, additional pairs of high-j nucleons will tend to be aligned, and just such a discontinuity appears to be observed(145) in the ^{122}Sn(^{40}Ar,4n)^{158}Er reaction at 166 MeV, in which large amounts of angular momenta are deposited (Fig. 3.21). Here the second discontinuity at $J = 28\hbar$ appears to make a further step towards the formation of an oblate nucleus in which all the angular momenta is carried by aligned particles.

At each backbend, two different rotational bands cross, and the excitation mechanism jumps from one to the other. The existence of two bands has been demonstrated *directly* in some cases by following the ground state band *beyond the backbending* region. Such is the case in ^{164}Er for which the γ-deexcitation spectra following Coulomb excitation with a ^{136}Xe beam, and the ^{164}Dy(α,4n) reaction, are compared(146) in Fig. 3.22. The spectrum for (α,4n) demonstrates how backbending manifests itself experimentally, where a gate is set on a certain (high-J) transition

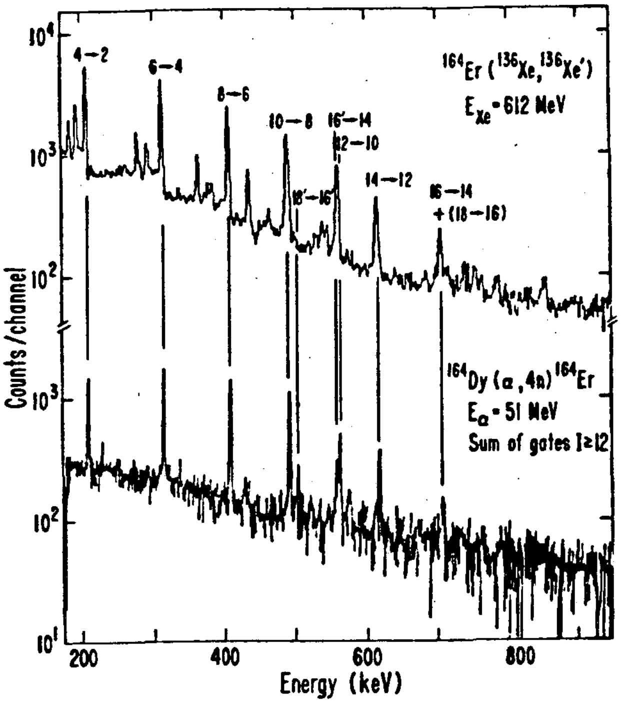

Fig. 3.22 XBL 763-2513A

and the coincidence E2 cascade to the lower levels is observed. It is clear that the transitions labeled 16'-14 and 18'-16' are "out of sequence" compared to the regular spacing of the 4-2, 6-4, 8-6, etc. transitions. Note, however, that in the upper spectrum from Coulomb excitation there are, in addition, regularly spaced transitions 16-14 and 18-16 which are the continuation of the ground-band *beyond the $J = 16$ backbending region* (compare Fig. 3.21). (Only recently have sufficiently heavy beams become available to Coulomb excite such high spin states.)

Guided by this introduction to high spin phenomena, let us now speculate(147,148) on the possible behavior of nuclei as even large amounts of energy and angular momentum are deposited (Fig. 3.23). The lower, approximately parabolic, line is the yrast line so there are no levels in the nucleus below this. The upper line gives the fission barrier, which sets an upper limit to the study of levels of the nucleus. The intersection of the two gives the effective maximum angular momentum for the nucleus. Nuclei in the rare earth region have prolate shapes near the ground state as a result of shell structure, and they have strong pairing correlations. The hatched region indicates where pairing correlations exist, which terminate as we have seen, around $I = 20$, where the two bands cross.

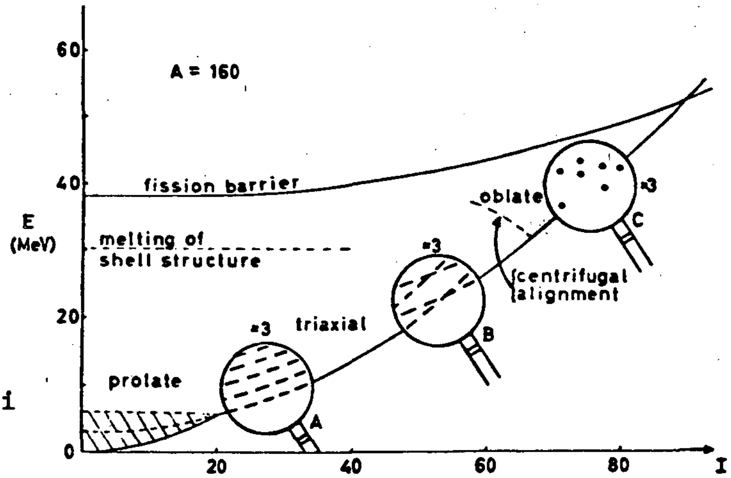

XBL 764-971 *Fig. 3.23*

Some insight into the region above I = 20 comes from the liquid drop model. A rigidly rotating charged drop prefers an oblate shape until shortly before fission. The large moment of inertia of oblate shapes minimizes the total energy. Although the nucleus cannot rotate about a symmetry axis, it has been shown(149) that for a Fermi gas the states obtained by aligning the angular momenta of individual particles along the symmetry axis is the same as would be obtained by rigid rotation about that axis. These deformation-aligned states in oblate nuclei therefore generally are lower than the rotation aligned states in prolate nuclei. At high angular momentum the nucleus becomes oblate and the angular momentum is carried by aligned individual nucleons (region C in the figure). This region may be identified by the occurrence of isomeric states,(147) due to the absence of smooth rotational band structure. At the very highest spins the nucleus may become triaxial before fission. The increase in deformation and moment of inertia is predicted to be so rapid that the rotational frequency will decrease, leading to a "super-backbend." Between the prolate and oblate regions, nuclei are also expected to become triaxial. Wobbling motion is then possible in addition to rotation about the axis with largest moment of inertia, and could give rise to a series of closely spaced parallel bands.(150) (Note that two aligned high-j orbits represent a triaxial bulge in prolate nuclei.)

How do we get an experimental handle on these new modes of motion of the nucleus? The problem is to learn about high spin states above I = 20, as discussed above, especially those along the yrast line, where the nucleus is thermally cool and does not have a high density of states. The remarkable feature of the (HI,xn) reaction is that it can locate us along different regions of the yrast line.(151) This works as follows: in Fig. 3.24, the compound nucleus ^{166}Yb is formed with an angular momentum distribution from J = 0 to J = ℓ_{max} at excitation energy $E_{CM} + Q \approx 60$ MeV by the partial cross sections:

$$\sigma_\ell = \pi \lambda\!\!\!^{-2} (2\ell + 1)\, T_\ell \tag{3.13}$$

The successive evaporation of x neutrons from these states is assumed to remove practically no angular momentum and an average of 2 MeV kinetic energy plus the binding energy of ≈ 8 MeV. Neutron evaporation continues until the available energy above the yrast line is less than 10 MeV. Since

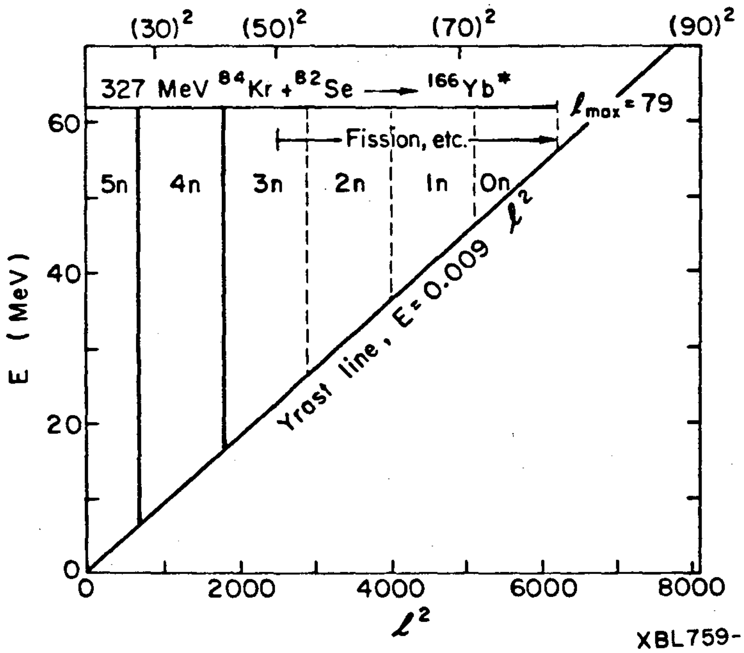

Fig. 3.24

XBL759-3919

$$E_y = \frac{\hbar^2}{2\mathcal{J}} \ell(\ell+1) \tag{3.14}$$

a given value of x occurs in the sharply defined "bin" ℓ_i to ℓ_f where:

$$\begin{aligned} E_y(\ell_i) + 10 &= E_{CM} + Q - 10x \\ E_y(\ell_f) &= E_{CM} + Q - 10x \end{aligned} \tag{3.15}$$

The partial cross section for the evaporation of x neutrons is then:

$$\sigma x = \pi\lambda^2 \sum_{\ell_i}^{\ell_f} (2\ell+1)T_\ell \approx \pi\lambda^2 \left[\ell_f(\ell_f+1) - \ell_i(\ell_i+1)\right] \tag{3.16}$$

As long as $0 < \ell_i < \ell_f < \ell_{max}$, it follows that

$$\sigma x = \pi\lambda^2 \frac{2\mathcal{J}}{\hbar^2} \cdot 10 \text{ , } \textit{independent of } x \text{ .} \tag{3.17}$$

(The largest and smallest bins can be truncated due to the limits $\ell_i = 0$, $\ell_f = \ell_{max}$.) Furthermore, the mean angular momentum $\bar{\ell}$ of the states on which the neutron evaporation chains terminate is predicted for each bin:

$$\bar{\ell} = \frac{2}{3} \frac{\ell_f^2 + \ell_f\ell_i + \ell_i^2}{\ell_f + \ell_i} \tag{3.18}$$

Channels corresponding to different numbers of evaporated neutrons have different angular momentum ranges and the highest angular momenta are in the channels with the fewest evaporated neutrons. These results have been demonstrated experimentally.(152)

A specific application is shown(151) in Fig. 3.25 for the initial production of A ~ 160, with an argon beam of 170 MeV. The initial excitation is 70 MeV and the 4n channel drops down to roughly 10 MeV above the yrast line, without removing much angular momentum. There is still a high density of levels, and there follows a high-energy statistical cascade of dipole transitions, which still do not carry off much angular momentum. Approaching the yrast line the level density becomes small, and the most likely mechanism is then stretched-E2 transitions along the yrast collective bands. Eventually these run into the discrete levels of the ground state band and generate spectra like Fig. 3.22. By setting gates on the lines corresponding to the 4n channel, in the discrete region one can look at the associated spectrum from the continuum observed in sodium iodide counters, with an experimental apparatus such as in Fig. 3.26.

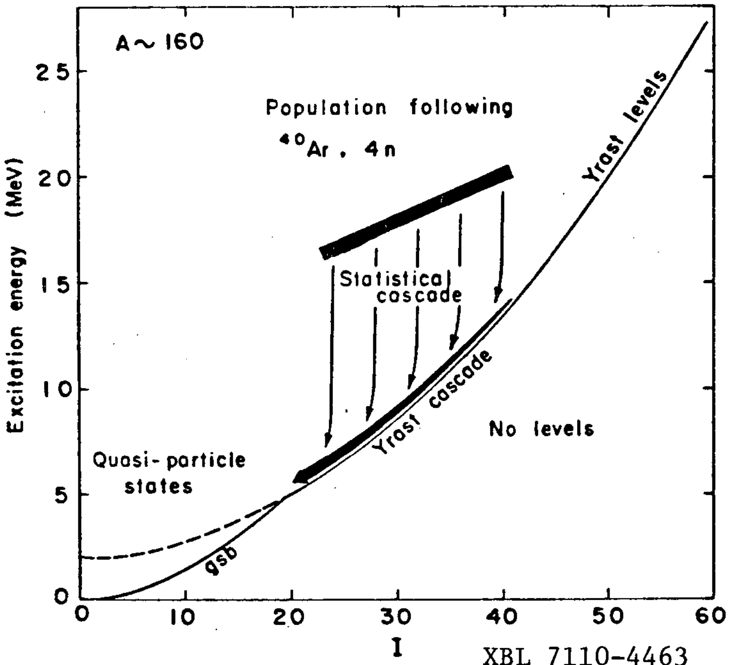

XBL 7110-4463

Fig. 3.25

The observed continuum spectrum associated with the $^{126}Te(^{40}Ar,4n)^{162}Yb$ is shown in Fig. 3.27 with the hollow squares.(153) The dots show the corrected spectrum after "efficiency unfolding." The exponential tail is associated with the statistical dipole emission and the lower energy

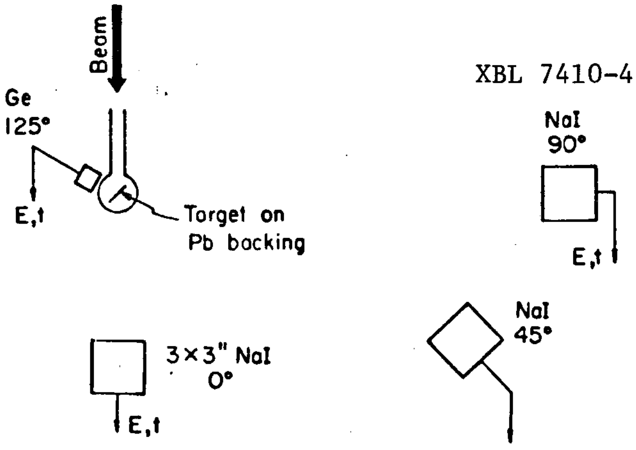

XBL 7410-4508

Fig. 3.26

bump with the E2 cascade. (The identification is confirmed by the anisotropy shown at the top of the figure, obtained by comparing the 0° and 90° sodium iodide detectors.) The integral bump gives the number of γ rays.

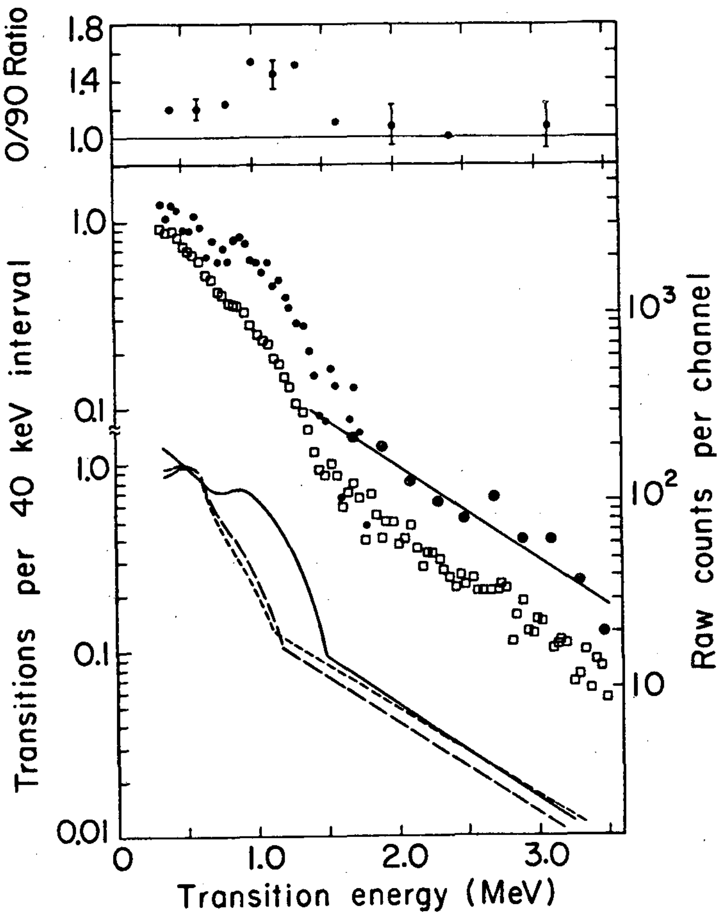

XBL 7511-9561

Fig. 3.27

We can then determine the average angular momentum $\bar{\ell}$ carried in the cascades as

$$\ell = 2(\bar{N}_\gamma - \delta) \qquad (3.19)$$

where δ is the number of statistical γ-rays removing no angular momentum. Now we can use our earlier theorems about the bins and the associated $\bar{\ell}$ of different xn reactions and compare theory and experiment, generating(154) the remarkable line in Fig. 3.28. The slope is not exactly one half, but close at 0.43 (i.e., 2.3ħ/γ-ray — presumably the neutrons take away *some* angular momentum anyway). If we also associate the bump edge with transitions from the states of highest spin in the bin, we can determine the moments of inertia $\mathcal{J}$ at these high spins from the relation

$$E_\gamma = \frac{\hbar^2}{2\mathcal{J}}(4I - 2) \qquad (3.20)$$

the expression for transition energies in a rotor.

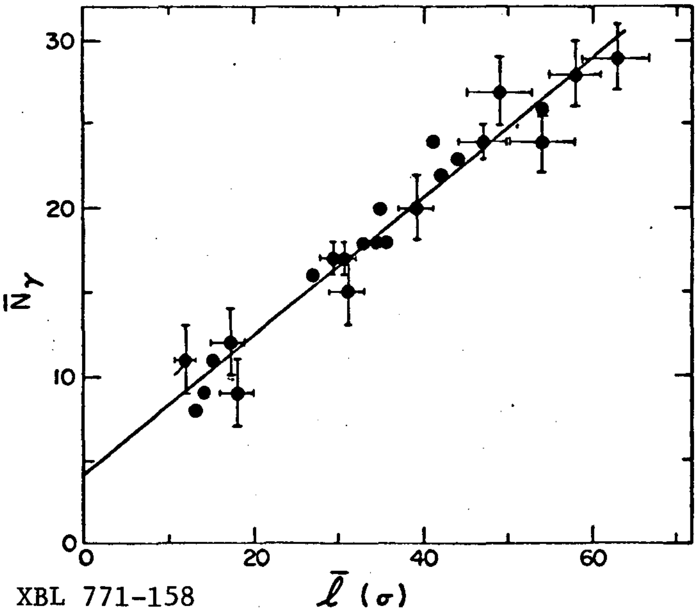

XBL 771-158

Fig. 3.28

The results are shown(153) in Fig. 3.29 for ^{162}Yb, plotted in the backbending fashion of Fig. 3.21. Since ^{162}Yb has not been tracked completely through a backbend, ^{160}Yb is also shown (open circles).

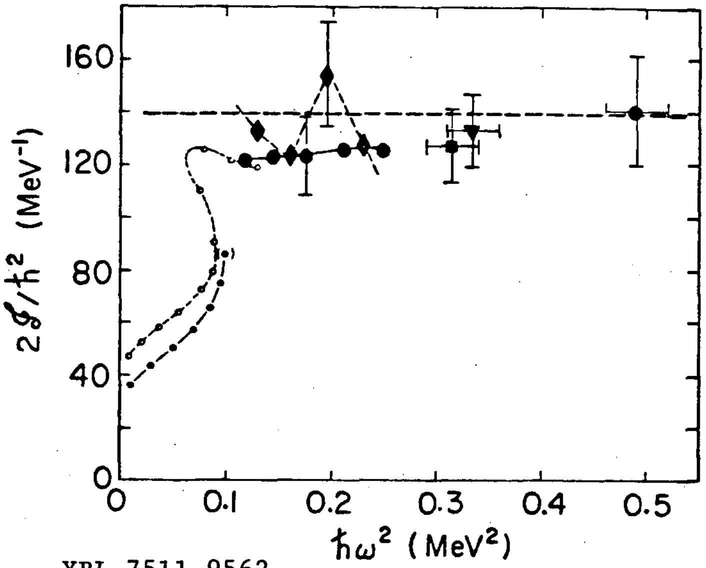

XBL 7511-9562

Fig. 3.29

At the highest rotational frequency, the moment of inertia approaches that of the rigid sphere with A = 162, viz

$$\mathcal{J} = 2/5\ MR^2\ ,$$

$$\frac{2\mathcal{J}}{\hbar^2} \approx 140\ \text{MeV}^{-1}. \tag{3.21}$$

The last point on the plot is associated with the (^{40}Ar,4n) reaction, which as we saw earlier, originates from angular momentum ≈ 35ħ. Since the deformed moment of inertia would be a little larger (≈ 10%), and since the measured values fall slightly below this line, some residual pairing correlations may still persist even at this high spin value.

An extension of these methods opens up the exciting possibility of measuring moments of inertia in the region where they change rapidly prior to fission, and may even serve as a probe for isomeric "yrast traps" as the nucleus becomes oblate.(155) These ideas lead us into the more macroscopic aspects of the heavy-ion interaction which will be the subject of the next two Chapters.

4.

HEAVY ION FUSION AND FISSION

4.1 Introduction

The main motivation for the construction of heavy-ion accelerators might have been the expectation that, once a nucleus was given enough kinetic energy to surmount the Coulomb barrier, the two nuclei would fuse to form a compound nucleus whose mass, charge, angular momentum, and energy are the sum of these of the initial nuclei together with the energy and angular momentum of relative motion. It was hoped that heavy-ion reactions could be used to produce superheavy nuclei. This undertaking has presented enormous obstacles. Schiffer has expressed the situation by a metaphor.(156) Suppose you lived in the age of Columbus and you were convinced that Columbus' idea of finding an easy trade route to the East Indies was wrong, that the earth was much larger than Columbus thought and he could never make to India. Would we have been unwise to discourage him from undertaking the voyage? He would certainly have missed something interesting on the way! This section — and the next — is about some of the valuable things that have been found on the way.

4.2 The Fission and Fusion Landscape

In this section we confront the distinctive macroscopic features of heavy ions ($A \gg 1$). In general, many degrees of freedom are necessary to specify accurately the shape of a dividing or fusing nuclear system, and it is believed that 3 is the absolute minimum.(157,158)

a) the separation coordinate α_2
b) the "necking" coordinate α_4
c) the mass asymmetry coordinate α_3

Regarding c), there exists a critical mass asymmetry (see Fig. 4.1). For mass asymmetries more extreme than the critical, i.e. a relatively light ion on a heavy target, the target nucleus tends to suck up the smaller, but for asymmetries less extreme the trend is reversed.(159) The existence of the critical point is the result of competition between electric and nuclear forces. The figure shows how difficult it is to make a superheavy element.

Now for a fixed value of the asymmetry, let us see what has been discovered(157,158) about the potential energy surfaces in $\alpha_2\alpha_4$ space (see Figs. 4.2 and 4.3). There are two misaligned valleys. One valley starts from the vicinity of the sphere (H) and after going

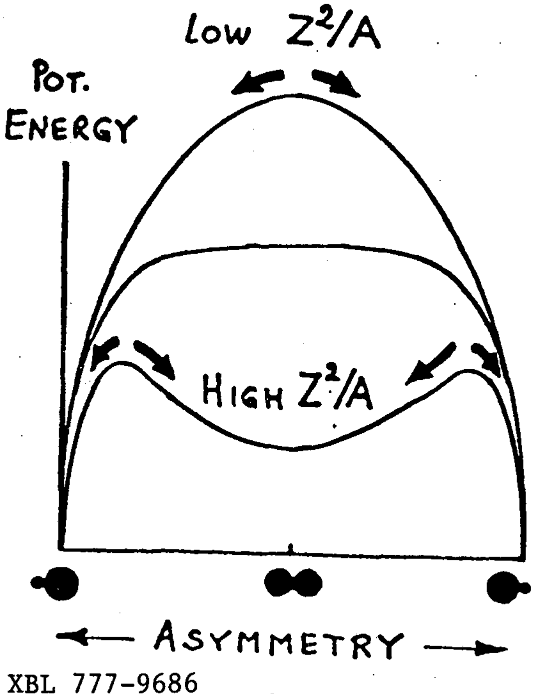

Fig. 4.1

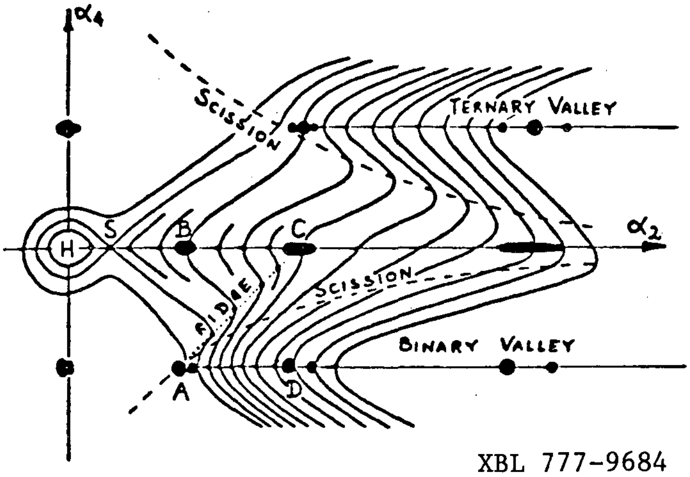

XBL 777-9684

Fig. 4.2

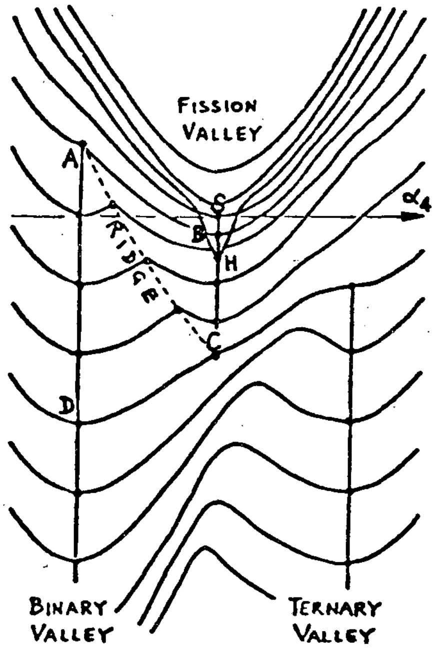

XBL 777-9685

Fig. 4.3

over to the saddle point hump at S, the energy goes down, but there is stability against changing of the necking coordinate for a fixed elongation coordinate. Below this valley is a roughly parallel two-fragment valley corresponding to approaching or separating fragments. (Further up there is a third ternary valley.) In the end-view of Fig. 4.3, one can see clearly the fission valley with its saddle and stable spherical shape and the misaligned two-fragment valley. Between the two is a ridge running from A to C (shell effects — such as the hole at H which marks the possible stability of a superheavy — put pock marks in this surface). In fission the nucleus deforms, goes over the saddle, and rolls down the fission valley. At C, equilibrium against necking is lost and the system is injected into the two-fragment valley. Because of the misalignment, the injection is off-axis and the system vibrates with some excitation energy (the difference between C and D ≈ 30 MeV). In fusion we proceed up the two-fragment valley corresponding to approaching nuclei. At point A, corresponding to tangency, equilibrium against an increasing eccentricity is lost and the system is injected into the fission valley, with excitation energy of the fused system equal to the difference between the energy at A and B. Systems such as $^{48}\mathrm{Ca} + {}^{248}\mathrm{Cm}$ appear to minimize this difference and therefore are promising candidates for reactions to form the compound nucleus with the minimum excitation. There is a problem however, that in general the point B is still some 10 or 15 MeV below the saddle that must be overcome to get into the magic hole H. One hopes to provide this extra energy by increasing the bombarding energy by 10 or 15 MeV over the Coulomb barrier. But if there are large damping effects (friction), only a fraction of this excess will go into the collective degree of freedom leading from B to S and the rest will go into heat (excitation). Therefore one has to increase the incident energy even further, and the system after making partial contact is immediately torn apart. So you see the problem of making superheavy elements is one of great delicacy, and the situation becomes even worse when the angular momentum of the colliding system is considered. So far attempts have probably failed.(160) (Other techniques have led to short-lived successes!(161))

4.3 Effects of Angular Momentum

It is well known that if a deformable fluid mass is set spinning it will flatten and eventually fly apart.(162) To discuss the equilibrium shapes of a rotating nucleus we set up an effective potential energy and look for configurations that are stationary:

$$\mathrm{P.E} = E_{\mathrm{Coul}} + E_{\mathrm{nuc}} + E_{\mathrm{rot}} \tag{4.1}$$

where

$$E_{\mathrm{rot}} = \frac{\hbar^2 \ell(\ell+1)}{2\mathcal{I}(\alpha_2\alpha_3\alpha_4)} \tag{4.2}$$

It is convenient to introduce two dimensionless numbers, specifying the relative sizes of the three energy components.(157,162) Choose the surface energy of a spherical drop as a unit:

$$E_S^{(0)} = 4\pi R^2\gamma = C_2 A^{2/3} \tag{4.3}$$

with $C_2 \approx 17.9$ MeV. Then specify the amount of charge on the nucleus by

$$x = \frac{\frac{1}{2}E_C^{\circ}}{E_S^{o}} \approx \frac{1}{50}\,\frac{Z^2}{A} \tag{4.4}$$

For the angular momentum, specify

$$y = \frac{E_{\mathrm{rot}}^{o}}{E_S^{o}} \approx \frac{\frac{1}{2}\hbar^2\ell^2}{\frac{2}{5}MR^2}\cdot\frac{1}{C_2\,A^{2/3}} \approx \frac{2\ell^2}{A^{7/3}} \tag{4.5}$$

In terms of these parameters, Fig. 4.4 illustrates some shapes, in each case for the ground-state (stable) shape and the saddle point (unstable shape) — labeled H and PP respectively. As the rotation speed increases, the ground state flattens and the saddle point thickens its neck. In the bottom figure the ground-state pseudospheroid loses stability and becomes triaxial, resembling a flattened cylinder with rounded edges, beginning to merge with the saddle shape. At slightly higher angular momenta the stable and unstable families merge and the fission barrier vanishes. Figure 4.5 shows the complete evolution, where the dotted line divides the x-y plane into two regions: to the right the saddle-point shape is stable against

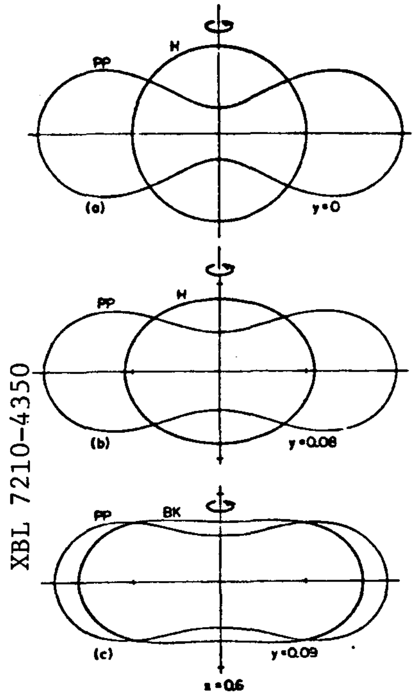

Fig. 4.4

When the plot is translated into an angular momentum plot versus the mass, assuming $N-Z = 0.4A^2/(200+A)$, we see that for vanishing of the fission barrier (Fig. 4.6), the resultant curve is ℓ_{II}. We see that no nucleus can support more than about 100ħ, and that neither heavy nor light nuclei can support many units. (The dashed curve shows the angular momentum required to lower the fission barrier of a nucleus to 8 MeV; this curve is indicative of the maximum angular momentum the nucleus could support and still survive the risk of fission in the de-excitation process.

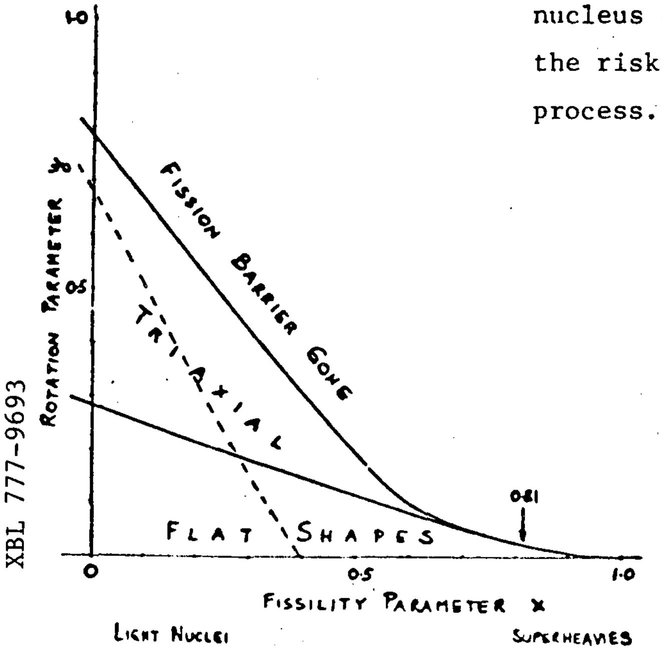

Fig. 4.5

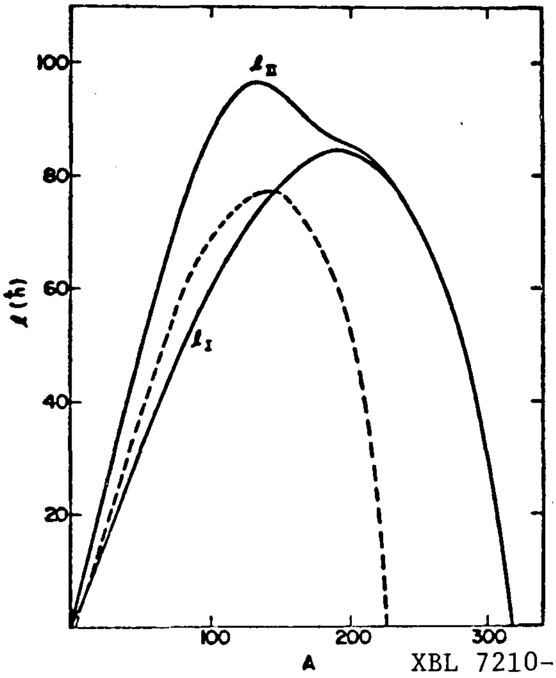

Fig. 4.6

XBL 7210-4342

4.4 *Application to Experiment*

By conservation of energy and angular momentum, it follows that the closest distance of approach of projectile and target is given by r_{min}, where for impact parameter b,

$$\left(\frac{b}{r_{min}}\right)^2 = \left(1 - \frac{V}{E}\right) \tag{4.6}$$

which, for given r_{min}, is a hyperbola for b^2 versus E. If r_{min} is chosen as the strong interaction radius $(R_1 + R_2)$, this curve divides the plane (b v E) into two regions: distant collisions where the nuclei pass each other without appreciable interaction, and close collisions where the corresponding πb^2 gives the reaction cross section. Because of diffuseness, this region is given some width in Fig. 4.7. The curves are constructed for $R_1 + R_2 + d$. The plane can be further subdivided by curves corresponding to the locus of fixed angular momentum ℓ:

$$\ell = b\sqrt{2\mu E} \qquad b^2 = \frac{\ell^2}{2\mu}\,\frac{1}{E} \qquad \mu = \text{reduced mass}$$

From Fig. 4.5, the value of y (or ℓ) at which the fission barrier vanishes can be inserted to construct the additional curves on Fig. 4.7 (both for zero fission barrier and where it has become equal to the binding energy of a nucleon, which marks where the de-excitation mode changes to nucleon emission and the compound nucleus would be detectable).

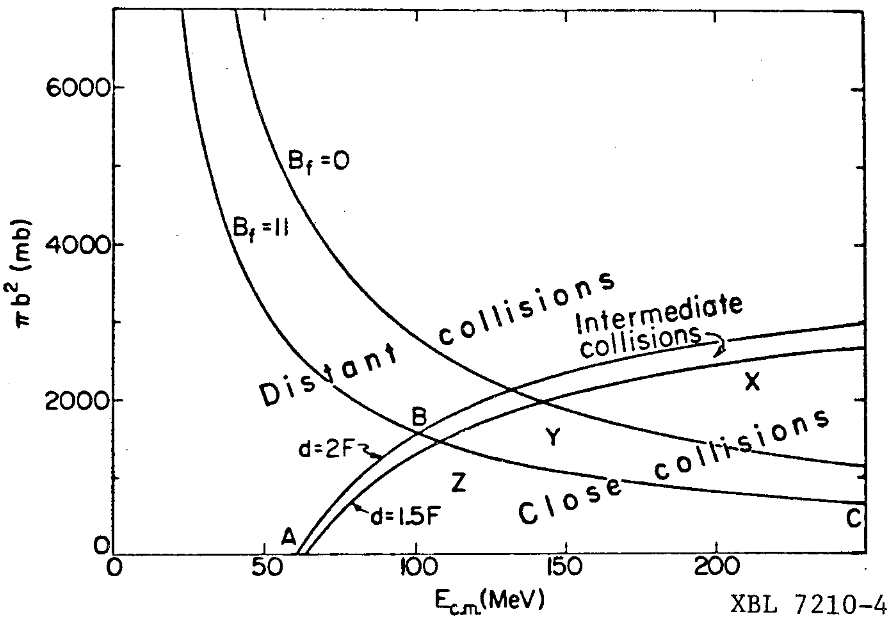

Fig. 4.7

XBL 7210-4343

To the left of $B_f = 0$, a compound nucleus could form, and to the left of $B_f = 11$ it would definitely survive. We shall see later however that the prediction of the *formation* of a compound nucleus is a dynamical question, beyond the scope of these considerations. Only if this critical curve lies *totally* above ABC, can the curve ABC represent the cross section for formation and survival of the compound nucleus. The figures are constructed for $^{20}Ne + ^{107}Ag$. Now we compare with actual data$^{(163)}$ for a much heavier system, Ar + Sb.

The fusion products are experimentally identified by detecting the evaporation residues after evaporation of nucleons and alpha particles and are shown in Fig. 4.8; the trend clearly follows that of Fig. 4.7. The line $B_f = 0$ is marked, and also a more precise calculation using the computer code ALICE, which deals more properly with particle evaporation. The results for fusion of lighter heavy-ions *do not* follow this trend, however, and reveal the influence of

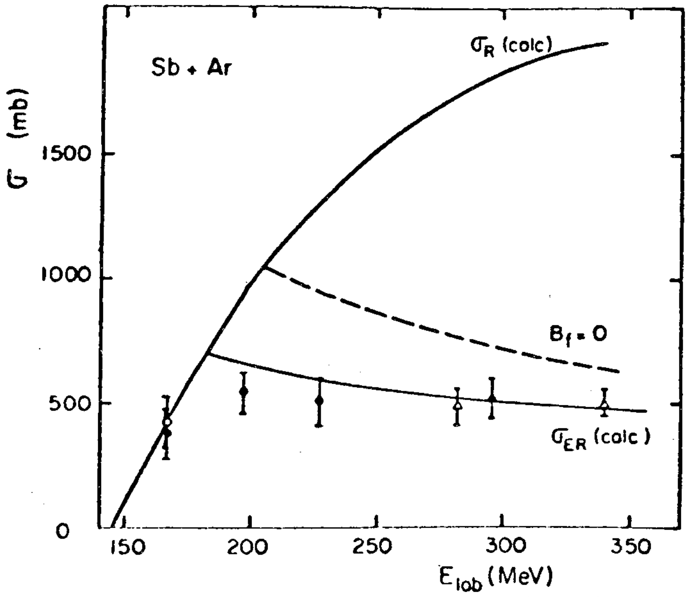

Fig. 4.8

XBL 777-9764

dynamics in the entrance channel. (For recent reviews, see Refs. 164 and 165.)

4.5 Dynamics of the Entrance Channel

In many cases we find that the fusion cross section is much less than the reaction cross section, although the fission barrier has still not disappeared. It appears that the ions have to reach a critical *distance* of overlap of nuclear matter before they fuse.(166,167)

In order to take into account both the effects of an interaction barrier *and* of a critical distance, we write(168) the fusion cross section and the total reaction cross section:

$$\sigma_f = \pi\lambda\!\!\!^{-2} \sum_0^\infty (2\ell + 1)\, T_\ell P_\ell \tag{4.7}$$

$$\sigma_R = \pi\lambda\!\!\!^{-2} \sum_0^\infty (2\ell + 1)\, T_\ell \tag{4.8}$$

where the T_ℓ are energy-dependent penetration probabilities through the barrier, and P_ℓ are the probabilities that fusion takes place after the barrier is passed. For P_ℓ we assume

$$P_\ell = \begin{cases} 1 & \ell \leqslant \ell_{cr} \\ 0 & \ell > \ell_{cr} \end{cases}$$

The transmission coefficients are approximated(169) by those of a parabolic barrier with ℓ-dependent frequencies $\hbar\omega_\ell$:

$$T_\ell(E) = \frac{1}{1 + \exp\left[\dfrac{2\pi(V_{B\ell} - E)}{\hbar\omega_\ell}\right]} \tag{4.9}$$

The barrier distance $R_{B\ell}$ is the solution of :

$$\frac{d}{dR}\left[V(R) + \frac{\hbar^2 \ell(\ell+1)}{2\mathcal{J}}\right]_{R_{B\ell}} = 0 \tag{4.10}$$

where $\mathcal{J}$ is the moment of inertia, whose value may be larger than μR^2 because of tangential friction leading to rigid body rotation of the dumbbell structure. For simplicity assume $\hbar\omega_\ell = \hbar\omega$ = constant, and $R_{B\ell} = R_B$ = constant (referring to Fig. 1.16, we see the latter is a good approximation); then $V_{B\ell} = V_B + \hbar^2\ell(\ell+1)/2\mathcal{J}_B$. Substituting in σ_f and converting the summation to an integral,

$$\sigma_f = \pi\bar{\lambda}^2 \int_0^{\ell_{cr}} d\ell \, \frac{1}{1 + \exp\left[2\pi\left(V_B + \frac{\hbar^2\ell(\ell+1)}{2\mathcal{J}_B} - E\right) / \hbar\omega\right]} \tag{4.11}$$

Now the transmission coefficients T_ℓ drop to zero within a few ℓ-values, and — as usual — we define ℓ_{max} to be where $T_\ell(E)$ drops to 0.5; then

$$\ell_{max}(\ell_{max} + 1) = \frac{2\mathcal{J}_B}{\hbar^2}(E - V_B) \tag{4.12}$$

This angular momentum limit has to be compared with that of the fusion cross section through ℓ_{cr}:

$$\ell_{cr}(\ell_{cr} + 1) = \frac{2\mathcal{J}_{cr}}{\hbar^2}(E - V_{cr}) \tag{4.13}$$

The integration can be carried out analytically to give:

$$\sigma_f = \frac{\hbar\omega\mathcal{J}_B}{2\mu E} \ln\left\{ \frac{1 + \exp\left[\frac{2\pi(E - V_B)}{\hbar\omega}\right]}{1 + \exp\left[2\pi\left(E - V_B - \mathcal{J}_{cr}\frac{(E - V_{cr})}{\mathcal{J}_B}\right) / \hbar\omega\right]} \right\} \tag{4.14}$$

At low energies

$$E \ll \frac{V_B - (\mathcal{J}_{cr}/\mathcal{J}_B)V_{cr}}{1 - \mathcal{J}_{cr}/\mathcal{J}_B} \tag{4.15}$$

the exponential in the denominator can be neglected and

$$\sigma_f = \frac{\hbar\omega\mathcal{J}_B}{2\mu E} \ln\left[1 + \exp\frac{2\pi(E - V_B)}{\hbar\omega}\right] \tag{4.16}$$

If further $E - V_B \gg \hbar\omega$,

$$\sigma_f = \frac{\pi\mathcal{J}_B}{\mu}\left(1 - \frac{V_B}{E}\right) \tag{4.17}$$

At high energies, on the other hand, where the reverse of the above criterion on E applies, we can drop the 1 in both numerator and denominator and

$$\sigma_f = \frac{\pi \mathcal{J}_{cr}}{\mu}\left(1 - \frac{V_{cr}}{E}\right) \tag{4.18}$$

Making the usual approximation $\mathcal{J} \approx \mu R^2$ we get $\sigma_f = \pi R_B^2(1 - V_B/E)$ at low energies (just the expression we used in constructing Fig. 4.7), and

$$\sigma_f = \pi R_{cr}^2 \left(1 - \frac{V_{cr}}{E}\right) \tag{4.19}$$

at high energies.

It turns out that $R_{cr} \approx 1.00\,(A_1^{1/3} + A_2^{1/3})$ for a wide range of ions. This interpenetration distance corresponds to the overlap of the half density radii of the nuclear matter distributions.(170) The radius is marked(171) on Fig. 4.9 for $^{16}O + ^{48}Ca$. Up to a certain critical energy, for all partial waves that surmount the outer barrier, the two ions succeed in interpenetrating to the critical distance (assuming there is not too much radial friction near the barrier top — dashed line) and fuse. Above this critical energy, however, the increasing centrifugal barrier does not allow the ions to penetrate for all partial waves and the fusion cross section will be smaller than σ_R, as the above formula indicates. This scheme is valid when the dynamical path

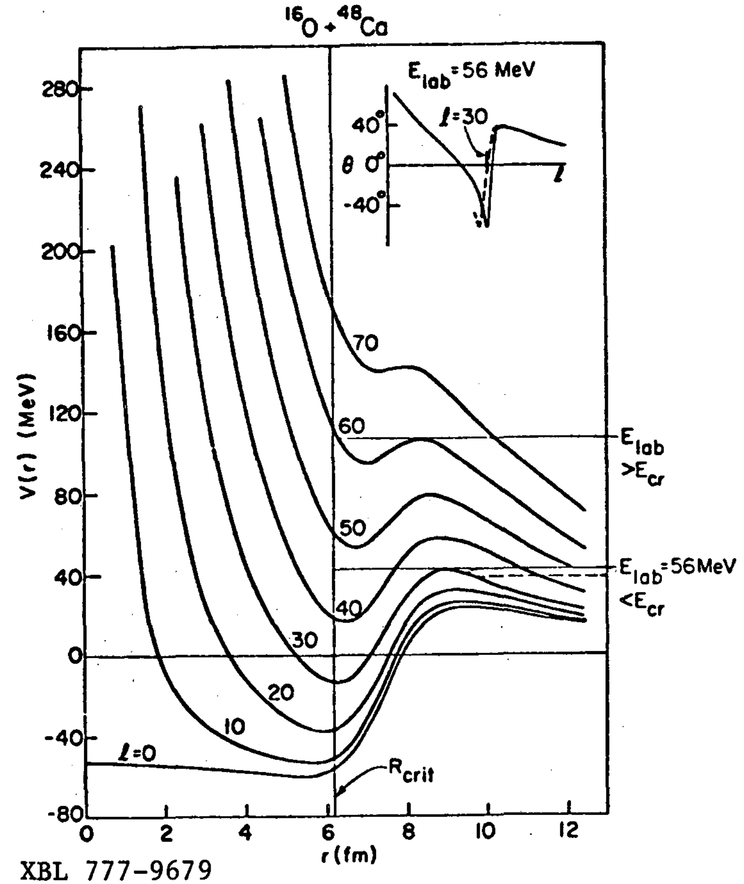

XBL 777-9679

Fig. 4.9

for fusion lies inside the saddle point. As we discussed for Figs. 4.2 and 4.3, such is not usually the case for heavy systems.

From these equations we can generate the schematic representation(172) of fusion and total reaction cross sections as a function of 1/E in Fig. 4.10. Region 1 corresponds to the discussion of the previous section. In region 2 we have passed the critical energy, and the fusion cross section changes slope — it may increase, stay constant, or decrease, depending on the value of V_{cr} at this point. Finally, in region 3 the limit of maximum angular momentum in the compound system is surpassed. Just these features seem to be present(173) in the fusion cross section for the $^{14}N + {}^{12}C$ system shown in Fig. 4.11. If the data are represented in terms of the critical angular momenta deduced from

$$\sigma_f = \pi\lambda\!\!\!^{-2}(J_{cr} + 1)^2 \qquad (4.20)$$

and the excitation energy in the compound system ^{26}Al, then the value $J(J+1) = 734\,\hbar^2$ corresponds(162) to the predicted liquid drop limit of 26.6ħ from Fig. 4.6 for A = 26. The predicted shape is that of a very deformed triaxial nucleus with

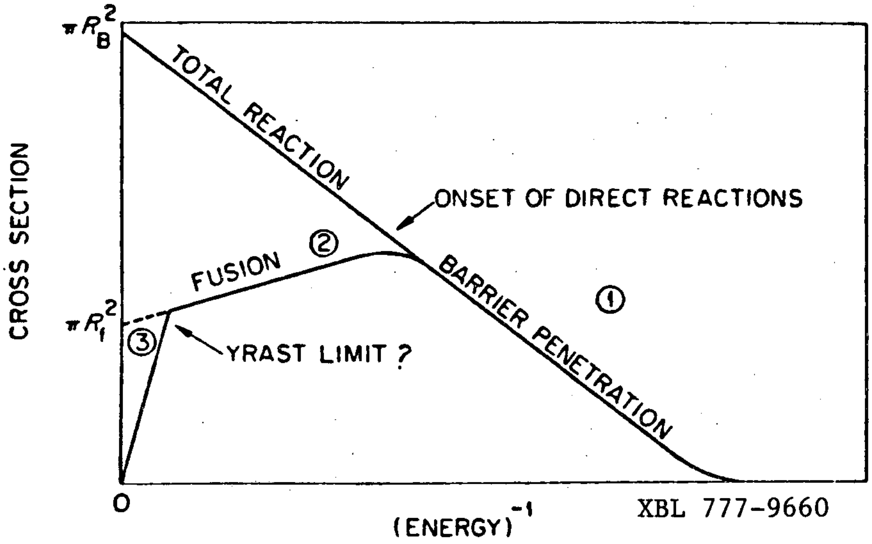

Characteristic Energy Regions for Fusion

Fig. 4.10

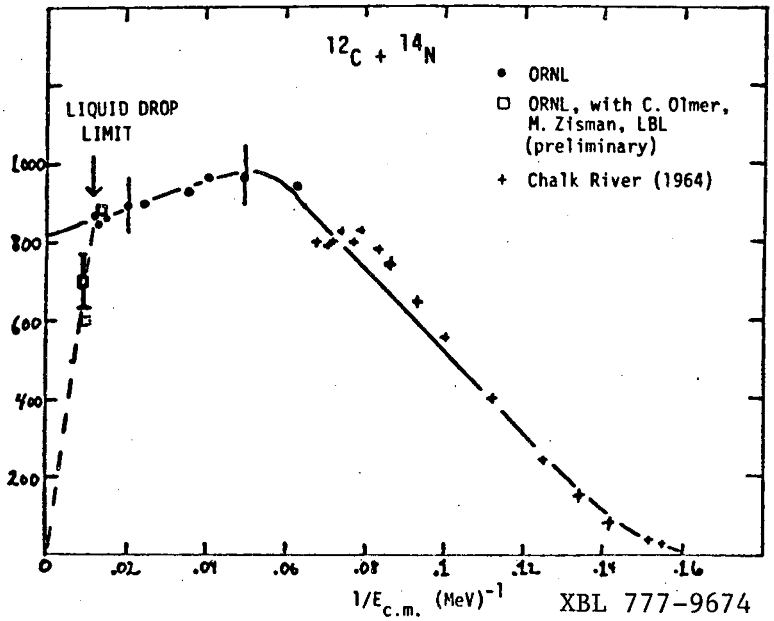

Fig. 4.11

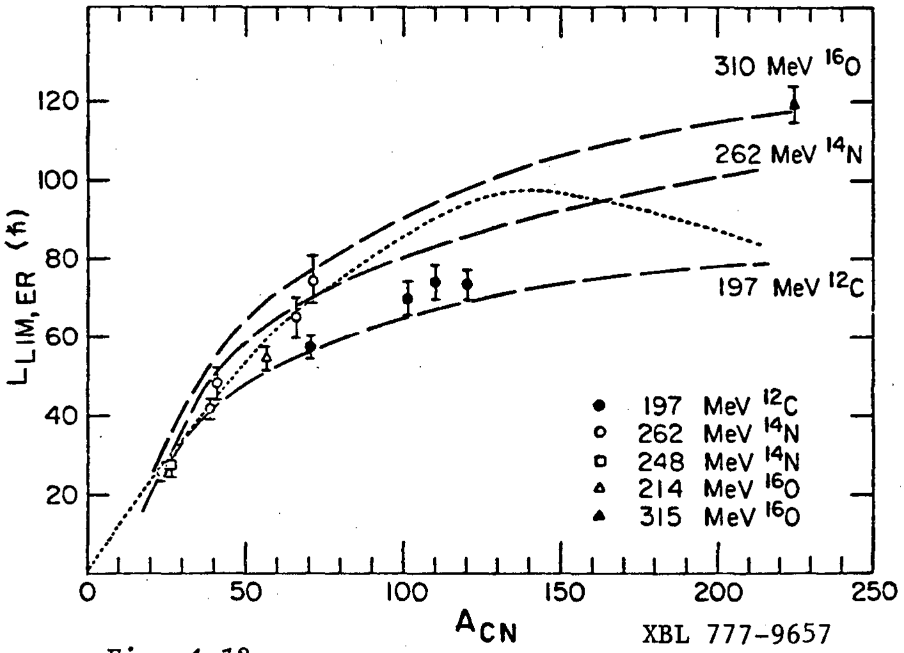

XBL 777-9657

Fig. 4.12

$R_{max} \approx 2R$ and $R_{min} \approx 0.4R$, R being the radius of the spherical ground state.

Since the slope and intercept beyond the critical energy defines V_{crit} and R_{crit} ($\approx 1.0(A_1^{1/3} + A_2^{1/3})$), these measurements can be used to determine the potential at much smaller interaction distances than is possible from elastic scattering$^{(38,174)}$ (remember $R_{1/4}$ etc. in Chapter 1) and indeed were used to construct some of the points in Fig. 1.15. The critical distance of approach implies the sudden approximation, i.e. a potential which conserves the structure of each nucleus.$^{(175)}$ At the opposite extreme is the adiabatic approach$^{(176)}$ in which there is a continuous change of the potential. This method also gives a good account of fusion cross sections for the highest energy light systems available and a theoretical calculation based on a proximity potential, allowing the two densities to undergo gradual deformation, and requiring that for fusion the value of dV/dR must not always stay negative.$^{(177)}$ is shown in Fig. 4.12 for several systems.

Also shown is the curve for the fission barrier becoming zero. We see that there are relatively few points *well above* this limit with the exception of the 310 MeV O^{16} + Pb point; this point was deduced from the difference between the direct reaction and the total cross section, which indeed probably results in fission.$^{(178,179)}$

Ultimately a full dynamical calculation is required, in which the fusion cross section would depend not only on the static shapes but also on coupling to internal degrees of freedom.$^{(180-184)}$ In the classical limit this approach — which has been developed — leads to an equation of motion with frictional forces. Then it becomes possible to describe incomplete fusion events also — the subject of Chapter 5.

Some of these concepts are illustrated schematically(185) in Fig. 4.13. The right half represents the idea that nuclei that pass over the barrier are absorbed in the hollow — though not unless the critical distance is reached. However, when the two nuclei overlap sufficiently for absorption to take place, the projectile sets the target spinning, reducing the *orbital* angular momentum, so that the system sees a lower value of ℓ. The left half shows how this process could actually allow the projectile to escape.

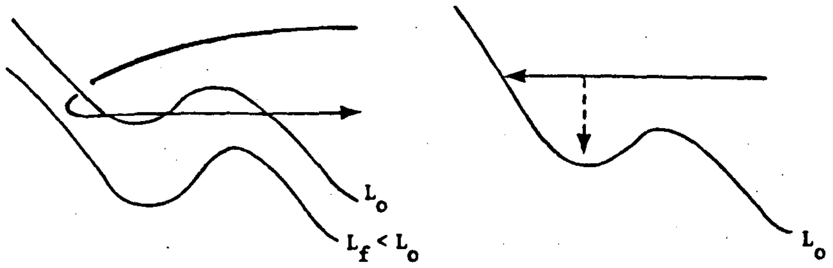

Fig. 4.13

4.6 Compound Nucleus Decay

Once formed, the compound nucleus has to decay, either by fission as we have seen, or by particle emission, from which important properties of the compound system become accessible — such as the temperature, distribution of angular momenta, moments of inertia, and degree of equilibration. Analysis of the data requires a comparison with the predictions of a statistical evaporation code. Remarkable progress has been made in refining the calculational(186,187) and experimental techniques. Experimental data and evaporation residues (the remnant of the compound nucleus after particle decay) can be obtained for individual A,Z by an apparatus which measures ΔE, E (to determine Z) and time-of-flight (to determine $A \propto Et^2$) — compare the discussion of particle identification techniques in Section 2. A "state of the art" example is shown in Fig. 4.14 for $^{40}Ar + ^{48}Ca$ at $E = 236$ MeV. In this particular experiment(188) evaporation residues were not being measured, but the figure demonstrates that it is possible to resolve individual Z up to 30 (in fact, up to 65 has been achieved) and individual A up to 60.

The measured evaporation residues in the reaction $^{19}F + ^{27}Al$ at 76 MeV are compared with statistical calculations(187) in the bottom part of Fig. 4.15. The upper sections decompose the calculation into contributions from different angular momenta in the compound nucleus. It is

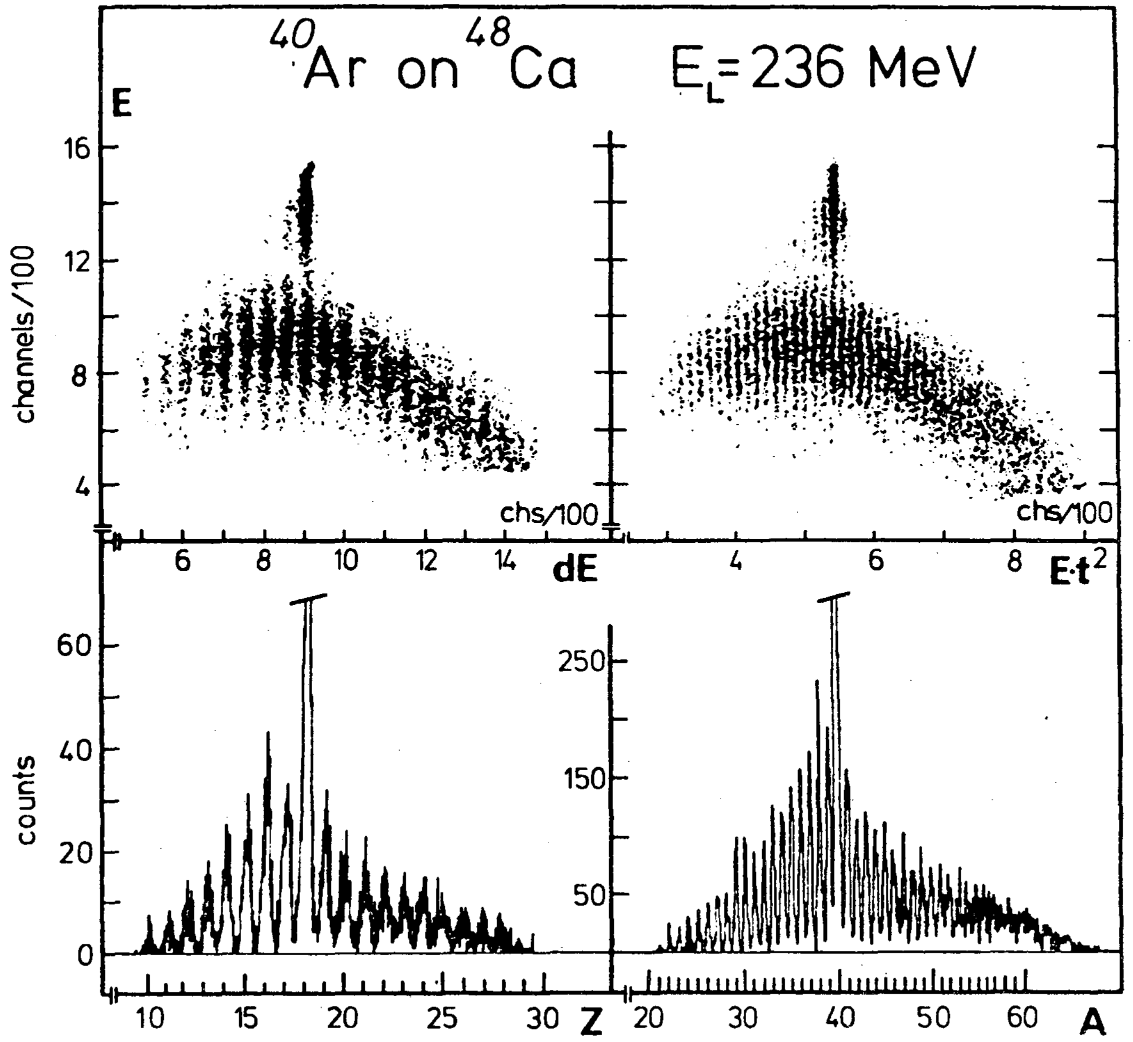

Fig. 4.14

XBL 777-9673

clear that increased α-particle emission is associated with higher angular momentum and therefore these residues probe the region of the energy-angular momentum space closest to the yrast line of the compound nucleus. A reconstruction of the "decay scheme" of the compound nucleus is shown in Fig. 4.16. (It is clear from this figure that our discussion of the particle emission down to the yrast line producing the γ-cascades in Section 3 is oversimplified for light nuclei — see Figs. 3.24 and 3.25).

An important input to the statistical calculations is the level density in the nucleus at (in this example) excitations up to 70 MeV, and angular momenta up to $40\hbar$. As Fig. 4.4 showed, nuclei in this region are likely to behave like liquid drops, and the influence of individual shell structure of a nucleus on the level density and pairing energy

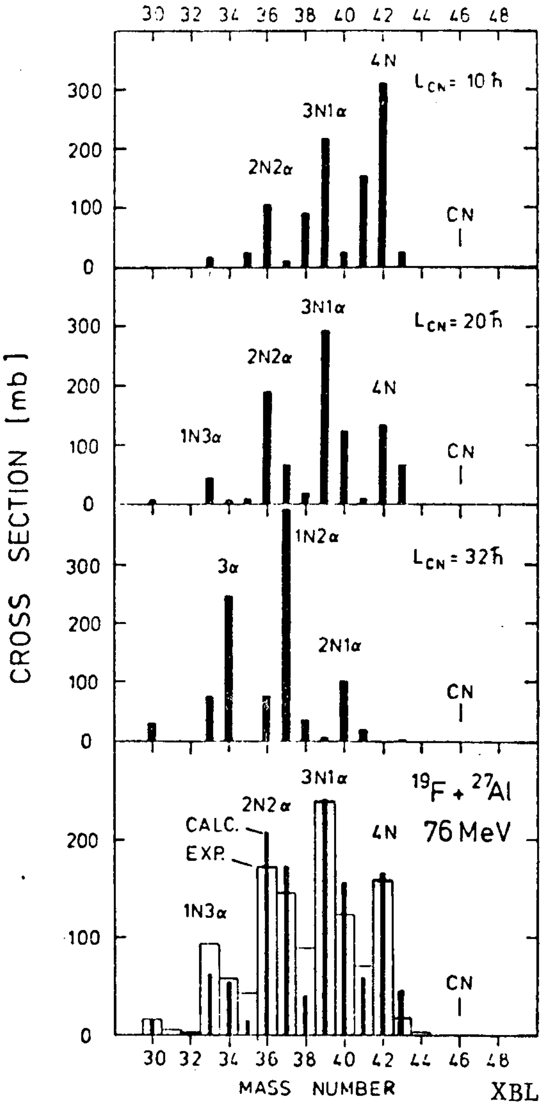

Fig. 4.15

XBL 777-9689

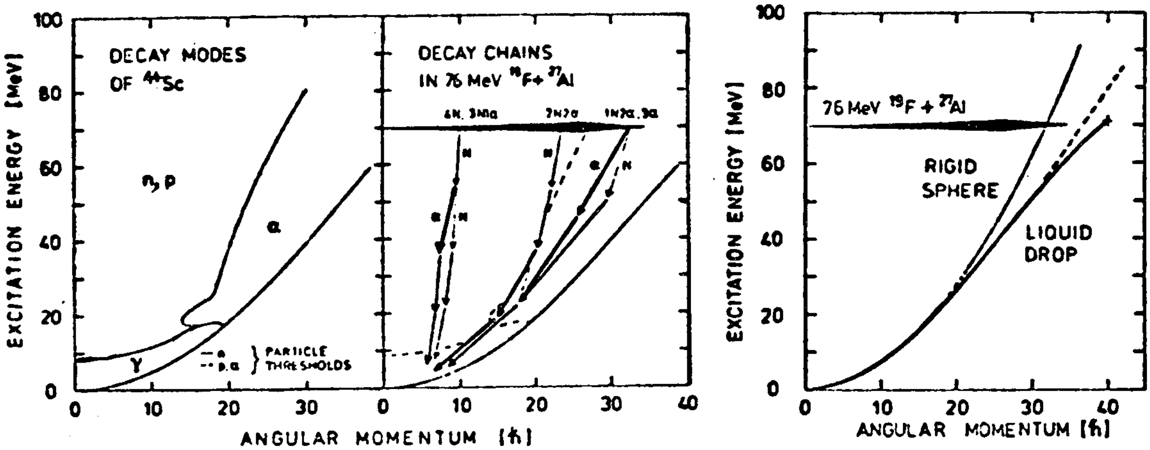

XBL 777-9678

Fig. 4.16

vanishes. We can make an appropriate allowance for the deformability under rotation by using:

$$\mathcal{J} = \mathcal{J}_o (1 + \delta L^2)$$

(This approximation is the first term in the more exact calculations leading to Fig. 4.4.) In this way we obtain an yrast line deviating from that of a sphere, as shown in the third section of Fig. 4.16. Because of the connection between the shape of the yrast line and the shape of the nucleus itself, information on the latter may be forthcoming from measuring the ratio between nucleon and α-particle emission (see the left-hand sections of the figure). The quantitative analysis yielded $2 \times 10^{-4} < \delta < 5 \times 10^{-4}$, which is to be compared with the prediction of 2.5×10^{-4} for the detailed shape calculation(162) (of the type leading to Fig. 4.4). It will certainly be exciting to learn more about the predicted exotic shapes that nuclei, under the influence of heavy-ion collisions, will assume from experiments such as these, and of the preceding section. (For a recent detailed review, see Ref. 172.)

4.7 *Microscopic Aspects*

So far we have ignored any effects of individual nucleons — the fundamental constituents of nuclear matter — on processes such as fusion. However, from a microscopic viewpoint, friction effects all lead ultimately to intrinsic excitations of the colliding nuclei. Figure 4.17 shows the configuration energies for a colliding $^{16}O + ^{16}O$ system in the two-center shell model (recall Chapter 2), as a function of the separation distance of the oscillator wells.(189,190) At distances less than 3.4 fm the lowest configuration becomes the ground state of ^{32}S, and at larger distances it is the $^{16}O - ^{16}O$ ground state. These level crossings may generate the interactions leading to fusion. The calculations predict that the critical radius for fusion should show a shell effect — beyond effects expected from the usual $A^{1/3}$ dependence.

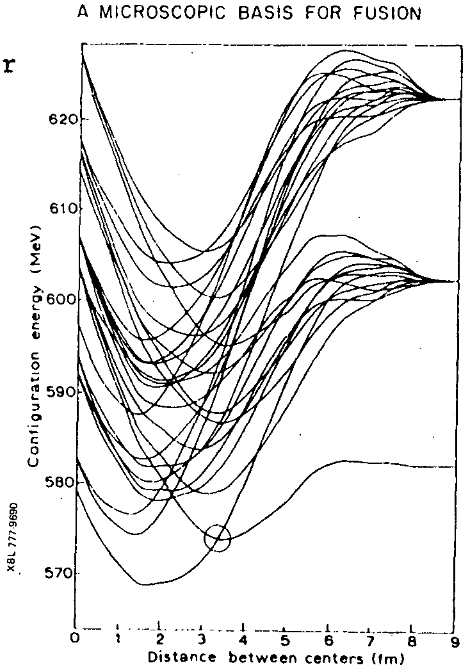

Fig. 4.17 Two-Center Shell Model

The measured values for the fusion cross sections of a variety of systems (see Ref. 172) in the p- and sd-shells are displayed in Fig. 4.18. The abrupt change of 200 mb takes place at the sd shell(191) (note, however, the point(192) for ^{12}C + ^{15}N!). The exact manner in which the valence nucleons affect the fusion cross section via the complexity of Fig. 4.17, remains to be worked out.(193) Another illustration is the recently discovered *oscillatory* fusion cross sections(171,191,194) for the system ^{12}C + ^{12}C and ^{12}C + ^{16}O, whereas the ^{12}C + ^{18}O system behaves according to the systematics we described in the previous section. These data are shown in Fig. 4.19. We recall resonances of similar width and spacing — although not always identical — in our discussion of quasimolecular states in Chapter 3.

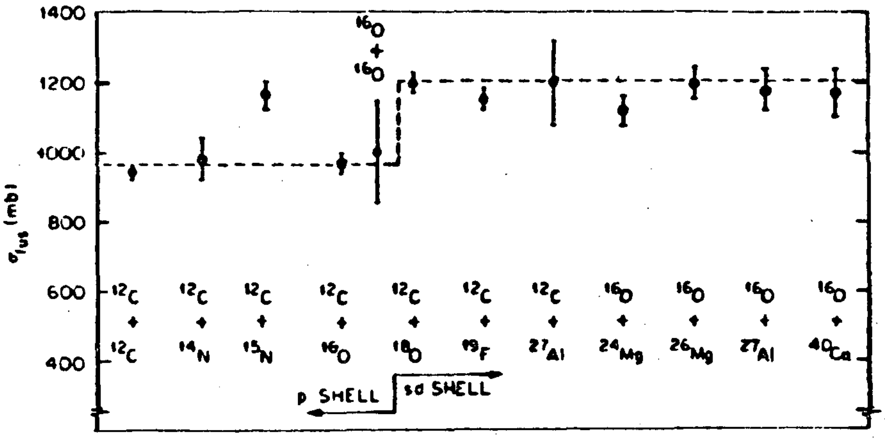

XBL 777-9705

Fig. 4.18

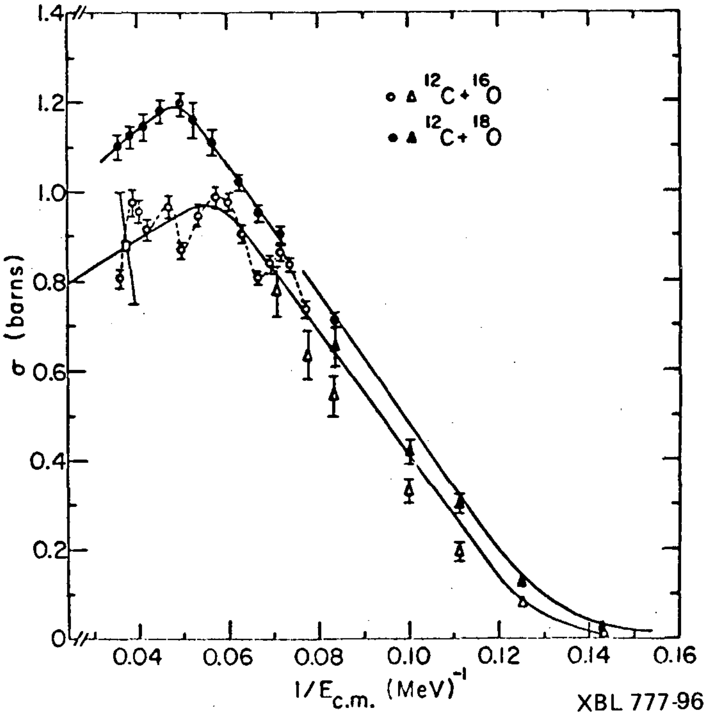

XBL 777-9682

Fig. 4.19

4.8 More Speculative Aspects

The extreme of upper angular momentum cut-off in fusion reactions appears well established. What about a lower cut-off also? There is some controversial evidence for this phenomenon.(165,195,196) A detailed study was made of evaporation residues from the formation of the compound system ^{158}Er by comparing the results of different formation experiments ^{16}O + ^{142}Nd, ^{40}Ar + ^{118}Sn, ^{84}Kr + ^{74}Ge, and ^{63}Cu + ^{96}Zr (the last giving a slightly different compound nucleus). The excitation functions for a particular evaporation channel (5n) are shown in Fig. 4.20. We recall from the "bin diagram" of Fig. 3.24 that this channel should be associated with the *same excitation energy region* of the compound nucleus, regardless of how it was formed, but the evidence in Fig. 4.20 clearly indicates a shift in the onset of this decay channel for the heavier projectiles. (The thresholds are indeed found to be identical for different light projectiles, C, O, and Ne.) Figure 3.24 also reminds us that the lower energy part of the curve must be associated with the low angular momentum population, since all the available excitation energy has to be removed by five neutrons. For the Kr case in Fig. 4.20 then, the large shift in the threshold implies a *lower limit in the J population of the compound nucleus.* The quantitative calculation in

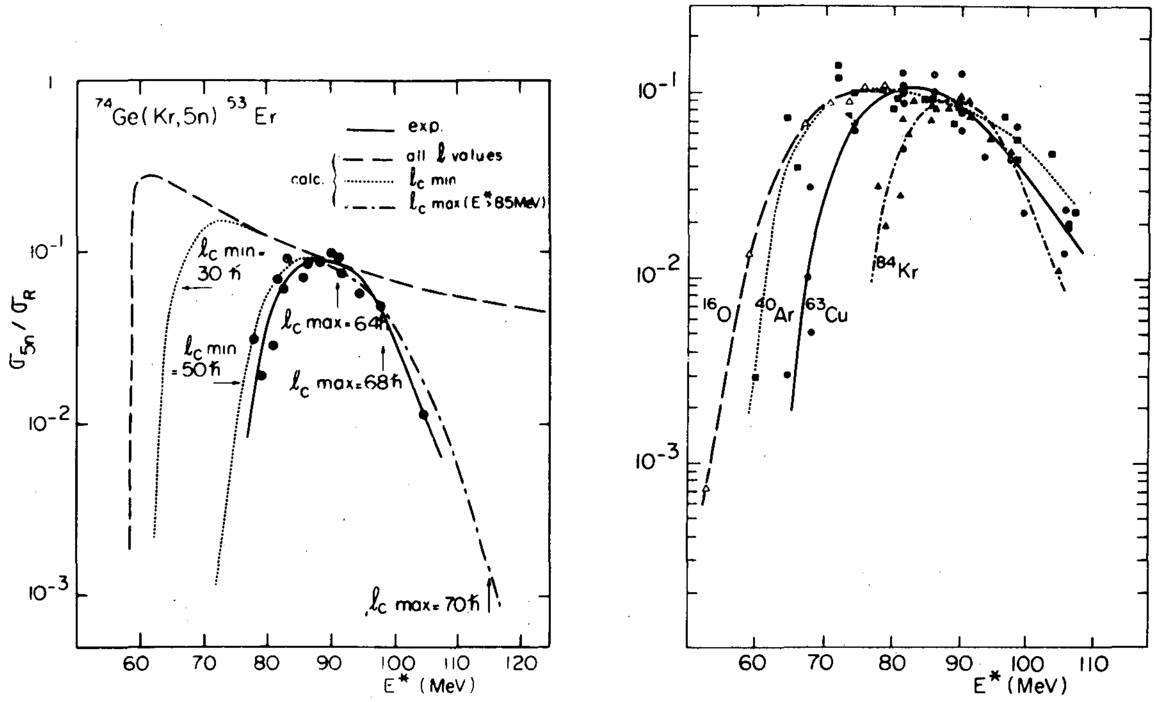

Fig. 4.20 XBL 777-9760

Fig. 4.20(b) indicates that $J_{lower} \approx 50\hbar$ would do the trick; as usual there is a J_{upper} of $68\hbar$ in this example (expected from Fig. 4.6). (Note, however, that there is no indication(197) for a lower cut-off in the measurement of fusion reactions by evaporation residues.)

Why might such a hindrance for low partial waves be expected? In general, fusion is inhibited by two main causes: the repulsive Coulomb (and centrifugal) potentials, expressed as Z_1Z_2/R^2, and dissipative forces proportional to the average velocity during the overlap of the nuclear matter densities. This velocity depends on (E - V), the energy above the barrier, and also on the product of the nuclear densities $\propto 1/R^2$. Therefore an interesting quantity is the ratio of $Z_1Z_2e^2/R^2$ to v'/R^2 which can be expressed via a "reduced" Sommerfeld parameter:

$$\eta' = \frac{Z_1Z_2e^2}{\hbar v'} \qquad (4.21)$$

When η' is large (heavy systems, low energies) there is an inhibition of fusion, even when the critical distance is reached. For intermediate systems such as Kr + Ge, v' is larger for intermediate impact parameters than for head-on collisions; therefore, η' might be sufficiently decreased to allow fusion for a range of ℓ-values.(198)

Some light (equally speculative) might be shed by the predictions of Time Dependent Hartree Fock Theory (TDHF)(199-202) which relate the subjects of this Chapter — fission and fusion — as well as providing an introduction to the next. We have been concerned largely with the "macrophysics" of nuclear matter. Of course this is not a new subject, since fission has been with us for a long time. But there have not been many studies of the *dynamics* of fission. It has mostly been an attempt to understand the energetics and other properties of the fission barrier. Is it possible to get some understanding of all these processes in some microscopic framework? A convenient starting point is the mean field or Hartree-Fock approximation, which has enjoyed great success in the static case.(203) This works because the density is high, the effective forces are strong, and the Pauli principle inhibits collisions. In a time-dependent generalization the rate of change of the mean field must be small enough so that it does not produce large excitations of the independent particles in a short time. The kinetic energy per nucleon should not be too large compared to the Fermi energy (≈ 30 MeV). The last Chapter will carry us beyond this regime.

The TDHF equations for the single particle wave functions ψ_n are given by

$$i \frac{\partial}{\partial t} \psi_n (\underline{r},t) = H(t)\psi_n(r,t)$$

$$H(t) = - \frac{h^2}{2m} \nabla^2 + V(t) \qquad (4.22)$$

and V(t) is an integral over the two-body interaction calculated self-consistently with the single particle wave functions. At each instant of time one has to calculate a mean field produced by the influence of all other particles. As the solutions are stepped in time, the self-consistent field is simply the Hartree-Fock potential at the previous step. The initial systems are represented by a product of single particle wave functions calculated in a moving potential; after the collision, one needs a mixture of both sets of wave functions.

A computer display of the density distributions of these calculations for ^{40}Ca + ^{40}Ca at 8 MeV/nucleon in a head-on collision is shown in Fig. 4.21(a), as a function of time.$^{(204)}$ (Because of the symmetry the complete picture should be visualized with an identical pattern below the bottom axis and to the left of the vertical axis.) The contour

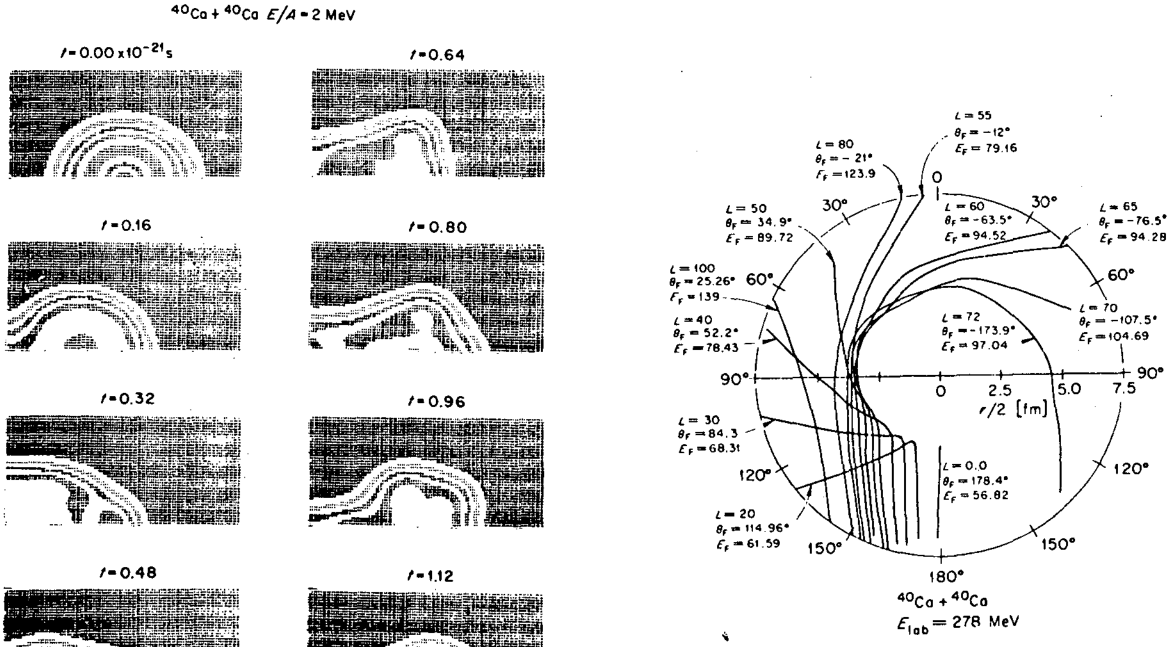

XBL 777-9761

Fig. 4.21

stripes mark density intervals of 0.04 nucleons/fm^3. We see that taking these calculations at face value (which is premature regarding the state of the art) the nuclei do not fuse, but separate after 0.65×10^{-21} sec oscillating in a predominantly octupole mode. In earlier stages of the diagram all the aspects of fission dynamics, including the neck formation and scission are in evidence. (Recall the phenomenological coordinate α_4 in Section 4.1.) In Fig. 4.21(b), a "trajectory diagram" is constructed showing the final energy and scattering angle for different partial waves. The small waves "bounce" backwards up to $\ell = 30$. Some waves fuse and others go into partial orbiting with deflection to negative angles. This diagram is considerably more sophisticated than the simple representations we sketched intuitively in Chapter 1, but they have the same features.

4.9 *Summary and Perspective*

Some of the paths taken by heavy-ion collisions, as they have emerged in this Chapter, are represented(165) in Fig. 4.22. The time scale is in units of $\tau = 10^{-22}$ sec. It shows how the composite system may proceed towards compound nuclear formation, preceded and succeeded by particle emission, and possibly ending in symmetric fission. *But there is also a new path*, where the composite system *never* fuses completely; rather, it separates on a relatively short time scale into two fragments, reminiscent of the initial ions which went into partial orbit. (Is there a connection with the quasimolecular states?) This is a new process(205) which has been given the name quasi-fission, damped colli-

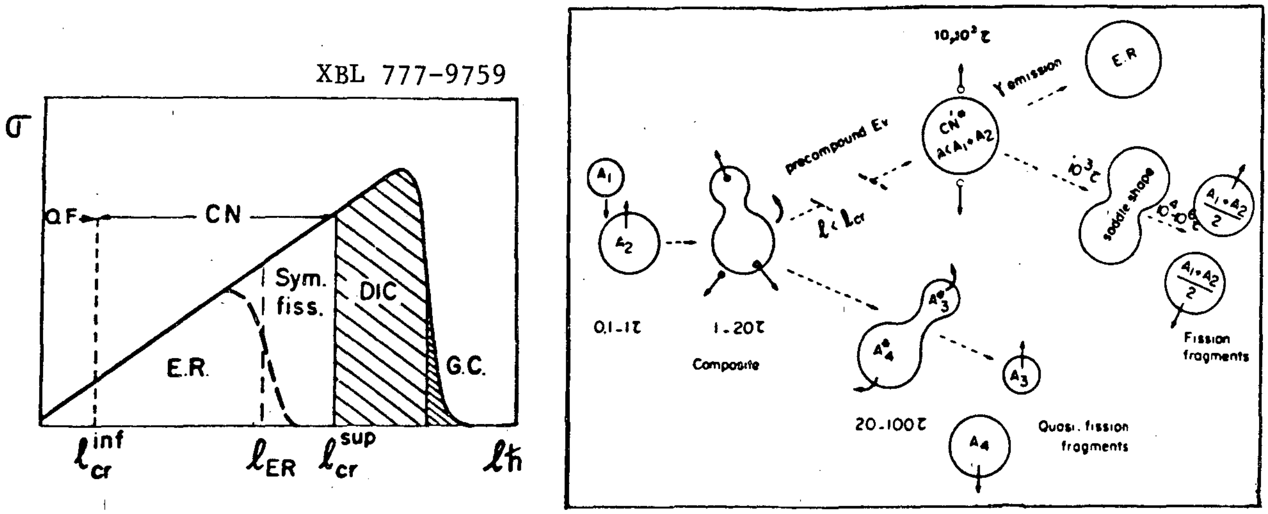
XBL 777-9759

Fig. 4.22

sions, deeply-inelastic scattering (most common) and (most uncommon), because they are *Characteristic of Heavy Ion Processes (CHIPS).*(201) Perhaps I could suggest a suitable compromise which captures both the spirit of these phenomena *and* the names, as FISSION CHIPS! A schematic division of the reaction cross section as a function of ℓ is given in Fig. 4.22. The sloping line represents the unitarity limit, $\sigma_\ell = \pi\lambda\!\!\!^{-2}(2\ell+1)$. For high partial waves (associated with the strong interaction radius), direct reactions such as transfer and inelastic scattering occur. Then at closer collisions come the CHIP processes (next section), until ℓ_{crit} allows the onset of fusion. For the upper ℓ values the system decays primarily by fission, and for lower values the compound nucleus survives to emit particles and leads to evaporation residues. Finally, there may exist the ℓ_{lower} boundary where the nuclei do not fuse and result in other "fission chips."

5.

DEEPLY-INELASTIC SCATTERING

5.1 *The Phenomenon*

When the history of nuclear physics in the seventies is written, surely the study of deeply-inelastic scattering (or fission chips) will emerge as one of the most important new directions in heavy-ion physics.(206) It is a subject which has captured the imaginations of nuclear chemists, nuclear physicists and theorists all over the world, who have abandoned their traditional areas of research in droves. They have created a monument which by sheer size alone inspires awe. Let us look at Fig. 5.1 to see how this new process fits with the scheme of heavy-ion reactions.(205)

The various terms used in the figure, such as *distant* and *touching* collisions are to be understood in the context of a matter density with diffuse surfaces, as discussed in the earlier Chapters, where we have parameterized the nuclear density

$$\rho = \frac{\rho_0}{\left\{1 + \exp\frac{(r-c)}{a}\right\}} \qquad (5.1)$$

Here c is the nuclear matter half-density radius. Distant collisions occur for the overlap of the extreme tails, i.e., $r > c_T + c_P + S$.

Touching or grazing collisions take place at distances equal to or less than this. The flux of touching collisions comprise the total reaction cross section, and is subdivided into a number of continuously evolving reaction processes. As the penetration depth increases, the energy loss and mass transfer as well as the reaction time increases.

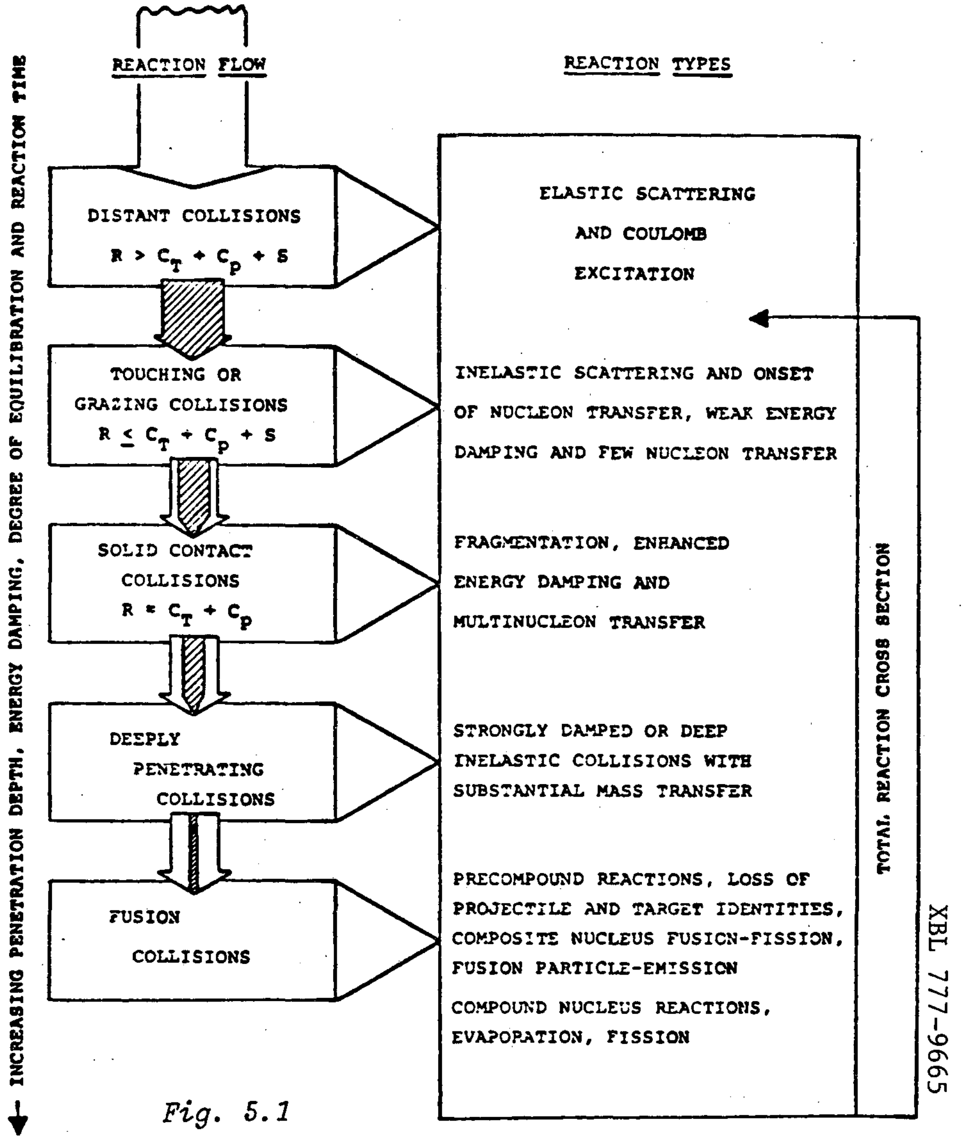

Fig. 5.1

XBL 777-9665

In light-ion reactions, solid contact ($r = c_T + c_P$) usually leads to fusion and a compound nucleus. This dominance is indicated by the open arrows in Fig. 5.1. For heavy ions the situation is very different. Much less cross section goes into the compound nucleus, and instead the new deeply-inelastic process takes over. These features were also illustrated in Fig. 4.22.

A powerful means of getting a global picture of the reaction processes comes from analyzing the mass distribution of reaction products after irradiation, using radiochemical techniques.(207) An example for $^{40}Ar + ^{238}U$ at 288 MeV is shown in Fig. 5.2. The mass distribution is decomposed into several components. The "rabbit-ears" close to the projectile and target mass (E,F) are quasi-elastic, few nucleon transfers. The broad curve A centered at half the combined target and projectile mass is symmetric fusion-fission, whereas the curves B are due to transfer-induced sequential fission of the target. In addition, there is a broad curve C which is associated with deeply-inelastic events

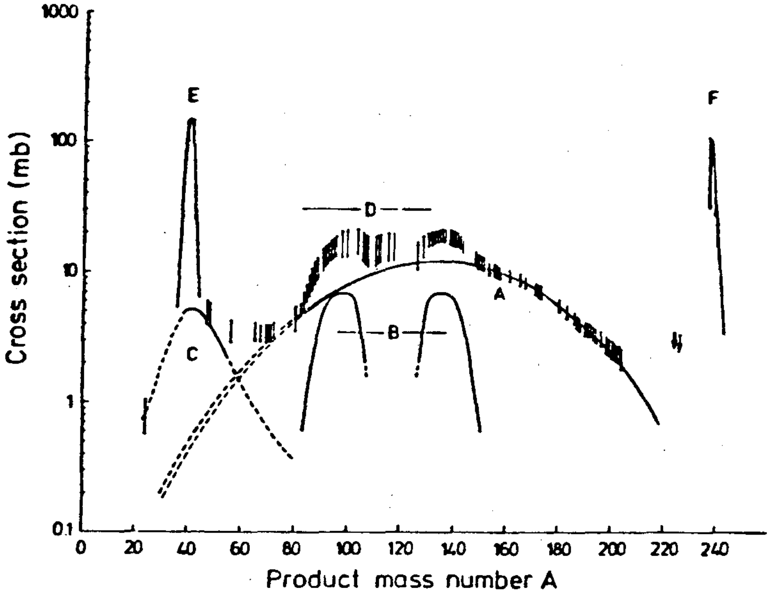

Fig. 5.2

XBL 777-9663

The energy spectra for a similar experiment $^{40}Ar + ^{232}Th$ at 388 MeV, taken with solid-state counter telescopes, is shown in Fig. 5.4 for a selection of different elements as a function of angle. These data were some of the first to address the new phenomenon of deeply-inelastic scattering,(208) but they illustrate very clearly the characteristic features. The spectra in general have two components: a high-energy component — referred to as "quasi-elastic" — with an energy not too far removed from (E_{inc} + Q), and a low-energy component, peaking close to the Coulomb barrier for the appropriate exit channel. (For example, Cl at 45° peaks at ≈ 140 MeV, and V_c ≈ 155 MeV.) This observation is the origin of the term "deeply-inelastic" or "strongly damped," because all the initial energy has been dissipated, and the fragments emerge with the Coulomb energy (like fission

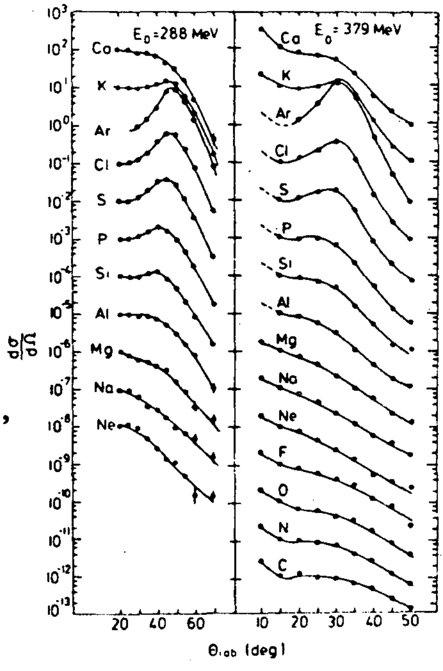

XBL 777-9762

Fig. 5.3

fragments). However, we notice that as we move towards forward angles, there is *a tendency for the two components to move together and merge into one.*

The corresponding angular distributions, shown in Fig. 5.3 for products with masses in the vicinity of the projectile have a grazing angle peak characteristic of the peripheral collisions we discussed in Chapters 2. Products far removed from the beam have much flatter distributions and, in many experiments, approach the $1/\sin\theta$ form characteristic of heavy-ion compound nuclear reactions (Chapter 3). The information from both Figs. 5.3 and 5.4 can be combined into the contour plot of Fig. 5.5, which shows a pronounced mountain at high energy close to the grazing angle, with a ridge running down to lower energies and smaller angles.(209) It merges with another ridge which *increases* in energy from large angles to more forward angles.

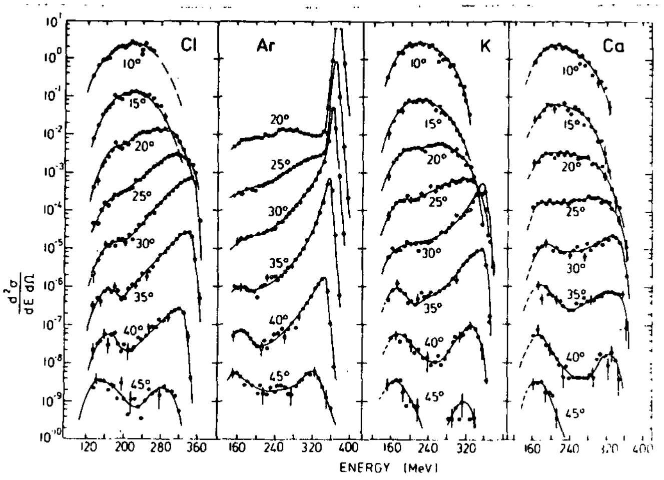

Fig. 5.4

XBL 777-9762

The presently accepted interpretation is illustrated schematically in Fig. 5.6. (Alternative interpretations based on a double rainbow cannot be excluded in all cases.(210)) The higher partial waves undergo grazing collisions, in the region of the maximum of the deflection function (compare Fig. 1.6) and lead to the large quasi-elastic peak. Between the grazing and the critical partial waves, the orbits are pulled around by the attractive potential and the two ions form a *temporary dimolecular system.* They do *not* fuse to form a compound nucleus, which happens for waves smaller than ℓ_{crit} (compare the discus-

XBL 746-963

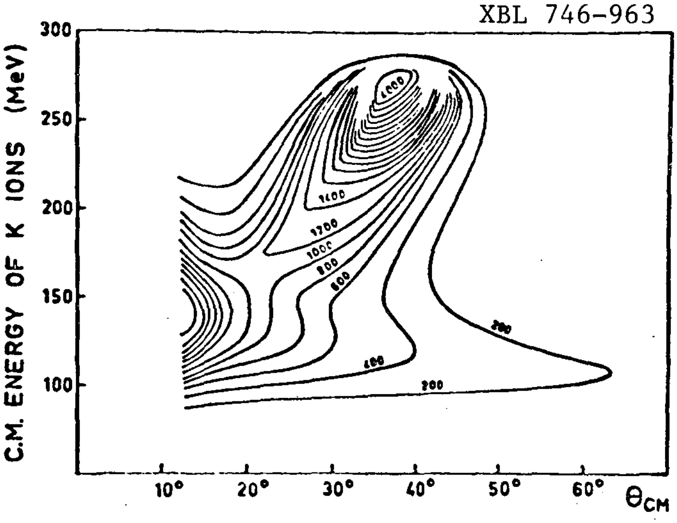

Fig. 5.5

sion in the last Chapter). The low-energy ridge in the contour plot is then naturally associated with *negative angle scattering*. The longer the association and the greater the angle of rotation, the more the angular distributions approach the form 1/sinθ. Figure 5.4 then suggests nucleon transfers will occur during the time the two nuclei are in contact and the magnitude of the exchange is correlated with the kinetic energy dissipation and with increasing angle of rotation. (Some of the many extensive reviews on this subject are given in Refs. 205, 211 through 216.)

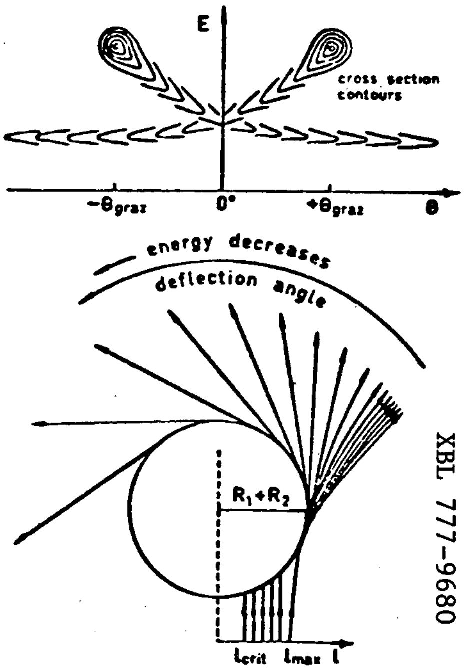

Fig. 5.6

5.2 *Justification of the Hypothesis of Dimolecular System Formation*

Before proceeding further with the logical analytical predictions of the rotating dimolecular model, we describe an experiment which gives *direct experimental insight* on its existence.(217) In a classical picture the two fragments come together with a high angular momentum in a peripheral collision, and the angular momentum is oriented perpendicular to the scattering plane. A consequence of Fig. 5.6 is that the *direction* of rotation of the quasi-elastic (positive angle) and deeply-inelastic (negative angle) fragments should be opposite.(209) Subsequent γ-radiation emitted from the highly excited fragments should be circularly polarized in the direction of angular momentum of the emitting nucleus. The direction of circular polarization can be measured by scattering the emitted γ-rays from the polarized electrons in magnetized iron. (Remember the classic experiment to measure parity violation in weak interactions.) The experimental apparatus, sketched in Fig. 5.7, used two polarimeters in a symmetric configuration normal to the plane defined by two heavy-ion counters at 35°, which detected fragments from the ^{40}Ar + Ag reaction at 300 MeV. An asymmetry in the count rate was observed which was of opposite sign for quasi-elastic and deeply-inelastic components, indicating that the fragments associated with these two processes spin in opposite directions. For this reaction, the result confirms that deeply inelastic scattering comes from negative angles.

In much heavier systems, such as ^{136}Xe + ^{209}Bi, the amount of orbiting, if any, is very small.(218) Thus the differential cross section in Fig. 5.8 for products with masses close to that of the projectile are all concentrated near the grazing angle. This process is also indicative of a fast nonequilibrium reaction, and leads to final products with large damping of the kinetic energy. In the case of Xe + Bi, the associated cross section amounts to the total reaction cross section, with little left over for compound nuclear formation.

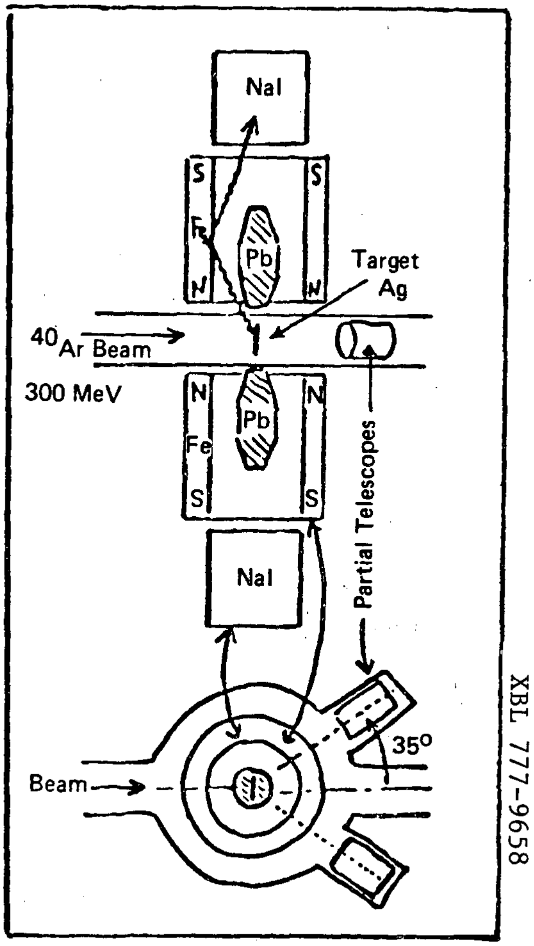

XBL 777-9658

Fig. 5.7

The nature of the continuum energy distribution in these collisions is different from the (superficially similar) continuum of Fig. 2.9(b). There the continuum was attributed to simple, peripheral transfer reactions to a high density of states in the residual nucleus, with an optimum Q-value, and the polarization of the outgoing light fragment was just *opposite* to that predicted for a deeply-inelastic collision.(72,73) The ultimate relationship between these microscopic transfer

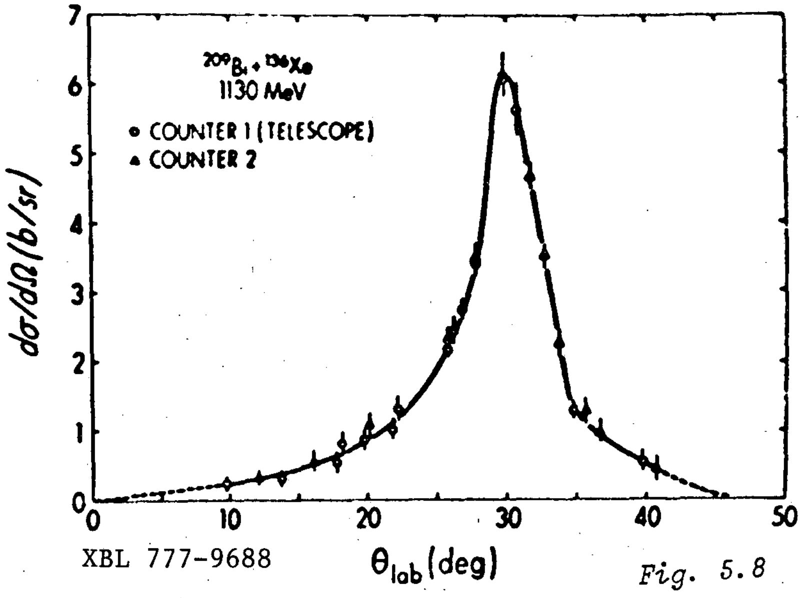

XBL 777-9688

Fig. 5.8

reactions, both direct and multistep, to the more macroscopic phenomena of orbiting dimolecular systems is a problem of great theoretical interest. It is certainly the case that there is a close similarity(171) between the evolution of the differential cross sections in Fig. 5.4 and those of Fig. 5.9, which pertain to direct and multistep reactions between ^{16}O and ^{48}Ca leading to *discrete final states,* for which the theoretical techniques described in Chapter 2 are well developed.(219) We shall not pursue this relationship further,(220) but proceed with the more macroscopic theoretical models.

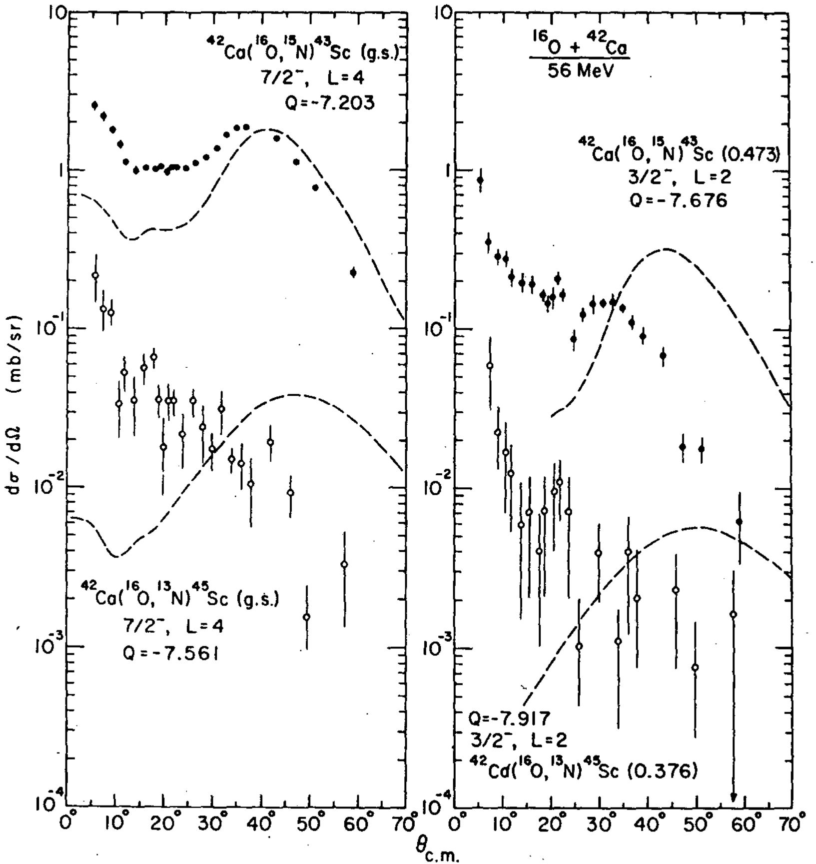

XBL 777-9681

Fig. 5.9

5.3 Theoretical Approaches to Deeply-Inelastic Scattering

Before describing the more formal approaches of diffusion theory, let us illustrate the basic ideas with a simple example.(221) As the two nuclei rotate in close contact, an exchange of nucleons, energy, angular momentum, mass and charge takes place continuously as a function of angle and time. The deeply-inelastic process therefore gives us a *direct handle on the progress of evolution of these quantities towards equilibration.* Consider the two nuclei as containers in which nucleons can have a random motion. A nucleon in nucleus 1 can escape through the neck and be absorbed by nucleus 2, and vice versa. Let the area of the interface of the composite system be A(t), and the window integral in the reaction,

$$\bar{A}\Delta t = \int_{\text{orbit}} A(t)\, dt \qquad (5.2)$$

The probability per second that a nucleon crosses the interface from 1 to 2 is $n_{12}A$ and similarly from 2 to 1 is $n_{21}A$. These rates depend on dynamics and are functions of time. This dependence will be weak if the number of transferred nucleons is much less than the total. So say n_{ik} = constant. Then the variance of the number transferred is:

$$\delta n = [(n_{12} + n_{21}) \int A(t)\, dt]^{\frac{1}{2}} \qquad (5.3)$$

while the flow of mass from 1 to 2 is

$$\langle n \rangle = (n_{12} - n_{21}) \int A(t)\, dt \qquad (5.4)$$

and the normalized distribution of the number transferred might be expected to be a Gaussian

$$P(n) = \frac{1}{\sqrt{2\pi}\, \delta n} \exp - \left[\frac{(n - \langle n \rangle)^2}{2\delta n^2}\right] \qquad (5.5)$$

Now a good guess for the transfer rate is:

$$n_{12} \approx n_{21} \approx \frac{1}{6} \rho v \qquad (5.6)$$

where ρ is the nuclear matter density, 0.17 nucleons/fm^3, and $v \approx 9 \times 10^{22}$ is the typical speed of a nucleon inside the nucleus. With an interface area of $\bar{A} = 10$ fm^2 and a typical direct reaction time of $t \approx 5 \times 10^{-22}$ sec for the collision of ^{40}Ar on ^{50}Ti at 236 MeV,(188) we get $\delta n \approx 5$. The Z and A distribution of fragments in this reaction are illustrated in Fig. 5.10 (which were obtained by combining the Z and A information of Fig. 4.14) and we see that the spread in A values is indeed *the order* of δn. (It is difficult to see the Gaussian profiles in the 2-D plot, but such indeed are the observed shapes.)

The generalization of this type of approach to diffusion processes in the rotating dinuclear system leads to the Focker-Planck equation(213, 215,222-224) for the population distribution of a macroscopic variable x as a function of time, P(x,t):

$$\frac{\partial P(x,t)}{\partial t} = -v\frac{\partial P(x,t)}{\partial x} + D\frac{\partial^2 P(x,t)}{\partial x^2} \qquad (5.7)$$

the solution of which is

$$P(x,t) = \frac{1}{\sqrt{4\pi Dt}}\exp\left[-\frac{(x-vt)^2}{4Dt}\right] \qquad (5.8)$$

The mean value of the distribution x moves with time at constant velocity, and the variance $\sigma^2 = \langle x - \langle x \rangle \rangle^2 = 2Dt$ increases linearly with time (see Fig. 5.11). The transport coefficients v and D are known as the drift and diffusion coefficients. The FWHM of the curve is given from $\Gamma^2 = 16\,\ell n\,2(Dt)$. Amongst the macroscopic variables which have been measured are kinetic energy, the N/Z degree of freedom and the mass asymmetry degree of freedom $A_1 - A_2/A_1 + A_2$.

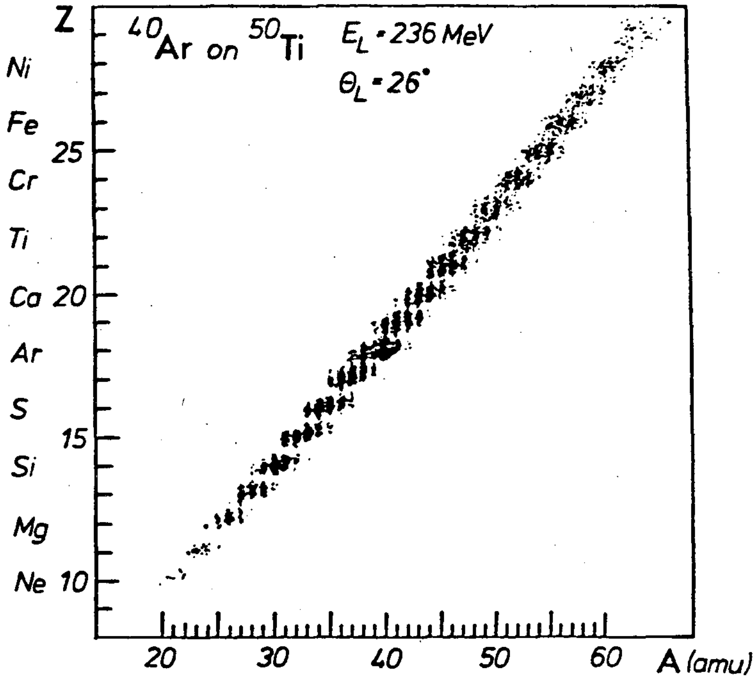

XBL 777-9666

Fig. 5.10

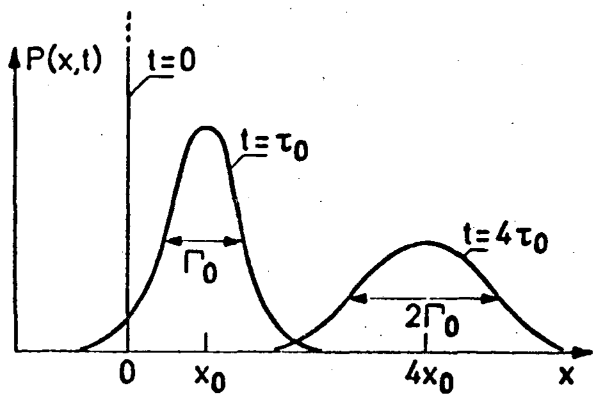

XBL 777-9664

Fig. 5.11

As an example of how these methods work,(225,226) consider the charge distribution as a function of angle. This can be derived from an analysis of distributions of cross sections such as Fig. 5.4 for each Z. They would be expected to have Gaussian distributions,

$$P(z,t) = \frac{1}{\sqrt{4\pi D_z t}} \exp\left[-\frac{(z - z_o - v_z t)^2}{4D_z t}\right] \tag{5.9}$$

where $z - z_o$ stands for the number of protons transferred during the interaction time t. The quantities v_z and D_z represent average proton drift and diffusion coefficients. In order to relate *angle* information to *time* information we write

$$\tau_{int} = \frac{1}{\overline{\omega}} (\theta_{gr} - \theta) \tag{5.10}$$

where τ_{int} is the interaction time for the rotating dinuclear system, rotating with mean rotational frequency $\overline{\omega}$. (The rotation is measured from the grazing angle.) Now,

$$\overline{\omega} \approx \frac{\hbar \ell}{\mathcal{I}} \tag{5.11}$$

where $\mathcal{I}$ is the moment of inertia of the system, and

$$\overline{\ell} \doteq \frac{2}{3} \frac{\ell_g^3 - \ell_{crit}^3}{\ell_g^2 - \ell_{crit}^2} \tag{5.12}$$

where we attribute deeply-inelastic collisions to the band of partial waves from ℓ_{crit} (inside of which fusion takes place) to ℓ_g (see Fig. 4.22).(227)

For the reaction Ar + Th depicted in Figs. 5.3 and 5.4 at 388 MeV, ℓ_g and ℓ_{crit} have been determined as 222 and 94 respectively.(208) For $\mathcal{I}$ we can assume rigid body rotation of the dinuclear complex

$$\mathcal{I} = \frac{2}{5} M_1 R_1^2 + \frac{2}{5} M_2 R_2^2 + \mu R^2 \quad . \tag{5.13}$$

The plot of Γ^2 versus θ in Fig. 5.12 can then be regarded as a plot of Γ^2 versus $\tau_{int} = t$, and the slope $\Gamma^2/t \propto D_z$. In fact, the same value of D_z is derived for the different reactions studied at different energies (on the figure, the t-scale is different for the different reactions, since this is transformed by $1/\overline{\ell}$). The derived value was $D_z \approx 10^{22}$ (charge units)^2/sec. Other quantities can be determined by similar analysis. One finds typically:(213,222)

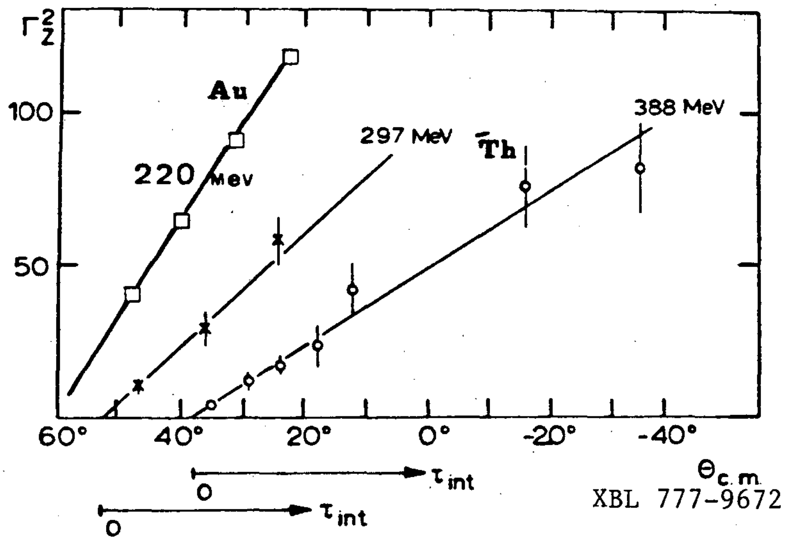

XBL 777-9672

Fig. 5.12

Energy drift coefficient $v_E \approx 4 \times 10^{23}$ MeV/sec

Energy diffusion coefficient $D_E \approx 4 \times 10^{24}$ $(\mathrm{MeV})^2$/sec

Charge drift coefficient $v_z \approx 10^{21}$ (charge units)/sec

Charge diffusion coefficient $D_z \approx 10^{22}$ (charge units)^2/sec

A more detailed treatment following these methods has recently been developed.(228)

The diffusion coefficients are related(215) to level densities, temperature and the potential energy of the intermediate complex, as a function, for example, of z and ℓ. The potential energy can be expressed(213,229)

$$V_z = E_{LD}(z) + E_{LD}(z_{tot} - z) + E_{Coul} + E_{rot} + \text{constant}$$

where E_{LD} can be computed from the liquid drop model. An example for the Kr + Ta system, with the constant adjusted to make $V_z = 0$ at the charge corresponding to the initial system, is shown in Fig. 5.13(a). As the angular momentum increases the potential minimum becomes more pronounced, resulting in a large driving force towards symmetry. This effect is reflected in the solution of the Fokker-Planck equation in Fig. 5.13(b). For $\ell = 0$ the flat potential leads to very broad z-distribution, which progressively narrows for higher ℓ-values.

A characteristic of the deeply-inelastic collision is the large energy damping. This energy loss also appears to take place rapidly while the two ions are in contact. On a microscopic picture the energy

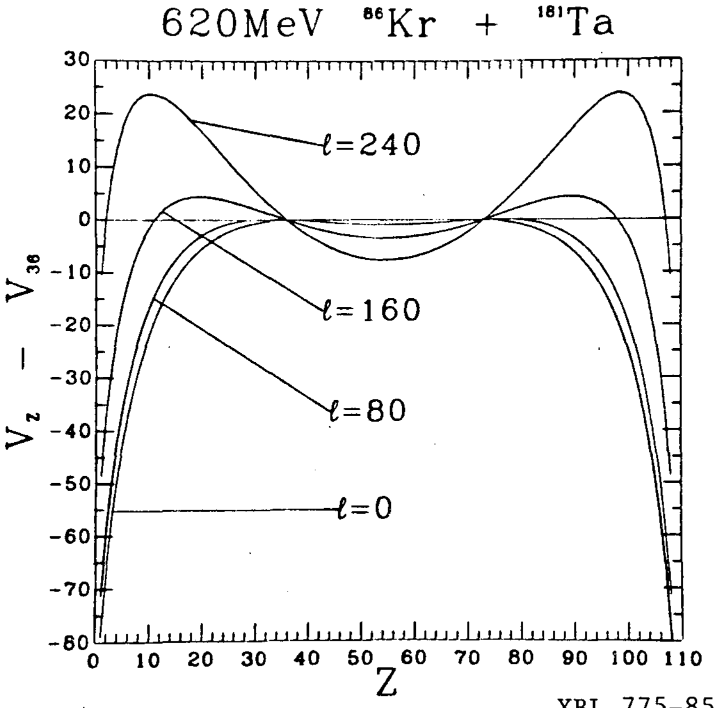

XBL 775-8598

Fig. 5.13(a)

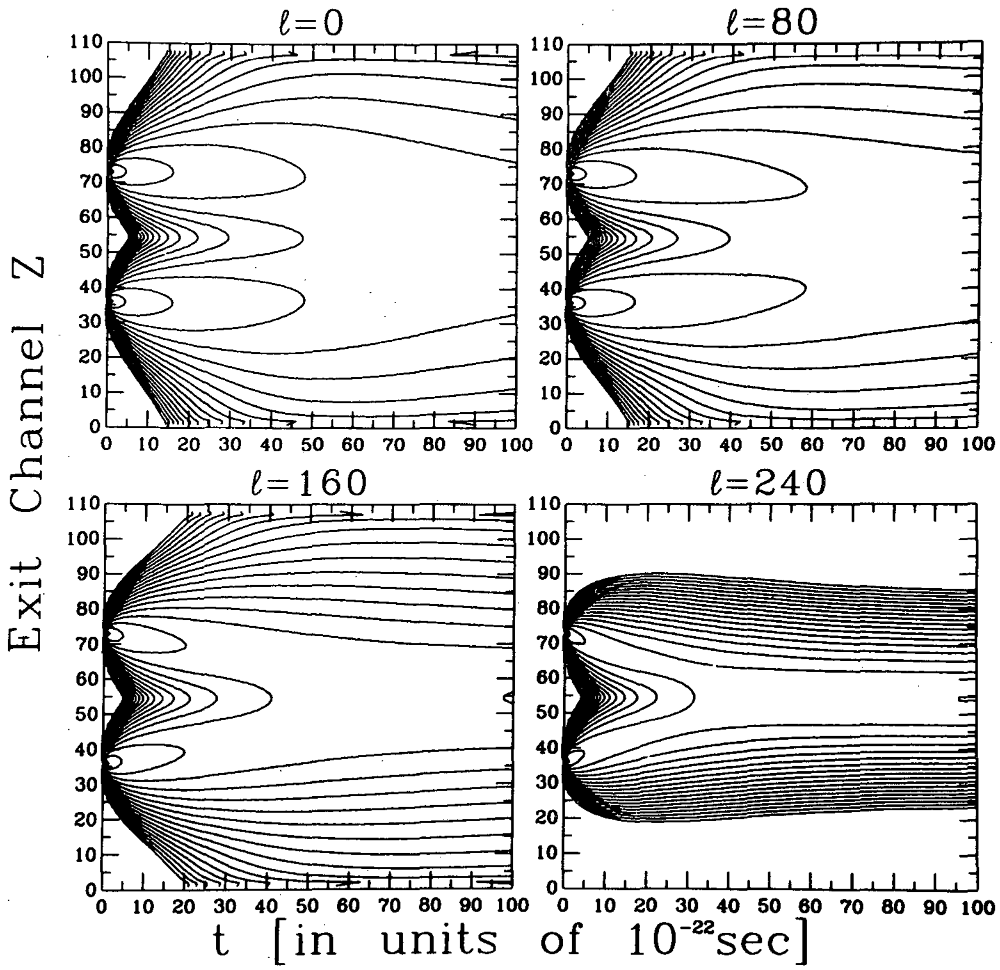

Fig. 5.13(b)

XBL 775-8600

loss could be mediated by particle-hole excitation and also by transfer of nucleons between the colliding ions. Such a nucleon, with mass m, deposits a momentum $\Delta p = m|\dot{r}|$, where $\dot{r}$ is determined from the energy of the system prior to the transfer, and the *resultant energy loss is therefore proportional to the energy available* ($\delta E \propto (\Delta p)^2$). This argument justifies the introduction of a frictional damping force proportional to the velocity(180,181,225,230)

$$F_t = - kv \tag{5.14}$$

Then we can write for the rate of energy loss

$$\frac{dE}{dt} = \mu v \frac{dv}{dt} = v \cdot F = -kv^2 = -2 \frac{k}{\mu} E \tag{5.15}$$

Integrating the expression,

$$\ell n\left(\frac{E_o}{E}\right) = 2 \frac{kt}{\mu} \tag{5.16}$$

Now we have just shown that a time scale is established by the relation $t = \Gamma_z^2/2D_z$, and therefore we expect that there should be a linear relation between $\ell n(E_o/E)$ and Γ_z^2; the gradient yields a value for $k/\mu D_z$. As Fig. 5.14(a) dramatically demonstrates,(226) there certainly is a clear correlation between the width of the charge distribution and the kinetic energy loss, which is shown on this figure for successive 50 MeV wide bins in the reaction of Bi + Xe.

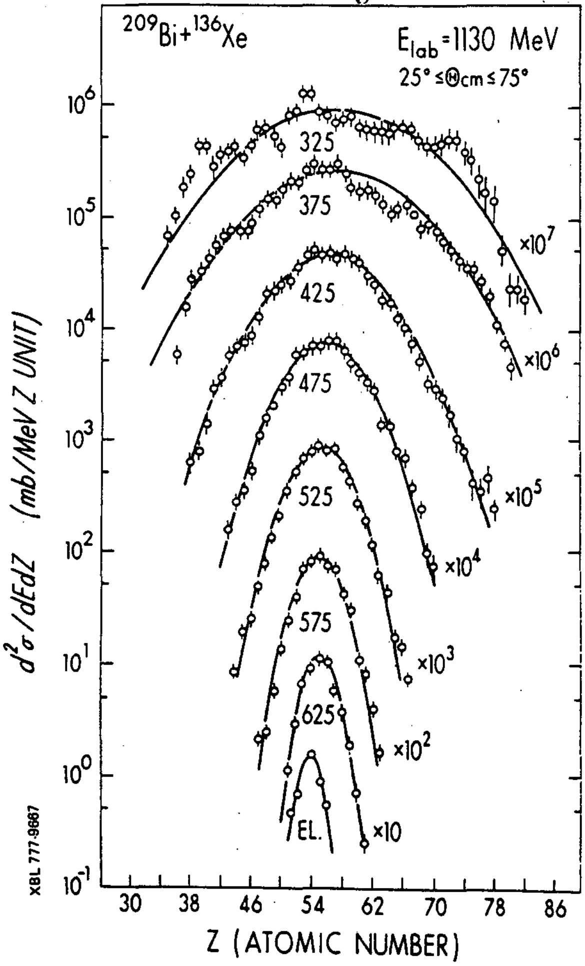

Fig. 5.14(a)

In Fig. 5.14(b), the values of σ_z^2 from Fig. 5.14(a) are plotted as a function of the interaction time $\tau(\ell)$ in units of 10^{-22} sec, and appear to increase linearly, i.e. $\sigma_z^2(\ell) = 2D_z(\ell)\ \tau(\ell)$. The time scale on the figure was derived from the deflection function. This deflection function was constructed by assuming a sharp

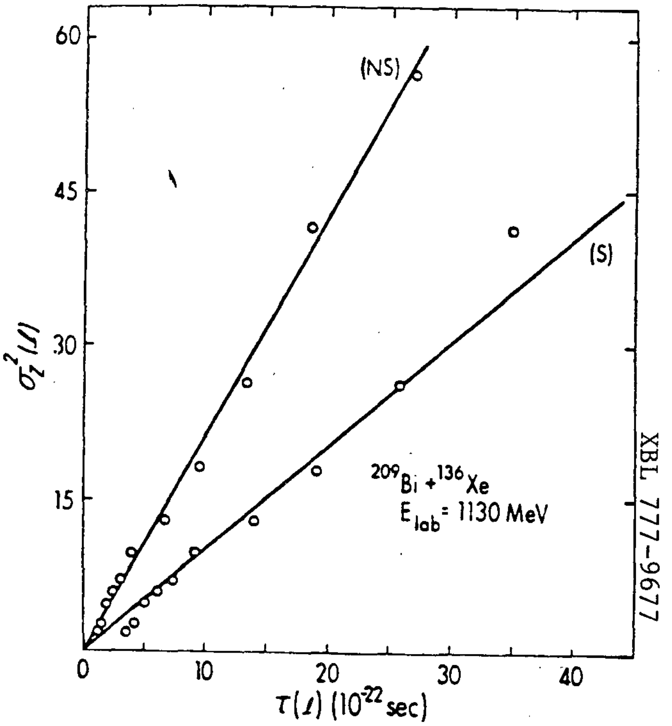

Fig. 5.14(b)

cut-off model, where the cross section up to ℓ_j is given by $\sigma_j = \pi ƛ^2(\ell_j + 1)^2$. Then using the experimental results on the cross section as a function of kinetic energy loss, the angular momentum can be related(231) to the energy loss by

$$\ell_i = \left[(\ell_j + 1)^2 - \frac{\Delta\sigma_{ij}}{\pi ƛ^2}\right]^{\frac{1}{2}} - 1$$

where $\Delta\sigma_{ij} = \sigma_j - \sigma_i$ is the cross section in an energy window between E_i and E_j. The average scattering angle for a particular energy loss is also an experimental quantity (see Fig. 5.5), so the curve of θ versus ℓ can be deduced as in Fig. 5.14(c). The angular momentum dependent interaction time is then calculated from the expression(232,233)

$$\tau(\ell) = \frac{\Delta\theta(\ell)\,\mathcal{J}(\ell)}{\hbar\ell} \qquad (5.17)$$

where $\Delta\theta$ is the difference between the Coulomb deflection angle (dashed) and the actual reaction angle. From these results we extract the values of Γ_z^2 (the FWHM of the Gaussian functions in Fig. 5.14(a)) as a function of E and construct the plot shown in Fig. 5.15, which is indeed remarkably linear. Since we previously deduced a value of D_z we can now use these results to calculate the coefficient of friction $k = 0.6 \times 10^{-21}$ MeV. sec. fm^{-2}.

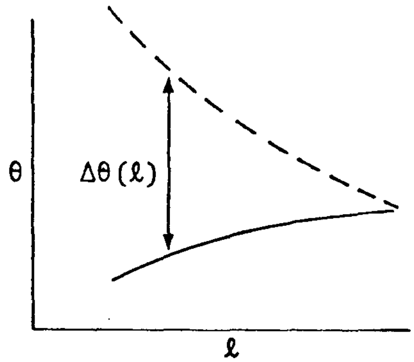

Fig. 5.14(c)

It is instructive to see how the large value of k can be understood,(234) using the simple model of matter transfer discussed in Section 5.3. Suppose that the speed of nucleus 1 relative to 2 is tangential and equal to v_t. The rate of nucleon "hits" from 2 to 1 through the window is:

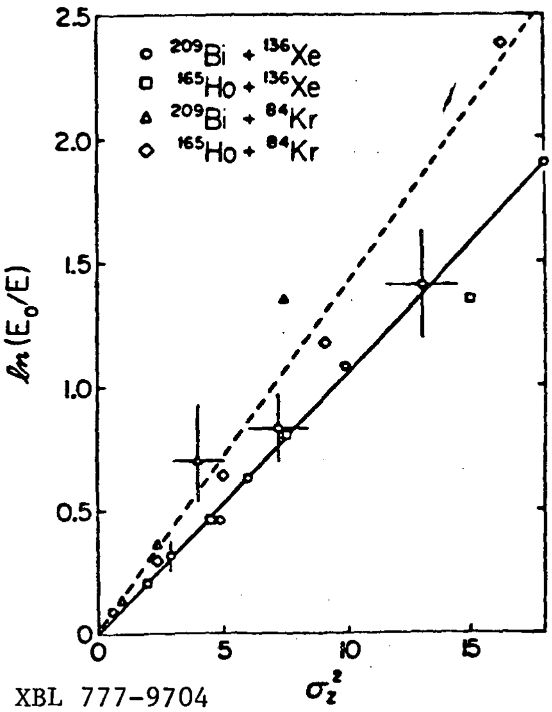

XBL 777-9704

Fig. 5.15

$$\frac{dn}{dt} = \frac{1}{2}\rho v A \cos\theta \, p(v) \qquad (5.18)$$

where θ is the inclination of the *nucleon* speed v, of distribution p(v). Each nucleon of mass m deposits the excess momentum $-mv_t$, and therefore the average force acting in the tangential direction is:

$$F_t = -\frac{1}{2} m\rho A v_t \int_0^{\pi/2} v\, p(v) \cos\theta \frac{d\Omega}{2\pi} dv$$

$$\approx -\frac{1}{4} m\rho A v_t \bar{v} \qquad (5.19)$$

By identifying this expression with the friction force $-kv$, we derive that

$$k \approx \frac{1}{4} m\rho A\bar{v} \qquad (5.20)$$

Assume, as in Equ. 5.2, a window area of $A \approx 10\ \text{fm}^2$, and the average nucleon speed $\bar{v} = 3/4\ v_F \approx 3/16\ c$ and the nucleon density of nuclear matter, $0.17\ \text{fm}^{-3}$. Then:

$$k \approx 200\ \text{MeV/fm} \cdot c \qquad (5.21)$$

i.e., 0.7×10^{-21}, in good agreement with the value extracted from experiment!

Therefore this mechanism of frictional dissipation is adequate for the early stages of deeply-inelastic reactions, where the window is open, i.e., whenever there is solid contact between the ions. The energy loss mediated by particle-hole excitation appears to be of comparable magnitude.(223) Another type of dissipation is caused by the "piston effect" of collisions of particles with moving potential surface.(230) There is also "two body" friction analogous to viscosity in liquids.(235) In order for the above treatment to be valid we require that v_t is small compared to the intrinsic speed v, otherwise the velocity distribution p(v) will change too much during the collision. In the last Chapter we shall consider such situations.

More generally, a friction force of the type we have been discussing can be represented(184) as

$$F = -k \int d^3r\, \rho_1 \rho_2\, |\dot{\vec{r}}| \qquad (5.22)$$

where ρ_1 and ρ_2 are the density distributions of the two nuclei and the integral is taken over the overlap region. The rate of dissipation has also been calculated using a proximity formalism (rather similar to our discussion of proximity potentials in Chapter 1), with the result(236,237)

$$\frac{dE}{dt} = 4\pi \frac{n_o}{\mu} \frac{R_T R_P}{R_T + R_P} b X(\xi_o) E \qquad (5.23)$$

where $n_o = 2.5\times 10^{-23}$ MeV•sec•fm^{-4} is the transfer flux density, R and b are the nuclear half-density radius and diffuseness, and $X(\xi_o)$ is a universal flux function. An application of this formalism to the above reactions for Kr and Xe on heavy targets yields(205)

$$\frac{1}{E}\frac{dE}{dt} \approx 10^{21} X(\xi_o) \approx 0.7 - 2.1\times 10^{21} \text{ sec}^{-1} \qquad (5.24)$$

which is actually in very good agreement with the value of $2k/\mu \approx 2\times 10^{21}$ sec which follows from Fig. 5.15.

These approaches all assume adiabaticity, i.e., an internal response time short compared to that in which the relative coordinates change, as well as frozen matter distributions. However, it is possible that the characteristic times over which the interaction matrix elements change may in fact be $\approx 10^{-23}$ sec in contradiction to the adiabaticity assumption.(238) There is a resultant strong coupling of collective modes of motion (e.g. giant resonances) to the relative motion, followed by their subsequent fast damping into particle-hole degrees of freedom. The interaction of collective and intrinsic degrees of freedom and the dissipative mechanisms is still under intensive study.

5.4 Dynamical Aspects

The previous section was intended to give the flavor of the approaches to understanding the diffusion processes in deeply-inelastic scattering. The evidence strongly suggests the idea of an intermediate complex consisting of two well defined fragments in contact, undergoing equilibration, and the time constants of these relaxation processes have been determined. Now we consider the transfer of orbital angular momentum into the rotation of the two fragments constituting the complex. The angular momentum transfer induced by the frictional forces passes through several stages.(184,234) Initially, a sliding friction term makes the two bodies start to roll on each other, and then a rolling friction term causes the two bodies to get stuck in rigid rotation.

At the onset of sliding the moment of inertia characterising the system is simply

$$\mathcal{J}_{NS} = \mu R^2 \tag{5.25}$$

where μ is the reduced mass and R the distance between the centers of the fragments. For the sticking configuration (using the theorem of parallel axes) the moment of inertia is

$$\mathcal{J}_S = \mu R^2 + \mathcal{J}_1 + \mathcal{J}_2 \tag{5.26}$$

where $\mathcal{J}_{1,2}$ are the moments of inertia of the fragments, $2/5\ M_i R_i^2$ The *maximum* value $\Delta\ell$ of orbital angular momentum transformed into intrinsic spin can then be calculated from $\ell_i \mathcal{J}_{NS} = \ell_f \mathcal{J}_S$ as

$$(\ell_i - \ell_f) = \Delta\ell = \frac{(\mathcal{J}_S - \mathcal{J}_{NS})}{\mathcal{J}_S}\ \ell_i \tag{5.27}$$

which appears as *intrinsic spin* of the fragments. For equal mass nuclei we obtain $\Delta\ell = 2/7\ \ell_i$, and the fraction varies depending on the mass asymmetry, as shown below:

$\alpha = \frac{M_1}{M_1+M_2}$	$\frac{\mathcal{J}_S}{\mathcal{J}_{NS}}$	$\frac{\Delta\ell}{\ell_i}$
0.1	2.87	0.65
0.2	1.83	0.45
0.3	1.54	0.35
0.4	1.43	0.30
0.5	1.40 = 7/5	0.29 = 2/7

In the case of *rolling* friction, however, the fraction $\Delta\ell/\ell_i = 2/7$ *independent of the masses of the two nuclei.*(184,234)

It is possible to measure $\Delta\ell$ from the γ-ray multiplicity associated with different fragments arising from the decay of the complex.(239-241) As discussed in Chapter 3 it is reasonable to assume that the intrinsic angular momentum is just twice the multiplicity (assuming that the angular momentum is carried off mainly by the E2 yrast cascade). An example is the ^{20}Ne + Ag system at 175 MeV for which energy spectra are shown in Fig. 5.16 at three different angles. We see that in proceeding

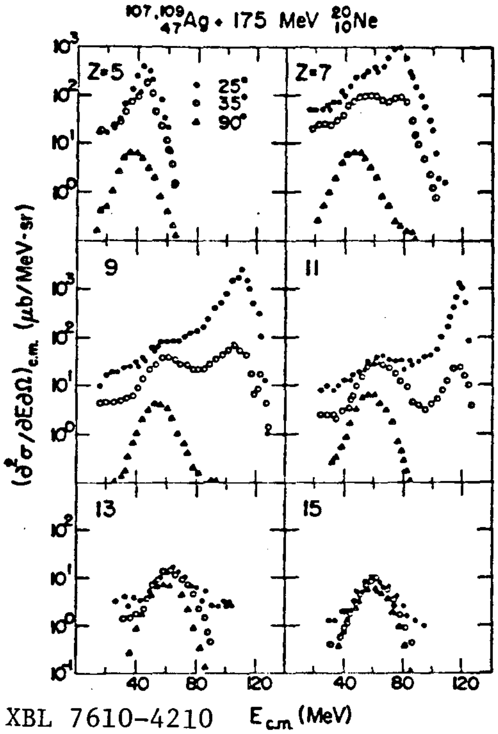

XBL 7610-4210

Fig. 5.16

to more backward angles the quasi-elastic component disappears and the deeply-inelastic dominates, just as in Fig. 5.5. The multiplicities as a function of the Z of the detected fragment are shown in Fig. 5.17 for the deeply-inelastic component. For comparison the predicted values for the cases of rolling and sticking are drawn for two values of entrance channel angular momenta (50ℏ and 70ℏ). The value 70ℏ is expected from the sum of the known evaporation residue cross section of 900 mb (corresponding to $\ell_{crit} = 57\hbar$) and the deeply-inelastic cross section of 400 mb, using our customary formulae. (The line for 50ℏ corresponds to the limit for compound nuclear formation.) Then the rolling limit is given by

$$\Delta\ell = \frac{2}{7}\,\ell_i = 20\hbar \doteqdot 2M_\gamma$$

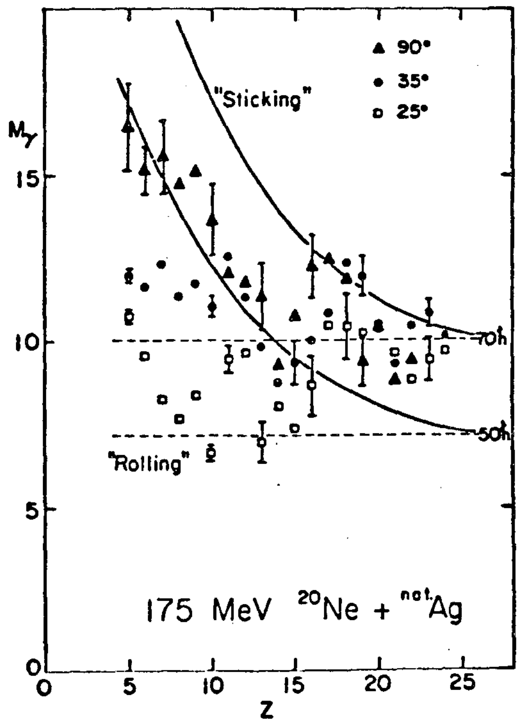

XBL 7611-4446 *Fig. 5.17*

At 90°, where the rotating dinuclear complex has remained in contact for a long time, the sticking limit appears to be reached, with ℓ_i between 50 and 70ℏ. At more forward angles the fragments appear to be still rolling on each other. These data furnish strong evidence that the intermediate complex approaches rigid rotation in a time comparable to the rotation period.

It is interesting to compare these results with a similar experiment where quasi-elastic *and* deeply-inelastic scattering were studied.(239) This system, shown in Fig. 5.18, for the ^{14}N + ^{93}Nb is rather similar to ^{14}N + ^{100}Mo at 120 MeV that we used in Chapter 2 (Fig. 2.9) to demonstrate that the continuum spectrum was populated by *two-body transfer reactions*, without any formation of an intermediate rotating dinuclear complex. In that case we expect (just the *recoil angular momentum* of Section 2)

$$\Delta\ell \approx \frac{\Delta M}{M}\,\ell_i \qquad (5.28)$$

where M is the mass transferred and M is the incident mass. This equation is represented by the solid V-shape in Fig. 5.18, which reproduces qualitatively the quasi-elastic data. The dotted line again represents the clutched limit, which is closer to the deeply-inelastic data points of products farther removed from the projectile mass.

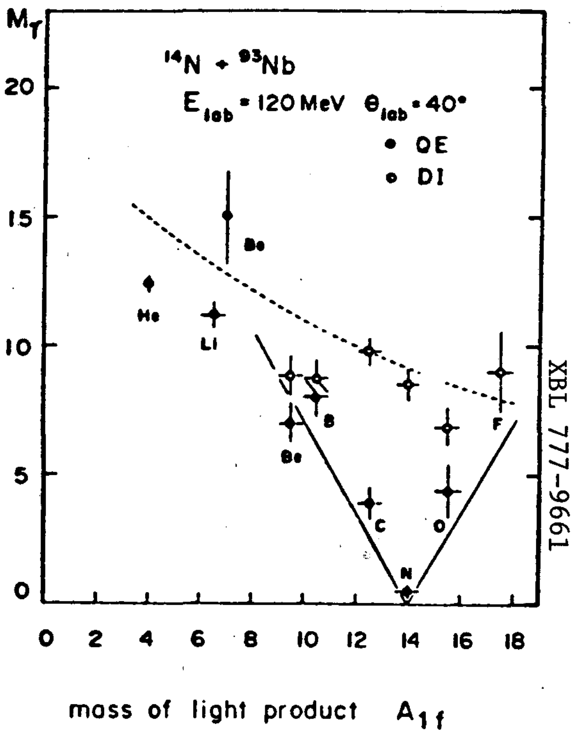

Fig. 5.18

Another classic experiment in this vein has capitalized on the fission decay mode (rather than γ-decay) which is dominant in heavy systems. The experimental arrangement$^{(242)}$ in which ^{209}Bi was bombarded with 610 MeV ^{86}Kr ions is shown in Fig. 5.19. The angular correlation of one of the fission fragments, in coincidence with a projectile-like fragment, was measured both in-plane and out-of-plane. Classical arguments tell us that the fission fragments should be most intense in the plane, if the target-like fragment has a large angular momentum perpendicular to the reaction plane. The out-of-plane correlation for the fission fragments depends on the quantum number K, the

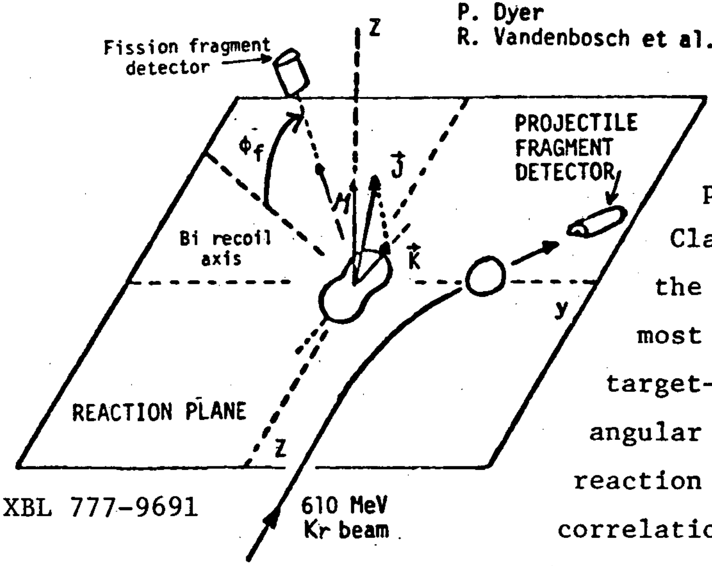

P. Dyer
R. Vandenbosch et al.

XBL 777-9691

Fig. 5.19

projection of the total angular momentum on the symmetry axis of the fissioning nucleus. Then,

$$\text{Yield} \propto \sum_{JMK} P(J)\ P(M)\ P(K)\ W^J_{MK}(\phi) \tag{5.29}$$

where

$$W^J_{MK}(\phi) \propto (2J+1)\ |d^J_{MK}(\phi)|^2 \tag{5.30}$$

The distribution P(K), P(M), and P(J) represent the probability for finding the system with these quantum numbers. P(K) can be determined from independent fission experiments. As a first estimate we can also assume complete alignment, so P(M) = P(J) with M = J. To determine P(J), the probability that a target-like fragment has angular momentum J, is the goal of the experiment. Assuming that the amount of angular momentum transferred, J, is proportional to the initial orbital momentum ℓ,

$$P(J) \propto (2J+1)$$

(because the partial deeply-inelastic cross section $\sigma_{DI}(\ell) \propto (2\ell+1)$). The distribution has an upper limit J_{max} to be determined.

The results are shown in Fig. 5.20, and indicate that $J_{max} = 58\hbar$, from a simultaneous fit to the in-plane and out-of-plane correlations. For the ^{86}Kr + ^{209}Bi system, the *fraction* of the initial orbital angular momentum transferred is 0.29 ℓ_i for sticking. The value of ℓ_i in this reaction is 235ħ and therefore the measured value of J = 58ħ is close to the sticking limit of 68ħ. This experiment is a refinement on the previously described γ-ray experiment, because in principle it could determine *the angular momentum associated with one of the fragments.* Now the angular momentum is divided between the fragments as follows:(243)

$$\text{For sticking:} \quad \frac{J_1}{J_2} = \left(\frac{M_1}{M_2}\right)^{5/3} \tag{5.31a}$$

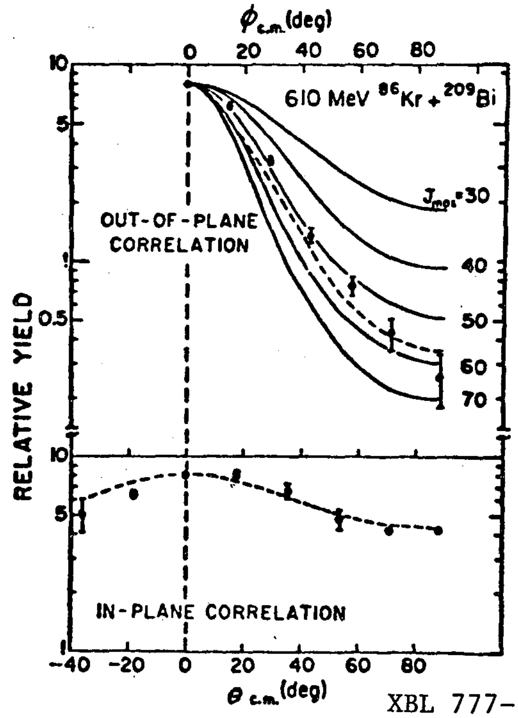

XBL 777-9659

Fig. 5.20

$$\text{For rolling:} \quad \left(\frac{J_1}{J_2}\right) = \left(\frac{M_1}{M_2}\right)^{1/3} \tag{5.31b}$$

As the asymmetry becomes larger, this becomes a highly sensitive method for distinguishing between rolling and sticking (e.g., $^{16}O + Pb$ gives the ratio $(J_1/J_2) = 66$ and 12.5 respectively).

In making dynamical calculations of the quantities discussed above, it is necessary to write down the equations of motion with all the conservative and dissipative forces included and solve them. These equations have the form:(183,184)

$$\mu \frac{d^2 r}{dt^2} = \frac{z_1 z_2 e^2}{r^2} - \frac{d}{dr} V_{nuc} + \frac{\ell^3}{\mu r^3} - k \frac{dr}{dt} \int \rho_1 \rho_2 \, d^3\tau \tag{5.32}$$

where the terms on the right-hand side are, respectively, the Coulomb, nuclear, centrifugal and frictional forces (in the form that we discussed above).

$$\frac{d\ell}{dt} = \frac{dJ_1}{dt} + \frac{dJ_2}{dt} \tag{5.33}$$

where J_1 and J_2 are the intrinsic angular momenta of the two ions, and

$$\frac{dJ_1}{dt} = k \int \rho_1 \rho_2 \, d^3\tau [(\dot{\theta} R - \dot{\theta}_1 R_1 - \dot{\theta}_2 R_2) \, R_1 - g^2(\dot{\theta}_1 - \dot{\theta}_2)] \tag{5.34}$$

(with a similar equation for J_2); the two terms in the square brackets correspond to the sliding and rolling friction.

These equations have been solved for the Kr + Bi case using a tangential friction component which was very weak compared to the radial component(244) and resulted in a total angular momentum transfer to *both* fragments of only 38ħ, considerably below the experimental value.

5.5 *Time Scales*

Coincidence experiments have also been performed with emitted light particles such as protons and alphas.(245) These give us further insight into the time scales of the reaction.(172) The time scale for fragments to move together and apart in a heavy-ion reaction can be estimated from the ratio of the radial momentum and the Coulomb force:(213)

$$\tau_{DI} \approx \frac{2\mu v}{F_{Coul}} \approx \frac{\sqrt{2}\,\hbar \ell}{E_{Coul}} \tag{5.35}$$

Considering the rotational motion, we have an angular velocity ω and an angle of rotation θ through which the fragments remain in contact. Therefore:

$$\tau_{DI} \approx \theta/\omega \tag{5.36}$$

Values of E_{rot}, ℓ and $\mathscr{J}$ can be estimated, so we can use

$$\omega = \frac{2E_{rot}}{\hbar\ell} \qquad \text{or} \qquad \omega = \frac{\hbar\ell}{\mathscr{J}} \tag{5.37}$$

to obtain ω. For example, a reasonable estimate of ℓ is $5/7\ \ell_i$, corresponding to rolling fragments, and $E_{rot} = E_{CM} - E_{Coul} + Q$. A typical rotation angle is $\theta \approx 1$ radian. Both estimates of τ then lead to values for most experiments studied of $4-20 \times 10^{-22}$ sec.

We can also estimate the time it takes an equilibrated excited nucleus to emit a particle. An empirical fit to the measured widths of compound nuclei for A = 20-100 yields:(114)

$$\Gamma(\text{MeV}) = 14 \exp(-4.69\sqrt{A/E^*}) \tag{5.38}$$

Relating the temperature T to the excitation energy by $E = aT^2$, where $a \approx A/8$, we have

$$\tau_{particle} \approx 0.5 \exp(13/T) \tag{5.39}$$

where T is in MeV and τ in units of 10^{-22} sec. An excitation energy of 1.2 MeV/A yields a temperature of 3 MeV and a lifetime of 4×10^{-21} sec. The quantities ω, τ, E^*/A, and T are related in Fig. 5.21 for an angular rotation of 1 radian. We see that if local temperatures of $\approx$3-5 MeV, i.e., excitation energies of 1-4 MeV per nucleon should be produced in deeply-inelastic collisions, then the lifetime for particle emission will be sufficiently short that the rotating dinuclear complex will emit particles before it scissions. We

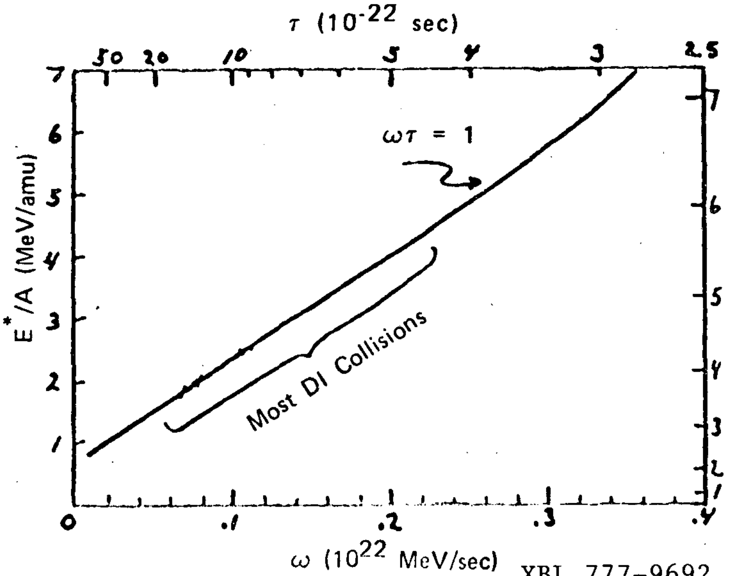

XBL 777-9692

Fig. 5.21

say *local* temperatures because *total* center of mass energies in deeply-inelastic experiments are < 10 MeV per *projectile* nucleon, and therefore the achievement of, say, 3 MeV/nucleon in some region requires a concentration of energy into a "hot-spot."(246-249) (The above discussion is based on Ref. 172.)

An experiment with this general philosophy in mind, used the $^{58}Ni + ^{16}O$ reaction at 92 MeV to study the angular correlation between alpha particles and deeply-inelastic scattering products.(250) The correlation is shown in Fig. 5.22, revealing a pronounced forward angle peaking, in dramatic contrast to the *isotropic* distribution expected from the classical equilibrated rotating nucleus. The interaction time $\tau_{DI} \approx \theta/\omega$ can now be estimated (using for θ the value $2\sigma_\theta$ where σ_θ is the standard deviation of the angular distribution of Fig. 5.22, and $\ell \approx 33\hbar$), $\tau_{DI} = 20 \times 10^{-22}$ sec. From Fig. 5.21 such a lifetime corresponds to a local temperature of 3.3 MeV. A statistical analysis of the alpha particle energy spectra observed in the experiment ($d\sigma \propto \exp(-E_\alpha/T)$) also yielded temperatures of 3-4 MeV for alpha particles emitted in the forward direction. Now using the expression $Ex = aT^2$ and the value of Ex extracted from the experiment of approximately 28 MeV, the value of $a = N/8$ yields $N \approx 18$ particles. (For a *fully equilibrated* system $N \approx 70$ and the temperature would have been only 1.8 MeV.) Such experiments can lead to a determination of the thermal conductivity and specific heat of nuclear matter.(249) Estimates of these quantities were made as early

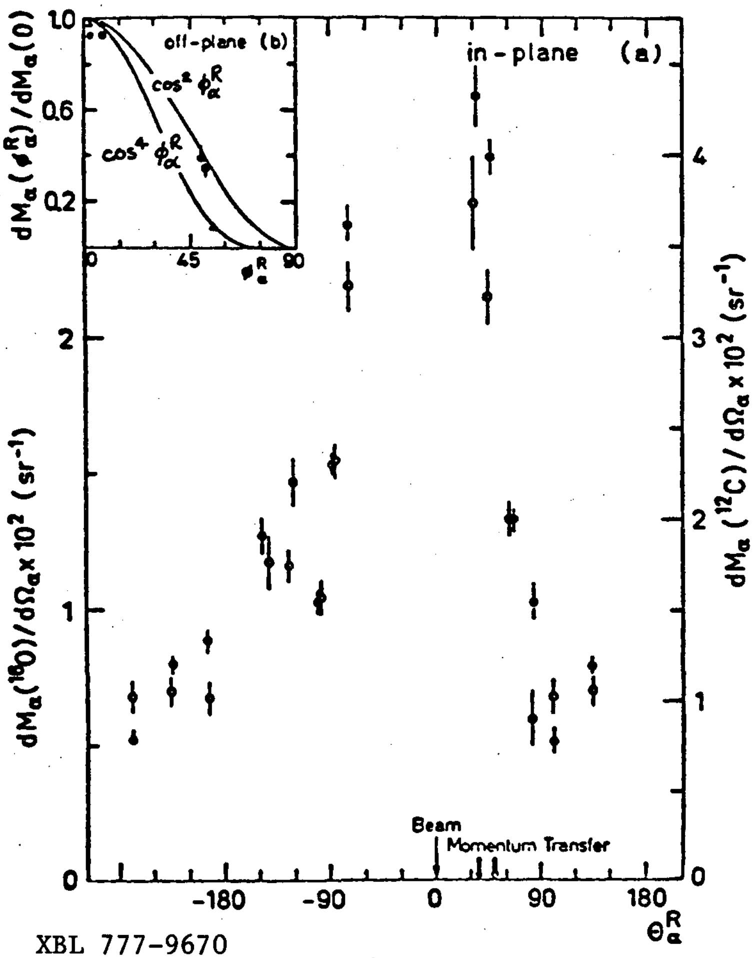

XBL 777-9670

Fig. 5.22

as 1938.(251)

A possible mechanism for the production of fast, non-equilibrium α-particles is the strong radial friction damping force, which ejects a particle on the opposite side of the nucleus from where the projectile and target first make contact (see Fig. 5.23).(252) This leads to a correlation with the α and the heavy fragment on the *same* side of the nucleus which could be consistent with the above experiment. Another possibility is illustrated in part (b) of the figure, which by similar arguments would attribute the α-production to strong *tangential* friction, certainly essential as we have seen to account for the results of γ-ray multiplicity and the fission fragment experiments. In the next chapter we begin to take the time scale of the reaction to still shorter values, and we shall see that, indeed, Fig. 5.23(b) may represent a possible process.

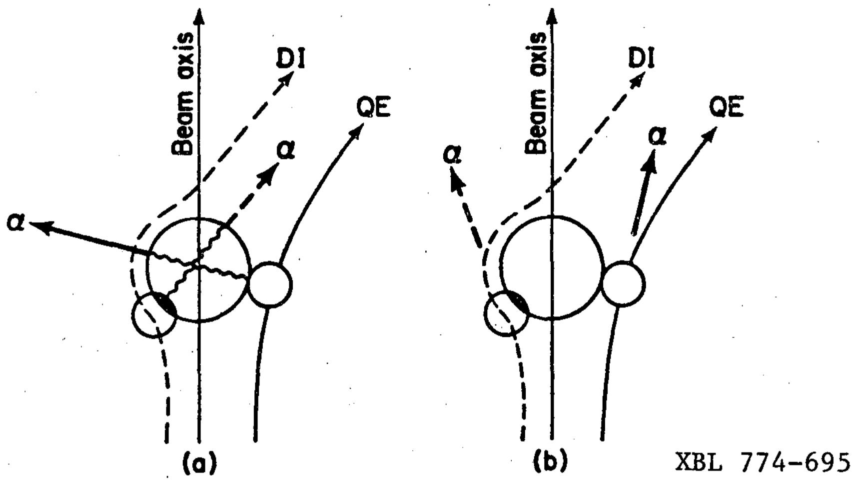

Fig. 5.23

6.

HEAVY ION REACTIONS FROM MeV/A to GeV/A

6.1 Introduction

In this chapter we return to the navigation chart of Fig. 1.2 with its characteristic landmarks to guide us over a vast new area of nuclear phenomena. Some possibilities for exploring the space away from the axes have always existed in the form of Nature's own accelerators, the Cosmic radiation, but it is the advent of laboratory facilities capable of accelerating heavy nuclei up to the GeV/nucleon region that has sharpened and focused the study of nuclear matter under extreme conditions of temperature and pressure.$^{(253-257)}$ An illustration of the facilities existing, or on the point of existing, is given in Fig. 6.1. The present Bevalac facility accelerates ions up to Fe from energies of 250 MeV/A to 2 GeV/A, and with the proposed improvement, the energy range will be broadened to encompass from 30 MeV/nucleon upwards across the whole mass range. Furthermore, the Berkeley and Texas A&M Cyclotrons have succeeded in accelerating heavy ions in the region of ^{16}O to 20 MeV/A, so that it is already possible to trace the evolution of heavy-ion reaction mechanisms across some of the critical boundaries of Fig. 1.2.

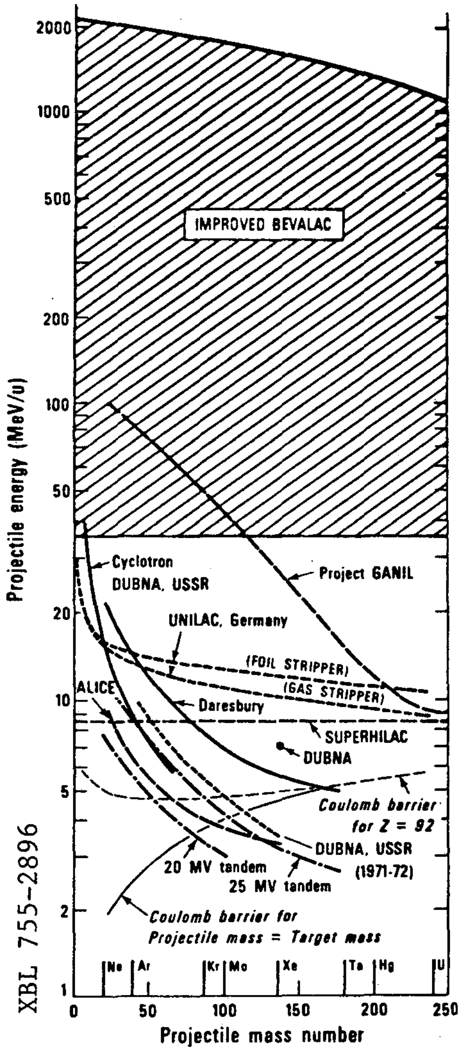

Fig. 6.1

6.2 *The Evolution of Peripheral Collisions with Energy*

Some characteristic times for heavy-ion collisions are displayed in Fig. 6.2, as a plot of collision energy versus mass.$^{(258)}$ The passing time for two heavy ions of radius R_1, R_2 and relative speed $v_p = \sqrt{\frac{2(E-V)}{\mu}}$ is

$$t_p \approx 2(R_1 + R_2)\sqrt{\frac{\mu}{2(E-V)}}$$

so that different reaction times appear as as set of radial lines on the plot. As we have seen in the previous chapters the region up to a few times 10^{-22} is characterized by a variety of direct reaction and partial equilibration phenomena. The bold line at 20 MeV/A, $v = 0.2$ c, corresponds to the first shaded area on Fig. 1.2; this energy is typical of the average Fermi energy

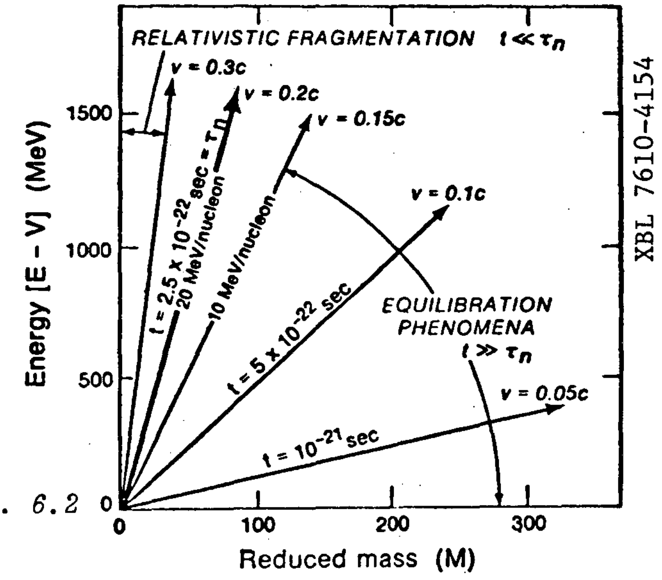

Fig. 6.2

of a nucleon in the nucleus. Beyond this region, peripheral collisions are characterized by rapid processes such as projectile fragmentation, and equilibration phenomena are less important.(259) The energy of 20 MeV/A also defines the threshold of the supersonic region where particle velocities exceed the velocity of sound in nuclear matter. Energy spectra(178,179) for reactions of ^{16}O on ^{208}Pb at 20 MeV are shown for a variety of reaction products in Fig. 6.3. The spectra have a strong quasi-elastic peak centered at energies close to, but slightly lower than, the energy of the product traveling with the beam velocity (labeled E_p). These peaks therefore could correspond to transfer reactions to a high density of states in the continuum(260,261) (i.e., an extension of the transfers to discrete states (compare Fig. 2.17)) with an optimum Q-value(262) (see Fig. 2.9(b)). Or they could be an early stage of the equilibration process(209) in deeply-inelastic scattering (compare Figs. 5.3 and 5.4). In order to build a conceptual bridge to the phenomena of deeply-inelastic scattering, we discuss some characteristic systematics of isotope production cross sections.

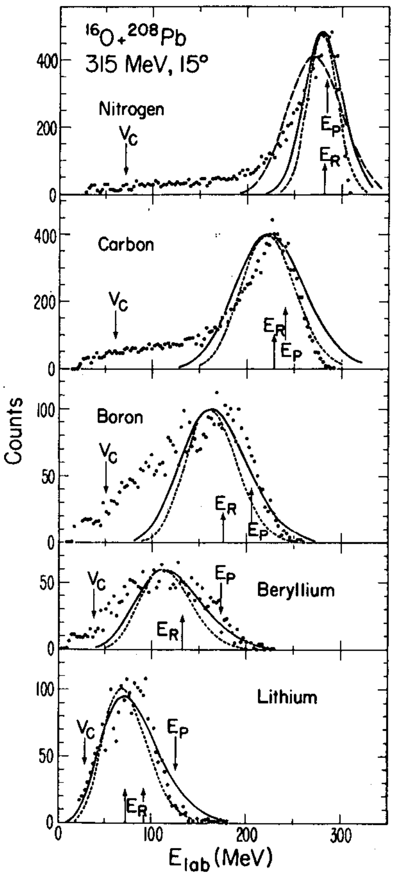

XBL 776-1141 A

Fig. 6.3

Figure 6.4 is a plot of the isotope production cross sections(211,212) versus the ground state Q-value for reactions of ^{16}O on ^{232}Th at 137 MeV. The cross sections were obtained by integrating continuum spectra similar to those of Fig. 6.3. The exponential dependence on Q_{gg} *over 5 orders of magnitude* would *not* be expected from a simple direct reaction model(263) relating the cross section to the Q-value at the *peak* of the distribution, which might well be 50 to 100 MeV more negative. These systematics do, however, have an interpretation in terms of a rotating dimolecular system, undergoing partial statistical equilibrium.(211,212,263,264)

In a statistical reaction the cross section is given by:(263)

$$\sigma \propto \rho_f(E^*) \cdot \propto \exp \frac{E^*}{T} \qquad (6.1)$$

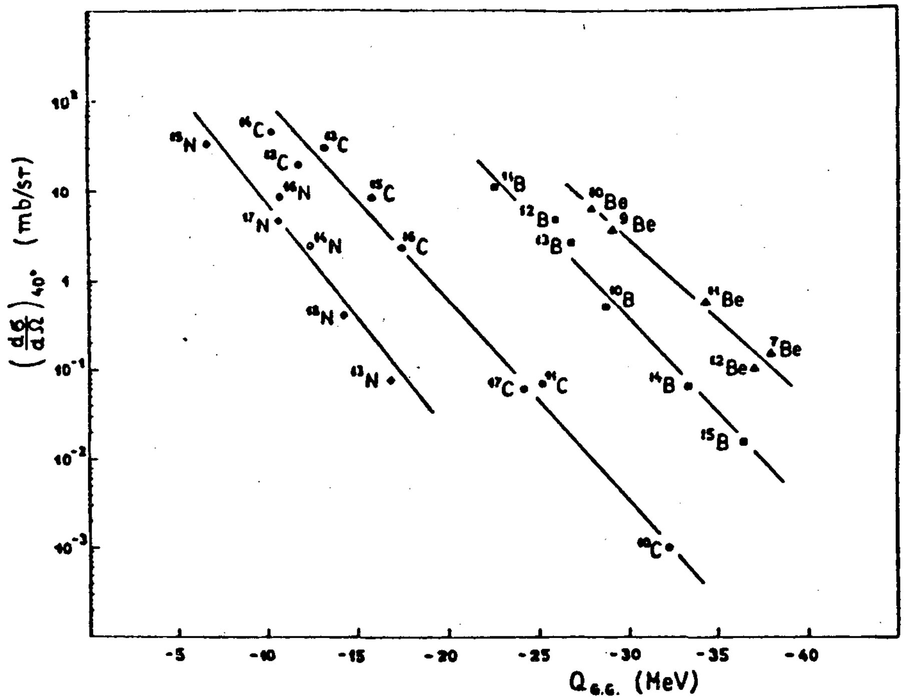

XBL 777-9668

Fig. 6.4

proportional to the level density of states at excitation E*, where T is the system temperature. The excitation energy can be written

$$E^* = Q_{gg} - Q \tag{6.2}$$

and the Q-value is made up of the change in Coulomb energy due to the transfer, the change in rotational energy and other excitation processes. Therefore

$$\therefore \sigma \propto \exp \frac{Q_{gg} - \Delta V_c}{T} \tag{6.3}$$

where we have included only the Coulomb term in Q, since some of the other terms are not coupled strongly to the degrees of freedom which take part in the statistical equilibrium.(263) This is just the expression required to explain the exponential dependence on Q_{gg} in Fig. 6.4, with a displacement between lines for successive charge transfer due to ΔV_c. The temperatures derived from the slopes are typically 2 MeV; this value is slightly higher than an equilibrated temperature for the mass 248 system at this energy, of ≈ 1.2 MeV, indicating *partial* equilibrium. It is intesting that these systematics can also be explained with a model of particle-hole excitations in the neck between the colliding nuclei.(265)

The data of Fig. 6.3, together with measurements on the same reaction ^{16}O + Pb at a lower energy of 140 MeV and a *much higher energy of*

33.6 GeV,$^{(266)}$ are displayed in this Q-value plot in Fig. 6.5. At 140 MeV the systematics are obeyed (although the data are much poorer and less extensive than those of Fig. 6.4), whereas the exponential dependence begins to fail at 20 MeV/A (315 MeV) and becomes totally irrelevant at 2.1 GeV/A, where some of the slopes have the opposite sign. As we discussed in the Introduction, equilibrating dimolecular systems are not likely to play a role at these relativistic energies. When we compare the ratios of the cross sections at 140 and 315 MeV, and at 315 MeV and 33.6 GeV in Fig. 6.6, it appears that at the two highest energies the *element* production cross sections are almost invariant, and therefore it is tempting to see if the 20 MeV/A data do not fit better into the relativistic fragmentation mould, of which Figs. 1.2 and 6.2 give intimations, particularly as an attempt to understand the continuum distributions as two-body transfer reactions (the dashed lines in Fig. 6.3) with the formulae of Chapter 2 (Eq. 2.19) is also apparently not relevant.$^{(178)}$

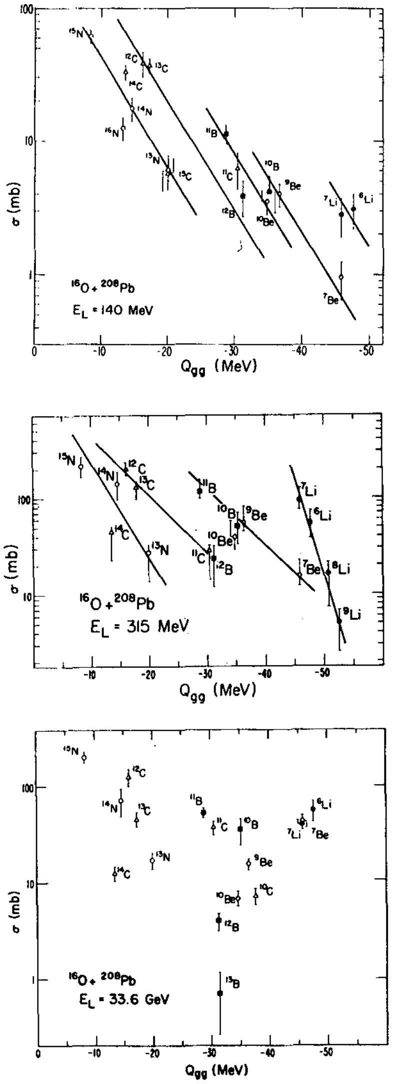

XBL 7610-4957

Fig. 6.5

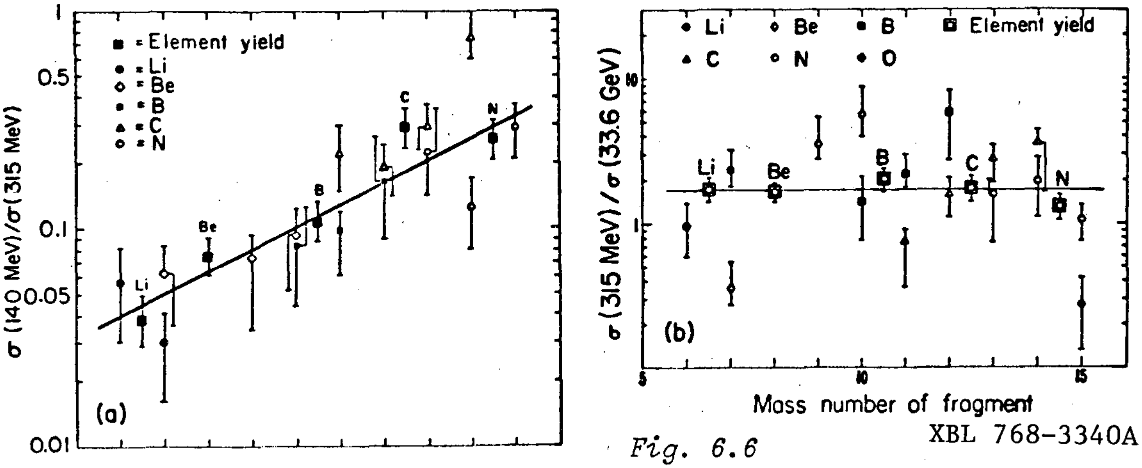

Fig. 6.6

XBL 768-3340A

6.3 Projectile Fragmentation Reactions

Continuum spectra of the type shown in Fig. 6.3 are also characteristic of projectile fragmentation reactions at relativistic energies,(259) as Fig. 6.7 shows. Here the spectrum is plotted in the projectile rest frame, so that a fragment emerging with beam velocity would correspond to $P_{\parallel} = 0$, where $P_{\parallel}$ is the longitudinal momentum in the projectile frame. In fact, just as in Fig. 6.3, the Gaussian-shaped distributions are shifted slightly below this point. In both energy regions this shift is well accounted for by the separation energy of the projectile into the observed fragment together with residual nucleons and alpha particles(267) (the arrows E_F in Fig. 6.3). In a fragmentation model these spectral distributions are governed(268) by the nucleon momenta in the projectile and have the form:

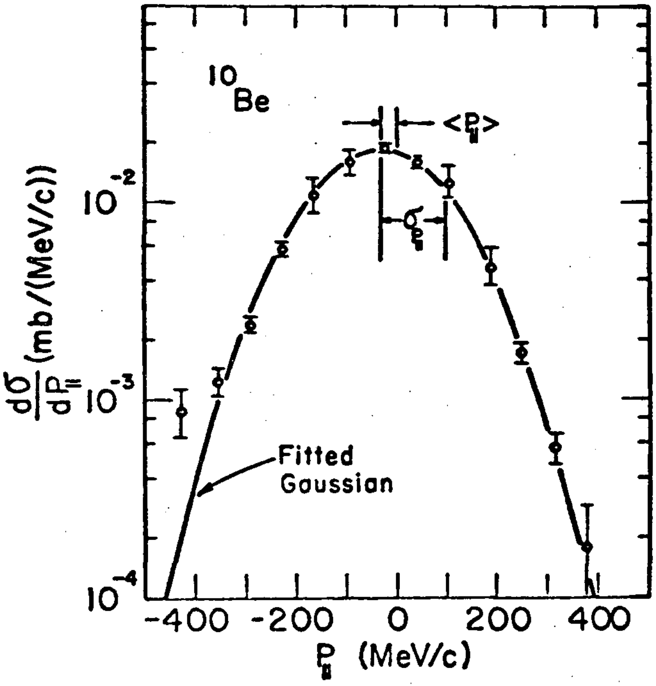

Fig. 6.7

$$\frac{d^3\sigma}{dp^3} \approx \exp - \frac{(p - p_0)^2}{2\sigma^2} \tag{6.4}$$

where p_0 is the momentum corresponding to the peak of the distribution, of width:

$$\sigma^2 = \sigma_0^2 \frac{F(A - F)}{(A - 1)} \tag{6.5}$$

F,A are the masses of the observed fragment and the projectile respectively. This value of σ^2 is just related to the mean square momentum of F nucleons in the projectile suddenly going off as a single fragment. Not surprisingly, therefore, it is also closely related to the Fermi momentum by $p_F = \sigma_0\sqrt{5}$ which has been measured as 235 MeV/c for ^{16}O. The analysis of the heavy-ion spectra yields σ_0 = 80 MeV/c or p_F = 192 MeV/c. However, it is not necessary that the fragment be liberated in this fast process. From the momentum spectrum alone it is not possible *to distinguish the alternative process of projectile excitation to an equilibrium temperature T, followed by a slow evaporation of the fragment.*(269-271) The two formulations are related by:

$$\sigma_0^2 = m_n T \frac{A - 1}{A} \qquad (6.6)$$

where m_n is the nucleon mass. The value of T = 7.8 MeV is derived for ^{16}O on ^{208}Pb. This latter approach has the elegant consequence that the *production cross sections* of isotopes can be predicted on the basis of systematics rather similar to those discussed above, *but in which the fragment emitter is now the projectile rather than the dinuclear complex.*(271) In this case,

$$\sigma(N,Z) = c \sum_i \exp\left(\frac{Q_i}{T}\right) \qquad (6.7)$$

where c is a universal constant for the reaction, Q_i are the Q-values for the various projectile fragmentation channels, and T is the temperature for which, to be consistent with the spectra analysis, we choose a value close to 7.8 MeV. The quantity c, derived from the above equation is plotted in Fig. 6.8 for the data at the three energies. For the data at 20 MeV/A and 2.1 GeV/A, the quantity c is *reasonably constant using a temperature of approximately 7 MeV.* The spectral distributions calculated with these parameters are shown in Fig. 6.3 and give an astonishingly good account of all the data.(272) Furthermore, the expression for the momentum distribution can be transformed into the laboratory frame yielding in an obvious fashion:

$$\frac{d^3\sigma}{dp^3} \to \frac{d^2\sigma}{dE_L d\Omega} \sim \sqrt{2M_F E_L} \times \exp\left[-\frac{M_F}{\sigma^2}\left(E_L - 2aE_L^{\frac{1}{2}}\cos\theta + a^2\right)\right] \qquad (6.8)$$

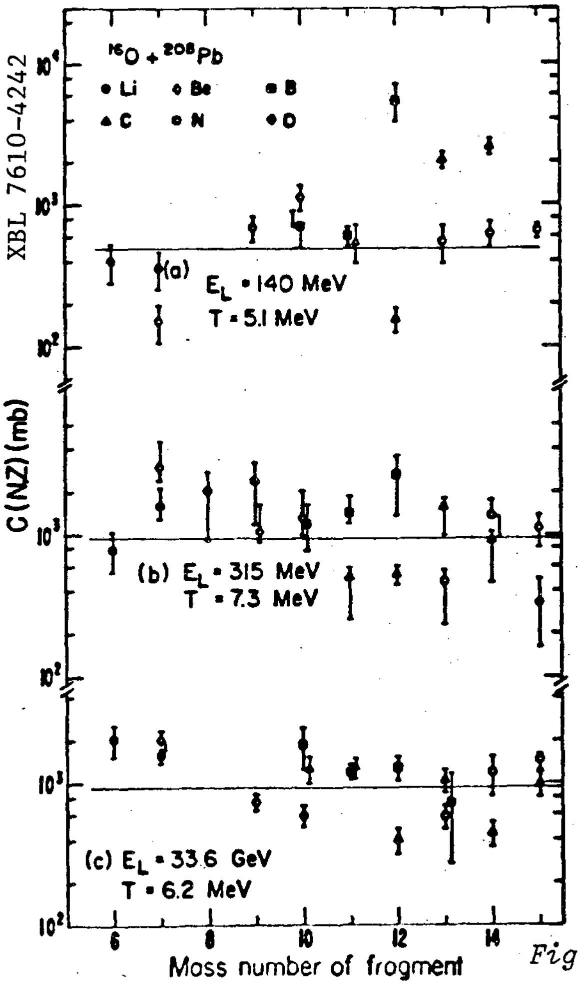

Fig. 6.8

where $a^2 = \frac{1}{2} M_F v_R^2$, and v_R is the velocity of the projectile frame approximately. More accurately it is the velocity corresponding to the peak of the energy distribution. These differential cross sections(272) are compared with experiment in Fig. 6.9, again giving a reasonable account of the evolution from steeply falling curves for fragments close to the projectile to the flattening for lighter fragments, for which the reduced longitudinal momentum allows the transverse momentum associated with the Fermi motion to scatter to wider angles. The solid lines were calculated with σ_o = 103 MeV/c (appropriate for the Fermi momentum) and the dashed lines used σ_o = 80 MeV/c corresponding to T = 7.3 MeV as required to explain isotope production cross sections. It is intriguing to note that this pattern of cross sections is very similar to those of Fig. 5.3 for deeply-inelastic reactions, where the flattening of the distribution for products far removed from the projectile was attributed to increased rotation of the dinuclear system. (The relationship of these approaches and the transition between them is left as an exercise in thought for the reader!)

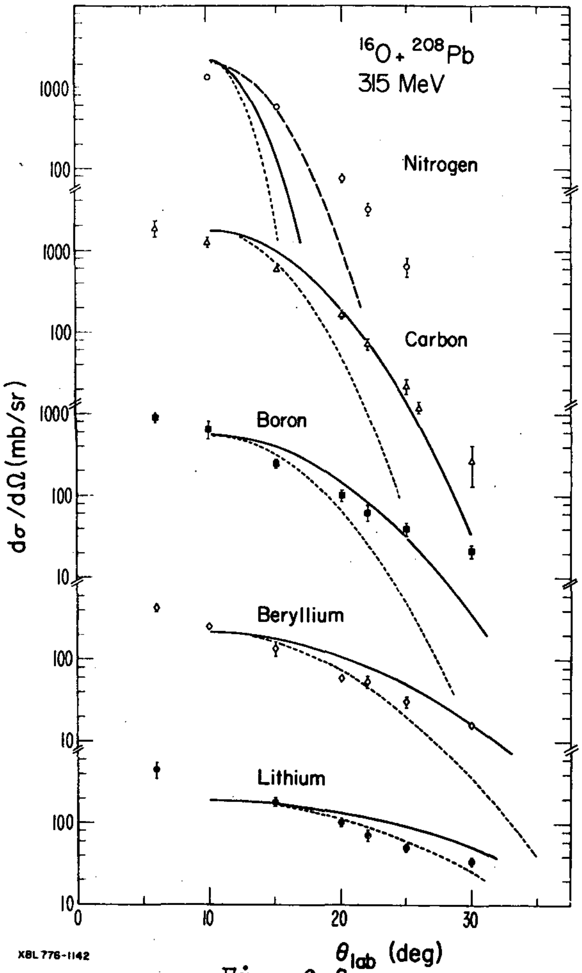

XBL 776-1142

Fig. 6.9

There are other similarities between the data at 20 MeV/A and at 2.1 GeV/A. For example, a logical consequence of Eq. (6.7) is that yields should depend only slightly on the target nucleus (which is a "spectator"), assuming that T does not vary too much for the high excitations and energies involved. The implication is that the cross sections *factorize*(273-275) into a projectile and target term:

$$\sigma_{AT}^F = \sigma_A^F \gamma_T \qquad (6.9)$$

This result does not follow from Eq. (6.3), since there are substantial ground state Q-value differences between different targets, and would lead typically to an order of magnitude change of cross section between Pb and Au targets. The factorization is indeed found to be valid at both 20 MeV/A and 2.1 GeV/A, but not at the lower energy of 140 MeV.(273-276)

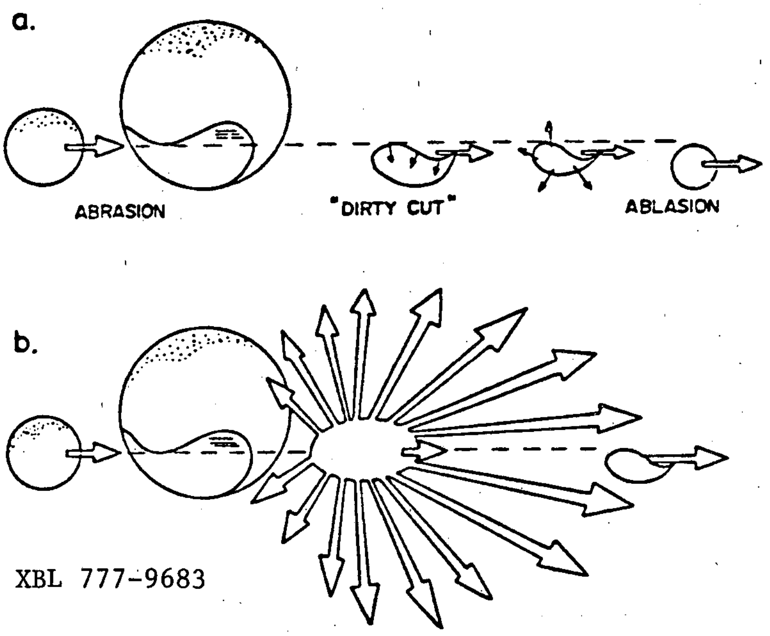

XBL 777-9683

Fig. 6.10

These similarities should not be taken to imply that nothing happens between 20 MeV and 2 GeV per nucleon. The two approaches outlined above, namely fast liberation of the cluster by fragmentation, or the slow statistical decay of an excited projectile, have been combined into the more formal approach of the abrasion-ablation model,(277-279) outlined schematically(256) in the top part of Fig. 6.10. The ^{16}O nucleus in the region of overlap with the target has a part sliced out.(280) The cross section for this process (abrasion) can be calculated using Glauber theory(281) or (next section) from geometrical considerations. The cut is not "clean" but creates a hot region which causes the subsequent fragment to be highly excited so that it proceeds to evaporate additional fragments (ablation). In the Glauber model at high energies the nucleus-nucleus cross section for an event in which n projectile nucleons are scattered from the projectile A is:

$$\sigma_n = \binom{A}{n}\int d^2\underline{b}\,(1-P(b))^n\,P(b)^{A-n} \qquad (6.10)$$

where

$$P(b) = \int dz\, d^2\underline{s}\,\rho_A(s-bz)\,\exp[-A_T\sigma_{NN}\int dz'\,\rho_T(s,z')] \qquad (6.11)$$

Here $(1-P(b))$ is the probability of finding a projectile nucleon in the overlap zone when b is the impact parameter. Equation (6.10) is then the cross section for n projectile nucleons to be in the overlap and $(A-n)$ outside. It turns out that σ_n changes very little between 20 MeV/A and 2 GeV/A in spite of a large change in σ_{NN}. However, at high energies the momentum transfer is sufficient to knock nucleons out, but at low energies they appear to stay in the prefragment and deposit their energy. The subsequent fate of the projectile fragment (the ablation stage) is rather different in the two cases. This model(283) appears to account both for the isotope differences and the element similarities in Fig. 6.6.

The consequence of the abrasion-ablation model for both regimes, however, is the existence of an initial heated zone. It is attractive therefore to speculate that the high equivalent temperatures of 8 MeV are to be associated with a small region of the interacting nuclei or "hot-spot."(246-250) The temperature of 8 MeV may then represent a natural limit for the observation of complex fragments, since it corresponds roughly to the nucleon binding energy in nuclear matter, and higher temperatures would lead to an explosion of the fragment. This study of the evolution of the reaction mechanism indicates that an increasing concentration of the energy takes place in a small region of the nucleus at 20 MeV/A and at higher energies in contrast to the almost equilibrated distribution observed in deeply-inelastic collisions at lower energies.

Evidence for a "hot-spot" with T ≈ 3 MeV was discussed in Chapter 5 (Fig. 5.20) in connection with the pre-equilibrium emission of alpha particles. Angular correlations of α-particles relative to the heavy fragments have also been measured(284) for the ^{16}O reaction on Pb and Au and 140 MeV and 315 MeV (the experimental configuration is shown below in Fig. 6.11) for the heavy-ion fragments in the quasi-elastic peak of the spectra (Fig. 6.3). The correlations are shown in Fig. 6.12, and are even narrower than in Fig. 5.20 (typically 30° FWHM at 20 MeV/A compared to 150°).(250) They peak in the direction of the heavy-ion detector with a double peak in

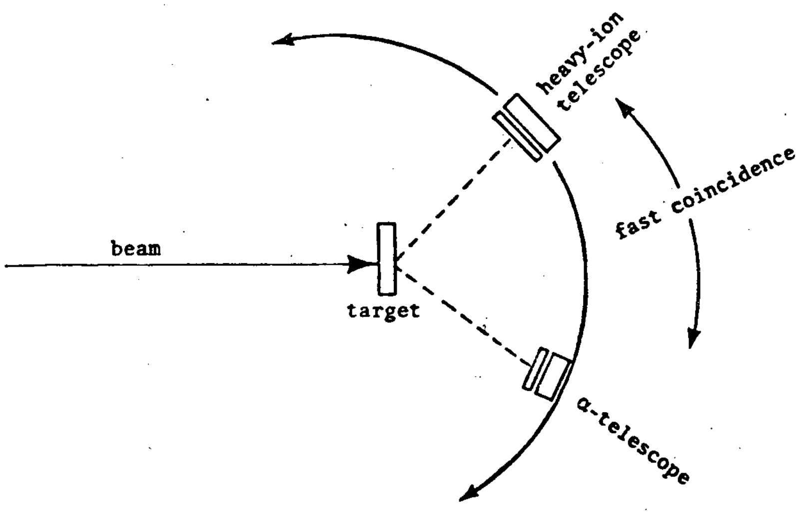

Fig. 6.11

the case of $^{12}C+\alpha$, indicative of projectile fragmentation. However, the correlation patterns for ^{13}C, ^{14}C and ^{14}N *which cannot arise from a simple projectile fragmentation* are very similar in overall shape. The interpretation might be emission of the fragments from the local heated region as illustrated in Fig. 5.22(b). This figure clearly indicates the interest of looking at deeply-inelastic processes in this way at energies in excess of 20 MeV/A — if they still exist.

6.4 More Central Collisions

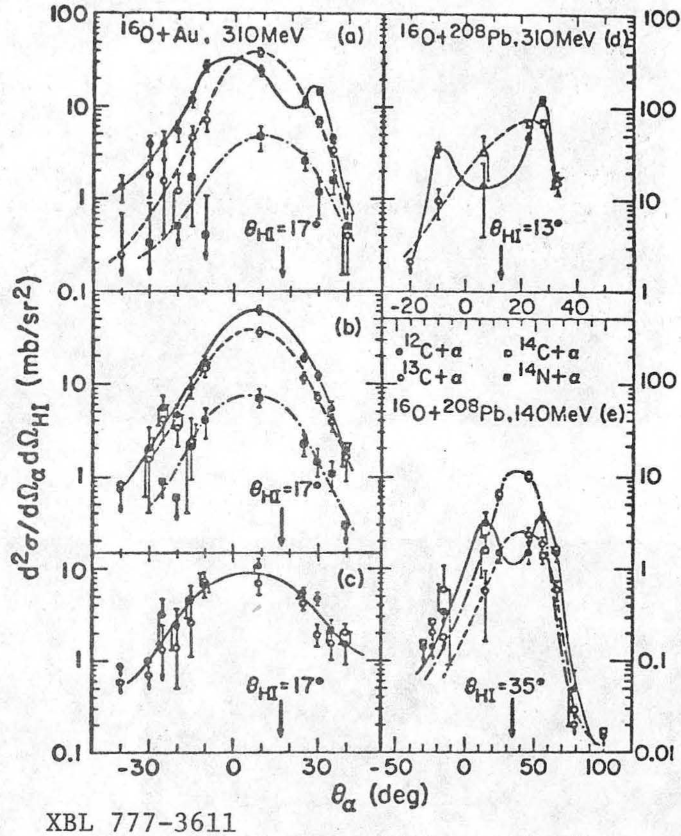

XBL 777-3611

Fig. 6.12

Peripheral collisions leave the bulk of the nuclear matter undisturbed, whereas central collisions lead to much more catastrophic events. An example of each type of collision is given in Fig. 6.13. For the peripheral collision of ^{12}C at 870 MeV/A a small number of particles continue in the projectile direction with high momentum.(285) For the central collision(286) in part (b), there is a star explosion and no projectile remnant is observed close to the zero degree scattering angle. For this system, Ar + Pb at 1.8 GeV/A, the total multiplicity of charged particles ranges up to 130, suggesting that almost all the protons of the incident system are separated, together with a copious production of mesons. Nuclei therefore are not transparent to each other, even at these energies. At lower incident energies we have seen that central collisions lead to fusion or fission processes. Although the nature of the central collision is very different in the two regimes, it appears that the onset of these more catastrophic events takes place at roughly the same overlap of the nuclear matter densities.(166,170) To see this, we write(178,179) the reaction cross section as the sum of peripheral and central cross sections

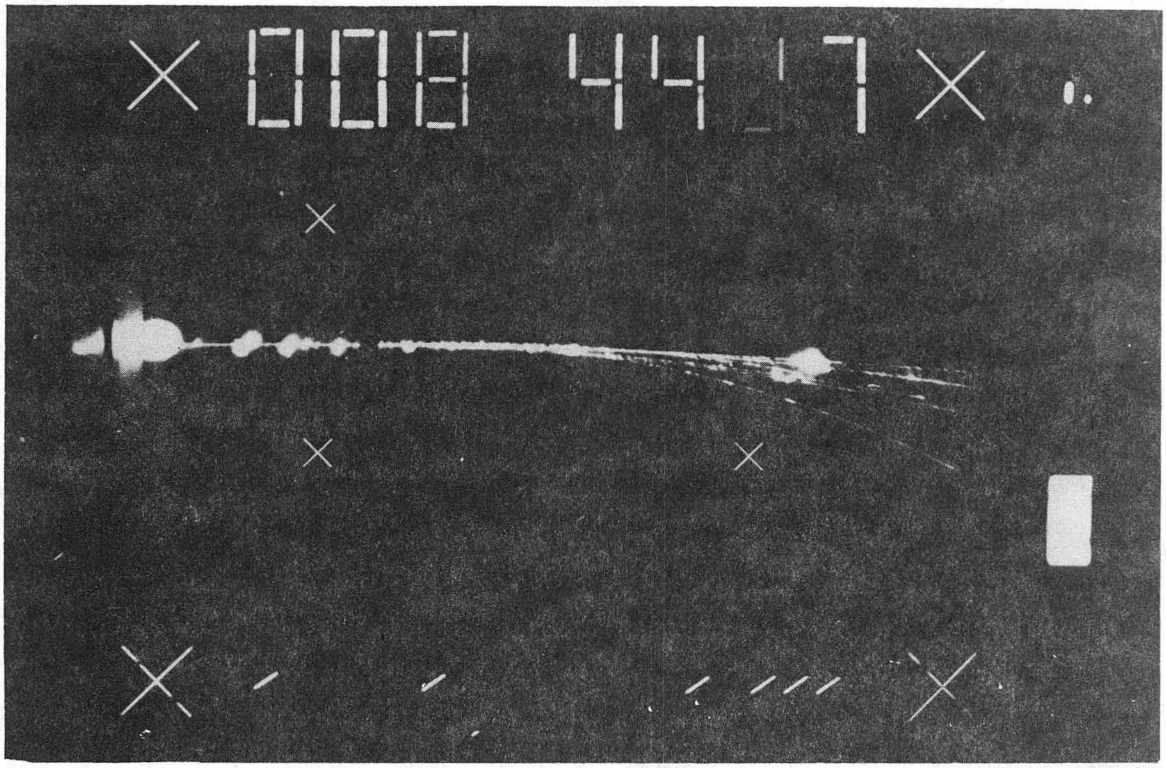

XBB 748-5727

Fig. 6.13(a)

Fig. 6.13(b) XBB 7511-8445

$$\sigma_R = \sigma_P + \sigma_c \tag{6.12}$$

and compare values of σ_c deduced from this equation by subtracting the summed peripheral cross sections of all reaction products in $^{16}O + ^{208}Pb$ at 20 MeV/A and 2.1 GeV/A (last section) from the reaction cross section, which has been measured directly at 2.1 GeV/A and was deduced from the optical model analysis of elastic scattering at 20 MeV/A.

Energy	Reaction	Peripheral σ (mb)	Total reaction σ (mb)	Central σ (mb)
20 MeV/A	$^{16}O + ^{208}Pb$	1295	3460	2160
2.1 GeV/A	$^{16}O + ^{208}Pb$	930	3100	2260

The reaction cross section has also been determined from ^{16}O reactions in emulsions in the energy range 75-150 MeV/A and appears to give similar values.(287) Such an energy independence would not be expected from the known (large) variation of the nucleon-nucleon cross section over the same energy region.(288)

In the central collisions of the type in Fig. 6.13(b), the most exotic features of high-energy heavy-ion collisions will be hidden — one says hidden because they must be separated from the large background of (possibly) trivial effects which are the outcome of the superposition of all the free nucleon-nucleon cross sections, properly folded with the particle distributions of position and momentum. The basic layout of a system designed to make quantitative studies of central collisions is shown in Fig. 6.14, which combines a particle identification telescope to identify a particular particle, with an array of plastic scintillators to determine the multiplicity of charged particles associated with each event.(289) A large multiplicity is used as a signature of a central collision.

Proton energy spectra from Ne and He bombardments of U are shown in Fig. 6.15 for angles of 30°, 60°, 90°, 120° and 150° (except for Ne). The spectra have Maxwellian shapes corresponding to high temperature. These spectra have been elegantly explained with a fireball model,(280, 289) illustrated schematically in Fig. 6.10(b). The model is an extension of the abrasion-ablation picture used previously for peripheral reactions.

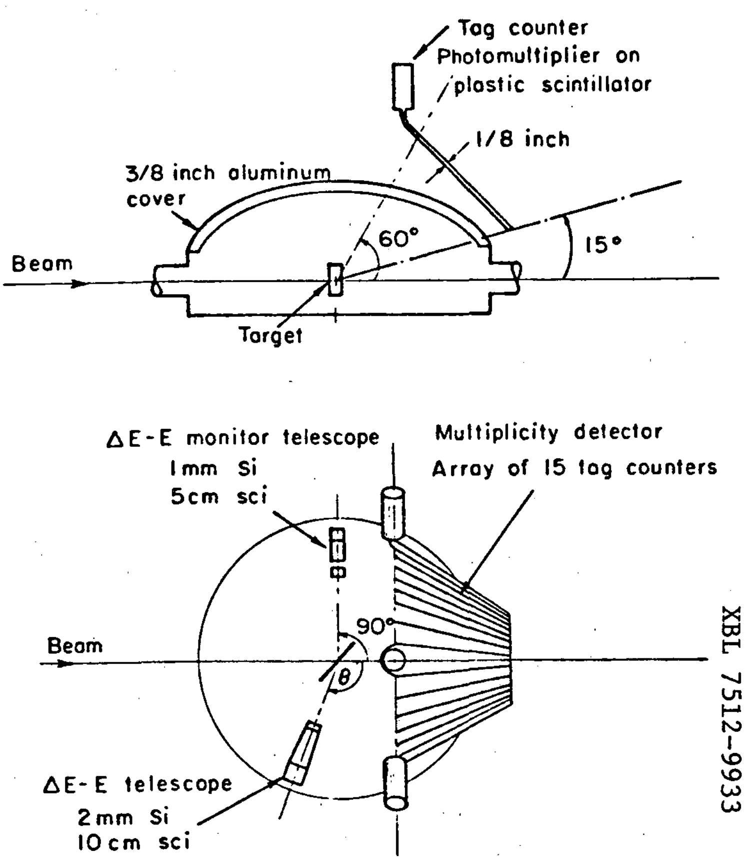

Fig. 6.14

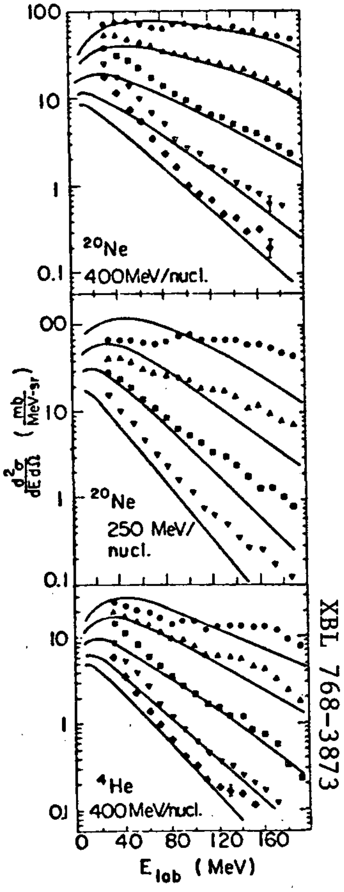

Fig. 6.15

In the more central collision, nucleons swept out from the target and projectile form a quasi-equilibrated fireball at high temperature, equal to the available energy per nucleon. The velocity of the fireball is assumed to be that of the center of mass system of the nucleons swept out. The fireball expands isotropically in its center of mass system with a Maxwellian distribution in energy.

Assuming spherical nuclei and straight-line trajectories, the participating volume of each nucleus is easily calculated as a function of impact parameter. The number of participating protons as well as the division between projectile and target are shown in Fig. 6.16 for Ne on U. At the bottom is the effective weight, 2πbN proton, given to each impact parameter. The velocity of the center of mass of the fireball is then given by

$$\beta_{cm} = \frac{P_{lab}}{E_{lab}} = \frac{N_p[t_i(t_i+2m)]^{\frac{1}{2}}}{(N_p+N_t)m + N_p t_i} \qquad (6.13)$$

where P_{lab} is the lab momentum, E_{lab} the total energy, t_i the projectile

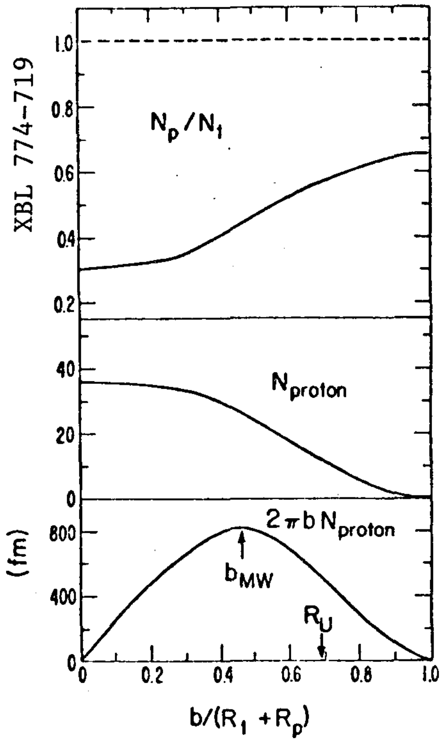

Fig. 6.16

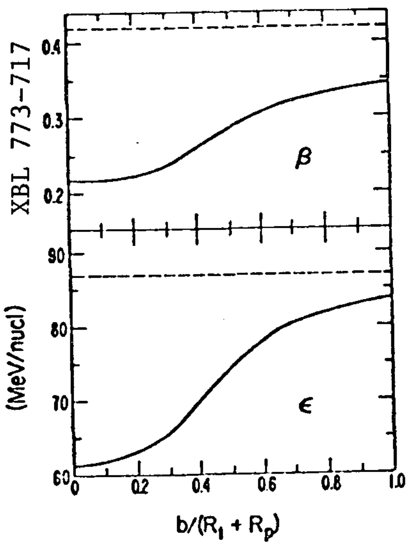

Fig. 6.17

incident energy/nucleon, and m the nuclear mass. The total energy in the center of mass of the fireball is

$$E_{cm} = \left[E_{lab}^2 - P_{lab}^2\right]^{\frac{1}{2}} \tag{6.14}$$

If one assumes there are sufficient degrees of freedom in the fireball, and that there is a mechanism to randomize the available energy, one can define a temperature T, which can be expressed (non-relativistically) by:

$$\varepsilon = 3/2T \tag{6.15}$$

where ε is the available kinetic energy per nucleon in the center of mass, i.e., $E_{cm}/(N_t + N_p)$. The quantities β and ε (calculated relativistically) are given in Fig. 6.17 as a function of impact parameter. The momentum distribution of the fireball nucleons in the center of mass is then:

$$\frac{d^2N}{p^2dpd\Omega} \propto (2\pi mT)^{-3/2} \; e^{-p^2/2mT} \tag{6.16}$$

where p is the momentum of a nucleon in the center of mass. Using the earlier expressions this distribution can be transformed to an energy distribution in the laboratory, which must then be integrated over impact parameter weighted appropriately (Fig. 6.16). The resultant distributions are shown in Fig. 6.15 (typical values of β and T can be derived from Fig. 6.17 at the point of maximum weight ($\beta \approx 0.25$ and $T \approx 50$ MeV). Excellent agreement with the data is obtained and is even further improved by a refined version of the model — the firestreak model.(290)

It is possible to advance further and explain the distributions of other fragments heavier than the proton with a *coalescence model*.(291)

If any number of protons and nucleons corresponding to a bound nucleus are emitted in the reaction with momenta differing by less than a "coalescence radius" p_o (a parameter to be adjusted), they are assumed to coalesce. The cross sections for these heavier nuclei are then trivially related to those for the proton. However, there are also thermodynamic models which extend the fireball concept to the emission of complex fragments.(292)

Fragments from central collisions may originate from several qualitatively different subsystems, such as the fireball, the target spectators, or even an explosion of the fused target projectile system. The detailed distribution of the longitudinal and transverse momenta of all the fragments give information on these subsystems. For this purpose it is convenient to characterize the distribution of longitudinal momentum by the *rapidity variable:*

$$y = \frac{1}{2} \ln \left[\frac{(E + p_{\parallel})}{(E - p_{\parallel})} \right] \qquad (6.17)$$

where E and $p_{\parallel}$ are the total energy and longitudinal momentum of the particle. (This variable is convenient in relativistic systems because it transforms in Galilean fashion in changing frames.) Contour plots of invariant cross sections, which are measured as a function of angle, are transformed to these variables in Fig. 6.18 for ^{3}He fragments in Ne + U.

In a peripheral collision (where we have seen in the previous section that fragments emerge with approximately the beam velocity) there would be a sharp peak at the projectile rapidity — and a corresponding one for the target. Although Fig. 6.18 shows(289) that this situation does not arise in these experiments (in which the multiplicity counters selected more central events) it is clear that the events are not emitted isotropically from *one* moving source, which would give contour lines centered around that rapidity. Recent data (obtained with very different techniques of stacked Lexan foil detectors) give evidence for emission of complex fragments from a source moving with very low velocity (near the target rapidity) at a high temperature.(293) This process may be evident in Fig. 6.19, but it gives clearer indication for the fireball moving with a rapidity intermediate between projectile and target.

An analysis shows that the other source moving with low velocity *and* high temperature cannot be accommodated in the framework of heavy-ion collisions presented in this section. These fragments appear to originate from *non-equilibrium* emission from a system like the *entire* target, when the internal energy does not have to reach the value of 3/2 T per nucleon. Various cooperative or nonthermal processes can be imagined, amongst which are compressional wave phenomena or the release of pre-existing clusters. These considerations lead us on to the last topic of these lectures. It is already clear, however, that experiments of the type discussed here are giving us a glimpse of nuclear matter under unusual conditions.

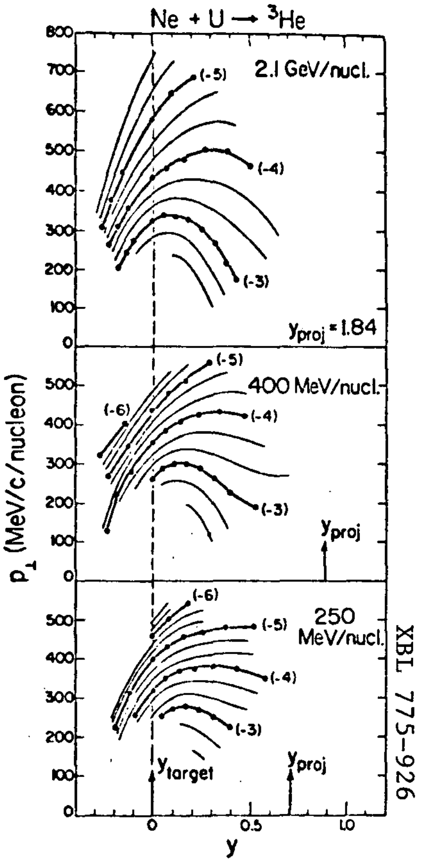

Fig. 6.18

6.5 *More Speculative Aspects*

An important basic question in complex nucleus-nucleus interactions is to what extent they can be traced back to quasi-free hadron-hadron collisions. Is the total energy available in the system, viz. $E_{inc}\ A_1A_2/A_1 + A_2$ GeV, the important quantity or is it just $\approx \left(\sqrt{2(E_{inc} + 2)} - 2\right)$ GeV that is available in $\leqslant A_1$ nucleon-nucleon reactions? The difference between these pictures is important. If we find pion production at 0.1 GeV/A, the former expression must be relevant, and *collective* phenomena are important, and have already been claimed to be observed.(294) Many experiments are in progress, and it is clear that the great majority of events can be easily explained in an independent nucleon-nucleon model.(295) There are also some indications in pion multiplicities for production via strong nucleon correlation effects, which hopefully may be a signature for shock wave effects.(256)

It has been suggested that a compressed zone of high energy density may be formed in a central collision, which propagates as a shock wave and could lead to the emission of energetic fragments upon impinging at the nuclear surface.(296-300) Such a propagation of high compression ($\rho > \rho_0$) and with velocities $v_s > 0.2c$ has been called a "shock wave." The progress of this wave is illustrated in Fig. 6.19. In the initial

NUCLEAR SHOCK WAVES

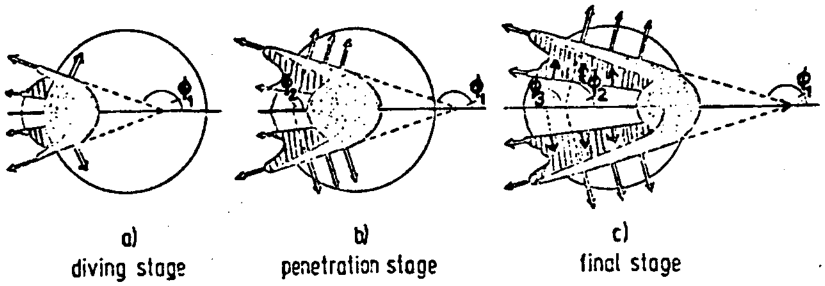

a) diving stage

b) penetration stage

c) final stage

XBL 764-1282

Doubling of nuclear density at 20 MeV/nucleon

Propagation velocity of shock front ≈ 0.2c

Fig. 6.19

phase a "splashing tidal wave" is expected at a backward angle $\sin\phi_1 = v_t/v_i$, where v_t is the expansion velocity of the shock compression zone. In the second stage a strong compression shock is created accompanied by a Mach cone traveling outwards in the direction ϕ_2, $\cos\phi_2 = v_s/v_i$, where v_s is the shock expansion velocity. In the final stage, matter is emitted in the directions ϕ_1 (splashing) and ϕ_2 (Mach).

In reality the projectile would slow down considerably and the simple Mach cone picture is distorted. The emission is then spread out over a wider angular region, which actually appears to be a feature of hydrodynamical calculations of collisions of nuclear matter, treated as a classical compressible fluid. The criterion for compressibility is whether flow velocities are comparable to the speed of sound. For nuclear matter with an incompressibility K(MeV) the speed of sound is:(301)

$$v_s = (K/9\mathrm{mo})^{\frac{1}{2}} \qquad (6.18)$$

and the projectile energy/nucleon above the Coulomb barrier required to reach such a velocity is:

$$E/A = K/18 \qquad (6.19)$$

For typical values of K between 150 and 300 MeV, v_s is derived to be 0.13 and 0.19c, or E/A of 8 and 17 MeV. Apparently compressibility will be important at the relativistic energies we have been discussing. For a hydrodynamic description to be valid, the mean free path of the microscopic particles should be small compared to the macroscopic dimensions. From the known nucleon-nucleon cross section of 40 mb at 2 GeV, we can estimate the mean free path $\lambda \approx 1/\rho\sigma \approx 2$ fm. So the criterion is only marginally fulfilled. The hydrodynamic equations have been solved(302) for collisions of ^{20}Ne on U (the reaction used for the fireball discussion) at 250 MeV/A. Figure 6.20 shows the time development of the density as represented by the distributions of particles, for different impact parameters. For the nearly central collision (labeled 0.1) the neon penetrates into the uranium nucleus and sets off a strong shock wave (clearly visible at 5.1×10^{-23} sec). Subsequently most of the energy of the projectile is thermalized and the nucleus expands. The other two sections illustrate an intermediate impact parameter (which should come close to the fireball description), and a peripheral collision in which we see a part of the projectile sheared off (just as in the abrasion picture). When the angular distributions for central collisions are computed from the distribution of nucleons in the final state they lead to rather featureless exponential forms, similar to the data in Fig. 6.15, with no sharp shock wave peak.

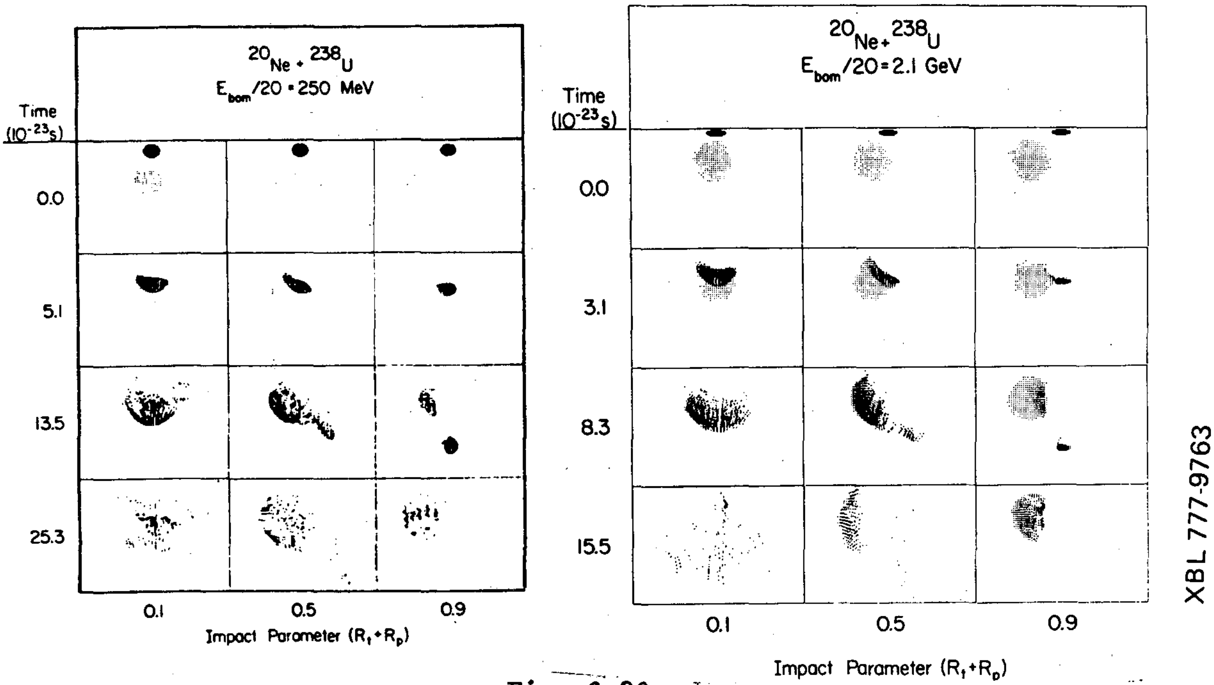

Fig. 6.20

Another way of treating the density problem is by introducing statistical microscopic calculations.(303-305) These make Monte Carlo simulations of colliding samples of almost free point nucleons. The nucleon-nucleon scattering follows the known cross sections, conservation of energy, momentum, and angular momentum. The position and velocity of each nucleon is known (in principle) at each time. These calculations indicate that the transparency effects are too large to give high enough compression to produce shock waves.

Nevertheless, they have been searched for,(306-309) and the first experiments made extensive studies of high multiplicity events in track detectors using AgCl crystals and emulsions. The distributions of $d\sigma/d\theta$ were measured for events with more than 15 prongs, and a typical example(306) appears in Fig. 6.21(b). The sharp peak seemed to shift its position in a way characteristic of Mach shocks withaa propagation velocity

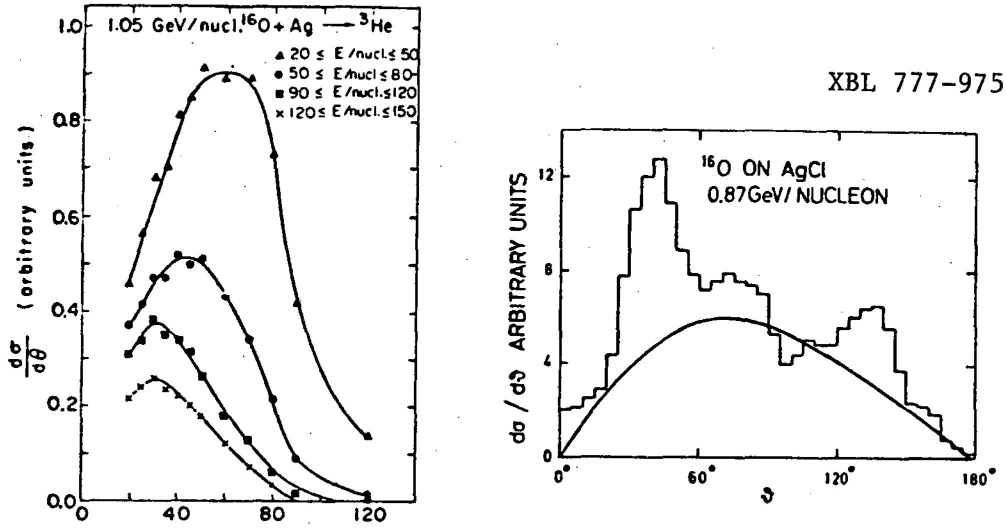

XBL 777-9758

Fig. 6.21

$$v_s = v_i \cos\theta(\text{peak}) \tag{6.20}$$

and the peak moves *backwards* with increasing energy. These peaks have not been found in other emulsion experiments, nor are they present in the differential cross sections obtained with the live counter techniques(308) (Fig. 6.14) which are shown in Fig. 6.21(a). It seems that the peaks are due to combinations of different particle types. However, the explanation of why these peaks move to more backward angles could still have a possible connection with shock-wave phenomena.(310)

Only the first generation of experiments have been completed, which have primarily looked at single particle inclusive spectra. There are many refinements in progress to search for collective effects of nuclear matter at extreme density and pressure — conditions which are also probably realized in the interior of neutron stars. As an indication of some of the exciting possibilities ahead, Fig. 6.22 shows the equation of state. This equation, at densities above twice normal, can be

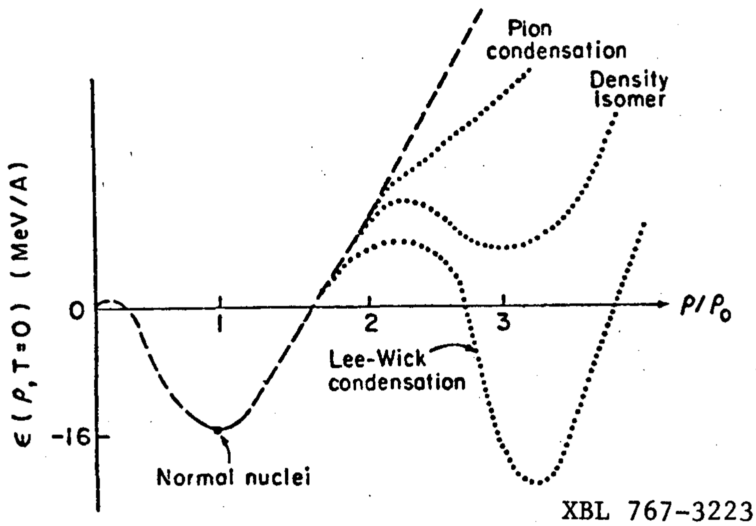

XBL 767-3223

Fig. 6.22

affected by collective phase transitions to Lee-Wick abnormal matter,$^{(311)}$ density isomers or higher order transitions to a pion condensate.$^{(312,313)}$ In the absence of these effects the energy would simply increase monotonically with density. Since the pressure in a hydrodynamic model is proportional to $dE/d\rho$, a possible change to negative slope above twice normal density would imply negative pressure, e.g., condensation to abnormal matter. Furthermore, at the temperatures reached in the collision (from 50 to 100 MeV as we have seen), a large fraction of the nucleons are excited to isobaric states, and there is even evidence that a limiting hadronic temperature has been reached.$^{(314)}$ These topics are all under intense discussion at the present time, and at the next Summer School in this series, it can be hoped that someone will be able to turn the speculation into experimental fact.

6.6 *Envoi*

In these chapters I have attempted to give an overview of current activities in the different areas of nuclear reactions with heavy ions. The approach has been "simple" in the sense that I have tried to write down simple analytic expressions to give an insight to the underlying physical processes. Such treatments are not meant to obscure the fact that the interaction between two complex nuclei is potentially one of staggering complexity, when expressed in a microscopic framework. Indeed, there were many "doubting Thomases" in the early stages of heavy-ion physics who believed the processes to be so complicated that it was hopeless to even imagine a qualitative understanding. But both in the microscopic and macroscopic domain, in the traditional and the new features of these reactions, impressive progress has been made in a remarkably short time. We have only to look at the quality of heavy-ion transfer *data* and the sophistication of our present microscopic reaction *theories* as applied to multistep processes in deformed rare-earth nuclei, to wonder whether our tools would be of poorer quality without the advent of heavy ions.

Researchers all over the world have plunged enthusiastically into heavy-ion research, and this spirit has found its way to the funding agencies and to the machine builders. They have seen this field as fresh territory, calling for new ideas and insights. There is the challenge of unifying high- and low-energy aspects of heavy-ion collisions, and of microscopic and macroscopic approaches. One is reminded of D. H. Wilkinson's comments(315) on the state of nuclear and elementary particle physics in Rutherford's day: "These subjects were simple but not easy. So many zero-order questions had to be answered in order to make even remote sense of what was going on. Such questions still exist, but we have to work in two complicated edifices which generate more complicated questions. I have tried to show that we should recognize that these two edifices have common intellectual foundations and that the growth of both will be the quicker and surer if the builders of each keep an eye on the progress of the other."

ACKNOWLEDGMENTS

I wish to thank the many workers in the field of heavy-ion physics who have written excellent reviews which helped me to prepare these chapters. Also I owe many thanks to my immediate colleagues in Berkeley, M. Buenerd, M. Bini, C. K. Gelbke, B. G. Harvey, D. L. Hendrie, J. L. Laville, J. Mahoney, A. Menchaca-Rocha, M. C. Mermaz, C. Olmer, and H. Wieman, and also to the wider milieu of research and research workers in Berkeley from whom I absorbed many ideas.

This work has been sponsored by the U.S. Department of Energy.

REFERENCES

Caveat

The list of references is not scholarly either in its completeness, or in its attention to historical development. The references are illustrative, and were readily accessible or well known to the author at the time of writing the paper.

1. Proceedings of the International Conference on Nuclear Reactions Induced by Heavy Ions, editors R. Bock and W. R. Hering (North-Holland, Amsterdam, 1970).
2. Proceedings of the International Conference on Heavy-Ion Physics (Dubna, 1971), JINR Report D7-5769.
3. Symposium on Heavy-Ion Reactions and Many-Particle Excitations (Saclay, 1971), Colloque du Journal de Physique 32, C6 (1971).
4. Proceedings of the Symposium on Heavy-Ion Scattering (Argonne, 1971), Argonne Report ANL-7837.
5. European Conference on Nuclear Physics (Aix-en-Provence, 1972), Colloque du Journal de Physique 33, C5 (1972).
6. Proceedings of Heavy-Ion Summer Study (Oak Ridge, 1972), editor S. T. Thornton, USAEC Report CONF-720669.
7. Proceedings of the Heavy-Ion Transfer Reaction Symposium (Argonne, 1973), Argonne Report PHY-1973B.
8. Proceedings of the International Conference on Nuclear Physics, editors J. de Boer and J. H. Mang (North-Holland, Amsterdam, 1973).
9. Proceedings of the International Conference on Reactions Between Complex Nuclei, editors R. L. Robinson, F. K. McGowan, J. B. Ball and J. H. Hamilton (North-Holland, Amsterdam, 1974).
10. Second High Energy Heavy-Ion Summer Study (Berkeley, 1974), Lawrence Berkeley Laboratory Report LBL-3675.
11. Proceedings of the Symposium on Classical and Quantum Mechanical Aspects of Heavy-Ion Collisions, editors H. L. Harvey, P. Braun-Munzinger and C. K. Gelbke, Lecture Notes in Physics 33 (Springer, Berlin/Heidelberg/New York, 1975).
12. Proceedings of the Symposium on Macroscopic Features of Heavy-Ion Collisions (Argonne, 1976), Argonne Report ANL/PHY-76-2.
13. Third Summer Study on High Energy Heavy Ions (Berkeley, 1976), Lawrence Berkeley Laboratory Report.

14. European Conference on Nuclear Physics with Heavy Ions (Caen, 1976), Colloque du Journal de Physique 37, C5 (1976).
15. Theoretical Aspects of Heavy-Ion Collisions (Falls Creek, Tennessee 1977), ORNL Report, to be published.
16. Proceedings of the International Conference on Nuclear Physics (Tokyo, 1977) (to be published).
17. D. A. Bromley, Ref. 8, p.22.
18. W. J. Swiatecki, Ref. 10, p.349.
19. R. Stock and A. M. Poskanzer, Comments on Nuclear and Particle Physics VII, 41 (1977).
20. R. A. Broglia and A. Winther, Phys. Reports C4, 153 (1972).
21. N. K. Glendenning, Rev. Mod. Phys. 47, 659 (1975).
22. W. E. Frahn, Ann. of Phys. 72, 524 (1972).
23. T. Koeling and R. A. Malfliet, Phys. Reports 22C, 181 (1975).
24. J. Knoll and R. Schaeffer, Ann. of Phys. 97, 307 (1976).
25. D. M. Brink, Lectures on Heavy-Ion Reactions (Orsay, March 1972) (unpublished).
26. J. S. Blair, Phys. Rev. 95, 1218 (1954).
27. W. E. Frahn, Ref. 11, p.102 and references therein.
28. J. B. Ball, C. B. Fulmer, E. E. Gross, M. L. Halbert, D. C. Hensley, C. A. Ludemann, M. J. Saltmarsh and G. R. Satchler, Nucl. Phys. A252, 208 (1975).
29. G. R. Satchler, Ref. 9, p.171.
30. C. Olmer, M. C. Mermaz, M. Buenerd, C. K. Gelbke, D. L. Hendrie, J. Mahoney, A. Menchaca-Rocha, D. K. Scott, M. H. Macfarlane and S. C. Pieper, Phys. Rev. Lett. 38, 476 (1977), and references therein.
31. D. A. Goldberg and S. M. Smith, Phys. Rev. Lett. 29, 500 (1972).
32. J. G. Cramer, R. M. DeVries, D. A. Goldberg, M. S. Zisman and C. F. Maguire, Phys. Rev. C14, 2158 (1976).
33. D. F. Jackson and R. C. Johnson, Phys. Lett. 49B, 249 (1974).
34. J. P. Vary and C. B. Dover, Phys. Rev. Lett. 31, 1510 (1973).
35. R. M. DeVries, D. A. Goldberg, J. W. Watson, M. S. Zisman and J. G. Cramer, Phys. Rev. Lett. 39, 450 (1977).
36. J. Wilczynski and K. Siwek-Wilczynska, Phys. Lett. 55B, 270 (1975); J. Wilczynski, Nucl. Phys. A216, 386 (1973).

37. W. D. Myers, Nucl. Phys. A204, 465 (1973).

38. J. Blocki, J. Randrup, W. J. Swiatecki, and C. F. Tsang, Lawrence Berkeley Laboratory Report LBL-5014 (1976), to be published in Ann. of Phys.

39. D. M. Brink, Ref. 14, p.C-47;
Fl. Stancu and D. M. Brink, Nucl. Phys. A 270, 236 (1976).

40. D. M. Brink and Fl. Stancu, Nucl. Phys. A 243, 175 (1975).

41. C. Ngô, B. Tamain, M. Beiner, R. J. Lombard, D. Mas and H. H. Duebler, Nucl. Phys. A 252, 237 (1975).

42. W. U. Schröder and J. R. Huizenga, University of Rochester Report UR-NSRL-144 (1977), to be published in Ann. Rev. of Nucl. Science.

43. P. R. Christensen and A. Winther, Phys. Lett. 65B, 19 (1976).

44. P. Braun-Munzinger, G. M. Berkowitz, T. M. Cormier, C. M. Jackcinski, J. W. Harris, J. Barrette and M. J. Levine, Phys. Rev. Lett. 38, 944 (1977).

45. K. W. McVoy, Ref. 11, p.127; Phys. Rev. C3, 1104 (1971).

46. C. E. Thorn, M. J. Levine, J. J. Kolata, C. Flaum, P. D. Bond and J. C. Sens, Phys. Rev. Lett. 38, 384 (1977).

47. W. G. Love, T. Teresawa and G. R. Satchler, Phys. Rev. Lett. 39, 6 (1977); and Nucl. Phys. A, to be published.

48. J. R. Huizenga, Ref. 12, p.1.

49. A. J. Baltz, S. K. Kauffmann, N. K. Glendenning, and K. Preuss, to be published in Phys. Rev. Lett; Nucl. Phys. A; Lawrence Berkeley Laboratory Report LBL-Preprint-6588 (1977).

50. J. Cerny, Proceedings of the Third International Conference on Nuclei far from Stability (Cargèse, 1976), CERN Report 76-13, p.225.

51. A. G. Artukh, V. V. Avdeichikov, L. P. Chelnokov, G. F. Gridnev, V. L. Mikheev, V. I. Vakatov, V. V. Volkov and J. Wilczynski, Phys. Lett. B 32, 43 (1970).

52. A. G. Artukh, V. V. Avdeichikov, J. Ero, G. F. Gridnev, V. L. Mikheev, V. V. Volkov and J. Wilczynski, Nucl. Phys. A160, 511 (1971).

53. G. T. Garvey, Comments on Nucl. and Particle Phys. V, 85 (1972).

54. O. L. Keller, Comments on Nucl. and Particle Phys. V, 95 (1972).

55. B. G. Harvey, J. Mahoney, F. G. Pühlhofer, F. S. Goulding, D. A. Landis, J. G. Faivre, D. G. Kovar, M. S. Zisman, J. R. Merwether, S. W. Cooper and D. L. Hendrie, Nucl. Instr. and Meth. 104, 21 (1972);

H. Homeyes, J. Mahoney and B. G. Harvey, Nucl. Instr. and Meth. 118, 311 (1974); B. G. Harvey, J. Mahoney et al., to be published.

56. P. Armbruster, Ref. 14, p.161.
57. G. C. Ball, W. G. Davies, J. S. Forster and H. R. Andrews, Phys. Lett. 60B, 265 (1976).
58. G. T. Garvey, W. J. Gerace, R. L. Jaffe, I. Talmi and I. Kelson, Rev. Mod. Phys. 41, S1 (1969).
59. N. A. Jelley, J. Cerny, D. P. Stahel and K. H. Wilcox, Phys. Rev. C11, 2049 (1975).
60. W. R. Phillips, Report on Progress in Phys. 40, 345 (1977).
61. A. J. Baltz and S. Kahana, Adv. in Phys., to be published.
62. H. T. Fortune, Ref. 16.
63. D. K. Scott, D. L. Hendrie, L. Kraus, C. F. Maguire, J. Mahoney, Y. Terrien and K. Yagi, Phys. Rev. Lett. 36, 226 (1976).
64. V. M. Strutinskii, Phys. Lett. 44B, 245 (1973).
65. S. K. Kahana, Ref. 9, p.189.
66. A. J. Baltz, Phys. Rev. Lett. 38, 1197 (1977).
67. W. A. Friedman, K. W. McVoy and G. W. T. Shuy, Phys. Rev. Lett. 33, 308 (1974).
68. D. K. Scott, Ref. 11, p.165.
69. W. F. Frahn, Heavy-Ion High Spin States and Nuclear Structure, Vol. 1 (IAEA, Vienna, 1975) p.157.
70. D. M. Brink, Phys. Lett. 40B, 37 (1972).
71. M. Anyas-Weiss, J. C. Cornell, P. S. Fisher, P. N. Hudson, A. Menchaca-Rocha, D. J. Millerer, A. D. Panagiotou, D. K. Scott, D. Strottman, D. M. Brink, B. Buck, P. J. Ellison and T. Engeland, Physics Reports 12C, 201 (1974);
K. G. Nair, H. Voit, C. W. Towsley, M. Hamm, J. D. Bronson and K. Nagatani, Phys. Rev. C12, 1575 (1975) and references therein.
72. K. Sugimoto, N. Takahashi, A. Mizobuchi, Y. Nojiri, T. Minamisono, M. Ishihara, K. Tanaka and H. Kamitsubo, Phys. Rev. Lett. 39, 323 (1977).
73. K. Tanaka, M. Ishihara, H. Kamitsubo, N. Takahashi, A. Mizobuchi, Y. Nojiri, T. Minamisono and K. Sugimoto, IPCR Report 45 (1977).
74. P. D. Bond, Brookhaven Report BNL-Preprint-(1977).
75. A. A. Pilt, D. J. Millener, H. Bradlow, O. Dietzsch, P. S. Fisher, W. J. Naude, W. D. M. Rae and D. Sinclair, Nucl. Phys. A273, 189 (1976).

76. N. Anantaram, R. M. DeVries, J. P. Draayer, H. E. Gove and J. P. Trentelman, Ref. 9, p.43.

77. M. C. Lemaire, Phys. Reports 7C, 280 (1973) and references therein.

78. R. M. DeVries, D. Shapira, W. G. Davies, G. C. Ball, J. S. Forster and W. McLatchie, Phys. Rev. Lett. 35, 835 (1975).

79. W. G. Davies, R. M. DeVries, C. C. Ball, J. S. Forster, M. McLatchie, D. Shapira, J. Toke and R. E. Warner, Nucl. Phys. A279, 477 (1976).

80. R. M. DeVries, J. S. Lilley and M. A. Franey, Phys. Rev. Lett. 37, 481 (1976).

81. D. F. Jackson and M. Rhoades-Brown, Nucl. Phys. A 286, 354 (1977).

82. R. A. Broglia and P. F. Bortignon, Phys. Lett. 65B, 221 (1976).

83. R. M. DeVries, D. Shapira, M. R. Clover, H. E. Gove, J. D. Garrett and G. Sorensen, Phys. Lett. 67B, 19 (1977).

84. K. R. Greider, Ref. 1, p.217.

85. One of the most recent techniques for evaluating this integral is given by D. H. Glockner, M. H. MacFarlane and S. C. Pieper, Argonne National Laboratory Report ANL-76-11 (1976).

86. C. Chasman, S. Kahana and M. Schneider, Phys. Rev. Lett. 31, 1074 (1973).

87. For a discussion of this $\Delta\ell = 1$ problem, see P. D. Bond, C. Chasman, J. D. Garrett, C. K. Gelbke, O. Hansen, M. J. Levine, A. Z. Schwarzschild and C. E. Thorn, Phys. Rev. Lett. 36, 300 (1976);
K. S. Low, T. Tamura and T. Udagawa, Phys. Lett. 67B, 59 (1977);
E. Seglie and R. J. Ascuitto, Phys. Rev. Lett. 39, 688 (1977).

88. For a recent summary, see K. S. Low, Ref. 14, p.C5-15.

89. P. D. Bond, M. J. Levine and C. E. Thorn, Phys. Lett. 68B, 327 (1977).

90. D. K. Scott, B. G. Harvey, D. L. Hendrie, U. Jahnke, L. Kraus, C. F. Maguire, J. Mahoney, Y. Terrien, K. Yagi and N. K. Glendenning, Phys. Rev. Lett. 34, 895 (1975).

91. P. D. Bond, H. J. Körner, M. C. Lemaire, D. J. Pisano and C. E. Thorn, Phys. Rev. C16, 177 (1977).

92. J. C. Peng, M. C. Mermaz, A. Greiner, N. Lisbona and K. S. Low, Phys. Rev. C15, 1331 (1977).

93. M. C. Lemaire and K. S. Low, Phys. Rev. C16, 183 (1977).

94. K. A. Erb, D. L. Hanson, R. J. Ascuitto, B. Sorensen, J. S. Vaagen and J. J. Kolata, Phys. Rev. Lett. 33, 1102 (1974).

95. B. Sorensen, Phys. Lett. 66B, 119 (1977).

96. T. Tamura, Phys. Reports 14C, 61 (1974).

97. T. Kammurri, Phys. Lett. 51B, 442 (1974).

98. R. A. Broglia, U. Götz, M. Ichimura, T. Kammurri and A. Winther, Phys. Lett. 45B, 23 (1973).

99. D. G. Kovar, F. D. Becchetti, B. G. Harvey, D. L. Hendrie, H. Homeyer, J. Mahoney, W. von Oertzen and M. A. Nagarajan, Phys. Rev. Lett. 30, 1075 (1973).

100. M. A. Nagarajan, Nucl. Phys. A196, 32 (1972); A209, 485 (1973).

101. G. R. Satchler, Ref. 7, p.145.

102. R. M. DeVries and K. I. Kubo, Phys. Rev. Lett. 30, 325 (1973).

103. K. S. Toth, J. L. C. Ford, G. R. Satchler, E. E. Gross, D. C. Hensley, S. T. Thornton and T. C. Schweitzer, Phys. Rev. C14, 1471 (1976).

104. K. Pruess, G. Delic, L. A. Charleton and N. K. Glendenning, Ref. 12, p.723.

105. G. Delic, K. Pruess, L. A. Charleton and N. K. Glendenning, Phys. Lett. 69B, 20 (1977).

106. L. A. Charleton, G. Delic, N. K. Glendenning, P. Lichtner and K. Pruess, contributed paper in Ref. 16.

107. W. von Oertzen and H. G. Bohlen, Phys. Reports 19C, 1 (1975) and references therein.

108. K. D. Hildenbrand, R. Bock, H. G. Bohlen, P. Braun-Munzinger, D. Fick, C. K. Gelbke, U. Weiss and W. Weiss, Nucl. Phys. A234, 167 (1974).

109. K. Dietrich, Ann. Phys. (N.Y.) 66, 480 (1971) and references therein.

110. For recent references on this subject, see H. V. Klapdor, H. Reiss and G. Rosner, Eighth Summer School on Nuclear Physics (Mikolajki, Poland, 1975), Nukleonika 21, 763 (1976).

111. H. V. Klapdor, G. Rosner, H. Reiss and M. Schrader, Nucl. Phys. A244, 157 (1975).

112. T. A. Belote, N. Anyas-Weiss, J. A. Becker, J. C. Cornell, P. S. Fisher, P. N. Hudson, A. Menchaca-Rocha, A. D. Panagiotou and D. K. Scott, Phys. Rev. Lett. 30, 450 (1973).

113. M. Böhning, Ref. 1, p.633.

114. R. G. Stokstad, Ref. 9, p.327.

115. N. Marquardt, J. L'Ecuyer, C. Cardinal, R. Volders, M. W. Greene, Ref. 8, Vol. 1, p.476.

116. H. V. Klapdor, H. Reiss, G. Rosner and M. Schrader, Phys. Lett. 49B, 431 (1974).

117. R. Middleton, J. D. Garrett, H. T. Fortune and R. R. Betts, Phys. Rev. Lett. 24, 1436 (1970); Phys. Rev. C4, 1987 (1971).

118. H. V. Klapdor, H. Reiss and G. Rosner, Phys. Lett. 58B, 279 (1975).

119. E. Vogt, Phys. Lett. 40B, 345 (1972).

120. D. A. Bromley, Second International Conference on Clustering Phenomena in Nuclei (Maryland, 1975).

121. H. Feshbach, Ref. 14, p.C5-177.

122. R. H. Siemssen, Proceedings of the International Symposium on Cluster Structure of Nuclei and Transfer Reactions Induced by Heavy Ions (Tokyo, Japan, 1975), p.233.

123. M. L. Halbert, C. B. Fulmer, S. Raman, M. J. Saltmarsh, A. H. Snell and P. H. Stetson, Phys. Lett. 51B, 341 (1974).

124. A. Gobbi, R. Wieland, L. Chua, D. Shapira and D. A. Bromley, Phys. Rev. C7, 30 (1973).

125. R. Vandenbosch, M. P. Webb and M. S. Zisman, Phys. Rev. Lett. 33, 842 (1974).

126. K. S. Low and T. Tamura, Phys. Lett. 40B, 32 (1972).

127. E. R. Cosman, T. M. Cormier, K. van Bibber, A. Sperduto, G. Young, J. Erskine, L. R. Greenwood and O. Hansen, Phys. Rev. Lett. 35, 265 (1975).

128. A. Arima, G. Scharff-Goldhaber and K. W. McVoy, Phys. Lett. 40B, 8 (1972).

129. K. Ikeda, Proceedings of the International Symposium on Cluster Structure of Nuclei and Transfer Reactions Induced by Heavy Ions (Tokyo, Japan, 1975), p.23.

130. B. Imanishi, Nucl. Phys. A125, 33 (1969).

131. Y. Kondo, T. Matsuse and Y. Abe, Proceedings of the Second International Conference on Clustering Phenomena in Nuclei (Maryland, 1975).

132. H. J. Fink, W. Scheid and W. Greiner, Nucl.Phys. A188, 259 (1972).

133. W. Greiner and W. Scheid, J. de Phys. 32, 91 (1971).

134. T. M. Cormier, J. Applegate, G. M. Berkowitz, P. Braun-Munzinger, P. M. Cormier, J. W. Harris, C. M. Jachcinski, L. L. Lee, J. Barrette and H. E. Wegner, Phys. Rev. Lett. 38, 940 (1977).

135. H. Doubre, J. C. Roynette, J. C. Jacmart, N. Poffé, M. Riou, E. Plagnol and P. de Saintignon, Phys. Rev. Lett. 35, 508 (1975).

136. H. Doubre, J. C. Jacmart, E. Plagnol, N. Poffé, M. Riou and J. C. Roynette, Phys. Rev. C15, 693 (1977).

137. W. E. Frahn and K. E. Rehm, to be published.

138. A. Johnson, H. Ryde and J. Sztarkier, Phys. Lett. 34B, 605 (1971).

139. For recent reviews, see D. Ward, Ref. 9, p.417; A. Faessler, Ref. 9, p.437.

140. F. S. Stephens, Comments on Nuclear and Particle Physics VI, 173 (1976); International School of Physics (Varenna, Italy, 1976).

141. M. A. J. Mariscotti, G. Scharff-Goldhaber and B. Buck, Phys. Rev. 178, 1864 (1969).

142. B. R. Mottelson and J. G. Valatin, Phys. Rev. Lett. 5, 511 (1960).

143. P. Thieberger, Phys. Lett. 45B, 417 (1973).

144. F. S. Stephens, Rev. Mod. Phys. 47, 43 (1975).

145. I. Y. Lee, M. M. Aleonard, M. A. Deleplanque, Y. El-Masri, J. O. Newton, R. S. Simon, R. M. Diamond and F. S. Stephens, Phys. Rev. Lett. 38, 1454 (1977).

146. I. Y. Lee, D. Cline, R. S. Simon, P. A. Butler, P. Colombani, M. W. Guidry, F. S. Stephens, R. M. Diamond, N. R. Johnson, and E. Eichler, Phys. Rev. Lett. 37, 420 (1976).

147. A. Bohr and B. R. Mottelson, Physica Scripta 10A, 13 (1974).

148. R. M. Diamond, Australian J. of Phys., to be published.

149. A. Bohr and B. R. Mottelson, Nuclear Structure (Benjamin, N.Y.) Vol. II.

150. B. R. Mottelson, Proceedings of the Nuclear Structure Symposium of the Thousand Lakes (Joutsa, Finland, 1970), Vol. II, p.148.

151. F. S. Stephens, Conference on Highly Excited States of Nuclei (Julich, Germany, 1975).

152. P. J. Tjøm, F. S. Stephens, R. M. Diamond, J. de Boer and W. E. Meyerhof, Phys. Rev. Lett. 33, 593 (1974).

153. R. S. Simon, M. V. Banaschik, P. Colombani, D. P. Soroka, F. S. Stephens and R. M. Diamond, Phys. Rev. Lett. 33, 596 (1974).

154. R. S. Simon, M. V. Banaschik, J. O. Newton, R. M. Diamond and F. S. Stephens, to be published in Nucl. Phys. A.

155. A. Faessler, M. Ploszajczak and K. R. S. Devi, Phys. Rev. Lett. 36, 1028 (1976); J. Pedersen, B. B. Back, F. M. Bernthal, S. Bjørnholm, J. Borggreen, O. Christensen, F. Folkmann, B. Herskind, T. L. Khoo, M. Neiman, F. Pühlhofer and G. Sletten, Phys. Rev. Lett. 39, 990 (1977).

156. J. P. Schiffer, Ref. 8, p.813.

157. W. J. Swiatecki, Rev. 5, p.C4-45.

158. W. J. Swiatecki and S. Björnholm, Phys. Reports 4C, 325 (1972).

159. R. M. Diamond, A. M. Poskanzer, F. S. Stephens, W. J. Swiatecki and D. Ward, Phys. Rev. Lett. 20, 802 (1968).

160. For a recent review, see G. N. Flerov, Proceedings of the Third International Conference on Nuclei far from Stability (Cargèse, Corsica, 1976) CERN Report 76-13; and G. N. Flerov, Ref. 16.

161. R. V. Gentry, T. A. Cahill, N. R. Fletcher, H. C. Kaufmann, L. R. Medsker, J. W. Nelson and R. Flocchini, Phys. Rev. Lett. 37, 11 (1976); N. R. Fletcher, Phys. Rev. Lett. 38, 479 (1977).

162. S. Cohen, F. Plasil and W. J. Swiatecki, Annals of Physics 82, 557 (1974).

163. H. Gauvin, D. Guerreau, Y. Le Beyec, M. Lefort, F. Plasil and X. Tarrago, Phys. Lett. 58B, 228 (1975).

164. M. Lefort, Ref. 11, p.274; M. Lefort, Reports on Prog. in Phys. 39, 129 (1976).

165. M. Lefort, Ref. 14, p.C5-57.

166. M. Lefort, J. Phys. A7, 107 (1974).

167. J. Galin, D. Guerreau, M. Lefort and X. Tarrago, Phys. Rev. C9, 1018 (1974).

168. D. Glas and U. Mosel, Nucl. Phys. A237, 429 (1975).

169. D. L. Hill and J. A. Wheeler, Phys. Rev. 89, 1102 (1953).

170. W. D. Myers, Nucl. Phys. A204, 465 (1973) and Ref. 9, p.1.

171. S. Vigdor, Ref. 12, p.95.

172. R. G. Stokstad, Ref. 16.

173. R. G. Stokstad, R. A. Dayras, J. Gomez del Campo, P. H. Stelson, C. Olmer and M. S. Zisman, to be published in Phys. Rev. C.

174. J. R. Huizenga and J. R. Birkelund, to be published.

175. E. Seglie, D. Sperber and A. Sherman, Phys. Rev. C11, 1227 (1975).

176. R. Bass, Phys. Lett. 47B, 139 (1973); Nucl. Phys. A231, 45 (1974); Phys. Rev. Lett. 39, 265 (1977).

177. J. Natowitz, Ref. 15.

178. C. K. Gelbke, C. Olmer, M. Buenerd, D. L. Hendrie, J. Mahoney, M. C. Mermaz and D. K. Scott, Phys. Reports, to be published.

179. M. Buenerd, C. K. Gelbke, B. G. Harvey, D. L. Hendrie, J. Mahoney, A. Menchaca-Rocha, C. Olmer and D. K. Scott, Phys. Rev. Lett. 37, 1191 (1976).

180. R. Beck and D. H. E. Gross, Phys. Lett. B47, 143 (1973).

181. D. H. E. Gross and H. Kalinowski, Phys. Lett. B48, 302 (1974).

182. J. P. Bondorf, M. I. Sobel, D. Sperber, Phys. Reports C15, 83 (1974).

183. K. Siwek-Wilczynska and J. Wilczynski, Nucl. Phys. A264, 115 (1976); Nukleonika 21, 517 (1976).

184. C. F. Tsang, Physica Scripta 10A, 90 (1974).

185. W. D. Myers, Ref. 9, p.1.

186. M. Hillman and Y. Eyal, Ref. 14, p.109.

187. F. Pühlhofer, Nucl. Phys. A280, 267 (1977).

188. J. Barrette, P. Braun-Munzinger, C. K. Gelbke, H. L. Harney, H. E. Wegner, B. Zeidman, K. D. Hildenbrand and U. Lynen, to be published.

189. D. Glas and U. Mosel, Phys. Lett. 49B, 301 (1974).

190. D. Glas and U. Mosel, Nucl. Phys. A264, 268 (1976).

191. P. Sperr, T. H. Braid, Y. Eisen, D. G. Kovar, F. W. Prosser, J. P. Schiffer, S. L. Tabor and S. Vigdor, Phys. Rev. Lett. 37, 321 (1976).

192. M. Conjeaud, S. Gary, S. Harar and J. P. Wieleckzo, Ref. 14, p.116.

193. D. Pelte and U. Smilansky, Ref. 14, p.103.

194. P. Sperr, S. Vigdor, Y. Eisen, W. Henning, D. G. Kovar, T. R. Ophel and B. Zeidman, Phys. Rev. Lett. 36, 405 (1976).

195. H. Gauvin, R. L. Hahn, Y. Le Beyec and M. Lefort, Phys. Rev. C10 722 (1974).

196. C. Cabot, H. Gauvin, Y. Le Beyec and M. Lefort, J. de Physique L36, 289 (1976).

197. H. C. Britt, B. H. Erkkila, P. D. Goldstone, R. H. Stokes, B. B. Back, F. Folkman, O. Christensen, B. Fernandez, J. D. Garrett, G. B. Hagemann, B. Herskind, D. L. Hillis, F. Plasil, R. L.

Ferguson, M. Blann and H. H. Gutbrod, LBL Preprint (1977).

198. J. Galin, Ref. 14, p.C5-83.

199. P. A. M. Dirac, Proceedings Camb. Phil. Soc. 26, 376 (1930).

200. P. Bonche, S. E. Koonin and J. W. Negele, Phys. Rev. C13, 1226 (1976).

201. For detailed reviews see, A. K. Kerman, Proceedings of the Enrico Fermi Summer School (Varenna, Italy, 1976); P. Bonche, Ref. 14, p.C5-213; J. W. Negele, Ref. 15.

202. Three-dimensional calculations are discussed by H. Flocard, S. E. Koonin and M. S. Weiss, LBL-Preprint-6546 (1977), to be published.

203. G. F. Bertsch and S. F. Tsai, Physics Reports 18C (1975).

204. S. E. Koonin, K. T. R. Davies, V. Maruhn-Rezwani, H. Feldmeier, S. J. Krieger and J. W. Negele, Phys. Rev. C15, 1359 (1977).

205. For a recent review, see W. U. Schröder and J. R. Huizenga, University of Rochester Report UR-NSR-144 (1977), to be published in Vol. 27 of Annual Review of Nucl. Science.

206. One of the earliest experiments related to this phenomenon is that of K. Kaufman and W. Wolfgang, Phys. Rev. 121, 192 (1961). Other early works include: G. F. Gridnev, V. V. Volkov, and J. Wilczynski, Nucl. Phys. A142, 385 (1970); J. Galin, D. Guerreau, M. Lefort, J. Péter and X. Tarrago, Nucl. Phys. A159, 461 (1970).

207. J. V. Kratz, J. O. Lilzenzin, A. E. Norris and G. T. Seaborg, Phys. Rev. C13, 2347 (1976).

208. A. G. Artukh, G. F. Gridnev, V. L. Mikheev, V. V. Volkov and J. Wilczynski, Nucl. Phys. A211, 299 (1973); A215, 91 (1973).

209. J. Wilczynski, Phys. Lett. B47, 484 (1973).

210. H. H. Deubler and K. Dietrich, Phys. Lett. 56B, 241 (1975).

211. V. V. Volkov, Ref. 9, p.363 and V. V. Volkov, Sov. J. of Nucl. Phys. 6, 420 (1976).

212. V. V. Volkov, Ref. 11, p.253.

213. L. G. Moretto, R. Schmitt, Ref. 14, p.C5-109.

214. J. Galin, Ref. 14, p.C5-83.

215. W. Norenberg, Ref. 14, p.C5-141.

216. H. A. Weidenmuller, Ref. 15.

217. W. Trautmann, J. de Boer, W. Dünnweber, G. Graw, R. Kopp, C. Lauterbach, H. Puchta and U. Lynen, Phys. Rev. Lett. 39, 1062 (1977).

218. W. U. Schröder, J. R. Birkelund, J. R. Huizenga, K. L. Wolf, J. P. Unik and V. E. Viola, Phys. Rev. Lett. 36, 514 (1976).

219. T. Udagawa, T. Tamura and K. S. Low, Phys. Rev. Lett. 34, 30 (1975).

220. T. Tamura, T. Udagawa, D. H. Feng and K.-K. Kan, Phys. Lett. 66B, 109 (1977).

221. J. P. Bondorf, Ref. 9, p.383.

222. W. Nörenberg, Phys. Lett. 52B, 289 (1974).

223. W. Nörenberg, Z. Physik A274, 241 (1975).

224. S. Ayik, B. Schurmann and W. Nörenberg, Z. Physik A277, 299 (1976).

225. J. R. Huizenga, Ref. 15.

226. J. R. Huizenga, J. R. Birkelund, W. U. Schröder, K. L. Wolf and V. E. Viola, Phys. Rev. Lett. 37, 885 (1976).

227. For a fuller discussion, see M. Lefort, Symposium on New Avenues in Nuclear Physics (Rehovot, Israel, 1976).

228. G. Wolschin and W. Nörenberg, Heidelberg Preprint MPI H-1977-V15.

229. B. Cauvin, R. P. Schmitt, G. J. Wozniak, P. Glassel, P. Russo, R. C. Jared, J. B. Moulton and L. G. Moretto, Nucl. Phys. A, to be published.

230. D. H. E. Gross, Nucl. Phys. A240, 472 (1975).

231. W. U. Schröder, J. R. Birkelund, J. R. Huizenga, K. L. Wolf and V. E. Viola, Phys. Rev. C16, 623 (1977).

232. J. P. Bondorf, J. R. Huizenga, M. I. Sobel and D. Sperber, Phys. Rev. C11, 1265 (1975).

233. J. R. Huizenga, Nucleonika 20, 291 (1975).

234. J. P. Bondorf, Ref. 14, p.C5-195.

235. K. Albrecht and W. Stocker, Nucl. Phys. A278, 95 (1977).

236. J. Randrup, Lawrence Berkeley Laboratory Preprint (1977).

237. J. Blocki, J. Randrup, W. J. Swiatecki and C. F. Tsang, Lawrence Berkeley Laboratory Report LBL-5014.

238. R. A. Broglia, C. H. Dasso and A. Winther, Phys. Lett. B61, 113 (1976).

239. M. Ishihara, T. Numao, T. Fukada, K. Tanaka and T. Inamura, Ref. 12, p.617.

240. P. Glassel, R. S. Simon, R. M. Diamond, R. C. Jared, I. Y. Lee, L. G. Moretto, J. O. Newton, R. Schmitt and F. S. Stephens, Phys. Rev. Lett. 38, 331 (1977).

241. M. Berlanger, M. A. Deleplanque, C. Gerschel, F. Hanappe, M. Leblanc, J. F. Mayault, C. Ngô, D. Paya, N. Perrin, J. Peter, B. Tamain and L. Valentin, J. Phys. Lettres 37, L323 (1976).

242. P. Dyer, R. J. Puigh, R. Vandenbosch, T. D. Thomas and M. S. Zisman, Phys. Rev. Lett. 39, 392 (1977).

243. K. Van Bibber, private communication.

244. D. H. E. Gross and H. Kalinowski, Ref. 11, p.194.

245. For a recent review, see J. Galin, Ref. 16.

246. H. Bethe, Phys. Rev. 53, 675 (1938).

247. R. M. Weiner, Phys. Rev. Lett. 32, 630 (1974).

248. R. Weiner and M. Westrom, Phys. Rev. Lett. 34, 1523 (1975).

249. R. Weiner and M. Westrom, Nucl. Phys. A286, 282 (1977).

250. H. Ho, R. Albrecht, W. Dunnweber, G. Graw, S. G. Steadman, J. P. Wurm, D. Disdier, V. Rauch and F. Schiebling, Z. Phys. A283, 235 (1977).

251. S. Tomonaga, Z. Phys. 110, 573 (1938).

252. D. H. E. Gross and J. Wilczynski, Phys. Lett. 67B, 1 (1977).

253. R. Stock, Chapter on Nuclear Reactions Between Relativistic Heavy Ions, in Heavy-Ion Collisions, editor R. Bock (North-Holland, Amsterdam, to be published).

254. For recent reviews, see Refs. 10 and 13.

255. R. Stock and A. M. Poskanzer, Comments on Nuclear and Particle Physics VII, 41 (1977).

256. B. Jakobsson, Heavy-Ion Reactions at High Energies, Publication CRN/PN-77-3 from Centre de Recherches Nucléaires de Strasbourg.

257. A. M. Poskanzer, Ref. 16 and LBL-Preprint-6586.

258. J. P. Bondorf, Nuclear Reactions and Nuclear Reactions with Heavy Ions, from Enrico Fermi Summer School (Varenna, Italy, 1974).

259. D. E. Greiner, P. J. Lindstrom, H. H. Heckman, B. Cork and F. S. Bieser, Phys. Rev. Lett. 35, 152 (1975).

260. H. Kamitsubo, Ref. 12, p.177; Proceedings of the International Conference on the Structure of Nuclei and Transfer Reactions Induced by Heavy Ions (Tokyo, 1975), p.623.

261. H. Kamitsubo, M. Yoshie, I. Kohno, S. Nakajima, I. Yamane and T. Mikumo, Ref. 7, p.549.

262. T. Mikumo, I. Kohno, K. Katori, T. Motobayashi, S. Nakajima, M. Yoshie and H. Kamitsubo, Phys. Rev. C14, 1458 (1976).

263. J. P. Bondorf, F. Dickmann, D. H. E. Gross and P. J. Siemens, Ref. 3, p.C6-145.

264. A. Y. Abul-Magd and K. I. El-Abed, Prog. of Th. Phys. (Japan) 53, 480 (1975) and references therein.

265. C. Toepffer, Phys. Rev. Lett. 27, 872 (1971).

266. P. J. Lindstrom, D. E. Greiner, H. H. Heckman, B. Cork and F. S. Bieser, LBL-Preprint-3650 (1975).

267. N. Masuda and F. Uchiyama, Phys. Rev. C15, 1598 (1977).

268. A. S. Goldhaber, Phys. Lett. 53B, 306 (1974), and references therein.

269. H. Feshbach and K. Huang, Phys. Lett. 47B, 300 (1973).

270. R. K. Bhaduri, Phys. Lett. 50B, 211 (1974).

271. V. K. Lukyanov and A. I. Titov, Phys. Lett. 57B, 10 (1975).

272. C. K. Gelbke, D. K. Scott, M. Bini, D. L. Hendrie, J. L. Laville, J. Mahoney, M. C. Mermaz and C. Olmer, LBL-Preprint-6551 (1977) and to be published in Phys. Lett. B (1977).

273. C. K. Gelbke, M. C. Mermaz, C. Olmer and D. K. Scott, Phys. Lett. 65B, 227 (1976).

274. H. Bøggild and T. Ferbel, Ann. Rev. of Nucl. Sci. 24, 451 (1974).

275. W. R. Frazer, L. Ingber, C. H. Mehta, C. H. Poon, D. Silverman, K. Stowe, P. D. Ting and H. Y. Tesian, Rev. Mod. Phys. 44, 284 (1972).

276. D. F. Jackson, University of Surrey Preprint (1977), to be published.

277. J. D. Bowman, W. J. Swiatecki and C. F. Tsang, LBL-Preprint-2908 (1973).

278. J. Hufner, K. Schafer and B. Schurmann, Phys. Rev. C12, 1888 (1975).

279. J. P. Bondorf and W. Nörenberg, Phys. Lett. 44B, 487 (1973).

280. G. D. Westfall, J. Gosset, P. J. Johansen, A. M. Poskanzer, W. G. Meyer, H. H. Gutbrod, A. Sandoval and R. Stock, Phys. Rev. Lett. 37, 1202 (1976).

281. R. J. Glauber, Lectures in Theoretical Physics, editors W. E. Brittin and L. G. Dunham (Interscience, N.Y., 1959), Vol. 1.

282. W. Czyz and L. C. Maximon, Ann. Phys. 52, 59 (1969).

283. J. Hufner, C. Sander and G. Wolschin, University of Heidelberg Preprint (1977).

284. C. K. Gelbke, M. Bini, C. Olmer, D. L. Hendrie, J. L. Laville, J. Mahoney, M. C. Mermaz, D. K. Scott and H. H. Wieman, LBL-Preprint-6563 (1977), to be published in Phys. Lett B. (1977).

285. See, for example, An Atlas of Heavy-Ion Fragmentation Topology, prepared by H. H. Heckman, D. E. Greiner, P. J. Lindstrom and D. D. Tuttle (unpublished).

286. L. S. Schroeder, Proceedings of Topical Meeting on Multiparticle Production of Nuclei at Very High Energy, ICTP (Trieste, 1976).

287. R. Kullberg, K. Kristiansson, B. Lindkvist and I. Otterlund, Nucl. Phys. A, to be published.

288. P. J. Karol, Phys. Rev. C14, 1203 (1975).

289. J. Gosset, H. H. Gutbrod, W. G. Meyer, A. M. Poskanzer, A. Sandoval, R. Stock and G. D. Westfall, Phys. Rev. C16, 629 (1977).

290. W. D. Myers, LBL-Preprint-6569 (1977), to be published in Nucl. Phys.

291. H. H. Gutbrod, A. Sandoval, P. J. Johansen, A. M. Poskanzer, J. Gosset, W. G. Meyer, G. D. Westfall and R. Stock, Phys. Rev. Lett. 37, 667 (1976).

292. A. Mekjian, LBL-Preprint-5819 (1976); Phys. Rev. Lett. 38, 640 (1977).

293. P. B. Price, J. Stevenson and K. Frankel, Phys. Rev. Lett. 39, 177 (1977).

294. P. J. McNulty, G. E. Farrell, R. C. Filz, W. Schimmerling and K. G. Vosburgh, Phys. Rev. Lett. 38, 1519 (1977).

295. R. K. Smith, Ref. 15.

296. A. E. Glassgold, W. Hechrotte and K. M. Watson, Ann. Phys. 6, 1 (1959).

297. W. Scheid, H. Muller and W. Greiner, Phys. Rev. Lett. 32, 741 (1974); 36, 88 (1976).

298. A. A. Amsden, G. F. Bertsch, F. H. Harlow and J. R. Nix, Phys. Rev. Lett. 35, 905 (1975).

299. M. I. Sobel, P. J. Siemens, J. P. Bondorf and H. A. Bethe, Nucl. Phys. A251, 502 (1975).

300. G. Chapline, M. Johnson, E. Teller and M. Weiss, Phys. Rev. D8, 4302 (1973).

301. J. A. Maruhn, Ref. 15.

302. A. A. Amsden, F. H. Harlow and J. R. Nix, Phys. Rev. C15, 2059 (1977) and references therein.

303. J. P. Bondorf, P. J. Siemens, H. Feldmeier, S. Garpman and E. C. Halbert, Z. Phys. 279, 385 (1976).

304. A. R. Bodmer and C. M. Panos, Phys. Rev. C15, 1342 (1977) and references therein.

305. A. R. Bodmer, Ref. 15.

306. H. G. Baumgart, J. U. Schott, Y. Sakamoto, E. Schopper, H. Stocker, J. Hofman, W. Scheid and W. Greiner, Z. Phys. A273, 359 (1975).

307. B. Jakobsson, R. Kullberg and I. Otterlund, Nucl. Phys. A276, 522 (1977).

308. A. M. Poskanzer, R. G. Sextro, A. M. Zebelman, H. H. Gutbrod, A. Sandoval and R. Stock, Phys. Rev. Lett. 35, 1701 (1975).

309. H. J. Crawford, P. B. Price, J. Stevenson and L. W. Wilson, Phys. Rev. Lett. 34, 329 (1975).

310. E. Schopper, Ref. 15.

311. T. D. Lee, Rev. Mod. Phys. 47, 267 (1975).

312. A. B. Migdal, O. A. Markin and I. I. Mishustin, Sov. Phys. JETP 39, 212 (1974).

313. R. F. Sawyer and D. J. Scalapino, Phys. Rev. D7, 953 (1973).

314. A. T. Laasanen, C. Ezell, L. J. Gutay, N. W. Schreiner, P. Schubelin, L. von Linden and F. Turkot, Phys. Rev. Lett. 38, 1 (1977).

315. D. H. Wilkinson, Proc. Phys. Soc. 80, 997 (1962).

TECHNICAL INFORMATION DEPARTMENT
LAWRENCE BERKELEY LABORATORY
UNIVERSITY OF CALIFORNIA
BERKELEY, CALIFORNIA 94720